THE ELECTRONIC STRUCTURE OF THE ION PAIR STATES OF MOLECULAR IODINE

By

Philip J. Jewsbury

DOCTOR OF PHILOSOPHY
EDINBURGH UNIVERSITY
1991.

This thesis was composed by myself and, except where due acknowledgement is made, is based on my own work carried out whilst a member of the laser chemistry group at Edinburgh University.

30th October 1991.

Date

Acknowledgements

I would like to thank my research supervisors, Dr. Kenneth Lawley, Professor Robert Donovan and Dr. Pat Langridge-Smith, for their continued encouragement whilst studying in Edinburgh. I am especially indebted to Kenneth Lawley for his patience in our many discussions of this work, in particular that covered in Chapter 6. The experimental work covered in this thesis would not have been possible without the expert help of Dr. Trevor Ridley; together these people have made my time in Edinburgh not only academically stimulating but an enjoyable experience. Thanks to the University of Edinburgh for supporting me financially, and to ICI plc for scholarship funding.

I would like to thank my parents, John and Margaret, and the rest of my family, Alison, Sue and Jessica, and the many friends who gave me the confidence to continue when I was struggling. Thanks to Vikki Bell, Andy Cooke and Kathleen McCormack for sharing the lonely road writing up; thanks to the members of the sports club-Tim Kirkpatrick, Fran van Dijk, Ken Dixon, and Charlotte Pomery; to Neeraj Malhotra and Kath Hind; to Dave Edwards and to Daniela de Lorenzo. Though they may not know it they have all helped me. Thanks to my friends from Cambridge for paying the taxes that paid my wages, and for making me feel good with my 'career' decision. Finally I need to mention Julia Cream, Clare Rowley and Katie Smith-this has been a 4/2 production and I enjoyed it.

Abstract

The electronic configurations of molecular states of iodine are studied through the Optical-Optical Double Resonance excitation of the ion pair states in low vibrational levels. The two photon OODR excitation of *ungerade* IP states from the *gerade* ground state is rationalised and the strength of u/g coupling at the intermediate step interpreted in terms of a hyperfine interaction first described by Broyer *et al.* The potential function of the $c1_g(ab)$ *gerade* coupling partner in the hyperfine Hamiltonian is derived, along with the lowest levels of a new IP state in the second cluster, the $H1_u(2)$ state. An OODR excitation scheme for populating the $0_u^-(2)$ IP state is proposed and the dominant component of the $c1_g(ab)$ state configuration is found for $R \approx 5.5$Å.

The radiative lifetimes of nine IP states in low vibrational levels are determined and combined with the relative fluorescent intensities of the IP→Valence charge transfer transitions to derive the Einstein A-coefficients for all the strong transitions from these IP states. A theoretical model is developed in terms of a separated atom description for the electronic configurations of these states and is used to predict the relative dipole strengths of the IP→Valence transitions. The Einstein A-coefficients are then interpreted to give the electronic configurations of the IP states around R_e^{IP} and the relative strengths of the transition dipoles for $p_\sigma \leftrightarrow p_\sigma$ and $p_\pi \leftrightarrow p_\pi$ electron transfer between ionic centres. A significant difference from the free ion configurations is found with the lowest energy IP states of a given symmetry adopting as low a p_σ occupancy at the cationic centre as the inter-electron repulsion and spin-orbit energies will allow. This stabilisation is driven by the field gradient due to the anionic charge. The model for the charge transfer transition accounts for the large difference in the summed dipole strengths that is observed for some u/g pairs, even though they have closely similar electronic configurations, and using this model the radiative intensities are shown to be consistent with results from other techniques that probe the electronic structure

of IP states. The transition dipole function for the $F0_u^+(2) \rightarrow X0_g^+(aa)$ transition is established over the range $3.13 \leq R \leq 4.12$Å and its form interpreted in terms of the same electron transfer model. The inferred changes in the electronic configuration of the $F0_u^+(2)$ state with internuclear separation are shown to be consistent with experimental results for related transitions and with *ab initio* calculations from other research groups.

A rationalisation for the observed energy ordering of the states within an ion pair cluster is proposed.

Contents

List of Tables

List of Figures

Thesis plan

Techniques

The first Part of this thesis discusses the experimental and theoretical background to this investigation into the electronic configurations of the ion pair states of iodine.

Chapter 1 discusses the electronic states of I_2, their spectroscopic properties where known, and the various descriptions of their electronic structure. The results of experiments that probe this structure are surveyed. The experimental techniques that have been used in the study of ion pair states are described, before concentrating on the multiphoton techniques used in this thesis. The development of the Optical-Optical Double Resonance technique as applied to the IP states of iodine is described and the leading experimental applications reviewed.

Chapter 2 describes the experimental configurations used in the spectroscopic studies pursued in this thesis. The quantum mechanical simulation program used in the analysis of dispersed fluorescence spectra is detailed and a semi-classical model for the interpretation of fluorescence spectra is discussed; their application to sample results from later Chapters is demonstrated.

Chapter 3 returns to the separated atom model for the molecular electronic wavefunction and develops a description for the configurations at the atomic centres, in particular the cationic centre in the ion pair states. The Russell-Saunders scheme is used as the zero order description with the cationic configuration refined using the familiar spin-orbit coupling to reproduce the term values of the

free cation. The effects of the intramolecular interactions on forming the diatomic are then discussed in terms of a charge-quadrupole interaction between the two ionic centres and a final description of the IP configurations is made assuming a point charge description at each ion, ie no orbital overlap between centres.

Investigations

The second Part of the thesis describes the various experimental investigations undertaken in trying to establish the electronic configurations of the ion pair states.

Chapter 4 discusses the two photon Optical-Optical Double Resonance excitation of the *ungerade* IP states from the *gerade* ground state, $X0_g^+(aa)$. The excitation scheme employs a hyperfine facilitated u/g coupling in the intermediate step and the potential function of the $c1_g(ab)$ state, the *gerade* coupling partner of the well known *ungerade* $B0_u^+(ab)$ state, is determined. As a consequence of this analysis the first few vibrational levels of a previously unknown ion pair state are reported. Knowing the potential functions for the two states involved in the hyperfine interaction, the strength of coupling is predicted from the hyperfine coupling matrix derived by Broyer *et al.* A comparison of the theoretical predictions with the experimental absorption intensities allows the dominant electronic configuration of the $c1_g(ab)$ state to be derived at large R. An OODR excitation scheme for the $0_u^-(2)$ state is proposed. The various OODR excitation schemes used in the thesis are then reviewed and a final experiment performed confirming the Franck-Condon window established by the $B \sim c$ coupled intermediate.

Chapter 5 describes the experimental determination of the radiative lifetimes of nine of the IP states in low v and the results are combined with those for the relative fluorescence intensities for all strong transitions from these states to the valence states to derive the Einstein A-coefficients for the IP→Valence transitions (Chapter 6). A model for the charge transfer process is developed and used to interpret the transition dipole strengths summed over all available transitions

from a given upper state: the IP configurations can then be deduced around R_e^{IP}, along with the transition dipole moments for $p_\sigma \leftrightarrow p_\sigma$ and $p_\pi \leftrightarrow p_\pi$ electron transfer between the two centres. The model accounts for the large differences between the summed dipole moments observed for certain u/g pairs by showing that some charge transfer transitions are only allowed from the *ungerade* state. The predictions of the model are then shown to be consistent with results from other groups studying hyperfine interactions at the cationic centre and with the success of the pure precession model in describing the rotational coupling between ion pair states. These experimental IP configurations are compared with those of the simple picture developed in Chapter 3: significant deviations from the free ion configurations are found.

Chapter 7 discusses the transition dipole moment as a function of R, and its use as a diagnostic for the changing electron configurations of states as the bond stretches. The dispersed fluorescence from the $F0_u^+(2) \rightarrow X0_g^+(aa)$ transition originating from excited vibrational states is analysed to derive the $F \rightarrow X$ transition dipole function over the range $3.13 \leq R \leq 4.12$Å. This is compared with a reported function for the only parallel transition of its *gerade* partner, the $f0_g^+(2)$ to $B0_u^+(ab)$ transition. The comparison of the two functions shows a strong transition moment developing only for the $F \rightarrow X$ transition, as predicted in Chapter 6 for such u/g pairs.

Part I

Techniques

Chapter 1 Introduction

All diatomic molecules have ion-pair (IP) states, that is electronic states that on diabatic dissociation give a pair of ions: those of the alkali, group IIA and IIIA halides have all been extensively studied [1, 2] but arguably the best known family is that of the halogen and interhalogen molecules. Recent interest in the IP states of these molecules has been driven in part by their use in rare gas-halide lasers and by their potential for supporting lasing systems themselves [3, 4, 5, 6, 7, 8, 9, 10]. The experimental study of diatomic ion-pair states has been aided by the timely development of multiphoton methods that have overcome a number of the drawbacks associated with single photon studies, namely the restrictions of one-photon selection rules, one electron excitations and limited Franck-Condon windows. The next section will introduce the halogen electronic states and their characteristic properties with particular reference to iodine. The implications for experimental methodology will be discussed in the final section where the techniques used to investigate the electronic structure of the IP states of iodine will be outlined.

1.1 The electronic states of Iodine

The lower energy electronic states of halogen diatomics can be placed in one of three groups according to their products on diabatic dissociation: valence states give ground state ^2P_J atoms, Rydberg states give one excited and one ground state atom, X*X, and ion-pair states give an X^+X^- pair of oppositely charged ions. The energy of the products at dissociation also increases in the same order.

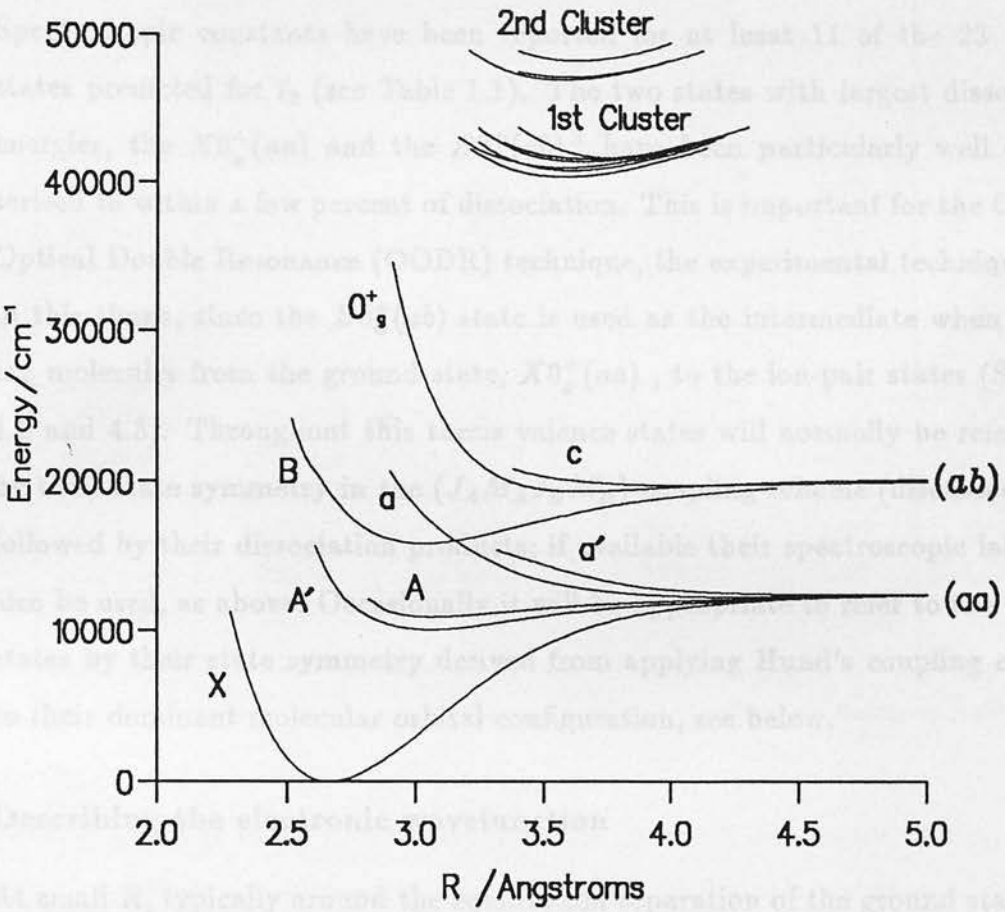

Figure 1.1. Potential curves for the electronic states studied in this thesis.

At smaller internuclear separations the strong Coulombic attraction characteristic of ion-pair states gives rise to avoided crossings with the Rydberg states, and the ion-pair states, having the lower T_e, will thus dissociate adiabatically to X*X atoms. However these avoided crossings occur at large R ($\gg$ 10Å) in regions outside the interest of most spectroscopy, and for I_2 these groups of electronic states are to a large extent independent of each other in the regions studied (with the notable exception of Rydberg/IP state interaction at small R). This is not in general true of the other members of the halogen and interhalogen family and I_2 is often used as a model system for the rest of the series. A schematic potential energy diagram for these low energy states of iodine is given in figure 1.1.

1.1.1 The Valence States

Spectroscopic constants have been reported for at least 11 of the 23 valence states predicted for I_2 (see Table 1.1). The two states with largest dissociation energies, the $X0_g^+(aa)$ and the $B0_u^+(ab)$,[1] have been particularly well characterised to within a few percent of dissociation. This is important for the Optical-Optical Double Resonance (OODR) technique, the experimental technique used in this thesis, since the $B0_u^+(ab)$ state is used as the intermediate when pumping molecules from the ground state, $X0_g^+(aa)$, to the ion-pair states (Sections 1.2 and 4.3). Throughout this thesis valence states will normally be referred to by their state symmetry in the $(J_A M_A J_B M_B)$ coupling scheme (discussed later) followed by their dissociation products; if available their spectroscopic label will also be used, as above. Occasionally it will be appropriate to refer to the valence states by their state symmetry derived from applying Hund's coupling case (a) to their dominant molecular orbital configuration, see below.

Describing the electronic wavefunction

At small R, typically around the equilibrium separation of the ground state (R_e^X =2.67Å), the electronic structure of the valence states is best described in terms of their dominant molecular orbital (MO) configuration, with possibly a small amount of mixing due to spin-orbit coupling and electron correlation. These MO configurations[2] are of the type $\sigma_g^m \pi_u^n \pi_g^p \sigma_u^q$ where only the valence molecular orbitals formed by the 5p atomic orbitals are included and m+n+p+q=10. The molecular orbitals are formed from the simplest LCAO approximation, thus the σ_g and π_g orbitals are for example $\{5p_\sigma^A + 5p_\sigma^B\}$ and $\{5p_\pi^A - 5p_\pi^B\}$ respectively. The $\sigma_{u,g}$(5s) and inner core orbitals are considered common to all valence states. Hund's coupling case (a) can then be applied to the dominant electronic configuration to give the state symmetry [24, p.219]. In this way Mulliken was able to assign the dominant MO configurations of all 43 of iodine's "sub-Rydberg"

[1] a and b refer to ground $^2P_{3/2}$ and excited state $^2P_{1/2}$ atomic dissociation products.
[2] conventionally the MO occupancy is written mnpq.

State	T_e (cm^{-1})	D_e (cm^{-1})	ω_e (cm^{-1})	R_e (Å)	Refs.
$b'2_u(ab)$	(19850)	(300)		(4.25)	[11]
$c1_g(ab)$	19685	465	29.6	4.05	[12]
$0_g^+(ab)$	19286.4	864	64.4	3.645	[13, 14]
$B0_u^+(ab)$	15769.05	4380.95	125.7	3.03	[15]
$a'0_g^+(aa)$	12410.5	136.7	17.7	4.64	[16, 17]
$B''1_u(aa)$	(12367)	(180)	(19.8)	(4.2)	[18]
$a1_g(aa)$	12248.3	298.9	23.6	4.31	[16, 18]
$0_u^-(aa)$	(12190)	(360)	(20.5)	(4.2)	[19]
$A1_u(aa)$	10907	1640.2	94.95	3.06	[20]
$A'2_u(aa)$	10042	2505	108.8	3.08	[21, 22]
$X0_g^+(aa)$	0.0	12547.2	214.55	2.67	[23]

Table 1.1. Principal spectroscopic constants for the known valence states of I_2

states from their state symmetries [25]: for example the ground state, X, has $^1\Sigma_g^+$ symmetry and 2440 occupancy. However Mulliken's ordering of the MO configurations has since proved incorrect in a few cases [15] and a revision of his assignments is given in Table 1.2.

Although appropriate for small internuclear separations the MO approach is no longer the most compact at large R. A series of experiments measuring the hyperfine constants of the $X0_g^+(aa)$ [26, 27], $a'0_g^+(aa)$ [16, 26], $a1_g(aa)$ [26] and $B0_u^+(ab)$ [26] valence states at large R has suggested that for $R > 4$Å the separated atom method gives the simplest description of the molecular wavefunction. This approach implies separate strong spin-orbit coupling at each atom centre as found at the dissociation limit; the resulting electronic angular momentum for the atom i, $\mathbf{J}_i$, is then coupled to the internuclear axis, giving M_{j_i} quantum numbers. Only J and M_j of the two atoms separately are treated as good quantum numbers. The molecular wavefunction is then formed from a product of these

MO configuration	case (a)	case(c)	JJ	Dissociation Products
0442	$^1\Sigma_g^+$	0_g^+	0_g^+	$I^+(^1S_0) + I^-(^1S_0)$
			0_u^+	
1342	$^1\Pi_u$	1_u	2_g	$I^+(^1D_2) + I^-(^1S_0)$
	$^3\Pi_u$	0_u^+	2_u	
		0_u^-	1_g	
		1_u	1_u	
		2_u	$0_g^+(f')$	
2242	$^1\Sigma_g^+$	0_g^+	$0_u^+(F')$	
	$^1\Delta_g$	2_g	$0_g^-(g)$	$I^+(^3P_{1,0}) + I^-(^1S_0)$
	$^3\Sigma_g^-$	0_g^+	0_u^-	
		1_g	$1_g(G)$	
1432	$^1\Pi_g$	1_g	$1_u(H)$	
	$^3\Pi_g$	0_g^+	$0_g^+(f)$	
		0_g^-	$0_u^+(F)$	
		1_g	$2_g(D')$	$I^+(^3P_2) + I^-(^1S_0)$
		2_g	$2_u(\delta)$	
2332	$^1\Sigma_u^+$	0_u^+	$1_g(\beta)$	
	$^1\Delta_u$	2_u	$1_u(\gamma)$	
	$^3\Sigma_u^-$	0_u^+	$0_g^+(E)$	
		1_u	$0_u^+(D)$	
	$^3\Sigma_u^+$	0_u^-	1_u	$I(^2P_{1/2}) + I(^2P_{1/2})$
		1_u	0_u^-	
	$^3\Delta_u$	1_u	0_g^+	
		2_u	2_g	$I(^2P_{3/2}) + I(^2P_{1/2})$
		3_u	$2_u(b')$	
	$^1\Sigma_u^-$	0_u^-	1_g	
1441	$^1\Sigma_u^+$	0_u^+	$1_g(c)$	
	$^3\Sigma_u^+$	0_u^-	1_u	
		1_u	1_u	
2422	$^1\Sigma_g^+$	0_g^+	0_g^-	
	$^1\Delta_g$	2_g	0_u^-	
	$^3\Sigma_g^-$	0_g^+	0_g^+	
		1_g	$0_u^+(B)$	
2341	$^1\Pi_g$	1_g	3_u	$I(^2P_{3/2}) + I(^2P_{3/2})$
	$^3\Pi_g$	0_g^+	$2_u(A')$	
		0_g^-	$1_u(B'')$	
		1_g	$1_u(A)$	
		2_g	2_g	
2431	$^1\Pi_u$	1_u	$1_g(a)$	
	$^3\Pi_u$	0_u^+	0_u^-	
		0_u^-	$0_u^-(B')$	
		1_u	$0_g^+(a')$	
		2_u	$0_g^+(X)$	
2440	$^1\Sigma_g^+$	0_g^+		

Table 1.2. Adiabatic correlation scheme for the "sub-Rydberg" states of I_2.

atomic wavefunctions, suitably symmetrised and normalised:

$$|\, n\Omega\rangle^{(+/-)}_{u,g} = \mathcal{N}.\mathcal{A}\ \{(|\, J_1M_1\rangle_A \,|\, J_2M_2\rangle_B \pm |\, J_2M_2\rangle_A \,|\, J_1M_1\rangle_B) \\ \pm(|\, J_1M_2\rangle_A \,|\, J_2M_1\rangle_B \pm |\, J_2M_1\rangle_A \,|\, J_1M_2\rangle_B)\} \qquad (1.1)$$

The state symmetry is described by the molecular electronic angular momentum along the internuclear axis, Ω, where $\Omega = M_{J_A} + M_{J_B}$, A and B labelling the two identical nuclei. The last pair of terms is only present for $\Omega = 0$ states and then only if new configurations are generated. The +/- parity is defined for $\Omega = 0$ states by the reflection of the space-spin coordinates through a nuclear plane, 0^+ states taking the positive sign that leads the second line. The u/g parity is defined by the usual inversion of space coordinates through the centre of symmetry, *gerade* states taking the negative sign in the inversion terms of the wavefunction. $\mathcal{N}$ is the normalisation term and $\mathcal{A}$ the partial antisymmetriser for electron exchange between the two atoms. n sequentially numbers states that have the same Ω value in ascending energy. The 23 molecular basis functions in this $(J_AM_AJ_BM_B)$ scheme are given in Table 1.3.

In general at any given R ($R \geq R_e^{IP}$) the molecular wavefunction for a given valence state will be dominated by one of the $(J_AM_AJ_BM_B)$ basis functions, ψ. However long-range breakdown of this basis set arises from the r^{-5} quadrupole-quadrupole interaction and as the asymptote is approached states with the same symmetry and dissociation products will mix strongly leading to fully coupled wavefunctions; for example at large R the wavefunctions for the $X0_g^+(aa)$ and $a'0_g^+(aa)$ states become [16]:

$$X\ {}^1\Sigma_g^+ :\ \frac{1}{\sqrt{2}}\{\psi^{aa}_{3/2} - \psi^{aa}_{1/2}\} \qquad (1.2)$$

$$a'\ {}^3\Pi_g :\ \frac{1}{\sqrt{2}}\{\psi^{aa}_{3/2} + \psi^{aa}_{1/2}\} \qquad (1.3)$$

Notation: To avoid ambiguity when referring to the $(J_AM_AJ_BM_B)$ eigenfunctions, ψ, a convention will be adopted throughout this thesis. The superscript will give the states of the atoms on dissociation, while the subscript will indicate

$\Omega^{(+/-)}_{u,g}$ symmetry	Molecular wavefunction
aa dissociation products	
0_g^+	$\frac{1}{\sqrt{2}}\{\|\frac{3}{2},\frac{1}{2}\rangle_A \|\frac{3}{2},-\frac{1}{2}\rangle_B - \|\frac{3}{2},-\frac{1}{2}\rangle_A \|\frac{3}{2},\frac{1}{2}\rangle_B\}$
0_g^+	$\frac{1}{\sqrt{2}}\{\|\frac{3}{2},\frac{3}{2}\rangle_A \|\frac{3}{2},-\frac{3}{2}\rangle_B - \|\frac{3}{2},-\frac{3}{2}\rangle_A \|\frac{3}{2},\frac{3}{2}\rangle_B\}$
0_u^-	$\frac{1}{\sqrt{2}}\{\|\frac{3}{2},\frac{1}{2}\rangle_A \|\frac{3}{2},-\frac{1}{2}\rangle_B + \|\frac{3}{2},-\frac{1}{2}\rangle_A \|\frac{3}{2},\frac{1}{2}\rangle_B\}$
0_u^-	$\frac{1}{\sqrt{2}}\{\|\frac{3}{2},\frac{3}{2}\rangle_A \|\frac{3}{2},-\frac{3}{2}\rangle_B + \|\frac{3}{2},-\frac{3}{2}\rangle_A \|\frac{3}{2},\frac{3}{2}\rangle_B\}$
1_g	$\frac{1}{\sqrt{2}}\{\|\frac{3}{2},\frac{3}{2}\rangle_A \|\frac{3}{2},-\frac{1}{2}\rangle_B - \|\frac{3}{2},-\frac{1}{2}\rangle_A \|\frac{3}{2},\frac{3}{2}\rangle_B\}$
1_u	$\frac{1}{\sqrt{2}}\{\|\frac{3}{2},\frac{3}{2}\rangle_A \|\frac{3}{2},-\frac{1}{2}\rangle_B + \|\frac{3}{2},-\frac{1}{2}\rangle_A \|\frac{3}{2},\frac{3}{2}\rangle_B\}$
1_u	$\|\frac{3}{2},\frac{1}{2}\rangle_A \|\frac{3}{2},\frac{1}{2}\rangle_B$
2_g	$\frac{1}{\sqrt{2}}\{\|\frac{3}{2},\frac{3}{2}\rangle_A \|\frac{3}{2},\frac{1}{2}\rangle_B - \|\frac{3}{2},\frac{1}{2}\rangle_A \|\frac{3}{2},\frac{3}{2}\rangle_B\}$
2_u	$\frac{1}{\sqrt{2}}\{\|\frac{3}{2},\frac{3}{2}\rangle_A \|\frac{3}{2},\frac{1}{2}\rangle_B + \|\frac{3}{2},\frac{1}{2}\rangle_A \|\frac{3}{2},\frac{3}{2}\rangle_B\}$
3_u	$\|\frac{3}{2},\frac{3}{2}\rangle_A \|\frac{3}{2},\frac{3}{2}\rangle_B$
ab dissociation products	
0_g^+	$\frac{1}{2}\{\|\frac{3}{2},\frac{1}{2}\rangle_A \|\frac{1}{2},-\frac{1}{2}\rangle_B - \|\frac{1}{2},-\frac{1}{2}\rangle_A \|\frac{3}{2},\frac{1}{2}\rangle_B + \|\frac{3}{2},-\frac{1}{2}\rangle_A \|\frac{1}{2},\frac{1}{2}\rangle_B - \|\frac{1}{2},\frac{1}{2}\rangle_A \|\frac{3}{2},-\frac{1}{2}\rangle_B\}$
0_g^-	$\frac{1}{2}\{\|\frac{3}{2},\frac{1}{2}\rangle_A \|\frac{1}{2},-\frac{1}{2}\rangle_B - \|\frac{1}{2},-\frac{1}{2}\rangle_A \|\frac{3}{2},\frac{1}{2}\rangle_B - \|\frac{3}{2},-\frac{1}{2}\rangle_A \|\frac{1}{2},\frac{1}{2}\rangle_B + \|\frac{1}{2},\frac{1}{2}\rangle_A \|\frac{3}{2},-\frac{1}{2}\rangle_B\}$
0_u^+	$\frac{1}{2}\{\|\frac{3}{2},\frac{1}{2}\rangle_A \|\frac{1}{2},-\frac{1}{2}\rangle_B + \|\frac{1}{2},-\frac{1}{2}\rangle_A \|\frac{3}{2},\frac{1}{2}\rangle_B + \|\frac{3}{2},-\frac{1}{2}\rangle_A \|\frac{1}{2},\frac{1}{2}\rangle_B + \|\frac{1}{2},\frac{1}{2}\rangle_A \|\frac{3}{2},-\frac{1}{2}\rangle_B\}$
0_u^-	$\frac{1}{2}\{\|\frac{3}{2},\frac{1}{2}\rangle_A \|\frac{1}{2},-\frac{1}{2}\rangle_B + \|\frac{1}{2},-\frac{1}{2}\rangle_A \|\frac{3}{2},\frac{1}{2}\rangle_B - \|\frac{3}{2},-\frac{1}{2}\rangle_A \|\frac{1}{2},\frac{1}{2}\rangle_B - \|\frac{1}{2},\frac{1}{2}\rangle_A \|\frac{3}{2},-\frac{1}{2}\rangle_B\}$
1_g	$\frac{1}{\sqrt{2}}\{\|\frac{3}{2},\frac{3}{2}\rangle_A \|\frac{1}{2},-\frac{1}{2}\rangle_B - \|\frac{1}{2},-\frac{1}{2}\rangle_A \|\frac{3}{2},\frac{3}{2}\rangle_B\}$
1_g	$\frac{1}{\sqrt{2}}\{\|\frac{3}{2},\frac{1}{2}\rangle_A \|\frac{1}{2},\frac{1}{2}\rangle_B - \|\frac{1}{2},\frac{1}{2}\rangle_A \|\frac{3}{2},\frac{1}{2}\rangle_B\}$
1_u	$\frac{1}{\sqrt{2}}\{\|\frac{3}{2},\frac{3}{2}\rangle_A \|\frac{1}{2},-\frac{1}{2}\rangle_B + \|\frac{1}{2},-\frac{1}{2}\rangle_A \|\frac{3}{2},\frac{3}{2}\rangle_B\}$
1_u	$\frac{1}{\sqrt{2}}\{\|\frac{3}{2},\frac{1}{2}\rangle_A \|\frac{1}{2},\frac{1}{2}\rangle_B + \|\frac{1}{2},\frac{1}{2}\rangle_A \|\frac{3}{2},\frac{1}{2}\rangle_B\}$
2_g	$\frac{1}{\sqrt{2}}\{\|\frac{3}{2},\frac{3}{2}\rangle_A \|\frac{1}{2},\frac{1}{2}\rangle_B - \|\frac{1}{2},\frac{1}{2}\rangle_A \|\frac{3}{2},\frac{3}{2}\rangle_B\}$
2_u	$\frac{1}{\sqrt{2}}\{\|\frac{3}{2},\frac{3}{2}\rangle_A \|\frac{1}{2},\frac{1}{2}\rangle_B + \|\frac{1}{2},\frac{1}{2}\rangle_A \|\frac{3}{2},\frac{3}{2}\rangle_B\}$
bb dissociation products	
0_g^+	$\frac{1}{\sqrt{2}}\{\|\frac{1}{2},\frac{1}{2}\rangle_A \|\frac{1}{2},-\frac{1}{2}\rangle_B - \|\frac{1}{2},-\frac{1}{2}\rangle_A \|\frac{1}{2},\frac{1}{2}\rangle_B\}$
0_u^-	$\frac{1}{\sqrt{2}}\{\|\frac{1}{2},\frac{1}{2}\rangle_A \|\frac{1}{2},-\frac{1}{2}\rangle_B + \|\frac{1}{2},-\frac{1}{2}\rangle_A \|\frac{1}{2},\frac{1}{2}\rangle_B\}$
1_u	$\|\frac{1}{2},\frac{1}{2}\rangle_A \|\frac{1}{2},\frac{1}{2}\rangle_B$

Table 1.3. Valence wavefunctions in the $(J_A M_A J_B M_B)$ coupling scheme (after [28]).

the atomic M_J values in the $(J_A M_A J_B M_B)$ eigenfunction: $\frac{3}{2}$ indicating that at least one of the atoms has $M_J = \frac{3}{2}$. Thus the eigenfunctions referred to above, $\psi^{aa}_{1/2}$ and $\psi^{aa}_{3/2}$, are the first and second entries in table 1.3 respectively. Occasionally it will be necessary to give the $\Omega^{(+/-)}_{u,g}$ symmetry of the eigenfunction as well.

This $(J_A M_A J_B M_B)$ coupling scheme has been called the $J_1 J_2$ model by Herzberg [24, p.319] and was used by Saute and Aubert-Frécon [28] when discussing the asymptotic behaviour of the valence state potentials. Most of the work in this thesis concerns fluorescence from low vibrational levels of the ion-pair states, with $R_e \approx 3.6$Å, so in general the electronic structure of the valence states will be described using this model. The full adiabatic scheme for the correlation of $(J_A M_A J_B M_B)$ valence states with MO configurations is shown in Table 1.2.

ψ_e as a function of R

A number of experimental studies have attempted to probe the transition from LCAO eigenfunctions to separated-atom eigenfunctions as the internuclear separation increases. Bacis *et al* [16, 26] measured the hyperfine charge-quadrupole coupling constant eQq as a function of vibrational level in the $X0^+_g(aa)$, $a1_g(aa)$ and $a'0^+_g(aa)$ states and also interpreted data from the literature for the $B0^+_u(ab)$ state. By comparing the experimental results with theoretical predictions for each basis, Bacis was able to show that a significant transition to essentially single separated-atom eigenfunctions had occurred by $R \approx 4$Å in the $X0^+_g(aa)$ and $B0^+_u(ab)$ states. Similar conclusions could not be reached for the $a'0^+_g(aa)$ state as both bases give the same theoretical prediction, but its large R_e value (4.6Å) suggests that the separated-atom basis is appropriate. They did find [16] that the eQq constant was decreasing in this state as v increased, reflecting the mixing of the $\psi^{aa}_{3/2}(0^+_g)$ and $\psi^{aa}_{1/2}(0^+_g)$ eigenfunctions in this basis as the dissociation limit is approached: the fully mixed state (equation (1.3)) is predicted a zero eQq interaction. Their results for the $a1_g(aa)$ state were limited but in close agreement with predictions for a separated-atom basis, not surprisingly given the large R_e

value of the state (4.3Å). Experiments by the same group to quantify $a' \sim a$ [16] and $X \sim a'$ [17] perturbations in terms of the separated-atom eigenfunctions have proved unsuccessful as the effects were too weak, due to Franck-Condon factors, for the resolution used. However they have interpreted an earlier result with this basis set and successfully reproduced the $X0_g^+(aa)$ state hyperfine spin-rotation constant, $C_{v=83}$, that arises from an heterogeneous interaction with the $a1_g(aa)$ state [27]. This perturbation has been quantified for higher v_X by Martin *et al* [17] and used to calculate the degree of mixing of the $\psi^{aa}_{3/2}(0_g^+)$ and $\psi^{aa}_{1/2}(0_g^+)$ eigenfunctions near $R = 5$Å. From their work and that of Saute and Aubert-Frécon [28] they concluded that the $X0_g^+(aa)$ and $a'0_g^+(aa)$ state wavefunctions are close to singular separated-atom eigenfunctions at intermediate and large separations:

$$\begin{aligned} X0_g^+(aa) &: 0.45\psi^{aa}_{3/2} - 0.90\psi^{aa}_{1/2} \\ a'0_g^+(aa) &: 0.90\psi^{aa}_{3/2} + 0.45\psi^{aa}_{1/2} \end{aligned}$$

The description of valence state wavefunctions will be discussed further in Chapters 3 and 6.

1.1.2 The Ion-Pair States

Iodine's ion-pair states lie from about 5eV above the ground state in a region of the potential energy diagram largely free from perturbation by other states (see Figure 1.1). The halogens have 20 IP states of which 13 have now been reported for iodine [40]: their principle spectroscopic constants are given in Table 1.4. Figure 1.2 demonstrates a number of properties characteristic of the halogen IP states: they all have large R_e values of close to 3.6Å and cluster in groups of molecular states dissociating diabatically to the same ion pair. They are all deeply bound to greater than 3eV and have similar potential functions with essentially Coulombic outer limbs; thus their Dunham parameters are all similar and properties of unknown states can be estimated from those already known in that cluster. All these characteristics are reflections of the similarity of the IP

State	T_e/cm^{-1}	ω_e/cm^{-1}	$R_e/\text{Å}$	Diss. Limits[a]	Refs.
third cluster					
$F'0_u^+(3)$	51706.2	131.0	3.48	$^1D_2 + {}^1S_0$	[29, 30]
$f'0_g^+(3)$	(51500)			$^1D_2 + {}^1S_0$	[31]
second cluster					
$H1_u(2)$	48280.3	107.7	3.63	$^3P_1 + {}^1S_0$	[12]
$G1_g(2)$	47559.1	106.6	3.53	$^3P_1 + {}^1S_0$	[20]
$F0_u^+(2)$	47217.35	96.3	3.60	$^3P_0 + {}^1S_0$	[32]
$g0_g^-(2)$	(47070)	(105.7)	(3.55)	$^3P_1 + {}^1S_0$	[19]
$f0_g^+(2)$	47025.9	104.2	3.57	$^3P_0 + {}^1S_0$	[33]
first cluster					
$\delta 2_u(1)$	41689	100.2	(4.0)	$^3P_2 + {}^1S_0$	[14, 34]
$\gamma 1_u(1)$	41621.3	95.0	3.67	$^3P_2 + {}^1S_0$	[34]
$E0_g^+(1)$	41411.8	101.4	3.65	$^3P_2 + {}^1S_0$	[35]
$D0_u^+(1)$	41028.6	95.0	3.58	$^3P_2 + {}^1S_0$	[36, 37]
$\beta 1_g(1)$	40821.0	105.0	3.61	$^3P_2 + {}^1S_0$	[38]
$D'2_g(1)$	40388.3	104.0	3.60	$^3P_2 + {}^1S_0$	[21, 39]

[a]The anionic Russell-Saunders state along with the major RS component of the cationic state.

Table 1.4. Principal spectroscopic constants for the ion-pair states of I_2.

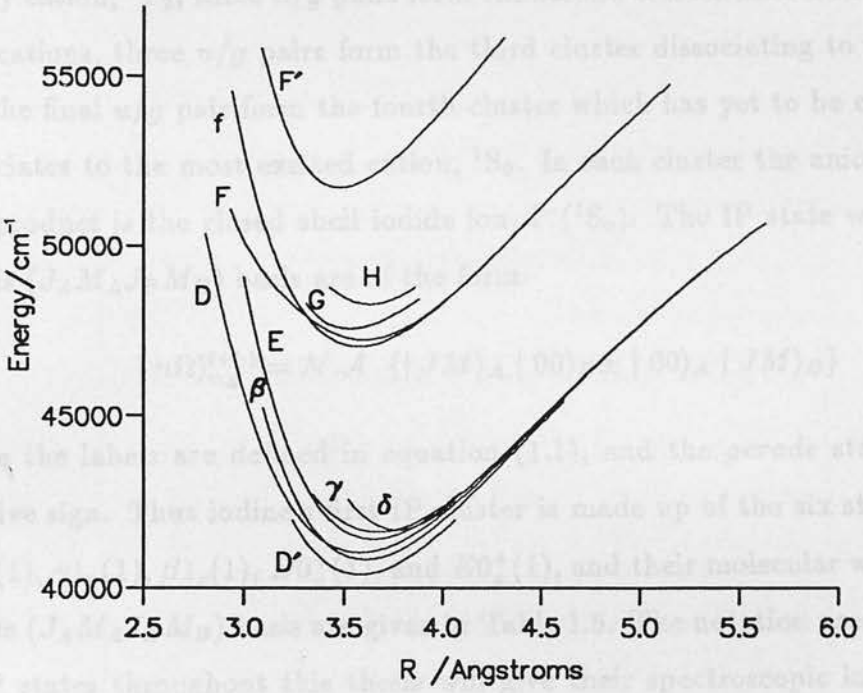

Figure 1.2. Experimental extent of the potential curves for the known IP states of I_2.

states' electronic structures.

The electronic wavefunction

At dissociation the IP states give a pair of oppositely charged ions whose anion $I^-(^1S_0)$ is common to all states, thus it is the state of the cation that differentiates the various molecular states as the nuclei approach and the electron clouds interact. The I^+ cation can take up one of five Russell-Saunders states: $^3P_2$, $^3P_0$, $^3P_1$, $^1D_2$ or $^1S_0$ in order of increasing energy.[3] When combined with the anion in the $(J_A M_A J_B M_B)$ coupling scheme these cationic states give rise to 20 IP states in four clusters;[4] three u/g pairs form the first cluster dissociating to the lowest

[3]The anomalous energy ordering of the I^+ $^3P_0$ and $^3P_1$ states demonstrates the jj mixing of the Russell-Saunders basis mainly through $^3P_2$ -$^1D_2$ and $^3P_0$ -$^1S_0$ interactions [41, p.301]. The RS functions still dominate the ionic configurations however, and so we shall use the Russell-Saunders description in later chapters as a framework in which to discuss this jj coupling.

[4]The energy separations between clusters at their potential minima are similar to those between their cationic states on dissociation: since the I^+ $^3P_0$ and $^3P_1$ states lie close in

energy cation, $^3P_2$, three u/g pairs form the second cluster dissociating to $^3P_0$ or $^3P_1$ cations, three u/g pairs form the third cluster dissociating to $^1D_2$ cations and the final u/g pair form the fourth cluster which has yet to be observed and dissociates to the most excited cation, $^1S_0$. In each cluster the anionic dissociation product is the closed shell iodide ion, $I^-(^1S_0)$. The IP state wavefunctions in this $(J_A M_A J_B M_B)$ basis are of the form

$$| n\Omega\rangle_{u,g}^{(+/-)} = \mathcal{N}.\mathcal{A}\ \{| JM\rangle_A \,|\, 00\rangle_B \pm |\, 00\rangle_A \,|\, JM\rangle_B\} \tag{1.4}$$

where the labels are defined in equation (1.1), and the *gerade* states take the positive sign. Thus iodine's first IP cluster is made up of the six states: $\delta 2_u(1)$, $D'2_g(1)$, $\gamma 1_u(1)$, $\beta 1_g(1)$, $D0_u^+(1)$, and $E0_g^+(1)$, and their molecular wavefunctions in this $(J_A M_A J_B M_B)$ basis are given in Table 1.5. The notation used in referring to IP states throughout this thesis will give their spectroscopic label, followed by their $(J_A M_A J_B M_B)$ symmetry and the number of the cluster to which they belong.

ψ_e as a function of R

The clustering of the IP states into groups with common diabatic dissociation products suggests there is little overlap of ionic orbitals centred on the two nuclei: even close to R_e the molecule is behaving as a pair of associated ion centres. This is supported[5] by Huzinaga's Gaussian basis sets for the $I^-(^1S_0)$ anion [43, p.423-426] which give the 5p orbital radius, $\langle r(5p)\rangle$, as approximately 1.42Å significantly less than half the IP equilibrium internuclear separation; the radius of the 5p orbital on the cation would be expected to be even shorter. While there may be negligible overlap between centres at large R, this must be a simplified picture at R_e^{IP} since there $V'(R)$ must change sign, that is the repulsive terms, ie antibonding terms, must begin to increasingly determine the shape of the potential. The electron overlap is antibonding in ion-pair states, ie the antibonding

energy [42, p.108] the molecular states they generate will together form the second cluster.

[5]The Gaussian basis may not be reliable at such large radii.

$\Omega_{u,g}^{(+/-)}$ symmetry	Molecular wavefunction
first and third clusters: $I^+(^3P_2$ or $^1D_2)^a + I^-(^1S_0)$	
0_g^+	$\frac{1}{\sqrt{2}}\{\|2,0\rangle_A \|0,0\rangle_B + \|0,0\rangle_A \|2,0\rangle_B\}$
0_u^+	$\frac{1}{\sqrt{2}}\{\|2,0\rangle_A \|0,0\rangle_B - \|0,0\rangle_A \|2,0\rangle_B\}$
1_g	$\frac{1}{\sqrt{2}}\{\|2,1\rangle_A \|0,0\rangle_B + \|0,0\rangle_A \|2,1\rangle_B\}$
1_u	$\frac{1}{\sqrt{2}}\{\|2,1\rangle_A \|0,0\rangle_B - \|0,0\rangle_A \|2,1\rangle_B\}$
2_g	$\frac{1}{\sqrt{2}}\{\|2,2\rangle_A \|0,0\rangle_B + \|0,0\rangle_A \|2,2\rangle_B\}$
2_u	$\frac{1}{\sqrt{2}}\{\|2,2\rangle_A \|0,0\rangle_B - \|0,0\rangle_A \|2,2\rangle_B\}$
second cluster: $I^+(^3P_1$ or $^3P_0) + I^-(^1S_0)$	
0_g^+	$\frac{1}{\sqrt{2}}\{\|0,0\rangle_A \|0,0\rangle_B + \|0,0\rangle_A \|0,0\rangle_B\}$
0_u^+	$\frac{1}{\sqrt{2}}\{\|0,0\rangle_A \|0,0\rangle_B - \|0,0\rangle_A \|0,0\rangle_B\}$
0_g^-	$\frac{1}{\sqrt{2}}\{\|1,0\rangle_A \|0,0\rangle_B + \|0,0\rangle_A \|1,0\rangle_B\}$
0_u^-	$\frac{1}{\sqrt{2}}\{\|1,0\rangle_A \|0,0\rangle_B - \|0,0\rangle_A \|1,0\rangle_B\}$
1_g	$\frac{1}{\sqrt{2}}\{\|1,1\rangle_A \|0,0\rangle_B + \|0,0\rangle_A \|1,1\rangle_B\}$
1_u	$\frac{1}{\sqrt{2}}\{\|1,1\rangle_A \|0,0\rangle_B - \|0,0\rangle_A \|1,1\rangle_B\}$
fourth cluster: $I^+(^1S_0) + I^-(^1S_0)$	
0_g^+	$\frac{1}{\sqrt{2}}\{\|0,0\rangle_A \|0,0\rangle_B + \|0,0\rangle_A \|0,0\rangle_B\}$
0_u^+	$\frac{1}{\sqrt{2}}\{\|0,0\rangle_A \|0,0\rangle_B - \|0,0\rangle_A \|0,0\rangle_B\}$

Table 1.5. Ion-pair wavefunctions in the $(J_A M_A J_B M_B)$ coupling scheme.

[a] Major Russell-Saunders component of the cationic state.

electrons in the dominant MO configurations outnumber the bonding electrons, and so around R_e the amount of overlap must be increasing significantly when compared to the forces of attraction.

The ion-pair potentials have been successfully modelled using modified Rittner functions [11, 44, 45, 46, and references therein]; Tellinghuisen has used four experimentally known attraction terms (ion-ion (R^{-1}), ion-quadrupole(R^{-3}), ion-induced dipole (R^{-4}) and induced dipole-induced dipole (R^{-6})), and two repulsion terms, empirically adjusted to give the correct inner branch behaviour:

$$V(R) = \left\{ b\exp(-\beta R^p) + \frac{c_{12}}{R^{12}} \right\} - \left\{ \frac{c_1}{R} + \frac{c_3}{R^3} + \frac{c_4}{R^4} + \frac{c_6}{R^6} \right\} .$$

At the potential minimum $V(R_e) = -D_e$, $V'(R_e) = 0$ and $V''(R_e) = 4\pi^2\omega_e^2\mu/h$ and the repulsion terms can be calculated from the spectroscopic parameters. In general we find that the repulsion terms and the attraction terms, without the Coulombic attraction, are approximately equal at the potential minima of these IP states since $D_e \approx e^2/R_e$ to within $< 5\%$. All ion-pair states have approximately the same equilibrium separation, thus they will have approximately the same D_e values; thus those of the same dissociation limit will tend to cluster at R_e. Furthermore the outer branches of their potentials will be essentially Coulombic and thus parallel, while only on the inner branches will significant differences be expected as their differing MO configurations assert their particular characteristics (see figure 1.2). Significant configuration interaction would thus only be expected at short R not on the Coulombic dominated outer limb [40]; calculations confirm this [47]. Using this picture Brand and Hoy and others [40, and references therein] have accounted semi-quantitatively for the clustering of halogen ion-pair states though they were unable to account for the detailed ordering within a cluster. This point is discussed further in Appendix A.

Although increasing significantly to determine the shape of the potential function, the electron exchange is small even at R_e, thus the most compact description

of the ion-pair state's electronic configuration will be the separated-ion model. Experiments have been designed to test the applicability of this model for the electronic structure in low v of these states by measuring their hyperfine charge-quadrupole coupling constant, eQq, or spin-rotation constant, C. Bacis *et al* have recorded the hyperfine structure of the $E0_g^+(1)$ [27, 48] and $f0_g^+(2)$ states [49], and compared their results with predictions for various proposed separated-atom wavefunctions to find the cationic parentage. Though they did suggest the most likely parent was the $^3P_2$ and $^3P_0$ respectively as expected, their results were not entirely conclusive partly because they assumed the Russell-Saunders eigenfunctions of Table 1.5 and ignored the jj mixing in the cationic wavefunction referred to earlier (see footnote 3). More recently Tiemann *et al* [50] repeated their experiment for the $E0_g^+(1)$ state and recorded the first hyperfine spectrum for the $\beta 1_g(1)$ state. Their results were in agreement with those of Bacis' group, and in a more thorough analysis they were able to show that the fuller description of the cationic wavefunction that includes jj mixing gives some improvement to the predictions but still does not completely describe the molecular wavefunction. Further work in this field is limited by the lack of data for the hyperfine eQq_{510} and a_J constants of the I^+ cation. The fuller description of the IP wavefunction will be described in Chapter 3, and the predictions for IP state hyperfine structure will be returned to in Chapter 6.

Bacis *et al* were able to show that a single MO configuration was inadequate to describe the electronic structure of these low v IP states [48, 49], not surprisingly given the large R_e^{IP} and small atomic orbital overlap of these states. However at high v levels ($v \approx 100$) the amplitude of the vibrational motion should enter regions where the MO description may be expected to be more appropriate. No measurements of hyperfine structure have been reported for such high levels but another experiment that demonstrates the evolution from separated-atom to MO schemes has been performed in Edinburgh: the measurement of the $f0_g^+(2) \rightarrow B0_u^+(ab)$ transition dipole moment function [15]. By recording and simulating the dispersed fluorescence from a high vibrational level in the f state ($v' = 88$)

the authors were able to deduce $\mu_{f\rightarrow B}(R)$ over the range $R = 2.80 - 5.30$Å (see figure 7.1). The dipole function could be determined absolutely as the fluorescent lifetime of the f ($v = 0$) level had also been measured, as had the relative Einstein $A_{f\rightarrow i}$ coefficients for transitions from the IP state (see Chapter 6). The transition dipole clearly demonstrates the evolution from MO to separated-atom schemes as R is increased: at short R the transition function is weak, reflecting the forbidden nature of the two electron $f \rightarrow B$ transition for their dominant MO configurations, 2242 and 2431 respectively. The increase in the dipole function at large R results from the strong charge transfer transition implied by the separated-ion wavefunction in the f state; furthermore the subsequent fall off in the function is predicted for charge transfer spectra which must decrease to zero as $R \rightarrow \infty$. A fuller discussion of this and other transition dipole moment functions reported in the literature will be given in Chapter 7, where the $F0_u^+(2)$ $\rightarrow X0_g^+(aa)$ function will be determined.

Donovan and co-workers have also explained an apparent contradiction in the analysis of Valence$\rightarrow$ IP absorption spectra when compared with IP$\rightarrow$Valence fluorescence [46]: the absorption cross-section for $X0_g^+(aa) \rightarrow D0_u^+(1)$ is much greater than for $X0_g^+(aa) \rightarrow F0_u^+(2)$ or $X0_g^+(aa) \rightarrow F'0_u^+(3)$, yet the fluorescence from each IP state is relatively strong. The $F \rightarrow X$ and $F' \rightarrow X$ transition dipoles must have changed by a factor of around 10 in the 1Å, reflecting the changing nature of the electronic structure of the IP states. Absorption at R_e^X lies in the region of R-space where single MO configurations dominate the electronic wavefunctions: the $D0_u^+(1)$ state's dominant configuration is 1441 (Table 1.2), for the $F0_u^+(2)$ and $F'0_u^+(3)$ states it is 2332, thus only the $D0_u^+(1)$ state can be populated by a one electron transition from the 2440 ground state, and the $X0_g^+(aa) \rightarrow D0_u^+(1)$ transition dominates the absorption spectrum. On the other hand transitions from the IP to valence states, at R_e^{IP}, are all dipole allowed charge transfers $I^+I^- \rightarrow I_2$ and the fluorescence from all three states are of similar intensity. The strength of the charge transfer dipole depends on the the degree of overlap between orbitals on the two centres and the detailed orbital occupancy of

each state (see Chapter 6). If the overlap $\langle p_\sigma^A | p_\sigma^B \rangle$ is much greater than $\langle p_\pi^A | p_\pi^B \rangle$ then the order of the dipole strengths should be $\mu_{F' \to X} > \mu_{F \to X} > \mu_{D \to X}$ and the weakly excited $F'0_u^+(3)$ state will be detected in fluorescence spectra. This simple explanation will be developed in greater detail in later chapters.

1.1.3 The Rydberg States

The lowest Rydberg states in iodine lie about 6eV vertically above the ground state. Although they are known to perturb high vibrational levels of IP states at their inner turning points, these levels are outside the region investigated in this thesis ($v \approx 200$ in the first IP cluster, around 7.2eV above the ground state) and will not be discussed further [51, 52, 53, 54].

1.2 Experimental Methodology

Iodine has been studied spectroscopically since the beginning of the century: $B0_u^+(ab) \to X0_g^+(aa)$ fluorescence excited by a mercury arc lamp was recorded by Wood in 1912 [55], while in 1913 McLennan reported a bound-free $D0_u^+(1) \to X0_g^+(aa)$ spectrum excited by I* atoms [56]. Having the simplest of all molecular geometries diatomics were soon used to test the new quantum theories of molecular structure, with I_2 often used as a model heavy atom system [57, 58, 59, 60, 61]. The early popularity of iodine arose partly from the advantages it offers the spectroscopist over other heavy diatomics: I_2 is a solid with a significant partial pressure at room temperature, is isotopically pure in its natural form, and absorbs and fluoresces strongly in the visible to ultra-violet range of the spectrum, however the recent spectroscopic interest in iodine has been inspired by Mulliken's review paper 'Iodine Revisited' published in 1971 [25]. This paper surveyed the existing spectral data and discusses the electronic structure of the 43 'sub-Rydberg' states in terms of simple MO configurations. Importantly Mulliken included a detailed energy diagram giving the likely form for the potential curves of many of these states and revealed the clearly defined regions of valence

and ion-pair states alluded to in the first section and demonstrated in figure 1.1. Mulliken suggested that the congestion of states often found with many electron molecules would be largely avoided for iodine, partly due to the large spin-orbit splittings of the dissociation products. Such a relatively 'clean' potential energy diagram lends itself to spectroscopic investigation and in the following decade a large number of workers reported their absorption and fluorescence studies. The results were often ambiguous, however, and their conclusions sometimes directly conflicted.

Early one photon absorption studies in the visible region recorded the $X0_g^+(aa) \rightarrow B0_u^+(ab)$ spectrum, though the limited Franck-Condon window from $X(v''=0)$ only allows significant absorption to $B(v' \approx 30)$. Steinfeld *et al* therefore systematically heated the iodine cell and analysed the absorption spectra of hot bands up to $v''=7$ to include the lower B state vibrational levels [62]. Absorption in the ultraviolet region excites the Cordes bands, first recorded in 1935, populating a long series of high lying vibrational levels ($v' \approx 100-200$) assigned to the $D0_u^+(1)$ state [63, 64]. The next 0_u^+ state reached in a one photon absorption from the ground state is expected to be the $F0_u^+(2)$ state found in the second IP cluster. The $X0_g^+(aa) \rightarrow F0_u^+(2)$ absorption spectrum lies in the vacuum ultraviolet, however vertical excitation in the Franck-Condon window of the $X(v''=0)$ state at these energies probes the region where low lying Rydberg states interact with IP states at the inner turning points of the IP vibrational motion [53]. The first record of absorption to high lying levels in the $F0_u^+(2)$ state ($v' \approx 225$) was therefore reported by Venkateswarlu in his survey of iodine's 0_u^+ Rydberg states in the vuv region [65]. He had to make a number of arbitrary assignments, however, since the Rydberg states at these energies all have similar spectroscopic constants. These high lying IP vibrational levels accessed by one photon absorption from the ground state have also been analysed using microwave discharge lamps to achieve state specific excitation with sufficiently high population density to record their dispersed fluorescence [45]. A detailed description of the ground state potential could then also be derived [66, and refs. therein].

These experimental techniques use either low intensity or fixed frequency excitation, and in each case low vibrational levels of the ion pair states could not be excited as, having significantly larger R_v, they lie well outside the Franck-Condon window of even the hot bands. Thus important spectroscopic parameters such as R_e and D_e could only be derived by extended extrapolation [45]. Low photon flux stops the spectroscopist from dispersing the fluorescence of the upper state and so only the Franck-Condon window of the ground state can be explored. Fixed frequency excitation can only investigate a small energy window of the absorption spectrum; furthermore the one photon selection rules only allow for excitation to 0_u^+ and 1_u states from the 0_g^+ ground state, thus only a small number of the excited states can be populated. Norrish overcame some of these restrictions by recording the absorption spectrum of a metastable excited state populated by flashphotolysis [67], however he was unable to convincingly assign the transition observed, and only 20 years later was Tellinghuisen able to rationalise his experiment as an $A'2_u(aa) \rightarrow D'2_g(1)$ absorption [68, 69].

The early attempts to overcome these limitations, before the advent of multiphoton techniques, typically used non-state specific excitation sources (eg. electric discharges or electron beams) with high noble gas pressures to collisionally quench the excited states and achieve approximate Boltzmann distributions among lower lying ion pair states [5, 6, 9, 21, 70, 71, 72]. The fluorescence from these states could then be dispersed since a high density of molecules are excited in the discharge. However the analysis of these spectra is far from straightforward as the excitation scheme is no longer state specific and a large number of vibrational levels are populated through the collisional cascade [11]. Such experiments have allowed for the characterisation of low vibrational levels of the lowest ion pair state, the $D'2_g(1)$, since these have the largest population in a thermalised distribution [21]. Workers were also able to assign the other strong transitions in this spectral region [6, 21, 70, 72]: $E0_g^+(1) \rightarrow B0_u^+(ab)$, $F0_u^+(2) \rightarrow X0_g^+(aa)$, $\beta 1_g(1) \rightarrow A1_u(aa)$ and $D0_u^+(1) \rightarrow X0_g^+(aa)$, transitions that are now known to have particularly large Einstein $A_{IP \rightarrow V}$ coefficients (see Chapter 6).

1.2.1 Multiphoton Techniques

With the development of high intensity tunable dye lasers operating in the visible and near uv regions came the opportunity to use multiphoton techniques in molecular spectroscopy [73]. In general multiphoton techniques take advantage of the high photon flux from a laser to populate highly excited states through multiple absorptions of photons with known energies.[6] The transition to the intermediate state(s) can be either resonant or non-resonant, ie through real or virtual states, though resonant absorption has the larger cross section. Using these techniques the one photon selection rules of the conventional absorption experiment are overcome: a *gerade* destination state can be reached from a *gerade* ground state by the absorption of an even number of photons. Furthermore rovibronic state selection can be achieved at each stage which leads to uncrowded spectra: a stepwise assignment of the states and their detailed rotational analysis is then entirely feasible. The multiphoton technique has therefore been exploited in a number of ways by

- scanning the wavelength of the final photon in the OODR scheme and probing for excitation to a destination state by detecting the flourescence of one of its transitions (fluorescence excitation spectra). This effectively gives the absorption spectrum of the (known) excited intermediate and thus spectral information about the destination state (see Chapter 4).

- dispersing the fluorescence from the (known) destination state. This allows analysis of the states reached in fluorescence, their Einstein $A_{IP\rightarrow V}$ coefficients and transition dipole functions (see Chapters 4 and 6).

[6] The states involved in the multiphoton excitation scheme will be referred to as either intermediate or destination states. Thus the conventional 2+1 Multiphoton Ionisation experiment has a two photon excitation scheme

$$ground \xrightarrow{h\nu_1} intermediate \xrightarrow{h\nu_2} destination$$

followed by a one photon ionisation step.

- using a short pulse of photons in the final excitation step. The decay in dispersed fluorescence from the destination state can then be recorded giving the state lifetime (see Chapter 5).

- allowing the absorption of a further photon by the destination state, so ionising the molecule. This is the Multiphoton Ionisation (MPI) technique, not used in this thesis but discussed further in the next section.

The two multiphoton techniques most often applied in the study of the halogens are Multiphoton Ionisation and Optical-Optical Double Resonance. The former is typically used when exploring the properties of Rydberg states [74], and the vibrationally excited IP states in that energy region, the latter to probe the low lying vibrational levels of the ion-pair states.

Multiphoton Ionisation

Multiphoton Ionisation was first applied to the halogens in the late 1970s to extend the range of known Rydberg states beyond those populated by a strong one photon absorption from the ground state [75, 76, 77]. The MPI technique populates the destination state through a vertical excitation scheme with multiple photon absorptions, then a final extra photon ionises the molecule. A typical MPI experiment scans the photon energy of the final step in the excitation scheme: a transition to the destination state is recorded as an increase in the potential between two plates in the sample cell following the change in ionisation signal. This gives a high collection efficiency and even weak absorptions can be detected. As with other multiphoton techniques, the MPI excitation scheme allows the population of specific rovibronic levels in a destination state of different symmetry from those reached by a conventional absorption experiment. The likely symmetry of the destination state can be assigned from the relative intensities of the MPI signal using variously polarised light [75, 76], from the rotational structure [53] or from quantum defect calculations [51, 78]. MPI is used either as a one colour experiment [51, 75, 78, 79], where virtual intermediate states are populated in a

non-resonant excitation scheme, or using two colours to populate specific bound rovibronic intermediate states [53, 76, 77]. The latter technique gives increased spectral simplicity and clarifies the spectral analysis of a poorly known system since the selection of a different intermediate state, and consequently a different intermediate state energy, causes a corresponding shift in the excitation frequency of the MPI signal. Thus the MPI signal can be distinguished from other multiphoton processes, a problem not always easy to resolve using one colour MPI.[7]

As with all spectroscopic techniques MPI does suffer from a number of drawbacks: the thermal population of the ground state leads to superimposed hot band structure which sometimes obscures the assignment of the spectrum; MPI is typically limited in the Franck-Condon window it explores (at least when a virtual intermediate is excited) and is restricted by the dye laser power available at the appropriate region of the spectrum. In spite of this, MPI is still the technique of choice for many groups studying halogen Rydberg states [51, 53, 78, 79].

Optical-Optical Double Resonance

A typical MPI experiment described above needs to be adapted for studying ion pair states in low vibrational levels since their large R_v values give vanishingly small Franck-Condon factors in the vertical MPI excitation scheme. Optical-Optical Double Resonance (OODR) is often the technique chosen to achieve excitation to states in low vibrational levels with large R_v. This technique uses a bound state as resonant intermediate whose R_v value lies somewhere between that of the ground and destination states, making a new Franck-Condon window available in the multiphoton scheme.

In the most flexible two colour experiment the first (tunable) photon selectively excites a single vibrationally excited level in the intermediate state through strong Franck-Condon overlap at R_v^{inner} of the intermediate state's vibrational motion. The second (tunable) photon pumps molecules from the intermediate

[7]Experiments using more than two colours usually have too many competing multiphoton processes to give useful spectra.

state to the destination state. The conventional OODR excitation scheme has strong Franck-Condon overlap in the second step at the outer turning point of the intermediate state's motion: this allows the spectroscopist to 'step' across the R-space of the potential energy diagram, accessing the IP states in their lowest vibrational levels (see figure 4.9). An example of this is the excitation scheme used by Rousseau and Williams [80] in one of the earliest OODR experiments to investigate the $E0_g^+(1)$ state of iodine. In their experiment Rousseau and Williams used a tunable laser in the first step, and a fixed frequency laser in the second step, of a two photon excitation scheme involving two parallel transitions.

Although selectively populating low IP vibrational levels for the first time in experimental conditions, Rousseau and Williams were still limited by one photon selection rules to reaching destination states with 0_g^+ or 1_g symmetry in the second step. In a logical extension of this work, Chen *et al* used a two photon pump from $B0_u^+(ab)$ to populate the $D0_u^+(1)$ state in the first IP cluster through a virtual $0_g^+(bb)$ intermediate state[8] [82]. However, with no $1_g(bb)$ state available, it seemed that no convenient multiphoton scheme could be devised to reach the $\delta 2_u(1)$ state predicted by Mulliken [25] if the $B0_u^+(ab)$ state were used as the first intermediate. Unfortunately there are no suitable (ab) states to replace the $B0_u^+(ab)$ state as intermediate for iodine: none can deliver the necessary Franck-Condon regime to access the IP states in a two photon OODR excitation.[9] Consequently alternative pumping schemes have been developed exciting vibrational levels of the $B0_u^+(ab)$ state close to dissociation where strong mixing with essentially repulsive potentials is expected [86]. This is still the excitation scheme favoured in this laboratory to populate the $D'2_g(1)$ state through a $B0_u^+(ab) \sim 1_u(ab)$ coupled

[8] Analogous experiments populating the $F0_u^+(2)$ and $F'0_u^+(3)$ states have also been performed [29, 30, 32, 81].

[9] Recent OODR experiments by Ishiwata *et al*, studying chlorine, have used the $A1_u(aa)$ state as intermediate in a two photon excitation scheme to populate the $\beta 1_g(1)$ state [83]; Ishiwata was also able to use a coupled $A1_u(aa) \sim A'2_u(aa)$ intermediate state to reach the $D'2_g(1)$ IP state [84]. The relatively small spin-orbit splitting in chlorine atoms, $\Delta E(^2P_{3/2} - {}^2P_{1/2}) = 881\text{cm}^{-1}$ [85], leads to a high density of states near the valence dissociation limits with the $B0_u^+(ab)$ state lying embedded in the weakly bound (aa) states, suggesting alternative coupled intermediate excitation schemes could be available.

intermediate (see Table 4.6). In this variation of the OODR excitation scheme, the significant Franck-Condon overlap giving access to the $D'2_g(1)$ ion pair state in low v occurs at the repulsive potential wall. Bacis *et al* have also successfully populated the $D'2_g(1)$ state following collisional transfer in the intermediate step from lower $B0_u^+(ab)$ state levels ($v \approx 32$) to a metastable $2_u(ab)$ reservoir state [22]. Although similar in effect, this excitation scheme has the drawbacks of needing significant buffer gas pressures to ensure efficient collisional transfer and a loss of state specificity in the intermediate step.

In a two colour, two photon OODR experiment, Danyluk and King [87] reported five states in the same region of the potential energy diagram as that predicted for the first IP cluster by Mulliken [25], however, since they had used the $B0_u^+(ab)$ state as intermediate, they assigned the symmetry of their destination states as 0_g^+ or 1_g. Danyluk and King reported the five states as closely clustered together, a surprising result if they all have the same symmetry, and gave a thorough analysis of the rovibrational levels used in the intermediate stage. They found it hard to reconcile the large outer turning point of the intermediate state's vibrational motion (> 7Å), with their picture for the excitation scheme: $X \rightarrow B$ pumping at the inner turning point, $B \rightarrow IP(v \approx 0)$ probing at the outer turning point. Their tentative suggestion of Franck-Condon factors enhanced by a strong $V \rightarrow IP$ transition dipole did not tally convincingly with the R_e^{IP} values they derived (≈ 3.6Å). Clearly the multiphoton excitation scheme was not yet fully understood. In a further development of their OODR experiment King *et al* [34] were able to assign one of the five states to the $E0_g^+(1)$ state by comparison with Tellinghuisen's analysis [88] of Rousseau and Williams data.

It is now thought that Danyluk and King accessed destination states with seemingly forbidden symmetries by using a perturbed rovibronic level in the intermediate state [89]. Reinterpretations of their data, with the benefit of hindsight, have shown them consistent with subsequent results from the many research groups working in this field. Rather than having the 0_g^+ and 1_g symmetries they

suggested, the 5 states they reported were 5 of the 6 members of the first IP cluster: the $\delta 2_u(1)$ and $\gamma 1_u(1)$ states were excited from a $B0_u^+(ab) \sim 1_g(ab)$ coupled intermediate state, and the $E0_g^+(1)$, $\beta 1_g(1)$ and $D'2_g(1)$ from a $B0_u^+(ab) \sim 1_u(ab)$ coupled intermediate. In spite of this salutary experience, many of the recent OODR experiments have not addressed the details of their excitation schemes since the data could be unambiguously assigned to a well known state without requiring a fuller investigation. In any case a discussion was in some senses redundant since *how* the population of low v IP states was achieved was at that time secondary to the spectroscopic properties themselves. However this luxury to ignore the mechanism of excitation is only allowable when exciting well known states: investigating poorly known states in this way could lead to incorrect symmetry assignments similar to those of Danyluk and King. Thus a clear resolution of the OODR excitation schemes used in this thesis will be given in Chapter 4. By careful use of $B0_u^+(ab)$ rovibronic levels coupled to other states at the second dissociation limit it has been possible to populate all six states in the first IP cluster and three of the six in the second (see Table 4.6). Indeed by extension it should be possible to excite 19 of the 20 IP states in low vibrational levels using these intermediates.

The OODR technique therefore can be used to prepare populations of iodine's ion pair states in low vibrational levels. Spectroscopists have exploited the OODR technique to deduce the Dunham parameters of these states from fluorescence excitation spectra, their dispersed fluorescence spectra, or using MPI detection (see Table 1.4). The properties of valence states can also be derived from the dispersed fluorescence of IP states (see Table 1.1). The OODR technique has also been used to record fluorescent lifetimes [90, 91, 92], transition dipole functions [15, 38, 91], Einstein $A_{IP \rightarrow V}$ coefficients [14], IP hyperfine structure [48, 49, 50], Ω-doubling [38] and other coupling interactions [32, 81]. These latter experiments help complete the description of a diatomic in the Born-Oppenheimer approximation since they give information on the detailed electronic structure of the states involved: it is the description of the electronic structure of iodine's IP states that

this thesis addresses.

Chapter 2 Experimental

This Chapter discusses the experimental configurations of the various spectroscopic techniques used in this thesis and the simulation methodology adopted in the analysis of dispersed fluorescence spectra. All experiments were performed in Edinburgh.

2.1 Experimental Configuration

Two colour Optical-Optical Double Resonance was used to excite the ion pair states of I_2, employing the $B0_u^+(ab)$ state as resonant intermediate. This section will first give a general description of the experimental configuration adopted for the spectroscopic study of the IP states in low v, then discuss the variations required for each of the three types of experiment performed. A typical experimental configuration used in recording the radiative lifetimes of the IP states is shown in figure 2.1.

The pulsed output from a high power excimer laser (Lambda Physik EMG 201 MSC), operating on the 308nm XeCl ($B \rightarrow X$) transition, was used to pump two dye lasers simultaneously. The first dye laser (Lambda Physik FL3002E) selectively excited single rovibronic levels of the $B0_u^+(ab)$ state; the second dye laser (Lambda Physik FL2002) pumped molecules from the B state to the various ion-pair states. The laser bandwidths ($< 0.2\text{cm}^{-1}$) are less than the rotational spacings for the transitions studied in this thesis and large populations of well defined single rovibronic IP levels can be achieved [93, 94]. The intermediate state chosen to access a particular destination state is given in Table 4.6 along

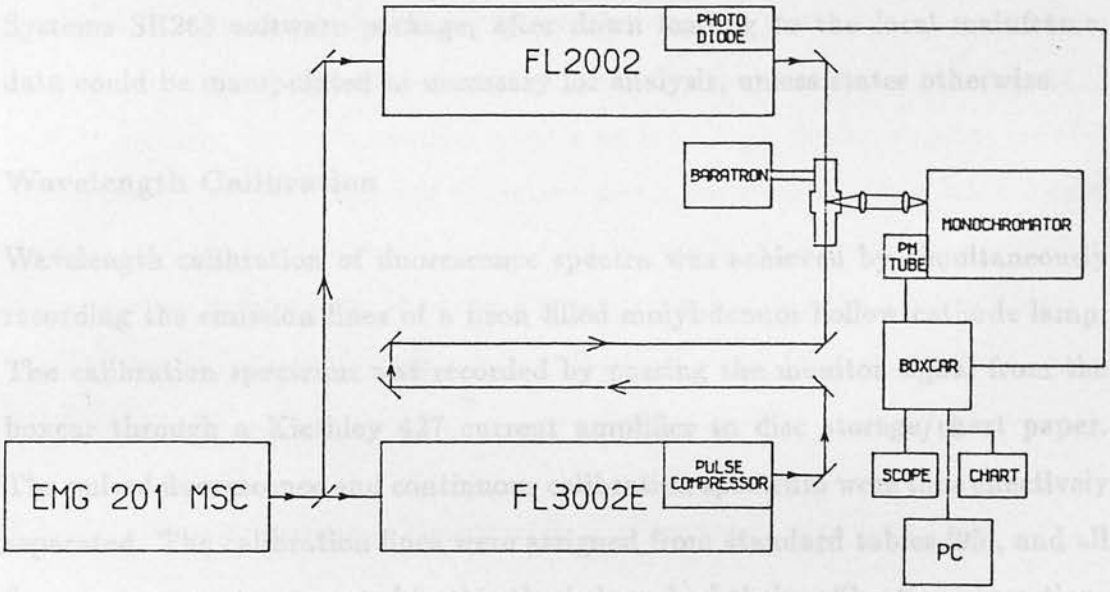

Figure 2.1. Schematic diagram of the experimental apparatus.

with the corresponding pump photon energies. The rationale behind the choice of intermediate level in a particular OODR excitation scheme is discussed in detail in Chapter 4. Coumarin 307 and Coumarin 102 were used as pump and probe dyes to access the $D'2_g(1)$ and $D0_u^+(1)$ states; Coumarin 307 and Coumarin 47 for the $\gamma 1_u(1)$ and $\delta 2_u(1)$ states; Rhodamine 6G and Bis MSB for the $E0_g^+(1)$ and $\beta 1_g(1)$ states; Rhodamine 6G and PTP for the $f0_g^+(2)$ state and Coumarin 307 with DMQ for the $F0_u^+(2)$ and $H1_u(2)$ states. The I_2 samples were held in cylindrical glass cells with spectrosil quartz windows and the path lengths so arranged that the collinear counterpropagating pulsed outputs from the two dye lasers arrived together in time. Fluorescence was collected at right angles to the laser paths and imaged onto the entrance slit of a monochromator (Jobin-Yvon HRS2: f/7,0.6m); dispersed fluorescence at the exit slit was monitored by a photomultiplier (Hamamatsu R928: rise time 2.2ns) whose transient output was fed into a Stanford Research Systems SR250 gated integrator (gate width less than 2ns). After processing the signal is output from the boxcar for display

on an IBM PC microcomputer and chart recorder/oscilloscope (Tektronix 2445). The gate scanning and data collection were controlled by a Stanford Research Systems SR265 software package; after down loading to the local mainframe, data could be manipulated as necessary for analysis, unless states otherwise.

Wavelength Calibration

Wavelength calibration of fluorescence spectra was achieved by simultaneously recording the emission lines of a neon filled molybdenum hollow cathode lamp. The calibration spectrum was recorded by passing the monitor signal from the boxcar through a Kiethley 427 current amplifier to disc storage/chart paper. The pulsed fluorescence and continuous calibration spectrum were thus effectively separated. The calibration lines were assigned from standard tables [95], and all fluorescence spectra reported in this thesis have had their calibration corrections applied.

Monochromator response function

This has been recorded as a function of wavelength for the detection system used in these experiments [93]; all spectra reported in this thesis are corrected for this function and the power dependence of the PM tube output (proportional to the photon energy [93]).

2.1.1 Dispersed Fluorescence Spectra

The fluorescence dispersed from a well known upper state is analysed in Chapter 4 to derive the $c1_g(ab)$ state potential, in Chapter 6 to derive the relative transition moments of all the major IP→Valence transitions near R_e^{IP}, and in Chapter 7 to derive the dipole moment of the $F0_u^+(2) \rightarrow X0_g^+(aa)$ transiton as a function of internuclear separation.

The experimental configuration used is essentially that described above, with the probe laser establishing an IP state population in a particular rovibronic level, ie working at a constant wavelength setting, and the monochromator scanned

over the fluorescence for the transition being monitored; in these experiments the boxcar is triggered by an electrical pulse from the excimer laser. To record dispersed fluorescence spectra at high resolution it is preferable to narrow the entrance slitwidth of the monochromator until the the vibrational spacings have been completely resolved, however narrowing the slitwidth also reduces the signal reaching the PM tube, and in some cases a compromise is struck between spectral resolution and signal intensity. For example in figure 4.5 the relatively low resolution results from the large slitwidth required for the weak calibration signal, however meaningful analysis is still possible provided the spectral peaks are still discrete.

2.1.2 Fluorescence Excitation Spectra

This technique is used in Chapter 4 to find the $T(v)$ terms of the four lowest vibrational levels of a previously unknown IP state. Essentially this is an absorption experiment where the successful absorption to an IP rovibronic level is detected by recording the fluorescence dispersed from one of the strong transitions in its radiative manifold.

The experimental configuration is essentially the same as that described above again with the boxcar triggered by the excimer. In this technique the probe laser is scanned over the wavelengths that correspond to excitation to the various vibrational levels in the IP state, and the monochromator is set to disperse the fluorescence at a wavelength common to a transition from each upper state; the monochromator slits are set to a large opening ($> 2000\mu$m) equivalent to a wavelength window of approximately 5nm. Consequently in the OODR fluorescence excitation experiment the absorption to an IP rovibronic level from a well known intermediate level is detected through the change in fluorescence intensity at the PM tube. Therefore a plot of this fluorescence intensity against the probe laser frequency (or wavelength) effectively gives the absorption spectrum of the *intermediate* $\rightarrow$ *destination* transition. For example the fluorescence excitation

spectrum recorded for the $c1_g(ab)(v = 14, J = 22) \xrightarrow{P,R} H1_u(2)(v = 0, 4)$ transition is shown in figure 4.1 and the peak positions can be analysed to give the Dunham parameters of the upper state (Table 4.1).

The relative peak intensities of two vibronic transitions in a fluorescence excitation spectrum will reflect the Franck-Condon and Hönl-London factors of the OODR absorption, and fluorescence, steps and the extent that the IP fluorescence falls within the detection window of the monochromator. Consequently care should be taken if interpreting these spectra in terms of coupling phenomena, for example predissociation in the destination state (see Chapter 4).

2.1.3 Radiative Lifetimes

The radiative lifetimes of nine of the 20 IP states of I_2 are determined in Chapter 5.

Essentially the same experimental configuration is adopted in these experiments though the role of the two dye lasers is reversed, FL2002 gives the pump photon and FL3002E the probe. This configuration is adopted so a pulse compressor (Lambda Physik FL90) can be mounted in the probe laser to shorten the photon pulses from the usual 15ns, to a 4ns peak width at half maximum (measured on the Tektronix 2445 oscilliscope). The time overlap of the two photon pulses, pump and probe, is much more significant in these time resolved experiments and the path lengths are adjusted so the pump laser can establish the intermediate state population which is then sampled by the shortened probe pulse. Both lasers output at fixed wavelength to establish an ion pair population whose decay with time is monitored by recording the time evolution of fluorescence from the strongest transition in each ion pair system. The monochromator is therefore set similarly to the fluorescence excitation experiment, at the wavelength of the strong radiative system and with wide slitwidth setting. The boxcar is triggered by the pump pulse using a photodiode and is scanned (using 1000 bins) across the fluorescence decay profile over 50, 75 or 100ns, depending on the lifetime of the state. The transitions monitored are given in table 5.1. The lifetimes of the

ion pair states lie in the range 5 – 40ns (see Chapter 5) and hence only for the longer lived states is a true exponential tail found for the fluorescence decay; for the shorter lived states the fluorescence decays too quicky and a significant part of the profile is convoluted with the probe pulse. Consequently for these states the data analysis requires a fitting proceedure that takes the dynamics of the convolution of probe pulse with fluorescent decay into account (see Chapter 5).

2.2 Analysis of Dispersed Fluorescence Spectra

Careful spectroscopic investigation has the potential to reveal much important information about the properties of molecular states, however interpreting experimental spectra is often difficult as a number of molecular phenomena may combine to leave a complex puzzle. Interpretations of such complex systems therefore rely on the experience gained from well understood models: the theoretical models developed for their molecular phenomena give a framework in which to rationalise the appearance of a complex spectrum.

In this thesis the analysis of dispersed fluorescence spectra uses familiar theoretical models to derive the electronic properties of certain of iodine's molecular states. This is normally the last step in the understanding of a diatomic's spectroscopy in the visible region since other molecular properties (vibration, rotation) normally obscure the influence of the electronic configuration. However the theory of the rotation and vibration of diatomics is now so well known that these properties are only of interest for the fundamental molecular properties they can reveal, the reduced mass of the molecule, the bond strength, etc, or for the occassions when accepted theory is inadequate. The routine computer calculation of accurate predictions for these two molecular motions allows us to infer the electronic configurations from the experimental spectrum. This is of fundamental importance since it gives an insight into the preferred electronic configuration

of a state and can be used to give a detailed picture for the bonding interactions in the molecule. Thus the spectroscopist is able to discuss the behaviour of the electrons, as well as the nuclei, when bonds are stretched, molecules excited, reactions proceed.

It is usual to interpret molecular spectra in terms of separate molecular properties: the vibrational, rotational and electronic state of the molecule. The theoretical justification for this distinction lies in the application of the Born-Oppenheimer approximation in solving the molecular Schrödinger equation; this is covered briefly in the following section. Using this approach we can perform quantum mechanical calculations for the transition between two vibronic states and thus simulate the fluorescence recorded in their spectra: a program has been developed in Edinburgh to perform such calculations and its application to problems addressed in this thesis will be discussed in a later section. When concordance between prediction and experiment is achieved we can discuss the spectroscopy in terms of the theoretical models used in the analysis, however it is often instructive to achieve a semi-classical interpretation when trying to picture the quantum mechanical behaviour exhibited by the molecule. This also allows the derivation of the salient properties as revealed by experiment before a full calculation is attempted; the most useful semi-classical model for the work in this thesis is discussed in the last section.

2.2.1 The Born-Oppenheimer Approximation

To achieve a quantum mechanical simulation of dispersed fluorescence we first need to consider the eigenfunctions, Ψ, and eigenenergies, E, of the diatomic Schrödinger equation

$$\hat{H} \,.\Psi(q;Q) = E.\Psi(q;Q), \tag{2.1}$$

where q and Q are the electronic and nuclear coordinates respectively. $\hat{H}$, the complete molecular Hamiltonian, includes the kinetic energy of the nuclei, $\hat{T}_n$, and of the electrons, $\hat{T}_e$, it includes the potential energy of interaction between the nuclei, $\hat{V}_{nn}$, between the electrons, $\hat{V}_{ee}$, and the attraction of electrons to the

nuclei, $\hat{V}_{en}$,

$$\hat{H} = (\hat{T}_n + \hat{T}_e) + (\hat{V}_{nn} + \hat{V}_{ee} + \hat{V}_{en}). \tag{2.2}$$

If we fix the nuclei such that $T_n = 0$ and V_{nn} is constant for a given Q (the clamped nucleus model), then we can define an effective Hamiltonian $\hat{H}_e$ where

$$\begin{aligned} \hat{H}_e &= \hat{H} - \hat{T}_n \\ &= \hat{T}_e + \hat{V}_{nn} + \hat{V}_{ee} + \hat{V}_{en}, \end{aligned} \tag{2.3}$$

at a given Q. Note that the molecular eigenstate, $\psi_e(q;Q)$, of this effective Hamiltonian at a given value of Q is still a function of both the nuclear and electronic coordinates.

Born and Oppenheimer were the first to suggest an approach that allows for the solution of the molecular Schrödinger equation (2.2): the Born-Oppenheimer approximation [96]. They suggested that the large differrence in the masses of the nuclei and electrons would allow the electrons to respond to any nuclear motion instantaneously, the electrons are said to follow the nuclei. Thus rather than solve the Schrödinger equation for a set of mobile nuclei and electrons, we can ignore the effect of the nuclear motion on the electronic wavefunction and find the electronic eigenstates at a given Q from the clamped nucleus Hamiltonian, $\hat{H}_e$. The molecular wavefunction is then separable into nuclear and electronic components

$$\Psi(q;Q) = \psi_n(Q)\psi_e(q;Q). \tag{2.4}$$

By assuming the independent electron model, ie that the electrons move in some sort of average electrostatic potential that reflects the potential of all the other electrons, then the eigenvalue E_e can be calculated at a given Q for a particular electronic state

$$\hat{H}_e \cdot \psi_e(q;Q) = E_e(Q)\psi_e(q;Q). \tag{2.5}$$

Whether calculated explicitly or not, $E_e(Q)$ establishes an effective potential surface (or for the diatomic a potential curve) in which the nuclei move. The eigenfunctions for the nuclear motion can then be found from the complete Hamiltonian which includes this potential energy and the kinetic energy of the unclamped

nuclei, $\hat{T}_n$:

$$\hat{H}\,.\Psi(q;Q) = \hat{H}\,.\psi_e(q;Q)\psi_n(Q) \tag{2.6}$$

$$= \hat{T}_n\,\psi_e(q;Q)\psi_n(Q) + [\hat{T}_e + \hat{V}_{nn} + \hat{V}_{ee} + \hat{V}_{en}]\psi_e(q;Q)\psi_n(Q) \tag{2.7}$$

$$= \psi_e(q;Q)[\hat{T}_n + E_e(Q)]\psi_n(Q) \tag{2.8}$$

$$\hat{H}\,.\psi_n(Q) = E.\psi_n(Q) \tag{2.9}$$

$\psi_n(Q)$ is the wavefunction for the nuclear motion, and in the absence of translational motion is the vibrational-rotational part of the molecular wavefunction. For a diatomic $\psi_n(Q)$ can be factorised into the rotational and vibrational components by adopting spherical coordinates and separating the angular (θ, ϕ) from the displacement (R) dependent terms.

Thus in the Born-Oppenheimer approximation

$$\Psi(q;Q) = \psi_e(q;R,\theta,\phi)\psi_{vib}(R)\psi_{rot}(\theta,\phi), \tag{2.10}$$

and so

$$E = E_e + E_{vib} + E_{rot}. \tag{2.11}$$

We have achieved the separation of the rotational, vibrational and electronic properties familiar in diatomic spectroscopy.

2.2.2 Simulation of dispersed fluorescence

The rate of spontaneous emission of photons from an excited state population in transition to a lower rovibronic state is proportional to the Einstein $A_{n'v'n''v''}$ coefficient

$$A_{n'v'n''v''} = \frac{64\pi^4}{3hc^3}\nu^3\langle n'v'J' \mid \mu(R) \mid n''v''J''\rangle^2, \tag{2.12}$$

where ν is the transition frequency and $\mu = \sum_i er_i$ is the electric dipole operator. In the Born-Oppenhiemer approximation the integral factorises into vibrational, rotational and electronic terms

$$A_{n'v'n''v''} = \frac{64\pi^4}{3hc^3}\nu^3\frac{S_{J'}}{2J'+1}\langle v' \mid \mu_{n'n''}(R) \mid v''\rangle^2, \tag{2.13}$$

where $S_{J'}$ is the rotational Hönl-London factor, and

$$\mu_{n'n''}(R) = \langle n' \mid \mu \mid n'' \rangle. \tag{2.14}$$

The fluorescence dispersed from a particular transition therefore carries information about the rotational, vibrational and electronic states of the two molecular levels involved: dispersed fluorescence spectra are analysed in Chapter 4 to give the lower state potential function, and in Chapter 7 fluorescence spectra give the transition dipole function, $|\mu_{F\rightarrow X}|$.

The efficient quantum mechanical simulation of the experimental spectra studied in this thesis is achieved using a program written in Edinburgh by Lawley and Austin. It is not intended to discuss the mathematics of their simulation procedure as the authors have already covered this in some detail [97, 98], however a knowledge of the programming philosophy is helpful to demonstrate its use in establishing molecular properties.

Simulation Methodology

In order to solve the radial nuclear Schrödinger equation (equation (2.9)) and derive the vibrational eigenfunctions and eigenenergies, the program requires the upper and lower state potential functions usually input as splined cubic functions between a small number of R, V points, typically experimental RKR pairs. Knowing the upper state rotational quantum number, the program calculates the effective centrifugal potentials for the two states

$$V_{eff}(R) = V(R) + \frac{h^2 J(J+1)}{8\pi^2 \mu R^2}, \tag{2.15}$$

where μ is now the reduced mass. No further allowance is made for the rotational part of the Einstein coefficient: the program is designed to reflect the OODR dispersed fluorescence experiment where a single well known upper state rovibrational level is populated leaving the Hönl-London factor redundant.

The program establishes the upper state eigenenergy and (normalised) vibrational eigenfunction using the Numerov method, then searches for the bound

vibrational levels in the lower state within the energy range of interest, calculating their energies and wavefunctions. Transitions to a lower state continuum are dealt with by the Cooley-Numerov method sampling the continuum at regular small steps in energy and integrating the dissociative wavefunction only over the range of the upper state function [98]. In effect this technique treats the continuum as having a high yet finite vibrational state density: this allows for the efficient calculation of quasi *bound* $\rightarrow$ *free* fluorescence intensities provided the step size is much smaller than the experimental resolution. Equation (2.13) is then calculated numerically for a particular pair of vibrational levels, using an electronic transition dipole function input over the same R grid as the potential functions; Franck-Condon factors are also calculated. At this stage of the calculation the spectrum resembles a series of sticks as a function of energy. Again to mimic the experiment the simulated spectrum is converted to units of length and convoluted with a gaussian slit function integrated over the experimental peak width deduced from the experimental spectrum. Thus the program quantum mechanically simulates the dispersed flourescence experiment to give a calculated spectrum in units of frequency per unit wavelength interval, where the wavelength interval is equivalent to the monochromator step between laser shots.

The result of this calculation will not yet be comparable with the output at the PM tube since the experimental detection is further affected by the monochromator response function and the photo-electric response of the PM tube. The former has been determined for the detection system used in this thesis by recording the output from a calibrated black-body source, and the photo-electric response of the PM tube is proportional to the energy of the incident photon [93]. Thus both the above factors can be removed from a digitised spectrum, and all spectra and simulations shown in this thesis therefore correspond to equation (2.13) convoluted with a gaussian slit function integrated in units of length over the experimental peak width.

Applications of the quantum mechanical simulation

Quantum mechanical simulations of dispersed fluorescence spectra have been used by many groups to interpret experimental spectra and determine the salient molecular properties in equation (2.13). Examples where such techniques have been applied to I_2 include:

- When one potential is well known, usually the upper state, comparison of simulation with experiment reveals the other potential over the Franck-Condon window of the upper vibrational wavefunction (Chapter 4, and [45, 88]). This is particularly important when *bound* → *free* spectra are analysed since other means of generating the potential, for example RKR inversion techniques, are not available [15, 18, 99, 100, and references therein].
- When both potential curves are well known then comparison of the calculation with experiment gives the transition dipole function (Chapter 7, and [15, 45, 88, 91]).
- The dispersed fluorescence from well known systems can be distinguished from that of overlapping systems or scattered laser light (Chapters 4, 6, and [101]).
- Franck-Condon overlap integrals have also been used to rationalise absorption schemes, and the strength of coupling between vibronic states (Chapter 4, and [18, 101, 102, 100]).

The black box application of these simulation techniques often leaves little insight into the underlying principles and a semi-classical model has been used by many workers to qualitatively interpret fluorescence spectra. This model is centred on the Franck-Condon principle and is outlined in the next section.

2.3 Interpreting the Fluorescence spectrum

The Franck-Condon principle is central to the semi-classical interpretation of electronic transitions, and is based on the same observation as the Born-Oppenheimer approximation: the nuclei are so massive when compared to the electrons that their motions can be treated separately. This implies that a change in electronic state of a molecule is so rapid compared with the vibrational motion that the position and momenta of the nuclei are conserved during the transition [24]. In the semi-classical model of a vibrating molecule a large fraction of the vibrational period is spent close to the turning points as it is the part of the motion with lowest kinetic energy. Therefore a primitive application of the Born-Oppenheimer approximation to vibronic transitions would predict a vertical transition from the turning points of the upper state to the turning points of vibrational levels in the lower electronic state, so conserving both the position and momentum of the nuclei. Consequently a picture could be developed of electronic transitions occurring almost exclusively at the stationary points in the vibrational motion, thereby in practice neglecting the nuclear momentum.

In the early 1970s Dalgarno [103] and Mulliken [104] demonstrated the significance of the nuclear kinetic energy when using the Franck-Condon principle to interpret the complex structure of fluorescence spectra from high vibrational levels. This important contribution was expanded by Tellinghuisen [105] whose quantum mechanical calculations supported their semi-classical model. This might be surprising since the Franck-Condon principle violates Heisenberg's uncertainty principle, both the position and momenta of the nuclei being specified, however from equation (2.13) we can give a wave mechanical formulation for the Franck-Condon principle- an electronic transition between two states is most probable over the range in R where the two vibrational wavefunctions build up significant overlap. To acquire a significant build up of vibrational overlap the two wavefunctions must have near constant phase difference over some range in R, the semi-classical stationary phase approximation, giving the kinetic energy aspect

of the Franck-Condon principle. The Born-Oppenheimer approximation already requires the conservation of nuclear position. Finally Tellinghuisen discussed the influence of the electronic transition moment on the fluorescence spectrum and a complete semi-classical interpretation of equation (2.13) had been achieved [100].

In the next section we outline this semi-classical model and use it to interpret the two common forms of fluorescence spectra observed for transitions from ion pair states. The predictions of the model are supported by calculations using the quantum mechanical programming described earlier.

2.3.1 A semi-classical model for fluorescence spectra

The details of the mathematics behind this model have been described elsewhere [98, 100, and references therein] and only the key features will be reproduced here.

The Franck-Condon principle states that the momenta of the nuclei are conserved during an electronic transition, that is their kinetic energy is constant. If $E_{v'}$ is the upper state vibrational eigenenergy and U' the upper state potential function, then the kinetic energy of the molecule at a given internuclear separation, $T(R)$, is

$$T(R) = E_{v'} - U'(R). \tag{2.16}$$

The Mulliken difference potential [104], $X(R)$, therefore describes the locus of energies in the lower electronic state that conserves the molecular kinetic energy in the electronic transition

$$X(R) = U''(R) + E_{v'} - U'(R). \tag{2.17}$$

Conservation of nuclear position during an electronic transition implies vertical transitions on a potential energy diagram of the two states, and the Franck-Condon allowed transitions will occur at constant R terminating on the Mulliken difference potential.

If the transition is to the bound region of $U''(R)$ then only the vibrational eigenstates of the lower state can be populated and only transitions to certain

energies, the eigenenergies will be allowed. Thus in this semiclassical model the *bound* → *bound* transitions will occur only at those internuclear separations where a vibrational eigenstate, v'', cuts the Mulliken potential, that is for all R^* where

$$X(R^*) = E_{v''}. \tag{2.18}$$

Transitions to the lower state continuum can occur for all R explored by the upper state wavefunction.

The relative strength of a particular transition can be judged by reference to equation (2.13):

$$A_{n'v'n''v''} = \frac{64\pi^4}{3hc^3}\nu^3 \frac{S_{J'}}{2J'+1}\langle v' \mid \mu_{n'n''}(R) \mid v''\rangle^2. \tag{2.19}$$

We can neglect the Hönl-London factor since it is common to all transitions from a given $\mid \Omega' v' J' \rangle$ state and need concentrate only on the second integral. This integral will only accumulate significantly over internuclear separations where the two vibrational functions have a stationary phase difference (the stationary phase approximation [106]) that is at values of R where the two wavefunctions have the same local wavenumber, $k(R)$, ie the semi-classical points of transition, R^*. Therefore assuming that the transition $v' \rightarrow v''$ occurs at the value of R^* satisfying equation (2.18), then it can be shown that if the Mulliken potential is approximated to a straight line in the region of R^*

$$\langle v' \mid \mu_e(R) \mid v''\rangle^2 \propto \mu_e^2(R^*)\cos^2(\phi_- \pm \frac{\pi}{4})[k(R^*)|\frac{dX(R^*)}{dR}|]^{-1}, \tag{2.20}$$

where ϕ_- is the phase difference between the two wavefunctions at R^*. Thus the intensity of transition to a particular lower state wavefunction is modulated by a $\cos^2$ function producing maxima and minima in the spectrum corresponding to regions of equal wavenumber in the upper and lower wavefunctions coming into and out of phase [98]. The intensity of a particular transition is also determined by the local velocity of the wave and the gradient of the difference potential, consequently transitions originating at R^* away from the turning points will have lower intensity due to the higher wave velocity. The ratio of the intensities at the red and blue ends of the spectrum, corresponding to transitions from the turning

points of the upper state vibrational motion, will be determined by the relative gradients of the Mulliken potential at these R and the R dependence of the dipole function. This latter factor tends to dominate for the transitions considered in this thesis and the blue end of the spectra have the larger intensity in spite of corresponding to a greater gradient in the difference potential (see later).

There are two common forms of spectra found in the fluorescence spectroscopy of ion pair states which correspond to whether the transition samples a monotonic or polytonic region of the difference potential, ie whether equation (2.18) has just the one or many (usually two) solutions. For some fluorescent systems the Mulliken potential does not exhibit a maximum and the function is monotonic over the whole spectrum, for other systems there is a maximum in the Mulliken potential and the function may be monotonic for short wavelength transitions, polytonic for the long wavelength, or *vice versa*. The next section will show how the semi-classical model can be used in the qualitative interpretation of experimental spectra.

Monotonic Mulliken potentials

Tellinghuisen *et al* have shown that if the fluorescence samples a monotonic Mulliken potential then equation (2.20) shows v' nodes [107]. If the fluorescence is to a continuum of vibrational states then the spectrum will 'reflect' the upper state wavefunction and the interval between the peaks will depend on the gradient of the lower potential since this determines the range of transition energies available to the upper state during its vibrational motion. However for *bound* $\rightarrow$ *bound* transitions not all transition energies are allowed thus if the fluctuation interval of the $\cos^2$ function is comparable to the vibrational spacing in a *bound* $\rightarrow$ *bound* spectrum then the inherent reflection structure may no longer be resolved.

A typical example of *bound* $\rightarrow$ *free* fluorescence to a monotonic Mulliken potential is shown in figure 2.2 (taken from Chapter 6); the difference potential is shown in figure 2.3. This spectrum clearly displays the reflection structure described by Tellinghuisen and a simple count of the spectral nodes confirms the

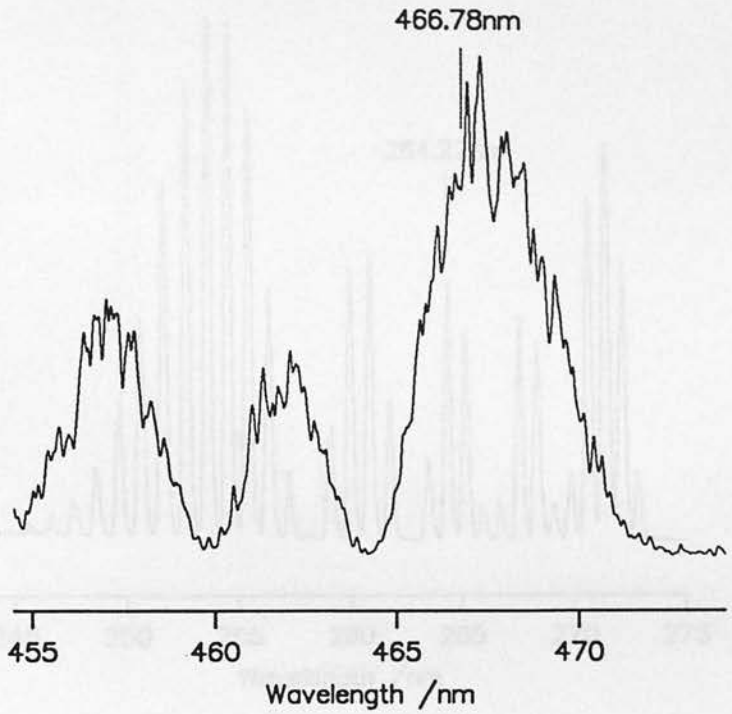

Figure 2.2. $\delta 2_u(1)(v' = 2) \rightarrow 2_g(ab)$ dispersed fluorescence.

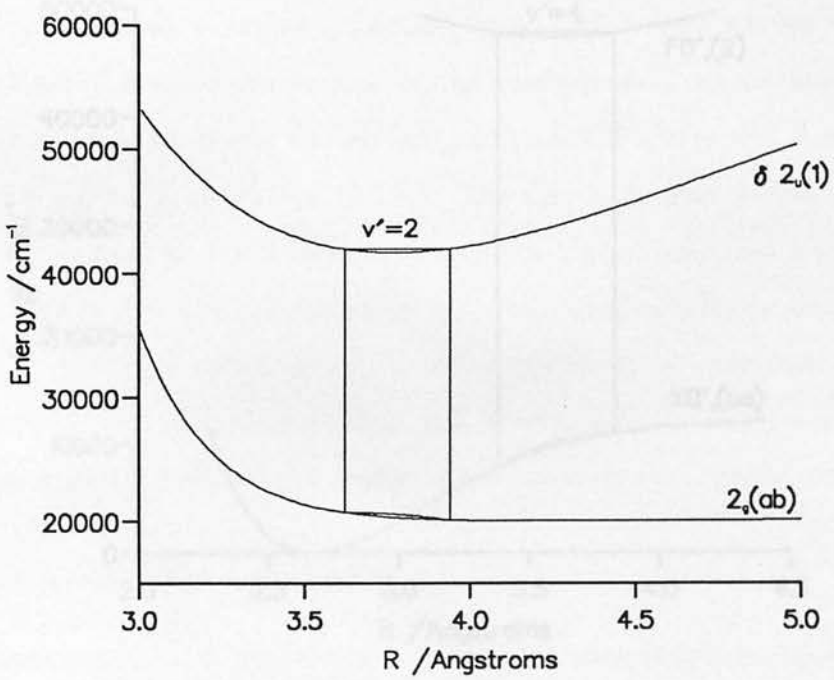

Figure 2.3. Mulliken difference potential for the $\delta 2_u(1)(v' = 2) \rightarrow 2_g(ab)$ transition.

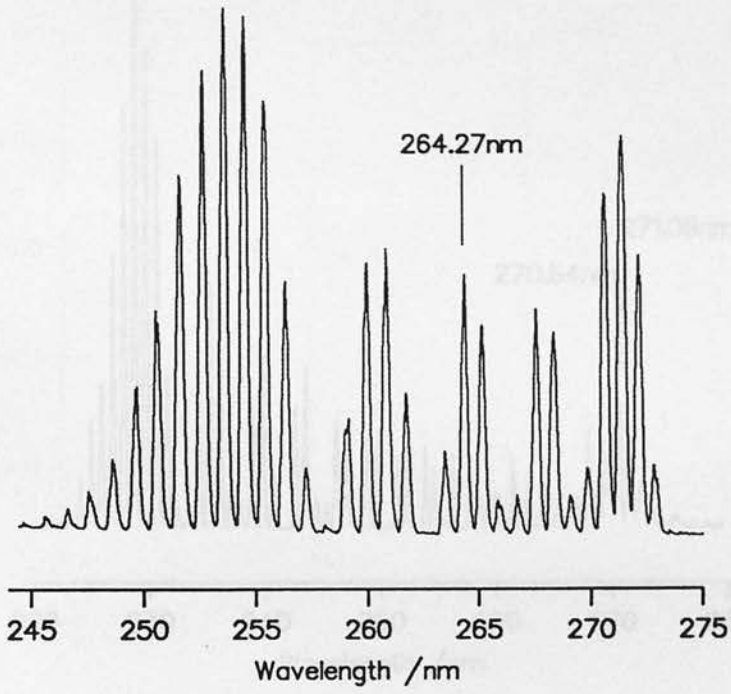

Figure 2.4. $F0_u^+(2)(v' = 4) \rightarrow X0_g^+(aa)$ dispersed fluorescence.

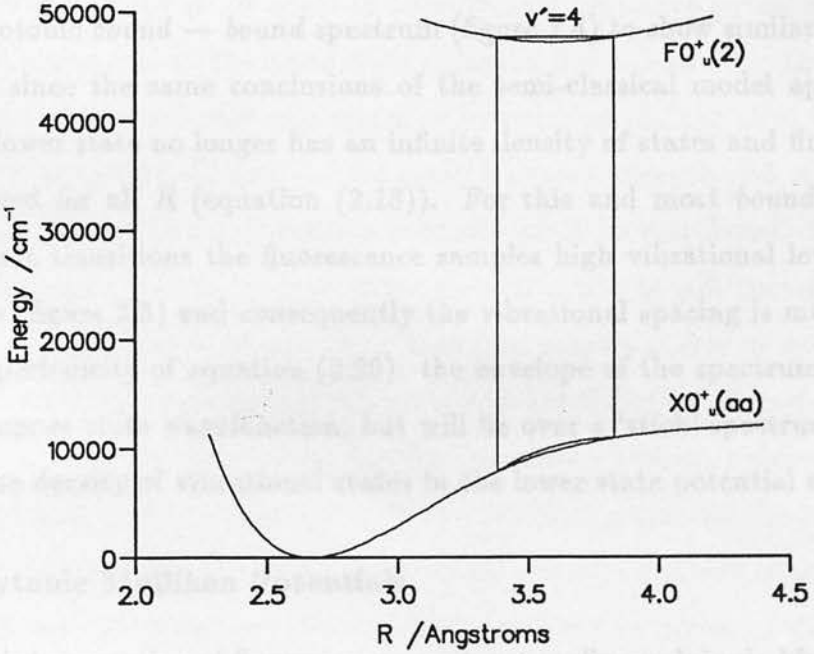

Figure 2.5. Mulliken difference potential for the $F0_u^+(2)(v' = 4) \rightarrow X0_g^+(aa)$ transition.

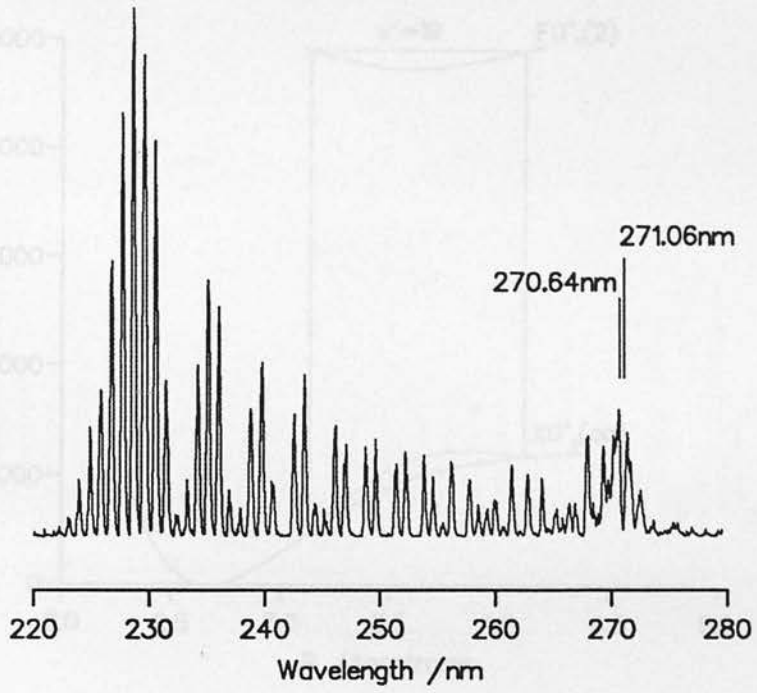

Figure 2.6. $F0_u^+(2)(v' = 19) \rightarrow X0_g^+(aa)$ dispersed fluorescence.

vibrational assignment of the upper state wavefunction ($v' = 2$). We expect the monotonic *bound* $\rightarrow$ *bound* spectrum (figure 2.4) to show similar reflection structure since the same conclusions of the semi-classical model apply except that the lower state no longer has an infinite density of states and fluorescence is not allowed for all R (equation (2.18)). For this and most *bound* $\rightarrow$ *bound* IP to valence transitions the fluorescence samples high vibrational levels of the lower state (figure 2.5) and consequently the vibrational spacing is much smaller than the periodicity of equation (2.20): the envelope of the spectrum will still reflect the upper state wavefunction, but will lie over a 'stick' spectrum corresponding to the density of vibrational states in the lower state potential well.

Polytonic Mulliken Potentials

The interpretation of fluorescence spectra sampling polytonic Mulliken potentials using the semi-classical model is very similar to that given above for a monotonic

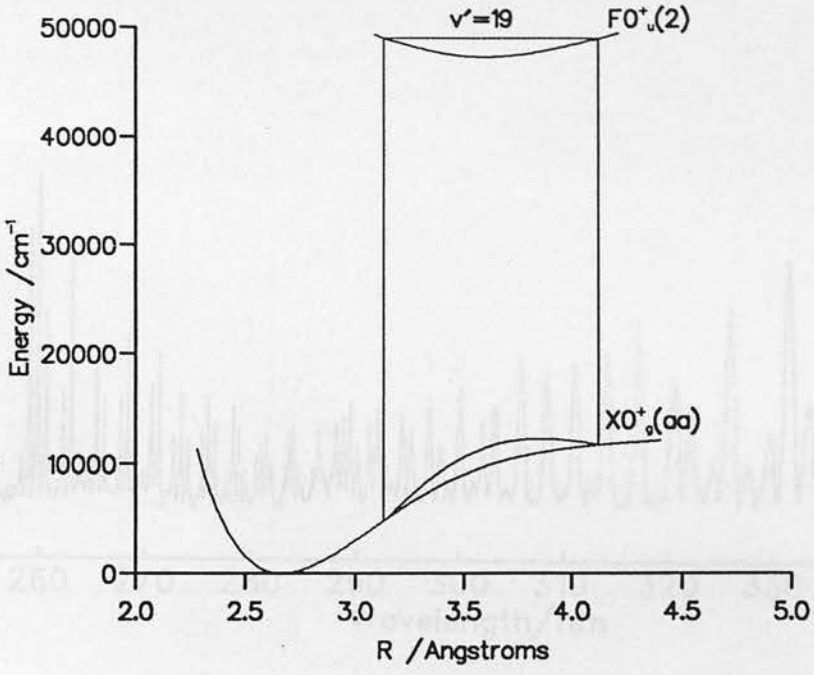

Figure 2.7. Mulliken difference potential for the $F0_u^+(2)(v' = 19) \rightarrow X0_g^+(aa)$ transition.

difference potential. In practice all polytonic difference potentials have a monotonic region, unless the lower state potential is flat, and over the polytonic region there is in general only two solutions to equation (2.18). Thus there will be two transition points, R_1^* and R_2^*, for a particular wavelength and the relative contribution of each to the transition intensity must be calculated. In the stationary phase approximation each of these transition points will contribute a term like that in equation (2.20) and these may sum constructively or destructively. Such spectra often show complex structure and are therefore termed 'internal diffraction' or 'interference' spectra: the fluoresecence no longer reflects the upper state wavefunction. At the maximum in the Mulliken potential the two semi-calssical transition points coincide and the model described above is no longer tenable, many methods have been developed to describe this region of the spectrum [100] but for interpretational purposes we need only know that our semi-classical model will be inappropriate at the red end of an interference spectrum. The form of the

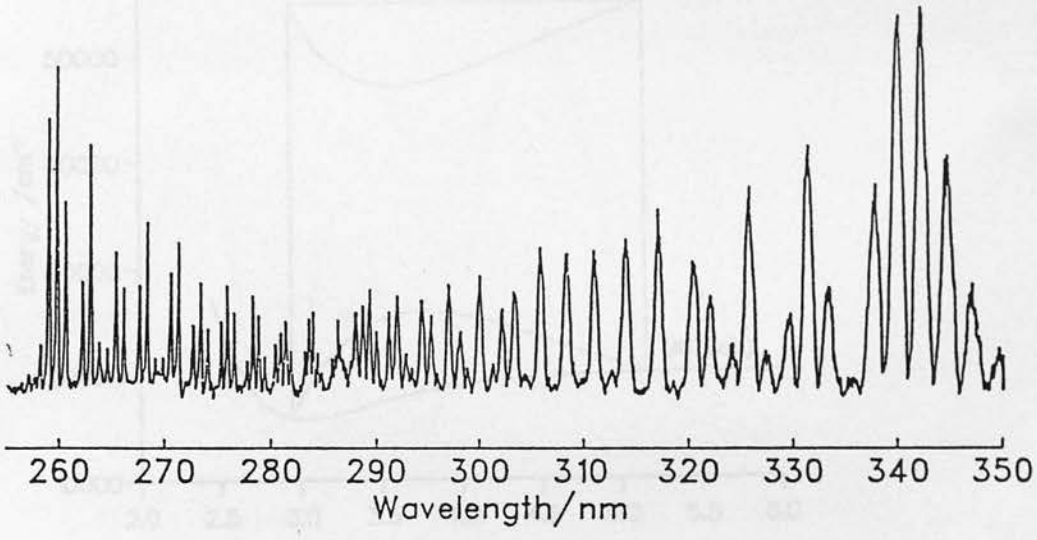

Figure 2.8. $f0_g^+(2)(v' = 88) \rightarrow B0_u^+(ab)$ dispersed fluorescence (from [15]).

Mulliken potential does tell us that the wavelength corresponding to this maximum is a constant of the fluorescence system, ie the red end of the spectrum lies at the same wavelength for a particular electronic transition whatever the vibrational level excited provided a polytonic Mulliken potential results. Increasing the vibrational energy of the initial state simply raises the energy of the difference potential by the same amount and λ_{max} remains the same [91].

Figures 2.8 and 2.6 give two examples of the fluorescence dispersed from transitions to polytonic Mulliken potentials (figures 2.9 and 2.7 respectively). In figure 2.8 the interference structure occurs almost exclusively in the *bound* $\rightarrow$ *free* region on account of the high vibrational excitation of the initial state, however this need not always be so as shown in figure 2.6 where no *bound* $\rightarrow$ *free* fluorescence is observed but interference structure is noticeable in the last group of peaks at the red end of the spectrum.

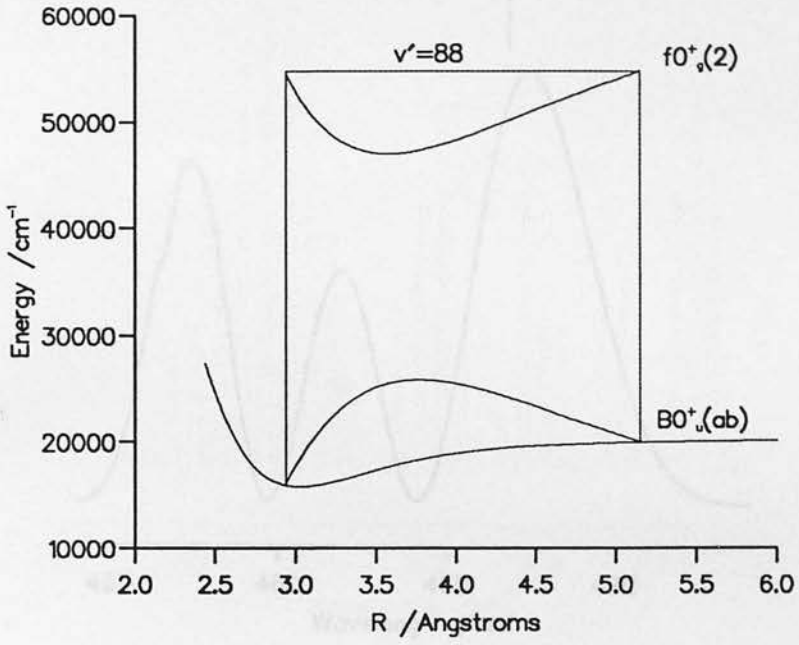

Figure 2.9. Mulliken difference potential for the $f0_g^+(2)(v' = 88) \rightarrow B0_u^+(ab)$ transition.

Quantum mechanical simulations

Figures 2.10 and 2.11 show quantum mechanical simulations of the reflection spectra.

The qualitative success of the semi-classical model in explaining the appearance of fluorescence spectra for transitions to monotonic Mulliken potentials is based on the strength of the assumptions used in the model: that transitions occur vertically where the phase difference between the two vibrational functions is stationary. The first assumption also underlies the Born-Oppenheimer approximation, however we can test the validity of the stationary phase approximation by determining how the overlap integral for the two vibrational functions accumulates with R (ie ignoring the effect of the dipole function). The intensity at $\lambda = 466.78$nm in the *bound* $\rightarrow$ *free* spectrum (figure 2.2) is associated with a transition at $R^* = 3.79$Å in the semi-classical model; figure 2.12 shows the Franck-Condon overlap of the two vibrational states involved in the transition,

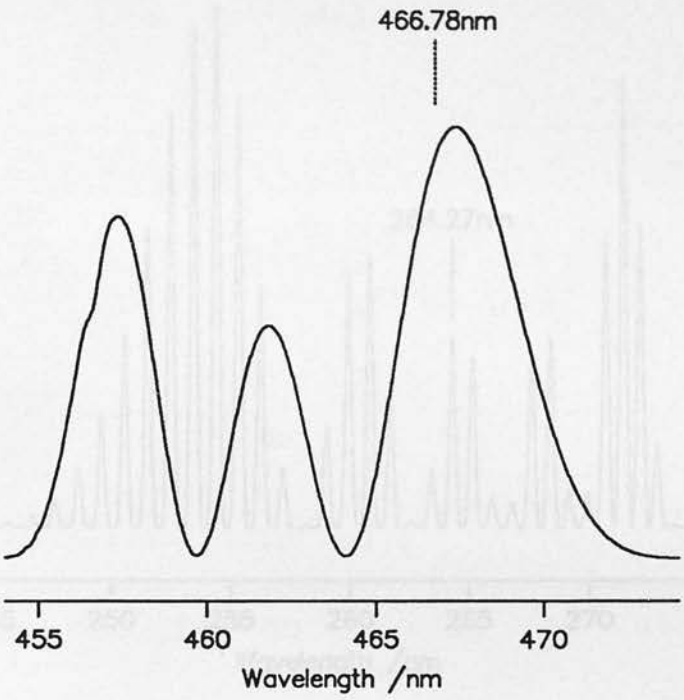

Figure 2.10. Quantum simulation of the $\delta 2_u(1)(v' = 2) \rightarrow 2_g(ab)$ dispersed fluorescence spectrum.

along with their product. It is clear from this quantum mechanical calculation that the overlap integral only builds up around the semi-classical transition point R^* as assumed in the constant phase approximation, though over perhaps a surprising large range in R, as much as 0.5Å. A similar conclusion is reached for the *bound* $\rightarrow$ *bound* spectrum shown in figure 2.4, where a peak at $\lambda = 264.27$nm ($R^* = 3.55$Å) is analysed in figure 2.13.

Furthermore as the fluorescence at a particular wavelength is associated in the semi-classical model with a transition at a particular R, reflection spectra can be used to determine first estimates of the relative change in the transition dipole as a function of R. The simulation shown in figure 2.11 uses the transition dipole function derived in Chapter 7 for the $F0_u^+(2) \rightarrow X0_g^+(aa)$ transition over the range $3.13 \leq R \leq 4.12$Å. Figure 2.14 shows the calculation in the Condon approximation of constant transition dipole and clearly the fluorescence at the longer wavelengths is too strong. This region of the spectrum is associated with

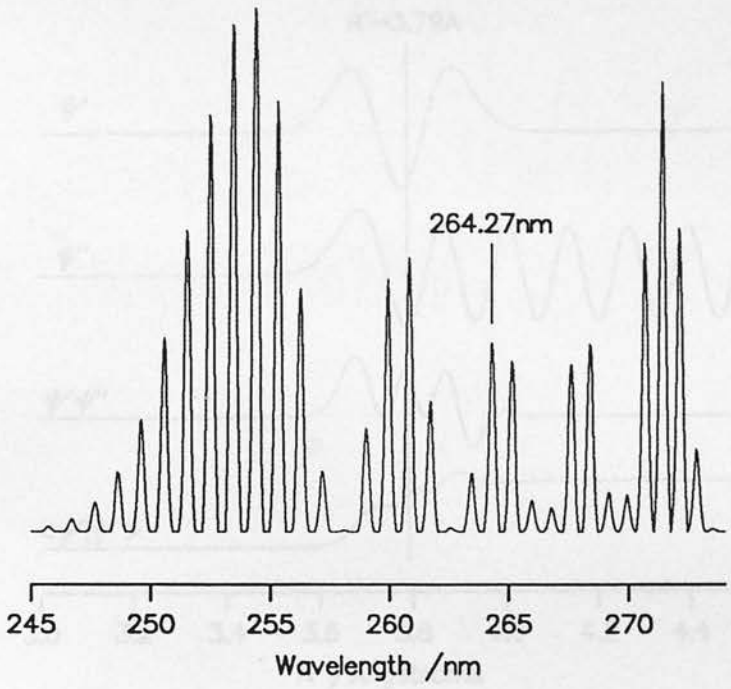

Figure 2.11. Quantum simulation of the $F0_u^+(2)(v'=4) \rightarrow X0_g^+(aa)$ dispersed fluorescence spectrum, with the transition dipole function included.

the longer internuclear separations where the gradient of the difference potential will be smaller: from equation (2.20) the transition dipole must therefore decay significantly with R to compensate (see figure 7.1).

The usual approach to derive an accurate transition dipole function from a reflection spectrum first calcualtes the r-centroid for the transition between two vibrational states, $\langle v' \mid r \mid v'' \rangle$, which is close to R^* for those levels [108]. Then in practice it is quickest to pursue an iterative comparison of quantum mechanical simulation with experimental spectrum, varying the dipole function appropriately at the various R^* until a suitable fit is found. This was the method used as a first step in deducing the $F \rightarrow X$ dipole in Chapter 7. Such an approach is not possible where a polytonic Mulliken potential is sampled since two or more points R^* are now involved in the semi-classical model and it would not be clear how the dipole influences the contribution at each. A generalisation of the r-centroid approximation has been suggested by Noda and Zare allowing for more than

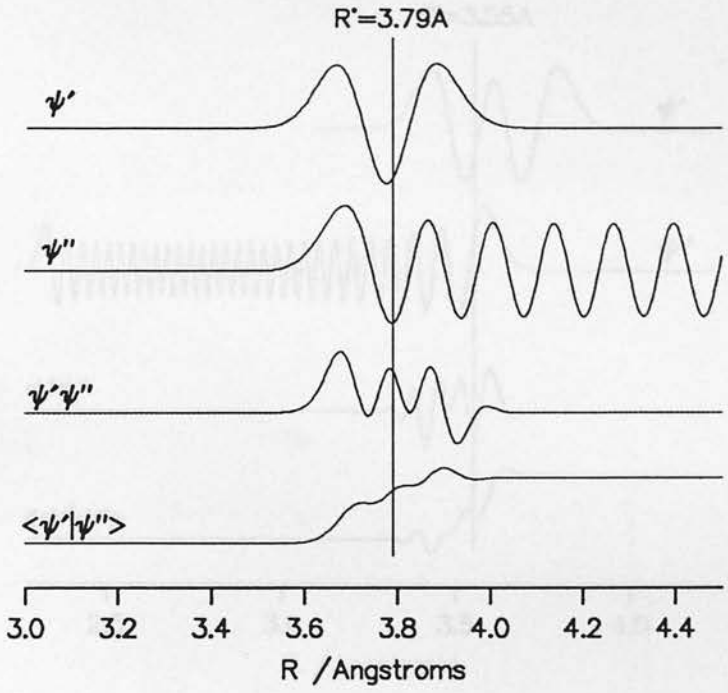

Figure 2.12. Vibrational wavefunctions for the $\delta 2_u(1)(v' = 2) \rightarrow 2_g(ab)$ transition at 466.78nm, their product $\psi'\psi''$ and Franck-Condon overlap, $\langle\psi'|\psi''\rangle$.

one semi-classical point of transition, though they prefer an alternative method where the dipole function is expressed as a power series and the moments of the series calculated from a least squares fit [108]. In practice it has been found that for the transtions considered in this thesis the dipole function can be deduced relatively quickly using an iterative comparison of experiment and calculation provided the function is known over a small range of R from the spectrum of a lower vibrational level with a monotonic difference potential. Even in the absence of this information the high v spectrum is likely to be monotonic over a certain range of R.

Figures 2.16 and 2.15 show the quantum mechanical simulation of the fluorescence spectra sampling a polytonic Mulliken potential, and once again a calculation of Franck-Condon integrals supports the stationary phase approximation of the semi-classical model. Figures 2.17 and 2.18 show the integrals for cases where the two semi-classical transition points sum constructively to give the peaks at

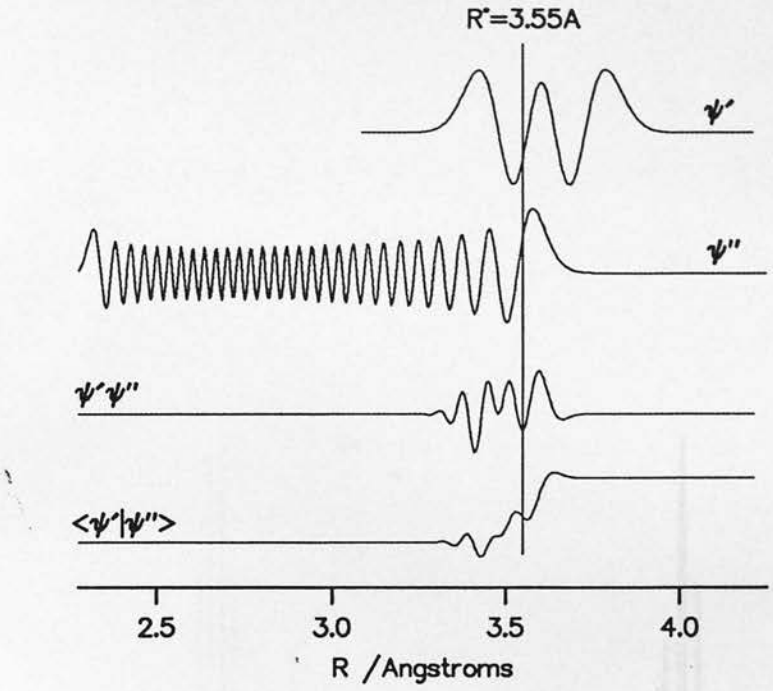

Figure 2.13. Vibrational wavefunctions for the $F0_u^+(2)(v' = 4) \rightarrow X0_g^+(aa)$ transition at 244.27nm, their product $\psi'\psi''$ and Franck-Condon overlap, $\langle\psi'|\psi''\rangle$.

$\lambda = 324.60$nm ($R^* = 3.35, 4.36$) and $\lambda = 270.64$nm ($R^* = 3.73, 4.0$Å) in figures 2.8 and 2.6 respectively; in figure 2.19 the Franck-Condon integral shows destructive interference between the two semi-classical transition points ($R^* = 3.38, 4.31$) leaving the dip at $\lambda = 327.30$nm, while in figure 2.20 the Franck-Condon integral accumulates largely around one of the two semi-classical transition points for $\lambda = 271.06$nm ($R^* = 3.75, 3.97$Å). This last case shows a limitation of the semi-classical model since the most significant accumulation of the Franck-Condon integral occurs outside the semi-classical transition points.

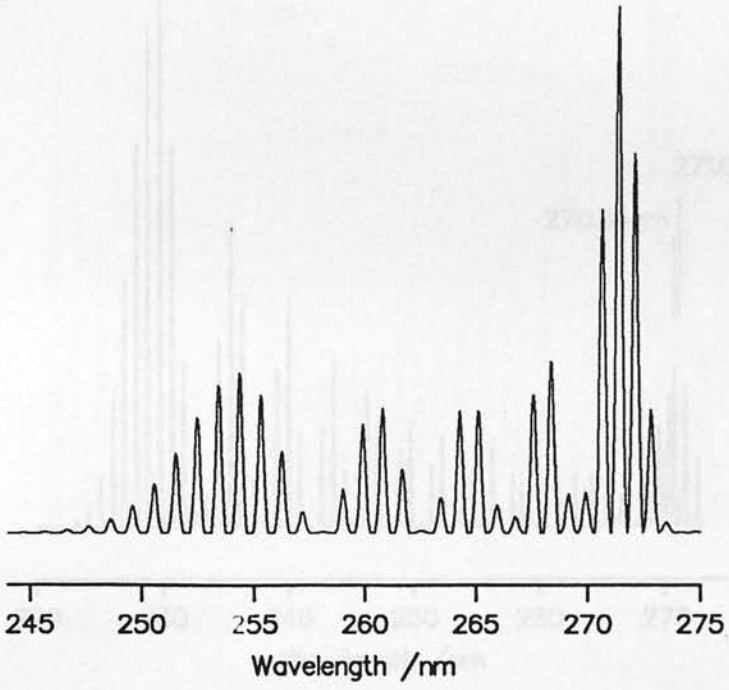

Figure 2.14. Quantum simulation of the $F0_u^+(2)(v' = 4) \rightarrow X0_g^+(aa)$ dispersed fluorescence spectrum in the Condon approximation of constant transition dipole function.

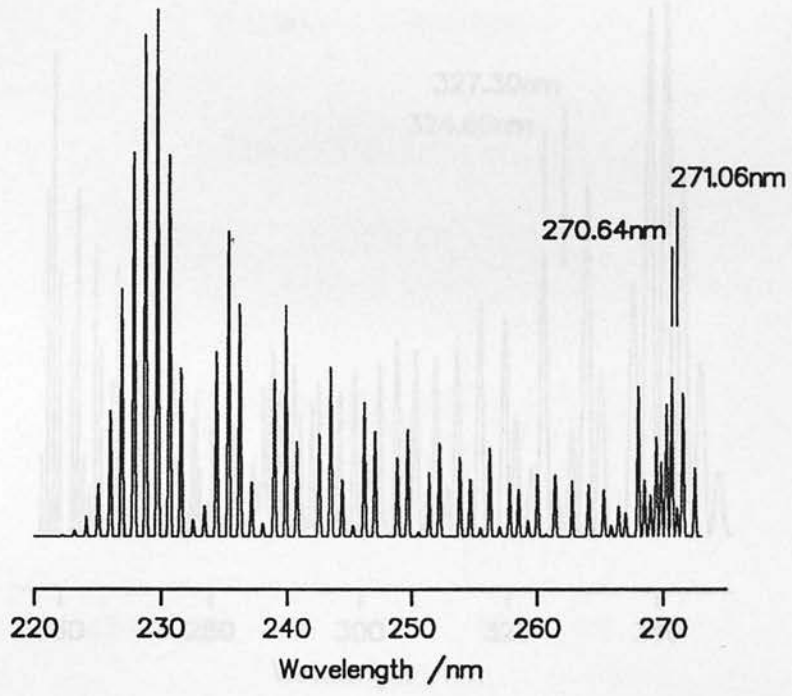

Figure 2.15. Quantum simulation of the $F0_u^+(2)(v' = 19) \rightarrow X0_g^+(aa)$ dispersed fluorescence spectrum.

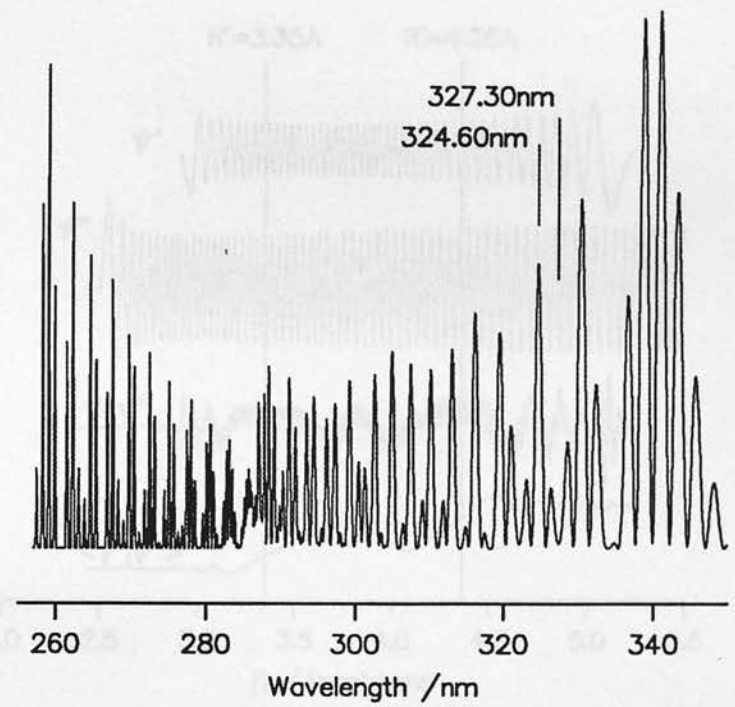

Figure 2.16. Quantum simulation of the $f0_g^+(2)(v' = 88) \rightarrow B0_u^+(ab)$ dispersed fluorescence spectrum.

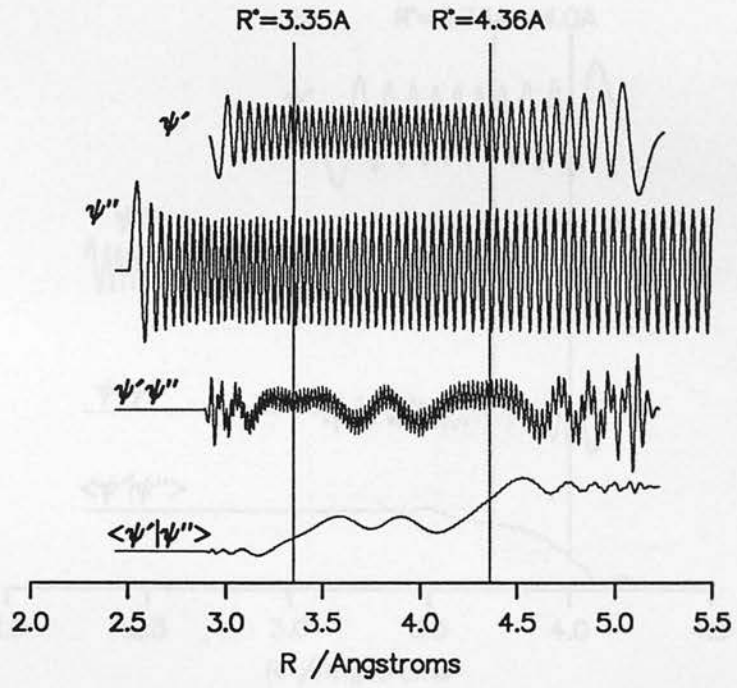

Figure 2.17. Vibrational wavefunctions for the $f0_g^+(2)(v' = 88) \rightarrow B0_u^+(ab)$ transition at 324.60nm, their product $\psi'\psi''$ and Franck-Condon overlap, $\langle\psi'|\psi''\rangle$.

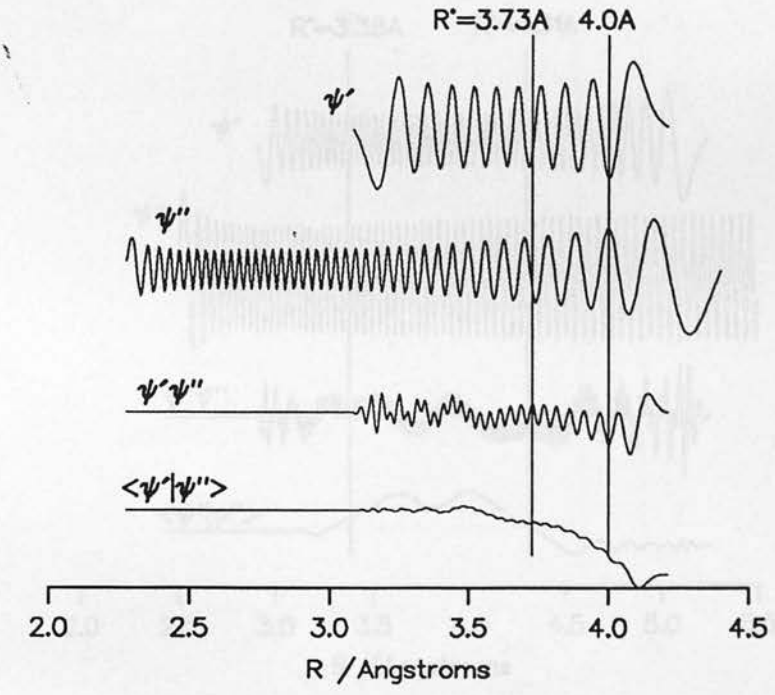

Figure 2.18. Vibrational wavefunctions for the $F0_u^+(2)(v' = 19) \rightarrow X0_g^+(aa)$ transition at 270.64nm, their product $\psi'\psi''$ and Franck-Condon overlap, $\langle\psi'|\psi''\rangle$.

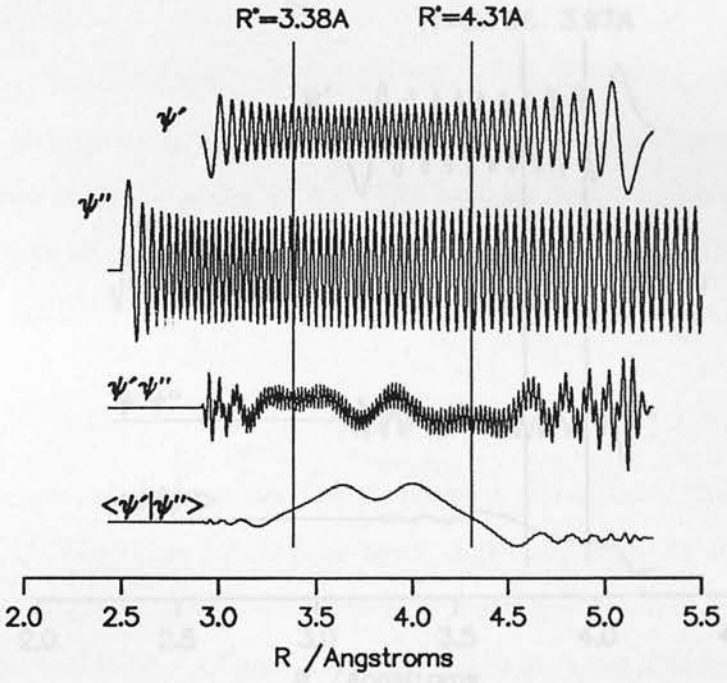

Figure 2.19. Vibrational wavefunctions for the $f0_g^+(2)(v' = 88) \rightarrow B0_u^+(ab)$ transition at 327.30nm, their product $\psi'\psi''$ and Franck-Condon overlap, $\langle\psi'|\psi''\rangle$.

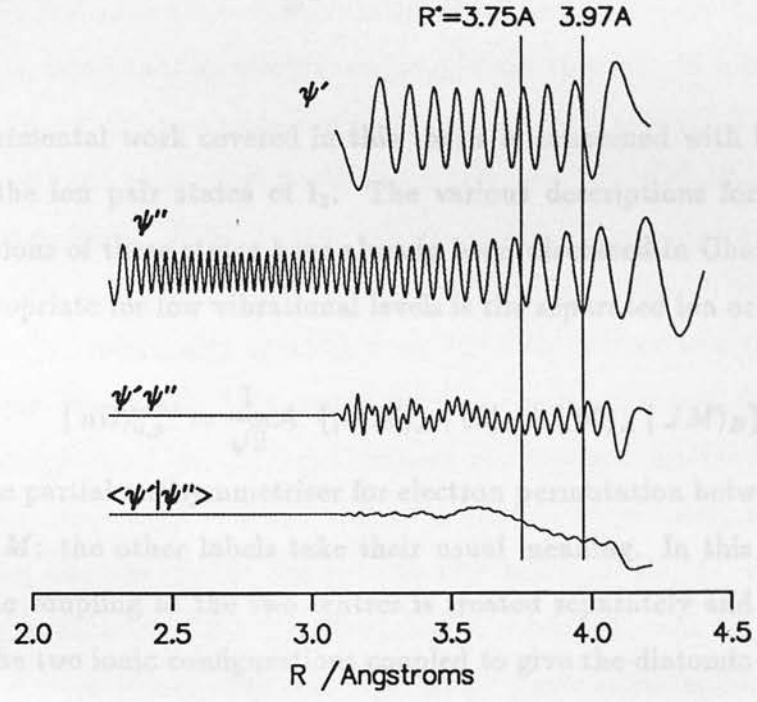

Figure 2.20. Vibrational wavefunctions for the $F0_u^+(2)(v' = 19) \rightarrow X0_g^+(aa)$ transition at 271.06nm, their product $\psi'\psi''$ and Franck-Condon overlap, $\langle\psi'|\psi''\rangle$.

Chapter 3 The Electronic Structure of Heavier Halogens at Large Separation

The experimental work covered in this thesis is concerned with low vibrational levels of the ion pair states of I_2. The various descriptions for the electronic wavefunctions of these states have already been discussed in Chapter 1, and the most appropriate for low vibrational levels is the separated ion or $(J_A M_A J_B M_B)$ scheme:

$$|\, n\Omega\rangle_{u,g}^{(+/-)} = \frac{1}{\sqrt{2}}\mathcal{A}\ \{|\, JM\rangle_A \,|\, 00\rangle_B \pm |\, 00\rangle_A \,|\, JM\rangle_B\}, \qquad (3.1)$$

with $\mathcal{A}$ the partial antisymmetriser for electron permutation between the centres and $\Omega = M$: the other labels take their usual meaning. In this $(J_A M_A J_B M_B)$ scheme the coupling at the two centres is treated separately and only as a final step are the two ionic configurations coupled to give the diatomic wavefunctions: the molecular state is characterised in terms of the angular momenta, J and M_J, of the separated centres. In effect the diatomic molecule is considered as a pair of loosely coupled atomic centres, yet in the discussion covered so far in this thesis the detailed orbital occupancy at each centre has not been considered.

The $(J_A M_A J_B M_B)$ scheme implies separate spin-orbit coupling at the two centres to give the appropriate space quantisation of the $\mathbf{J_i}$ vectors: the coupling between $\mathbf{L_i}$ and $\mathbf{S_i}$ is strong compared to the coupling of $\mathbf{L_i}$ to the internuclear axis [24, p.319], thus the ionic configurations in equation (3.1) would be best described

The work covered in this chapter has been published in Chemical Physics [109].

at zero order by the familiar Russell-Saunders scheme [110]. The characteristic clustering of ion pair states with others having the same ionic dissociation products even down to R_e suggests that over that range in R the $|\,JM\rangle$ wavefunctions of equation (3.1) have configurations close to those of their diabatic dissociation products, $I^+(^3P_2)$ and $I^-(^1S_0)$ for example in iodine's first IP cluster. However these dissociation products will not have pure Russell-Saunders configurations since the RS scheme neglects spin-orbit coupling and we would not expect such a simple description to be entirely successful for a heavy atom like iodine: it is known from the anomalous energy ordering of the $I^+(^3P_J)$ multiplet [42, p.108] that there is significant spin-orbit coupling in the free ion. In a later section we refine the Russell-Saunders description to allow for this spin-orbit coupling which mixes the cationic configurations $^3P_2$ with $^1D_2$, and $^3P_0$ with $^1S_0$.

Furthermore the $(J_A M_A J_B M_B)$ scheme treats the coupling at the two centres separately in deriving their atomic configurations: the electrostatic field is assumed to be spherically symmetric at the two centres and the three p orbitals remain degenerate. However as the two nuclei approach, and a cylindrical field symmetry develops, we would expect electrostatic interactions, primarily charge(I^-)-quadrupole(I^+) for IP states, to lift this degeneracy. Subsequently at small R the electron clouds interact strongly and a single MO description will emerge for each state. For the IP states of iodine the sum of the ionic radii of the $5p$ orbitals is less than the equilibrium internuclear separation and little orbital overlap between centres occurs even at R_e, justifying the choice of the separated atom scheme, rather than an MO approach, in describing the electronic wavefunction. The most significant intramolecular interaction, after the Coulombic attraction between the ionic charges, is therefore that of the electronic quadrupole of the cation with the Stark field gradient of the anion. This mixes cationic configurations with the same total spin and M_J and is discussed in a later section.

Although these perturbations do significantly alter the electronic structure of

iodine's ion pair states, the Russell-Saunders functions still dominate the molecular configurations at R_e^{IP} and consequently the RS configurations will be used as the basis in which the perturbations are discussed. In this thesis the ion pair electronic structures are described using the Russell-Saunders scheme at the two centres separately, allowing for the spin-orbit and electrostatic interactions by the usual superposition of basis configurations at the cationic centre, then coupling the two ionic functions in the $(J_A M_A J_B M_B)$ scheme to give the molecular wavefunction. The extent to which this approach is applicable to the halogen and interhalogen molecular states at large R depends on the strength of the spin-orbit coupling at the atomic centres: this ensures that J_i, rather than L_i, remains a good quantum number in the molecule. This requirement must be balanced against that of the Russell-Saunders scheme which needs the spin-orbit coupling to be weak compared to the inter-electron repulsion at a centre, however overall the weaker the spin-orbit interaction the larger the separation at which our approach will break down. Among the halogens this model will therefore be of more use for compounds of I and Br; in Cl_2 the model, if applicable to any extent, could only be used beyond the outer minimum of the IP states, and not at the inner Rydbergised minimum.

The first section of this Chapter therefore introduces the Russell-Saunders description for the ionic configurations and later sections discuss each of the perturbations in turn. Since the anion can only take one state, $^1S_0$, we discuss these perturbations in terms of their mixing of cationic RS configurations and the implications this has for the molecular wavefunction. A description for the valence states, which are not considered in the same detail in this thesis, will be given in the final section.

3.1 The RS description of atomic configurations

Condon and Shortley have discussed the Russell-Saunders coupling scheme at length [41], describing it as an intermediate approximation where the Coulomb interaction between electrons is taken to be strong and the spin-orbit interaction neglected, or at least treated as small compared to the inter-electron repulsion. This inter-electron interaction couples the electronic orbital angular momenta together to form the resultant, L, and causes the large energy difference between states of different spin multiplicity. The electron spins couple to form S, and the weak spin-orbit operator then couples S to the resultant orbital angular momentum to give the total angular momentum for the state, J=L+S. The atomic state is then described by its term symbol, $^{2S+1}L_J$. In the separated ion coupling scheme, the internuclear axis defines a fourth quantum number for the state, the resultant of the total angular momentum along the internuclear axis, M_J. We now need to determine how the term symbol of a Russell-Saunders state also defines the electronic occupancy in the valence shell at the centre.

We are concerned with Russell-Saunders configurations for the $I^+(p^4)$ and $I^-(p^6)$ configurations. There are six spin-orbitals available, which are described by their atomic m_l and m_s values: the p orbital has one unit of orbital angular momentum which can be orientated relative to a z-axis such that $m_l = 0, \pm 1$; m_s can take $\pm\frac{1}{2}$. Since we shall be using these RS configurations to form diatomic wavefunctions, the z-axis can be taken as parallel to the internuclear axis, and the configurations will be differentiated by their M_J component along that axis.[1]

The simplest case to describe for the p^4 configuration is the $|\,^1D_{22}\rangle$ configuration: to achieve a singlet state all electron spins must be paired, and to achieve $L = 2$, both the $m_l = +1$ orbitals must be occupied and the $m_l = -1$ orbitals empty. Written as a Slater determinant [111, 112], the $^1D_{22}$ state therefore has

[1]The z-axis is not defined in the Russell-Saunders scheme and can be taken in any arbitrary direction, however transforming the axes transforms the occupancy of a $|\,^{2S+1}L_J\rangle$ state amongst its $(2J+1)$ M_J components.

$\|1^+1^-0^+0^-\|$ occupancy. In general

$$|\,^{2S+1}\mathrm{L}_{\mathrm{JM}}\rangle = \sum_{k,M_L,M_S} \langle kM_LM_S|LSJM_J\rangle \Delta^{(n)}(kM_LM_S), \tag{3.2}$$

where $\Delta^{(n)}(kM_LM_S)$ is a single Slater determinant of n p-type spin-orbitals with resultant components M_L and M_S; k numbers the determinants sequentially if more than one combination of spins and spatial orbitals is possible for a given value of M_L and M_S. Thus

$$\Delta^{(4)}(120) \equiv \quad \|1^+1^-0^+0^-\|, \tag{3.3}$$

$$\Delta^{(4)}(100) \equiv \quad \|1^+1^-\underline{1}^+\underline{1}^-\|, \tag{3.4}$$

$$\Delta^{(4)}(200) \equiv \quad \|1^+0^+0^-\underline{1}^-\|, \tag{3.5}$$

$$\Delta^{(4)}(300) \equiv \quad \|1^+0^+0^-\underline{1}^+\|, \text{etc.} \tag{3.6}$$

Interchanging columns in a determinant introduces a sign change in the wavefunction, ie $\|1^+0^+0^-\underline{1}^+\| = -\|1^+0^-0^+\underline{1}^+\|$, and the overall sign of any $\Delta^{(n)}$ is based on the canonical order

$$\Delta^{(6)} = \|1^+1^-0^+0^-\underline{1}^+\underline{1}^-\|. \tag{3.7}$$

The rules for generating the coefficients $\langle kM_LM_S|LSJM_J\rangle$ using ladder operators are quite standard (see for example [41, p.226]) but specific values for the p^4 and p^5 configurations, which we shall use frequently in this thesis, are tabulated here for ease of reference. Table 3.1 therefore gives the spin-orbital occupancy implied in the Russell-Saunders scheme by the state symbols for the p^4 configuration.

The molecular wavefunction can therefore be readily built up for the IP state from these Russell-Saunders functions: the Ω value of the IP state, and its dissociation products, determine which of the possible Russell-Saunders configurations is included in equation (3.1). The $\Omega = 2$ state of the third cluster, dissociation products $\mathrm{I}^+(^1\mathrm{D}_2)$ and $\mathrm{I}^-(^1\mathrm{S}_0)$, is therefore described by

$$\begin{aligned} |\,2_{g,u}(3)\rangle_{RS} = \quad & \tfrac{1}{\sqrt{2}}\{|\,^1\mathrm{D}_{22}\rangle_a\,|\,^1\mathrm{S}_{00}\rangle_b \pm |\,^1\mathrm{S}_{00}\rangle_a\,|\,^1\mathrm{D}_{22}\rangle_b\} \\ = \quad & \tfrac{1}{\sqrt{2}}\{\|1^+1^-0^+0^-\|_a\|1^+1^-0^+0^-\underline{1}^+\underline{1}^-\|_b \\ & \pm\|1^+1^-0^+0^-\underline{1}^+\underline{1}^-\|_a\|1^+1^-0^+0^-\|_b\}. \end{aligned} \tag{3.8}$$

State	Configuration
$\|\,^1S_0\rangle$	$\frac{1}{\sqrt{3}}[\|1^-0^+0^-\underline{1}^+\| - \|1^+0^+0^-\underline{1}^-\| - \|1^+1^-\underline{1}^+\underline{1}^-\|]$
$\|\,^1D_{22}\rangle$	$\|1^+1^-0^+0^-\|$
$\|\,^1D_{21}\rangle$	$\frac{1}{\sqrt{2}}[\|1^+1^-0^+\underline{1}^-\| - \|1^+1^-0^-\underline{1}^+\|]$
$\|\,^1D_{20}\rangle$	$\frac{1}{\sqrt{6}}[\|1^-0^+0^-\underline{1}^+\| - \|1^+0^+0^-\underline{1}^-\| + 2\|1^+1^-\underline{1}^+\underline{1}^-\|]$
$\|\,^3P_{00}\rangle$	$\frac{-1}{\sqrt{6}}[\|1^+0^+0^-\underline{1}^-\| + \|1^-0^+0^-\underline{1}^+\| + \sqrt{2}\|1^+0^+\underline{1}^+\underline{1}^-\| + \sqrt{2}\|1^+1^-0^-\underline{1}^-\|]$
$\|\,^3P_{11}\rangle$	$\frac{-1}{2}[\sqrt{2}\|1^+0^+0^-\underline{1}^+\| + \|1^+1^-0^-\underline{1}^+\| + \|1^+1^-0^+\underline{1}^-\|]$
$\|\,^3P_{10}\rangle$	$\frac{1}{\sqrt{2}}[\|1^+0^+\underline{1}^+\underline{1}^-\| - \|1^+1^-0^-\underline{1}^-\|]$
$\|\,^3P_{22}\rangle$	$\|1^+1^-0^+\underline{1}^+\|$
$\|\,^3P_{21}\rangle$	$\frac{1}{2}[\sqrt{2}\|1^+0^+0^-\underline{1}^+\| - \|1^+1^-0^-\underline{1}^+\| - \|1^+1^-0^+\underline{1}^-\|]$
$\|\,^3P_{20}\rangle$	$\frac{1}{\sqrt{6}}[\sqrt{2}\|1^+0^+0^-\underline{1}^-\| + \sqrt{2}\|1^-0^+0^-\underline{1}^+\| - \|1^+0^+\underline{1}^+\underline{1}^-\| - \|1^+1^-0^-\underline{1}^-\|]$

Table 3.1. Russell-Saunders configurations for p^4 occupancy.

State	Configuration
$\|\,^2P_{\frac{3}{2}\frac{3}{2}}\rangle$	$\|1^+1^-0^+0^-\underline{1}^+\|$
$\|\,^2P_{\frac{3}{2}-\frac{3}{2}}\rangle$	$-\|1^-0^+0^-\underline{1}^+\underline{1}^-\|$
$\|\,^2P_{\frac{3}{2}\frac{1}{2}}\rangle$	$\frac{1}{\sqrt{3}}[\|1^+1^-0^+0^-\underline{1}^-\| - \sqrt{2}\|1^+1^-0^+\underline{1}^+\underline{1}^-\|]$
$\|\,^2P_{\frac{3}{2}-\frac{1}{2}}\rangle$	$\frac{-1}{\sqrt{3}}[\|1^+0^+0^-\underline{1}^+\underline{1}^-\| - \sqrt{2}\|1^+1^-0^-\underline{1}^+\underline{1}^-\|]$
$\|\,^2P_{\frac{1}{2}\frac{1}{2}}\rangle$	$\frac{1}{\sqrt{3}}[\sqrt{2}\|1^+1^-0^+0^-\underline{1}^-\| + \|1^+1^-0^+\underline{1}^+\underline{1}^-\|]$
$\|\,^2P_{\frac{1}{2}-\frac{1}{2}}\rangle$	$\frac{1}{\sqrt{3}}[\sqrt{2}\|1^+0^+0^-\underline{1}^+\underline{1}^-\| + \|1^+1^-0^-\underline{1}^+\underline{1}^-\|]$

Table 3.2. Russell-Saunders configurations for p^5 occupancy.

However we would not expect this simple description neglecting spin-orbit coupling at the cationic centre to hold true for iodine (it is known that even in the free ion I^+ there is partial jj coupling) therefore the next section considers the extent of this coupling and its effect on the ion pair wavefunction.

3.2 Breakdown of the RS scheme: spin-orbit interactions

Russell-Saunders coupling, in which the spin-orbit interaction is considered small compared to the inter-electron repulsion, separates the p^n configuration into different terms characterised by their L and S quantum numbers: the inter-electron repulsion does not lift the J degeneracy. As Condon and Shortley have discussed [41], the spin-orbit operator, $\mathbf{L.S}$, commutes with $\mathbf{J}$ but not with $\mathbf{L}$ and $\mathbf{S}$, thus J still labels states when spin-orbit coupling is introduced, though L and S are no longer good quantum numbers. Thus when spin-orbit coupling is considered states with different L and S but the same J can be mixed: we shall find later that in the case of I^+ the lowest energy state does not have a pure $^3P_2$ configuration but about 90% $^3P_2$ character and about 10% $^1D_2$ character. However the Russell-Saunders state still dominates the configuration, and therefore in this regime we expect the dominant inter-electron repulsion to determine the ordering of the ^{2S+1}L terms and the spin-orbit operator to lift their J degeneracy, leaving terms effectively characterised by their S and L quantum numbers but distinguished by their different J values. The diagonal elements of the spin-orbit operator lift the J degeneracy of a multiplet, and the off-diagonal terms, by mixing in other RS states, for example the $^3P_2 - {}^1D_2$ interaction above, can give the multiplet an anomalous ordering. Thus for the p^4 configuration the spin-orbit operator is responsible for separating the three ^3P_J terms, with the $J = 0$ state pushed lower in energy than the $J = 1$ state by the $^3P_0 - {}^1S_0$ interaction.

In this section we shall calculate the extent of spin-orbit coupling in the $I^+(p^4)$ configuration from the experimental term values, then solve for the eigenfunctions

as linear combinations of our zero order RS functions. We can then substitute these improved functions into equation (3.1) to generate the molecular wavefunctions in the $(J_A M_A J_B M_B)$ coupling scheme, assuming no intramolecular interaction. We shall use these functions in later Chapters where experimental evidence will reveal the extent of the intramolecular interactions discussed in the next section.

The spin-orbit operator, $\hat{H}_{SO}$, can be written as [41]

$$\hat{H}_{SO} = \lambda \mathrm{L.S}, \tag{3.9}$$

where λ is the many electron spin-orbit coupling constant for the configuration being considered. Neglecting spin-other orbit interactions, we can rewrite (3.9) as

$$\hat{H}_{SO} = \sum_i \xi(r_i) \mathrm{l_i.s_i}, \tag{3.10}$$

where the sum is over all electrons in open shells and $\xi(r)$ is the one electron equivalent of λ. The scalar product can be expanded

$$\mathrm{l_i.s_i} = [\hat{l}_x \hat{s}_x + \hat{l}_y \hat{s}_y + \hat{l}_z \hat{s}_z] \tag{3.11}$$

$$= [\tfrac{1}{2}(\hat{l}_+ \hat{s}_- + \hat{l}_- \hat{s}_+) + \hat{l}_z \hat{s}_z], \tag{3.12}$$

where the ladder operators take their usual form, $\hat{l}_\pm = \hat{l}_x \pm i\, \hat{l}_y$, operating on the spinorbitals $\mid l, m_l, s, m_s \rangle$ with the effect

$$\hat{l}_\pm \mid l, m_l, s, m_s \rangle = [l(l+1) - m_l(m_l \pm 1)]^{\frac{1}{2}} \mid l, m_l \pm 1, s, m_s \rangle, \tag{3.13}$$

$$\hat{s}_\pm \mid l, m_l, s, m_s \rangle = [s(s+1) - m_s(m_s \pm 1)]^{\frac{1}{2}} \mid l, m_l, s, m_s \pm 1 \rangle. \tag{3.14}$$

The degree of spin-orbit coupling between two terms is a sum of the spin-orbit interactions between the one electron spinorbitals in the particular microstates being considered, the off-diagonal matrix elements being calculated using the formulae above and the diagonal elements from

$$\hat{l}_z \hat{s}_z \mid l, m_l, s, m_s \rangle = m_l m_s \mid l, m_l, s, m_s \rangle. \tag{3.15}$$

So, for example, the diagonal matrix element of the spin-orbit operator for the $^3P_{22}$ state, $\|1^+1^-0^+\underline{1}^+\|$, is $-\frac{1}{2}\zeta_{5p}$, where $\zeta_{nl} = \langle nl \mid \xi(r) \mid nl\rangle$ is the effective one-electron spin-orbit coupling constant for an electron in a ϕ_{nl} orbital. The strength of interaction coupling the $^3P_2$ and $^1D_2$ configurations, $\langle\|1^+1^-0^+\underline{1}^+\| \, |\hat{H}_{SO}| \, \|1^+1^-0^+0^-\|\rangle$, is $\frac{1}{\sqrt{2}}\zeta_{5p}$ with the ladder operators $\hat{l}_-\hat{s}_+$ acting on the $\|0^-\|$ orbital.

Including Condon and Shortley's results for the Coulombic repulsion interaction, $\hat{H}_{r_{ij}}$, our energy matrix for the spin-orbit coupling of the p^4 Russell-Saunders states becomes

$$
\begin{aligned}
\langle {}^1S_0 \, |\hat{H}_{r_{ij}} + \hat{H}_{SO} \, | \, {}^1S_0\rangle &= \quad 10F_2, \\
\langle {}^1D_2 \, |\hat{H}_{r_{ij}} + \hat{H}_{SO} \, | \, {}^1D_2\rangle &= \quad F_2, \\
\langle {}^3P_2 \, |\hat{H}_{r_{ij}} + \hat{H}_{SO} \, | \, {}^3P_2\rangle &= -5F_2 - \tfrac{1}{2}\zeta_{5p}, \\
\langle {}^3P_1 \, |\hat{H}_{r_{ij}} + \hat{H}_{SO} \, | \, {}^3P_1\rangle &= -5F_2 + \tfrac{1}{2}\zeta_{5p}, \\
\langle {}^3P_0 \, |\hat{H}_{r_{ij}} + \hat{H}_{SO} \, | \, {}^3P_0\rangle &= -5F_2 + \zeta_{5p}, \\
\langle {}^3P_0 \, |\hat{H}_{r_{ij}} + \hat{H}_{SO} \, | \, {}^1S_0\rangle &= \quad -\sqrt{2}\zeta_{5p}, \\
\langle {}^3P_2 \, |\hat{H}_{r_{ij}} + \hat{H}_{SO} \, | \, {}^1D_2\rangle &= \quad \tfrac{1}{\sqrt{2}}\zeta_{5p},
\end{aligned}
$$

where F_2 is the Coulomb repulsion energy between $5p$ electrons. The spin-orbit operator is therefore able to lift the J degeneracy of the Russell-Saunders scheme: the diagonal terms $\langle JM \, |\hat{H}_{SO}| \, JM\rangle$ are different for different J states of a multiplet. It is also responsible for mixing Russell-Saunders states with different L and S but the same J, for example the $^3P_0$ with the $^1S_0$ in the $I^+(p^4)$ configuration.

On solving the energy matrix using the observed $T_e^{I^+}$ values [42, p.108] it becomes clear that in this over determined case all four intervals cannot be fitted with just the two parameters, and we choose to optimise the lowest three as this reproduces the energy ordering of the anomalous ^3P_J multiplet and so should most closely reflect the effective spin-orbit coupling. These intervals yield the parameter values of $\zeta_{5p} = 5764\text{cm}^{-1}$ and $F_2 = 1368\text{cm}^{-1}$, and the eigenvectors given in Table 3.3; the vectors for the four interval optimised fit are included

JM State	T_J(Obs)	T_J(Calc)	Eigenfunction
$\|2M(1)\rangle$	0	0 (0)	$0.950\,\|\,^3P_2\rangle_{RS} - 0.312\,\|\,^1D_2\rangle_{RS}$ $(0.964\,\|\,^3P_2\rangle_{RS} - 0.266\,\|\,^1D_2\rangle_{RS})$
$\|00(2)\rangle$	6451	6367 (6649)	$0.914\,\|\,^3P_0\rangle_{RS} + 0.405\,\|\,^1S_0\rangle_{RS}$ $(0.947\,\|\,^3P_0\rangle_{RS} + 0.322\,\|\,^1S_0\rangle_{RS})$
$\|1M(2)\rangle$	7090	7100 (6547)	$\|\,^3P_1\rangle_{RS}$ $(\|\,^3P_1\rangle_{RS})$
$\|2M(3)\rangle$	13731	13765 (15116)	$0.312\,\|\,^3P_2\rangle_{RS} + 0.950\,\|\,^1D_2\rangle_{RS}$ $(0.266\,\|\,^3P_2\rangle_{RS} + 0.964\,\|\,^1D_2\rangle_{RS})$
$\|00(4)\rangle$	32629	28359 (32045)	$0.405\,\|\,^3P_0\rangle_{RS} - 0.914\,\|\,^1S_0\rangle_{RS}$ $(0.322\,\|\,^3P_0\rangle_{RS} - 0.947\,\|\,^1S_0\rangle_{RS})$

Table 3.3. I^+eigenfunctions after partial jj coupling. Only the first three term differences are fitted: term values are taken from [42]. Eigenfunctions in parentheses are the results from the complete four interval fit ($\zeta = 5479\text{cm}^{-1}$, $F_2 = 1707\text{cm}^{-1}$).

for comparison. The departures from the Russell-Saunders coupling scheme are quite large, but the dominant component of each $|\ JM\rangle$ state is still the RS configuration with coefficients of > 0.9.

We can now see the origins of the ordering adopted by the IP clusters, which in the separated ion model will follow the T_e order observed for I^+. The third and fourth clusters with cationic parentage $^1D_2$ and $^1S_0$ have highest energy on account of the larger inter-electron repulsion implied by their singlet nature, with the $^1D_2$ state lying the lower in energy of the two. The first and second clusters are split by the spin-orbit operator, with the $^3P_0$ term stabilised to lower energy than the $^3P_1$ by its interaction with the distant $^1S_0$ state. The splitting of states within a cluster arises from the intramolecular interactions discussed in the next section. It should be borne in mind that when the dissociation products of the IP clusters are routinely referred to as $^3P_2$ for the first cluster, $^3P_{1,0}$ for the second, etc, this is in fact inaccurate as the ions have appreciable spin-orbit components and the RS scheme gives only the dominant configuration.

3.3 Intramolecular coupling: the charge-quadrupole interaction

By treating the molecular wavefunction as a product of two atomic functions, the $(J_A M_A J_B M_B)$ scheme treats the diatomic as a pair of loosely associated atoms with the coupling being considered at each centre separately. However as the two nuclei approach there will be some interaction between the two centres and the development of a Coulombic field with cylindrical rather than spherical symmetry, lifting the p orbital degeneracy. As the orbital overlap increases at shorter R, this will lead eventually to a single MO configuration emerging for each electronic state: the separated atom approach neglects these intramolecular interactions, and can only be valid when they are small.

We have found in Chapter 1 that the $(J_A M_A J_B M_B)$ scheme is appropriate to describe the electronic structure of the IP states of I_2 for $R \geq R_e$: the sum of the

ionic radii for the valence orbitals is significantly less than R_e^{IP} and consequently orbital overlap between the two centres is expected to be small. However there must be significant intramolecular interactions as the molecule is strongly bound: there must be some centre-centre interaction that is not mediated through orbital overlap. Section 1.1.2 demonstrated that most of the bond energy for the IP states ($> 95\%$) arises from the strong Coulombic attraction between ions of opposite charge. This does not mix RS configurations at the cationic centre but the next electrostatic interaction for the IP pair states, that between the anionic field gradient and the cationic quadrupole, will. Its effect depends on the axial component of the total electronic angular momentum, ie on M_J. The charge-quadrupole interaction is therefore primarily responsible for separating the different Ω components of a particular ion pair cluster, ie states having the same diabatic dissociation products. The $2_{u,g}(1)$ states with predominantly $^3P_{22}$ and $^1S_0$ parentage will have a different charge-quadrupole interaction from the other members of its cluster, which have largely $^3P_{21}$ and $^3P_{20}$ configurations at the cationic centre. As with the spin-orbit operator, the diagonal matrix elements are different for different M_J and the off-diagonal elements are able to mix different RS configurations.

This section discusses the charge-quadrupole interaction for the ion pair states of I^+, and derives the coupling matrix between RS states. The degree to which this interaction mixes cationic states is suggested, and will be compared later with the electronic configurations derived from experiment in Chapter 6.

Buckingham has described the interaction of a charge distribution with an external field [113], and we apply his results to find the energy of interaction between the $I^+(p^4)$ quadrupole and the field gradient due to the anionic charge. The matrix elements for the charge-quadrupole interaction under Russell-Saunders coupling are

$$\langle JM \mid \frac{1}{2}\Theta_{zz}F'_{zz} \mid JM\rangle = \frac{e^2\langle\rho^2\rangle_+}{4\pi\epsilon_0 r_{AB}^3}\langle {}^{2S+1}L_{J_1M} \mid \sum_i P_{20}(\theta_i) \mid {}^{2S+1}L_{J_2M}\rangle, \qquad (3.16)$$

where r_{AB} is the interionic separation, F'_{zz} the field gradient, $\langle\rho^2\rangle_+ = \langle nl \mid \rho^2 \mid nl\rangle$

the mean square electron radius of a cationic valence orbital; the sum is over all electrons in the cationic valence shell, and P_{20} is the Legendre polynomial $(3\cos^2\theta - 1)$. It is assumed that the radial form of the valence orbitals is the same in both states of the cation, and there is negligible overlap between the electron clouds such that the two centres can be treated as point charges. The interaction can therefore couple RS states of the same M_J and spin multiplicity.

As was found for the spin-orbit operator, the degree of electrostatic charge-quadrupole coupling depends on the particular cationic microstate being considered. The contribution of each electron to the angular integrals can be calculated from standard theory (see [114]):

$$\langle Y_{11} \mid P_{20}(\theta) \mid Y_{11}\rangle = -\tfrac{1}{5}, \tag{3.17}$$

$$\langle Y_{10} \mid P_{20}(\theta) \mid Y_{10}\rangle = \tfrac{2}{5}. \tag{3.18}$$

Thus the diagonal matrix element for the $^3P_{22}$ Russell-Saunders configuration, $\|1^+1^-0^+\underline{1}^+\|$, is $-\frac{1}{5}Q$, with $Q = e^2\langle\rho^2\rangle_+/4\pi\epsilon_0 r_{AB}^3$. Off-diagonal terms arise when a microstate is common to more than one RS configuration, for example the microstates of the $^3P_{20}$ configuration are present in the $^3P_{00}$ configuration, and their coupling element is $\frac{\sqrt{2}}{5}Q$. The complete set of the angular integrals for the p^4 configuration is

$$\langle {}^1D_{22} \mid P_{20}(\theta_i) \mid {}^1D_{22}\rangle = \tfrac{2}{5},$$

$$\langle {}^1D_{21} \mid P_{20}(\theta_i) \mid {}^1D_{21}\rangle = -\tfrac{1}{5},$$

$$\langle {}^1D_{20} \mid P_{20}(\theta_i) \mid {}^1D_{20}\rangle = -\tfrac{2}{5},$$

$$\langle {}^3P_{22} \mid P_{20}(\theta_i) \mid {}^3P_{22}\rangle = -\tfrac{1}{5},$$

$$\langle {}^3P_{21} \mid P_{20}(\theta_i) \mid {}^3P_{21}\rangle = \tfrac{1}{10},$$

$$\langle {}^3P_{20} \mid P_{20}(\theta_i) \mid {}^3P_{20}\rangle = \tfrac{1}{5},$$

$$\langle {}^3P_{11} \mid P_{20}(\theta_i) \mid {}^3P_{11}\rangle = \tfrac{1}{10},$$

$$\langle {}^3P_{10} \mid P_{20}(\theta_i) \mid {}^3P_{10}\rangle = -\tfrac{1}{5},$$

$$\langle {}^3P_{20} \mid P_{20}(\theta_i) \mid {}^3P_{00}\rangle = \tfrac{\sqrt{2}}{5},$$

$$\langle {}^1S_{00} \mid P_{20}(\theta_i) \mid {}^1D_{20}\rangle = -\tfrac{2\sqrt{2}}{5},$$

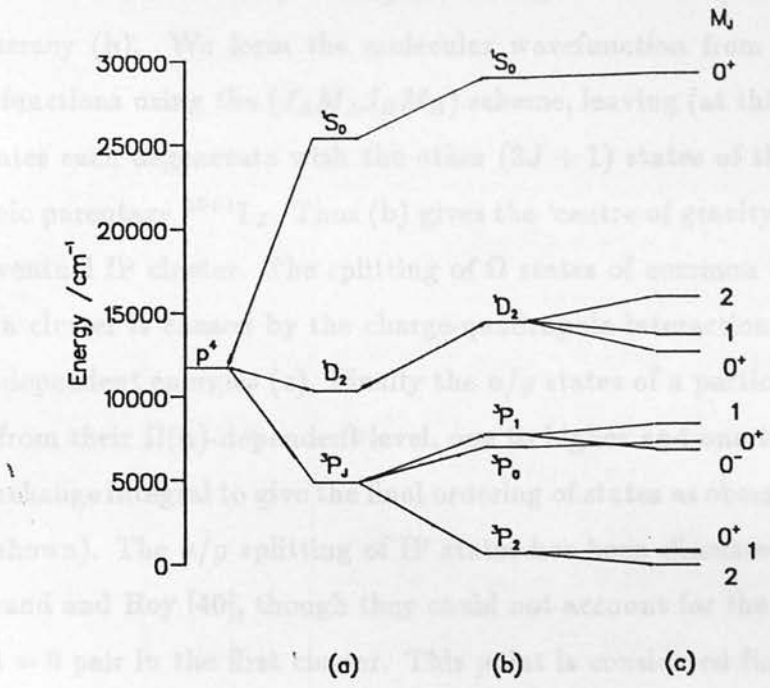

Figure 3.1. Coupling interactions invoked in describing the cationic configurations: (a) Russell-Saunders (b) spin-orbit (c) charge-quadrupole.

$$\langle {}^3\mathrm{P}_{21} \mid P_{20}(\theta_i) \mid {}^3\mathrm{P}_{11} \rangle = \tfrac{3}{10},$$

(zero elements omitted). The charge-quadrupole interaction favours p_π occupancy over p_σ though this stabilisation will be balanced by the increased inter-electron repulsion in some microstates with low p_σ occupancy, for example $\|1^+1^-1^+1^-\|$, and the strength of the spin-orbit interaction. We are now in a position to give our final description of the IP wavefunction, ready for refinement in the light of the experimental results presented in later Chapters.

3.4 The electronic structure of IP states

Figure 3.1 shows schematically the various coupling schemes used in this thesis to describe the IP configuration. Briefly the ionic configurations are described in the Russell-Saunders scheme (a), with the inter-electron repulsion separating

the various terms of the p^4 configuration. Spin-orbit coupling then lifts the J degeneracy (b). We form the molecular wavefunction from a product of the ionic functions using the $(J_A M_A J_B M_B)$ scheme, leaving (at this stage) a stack of IP states each degenerate with the other $(2J+1)$ states of the same dominant cationic parentage $^{2S+1}L_J$. Thus (b) gives the 'centre of gravity' for the energy of the eventual IP cluster. The splitting of Ω states of common ionic parentage to form a cluster is caused by the charge-quadrupole interaction, leaving states at $\Omega(n)$-dependent energies (c). Finally the u/g states of a particular $\Omega(n)$ pair are split from their $\Omega(n)$-dependent level, one to higher and one to lower energy, by the exchange integral to give the final ordering of states as observed in experiment (not shown). The u/g splitting of IP states has been discussed for the halogens by Brand and Hoy [40], though they could not account for the energy reversal of the $\Omega = 0$ pair in the first cluster. This point is considered further in Appendix A.

When deriving the eigenfunctions we assume that the spin-orbit coupling at R_e^{IP} is close to that of the free ion, and we take these eigenfunctions (Table 3.3) as the input to the charge-quadrupole matrix. The intramolecular charge-quadrupole interaction is then allowed to mix RS states of the same M_J and spin multiplicity as described in the previous section to generate our final functions. For low IP vibrational levels $r_{AB} \approx R_e^{IP}$ and thus the strength of the charge-quadrupole interaction $Q \approx 4500\text{cm}^{-1}$ where $\langle\rho^2\rangle_+ = 1.87\text{Å}^2$ [115], assuming a point charge model for the two centres. This gives the final eigenfunctions listed in Table 3.4. However this extent of intramolecular interaction separates the members of a cluster too far to reproduce the close T_e clustering observed for states with the same diabatic dissociation products (figure 3.2). In Chapter 6 we deduce the electronic configurations of the IP states from the dipole moments of their transitions to the valence states and there we will consider their reconciliation with the configurations derived using this theory.

JM State	Eigenfunction
$\|\, 22(1)\rangle$	$0.965 \,\|\, {}^3P_{22}\rangle_{RS} - 0.264 \,\|\, {}^1D_{22}\rangle_{RS}$
$\|\, 21(1)\rangle$	$0.929 \,\|\, {}^3P_{21}\rangle_{RS} - 0.168 \,\|\, {}^3P_{11}\rangle_{RS}$ $-0.331 \,\|\, {}^1D_{21}\rangle_{RS}$
$\|\, 20(1)\rangle$	$0.896 \,\|\, {}^3P_{20}\rangle_{RS} - 0.207 \,\|\, {}^3P_{00}\rangle_{RS}$ $-0.377 \,\|\, {}^1D_{20}\rangle_{RS} - 0.108 \,\|\, {}^1S_{00}\rangle_{RS}$
$\|\, 00(2)\rangle$	$0.251 \,\|\, {}^3P_{20}\rangle_{RS} + 0.883 \,\|\, {}^3P_{00}\rangle_{RS}$ $-0.003 \,\|\, {}^1D_{20}\rangle_{RS} + 0.398 \,\|\, {}^1S_{00}\rangle_{RS}$
$\|\, 11(2)\rangle$	$-0.129 \,\|\, {}^3P_{21}\rangle_{RS} - 0.982 \,\|\, {}^3P_{11}\rangle_{RS}$ $+0.138 \,\|\, {}^1D_{21}\rangle_{RS}$
$\|\, 10(2)\rangle$	$\|\, {}^3P_{10}\rangle_{RS}$
$\|\, 22(3)\rangle$	$0.264 \,\|\, {}^3P_{22}\rangle_{RS} + 0.965 \,\|\, {}^1D_{22}\rangle_{RS}$
$\|\, 21(3)\rangle$	$0.348 \,\|\, {}^3P_{21}\rangle_{RS} + 0.085 \,\|\, {}^3P_{11}\rangle_{RS}$ $+0.934 \,\|\, {}^1D_{21}\rangle_{RS}$
$\|\, 20(3)\rangle$	$-0.364 \,\|\, {}^3P_{20}\rangle_{RS} + 0.142 \,\|\, {}^3P_{00}\rangle_{RS}$ $-0.916 \,\|\, {}^1D_{20}\rangle_{RS} - 0.092 \,\|\, {}^1S_{00}\rangle_{RS}$
$\|\, 00(4)\rangle$	$-0.040 \,\|\, {}^3P_{20}\rangle_{RS} - 0.397 \,\|\, {}^3P_{00}\rangle_{RS}$ $-0.137 \,\|\, {}^1D_{20}\rangle_{RS} + 0.906 \,\|\, {}^1S_{00}\rangle_{RS}$

Table 3.4. I^+eigenfunctions after partial jj-coupling and charge-quadrupole interaction, with $Q = 4500\text{cm}^{-1}$.

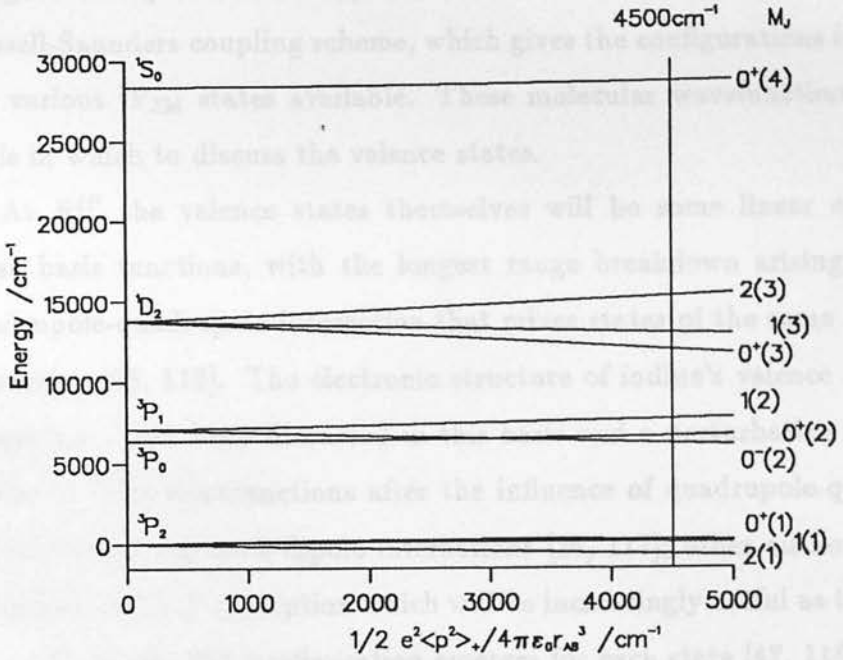

Figure 3.2. I^+ term values as a function of the intramolecular charge-quadrupole interaction.

3.5 Describing the electronic structure of a Valence state

The separated atom basis functions for the valence states are given by

$$|\, n\Omega\rangle_{u,g}^{(+/-)} = \mathcal{N}.\mathcal{A}\ \{(|\, J_1M_1\rangle_A \,|\, J_2M_2\rangle_B \pm |\, J_2M_2\rangle_A \,|\, J_1M_1\rangle_B) \pm (|\, J_1M_2\rangle_A \,|\, J_2M_1\rangle_B \pm |\, J_2M_1\rangle_A \,|\, J_1M_2\rangle_B)\}, \qquad (3.19)$$

where $\Omega = |M_1 + M_2|$ and the last pair of terms will only be present for the $\Omega = 0$ case, and then only if a new configuration is generated; $\mathcal{N}$ is the normalisation integral. The p^5 orbital occupancy at the two centres is again found using the Russell-Saunders coupling scheme, which gives the configurations in Table 3.2 for the various $^2P_{JM}$ states available. These molecular wavefunctions then form a basis in which to discuss the valence states.

At R_e^{IP} the valence states themselves will be some linear combination of these basis functions, with the longest range breakdown arising from the r^{-5} quadrupole-quadrupole interaction that mixes states of the same $(J_AM_AJ_BM_B)$ symmetry [25, 116]. The electronic structure of iodine's valence states at large separations have been discussed in this basis and a perturbative approach used to derive their wavefunctions after the influence of quadrupole-quadrupole and induced dipole-induced dipole interactions [28, 117]; other authors have used a Molecular Orbital description which will be increasingly useful as the bond shortens and a single MO configuration emerges for each state [47, 118]. However we shall treat the mixing of valence states empirically deriving their wavefunctions from the experimental results for transition dipole moments at R_e^{IP} discussed in Chapter 6. There we favour the separated atom approach since a charge transfer transition from an IP to a valence state can be readily modelled in that basis. The transition involves a transfer of an electron from the anionic centre to a vacant orbital at the cationic centre leaving a p^5 occupancy at each centre. The relative strength of a transition to a particular valence state compared with that to other valence states can be found from the projection of this $\mu \,|\, \Omega(n)\rangle$ vector onto the

valence state wavefunction. The calculation of transition dipole moments in this manner will be discussed in greater detail in Chapter 6, where it is shown that a knowledge of the fluorescence intensities from a given ion pair state can be used to derive the IP and Valence state configurations.

Part II

Investigations

Chapter 4 OODR excitation of ungerade IP states

As noted in Chapter 1, the early OODR experiments of King *et al* [34, 87] led to incorrect symmetry assignments of the destination IP states because the excitation scheme had not been fully understood. In trying to rationalise King's excitation scheme, Guy *et al* pointed out that low v IP levels could not be reached directly from the $B0_u^+(ab)$ levels King had used since the Franck-Condon factors were vanishingly small [72]. It was not until five years after the original experiment that Broyer *et al* reconciled King's data with that reported from other OODR experiments by suggesting he had populated five of the six members of the first IP cluster through a perturbed intermediate level [89]. In their study of the first ion pair cluster, Broyer *et al* used intermediate levels they knew to be unperturbed to access the two states available in a one photon absorption from the $B0_u^+(ab)$ state: the $E0_g^+(1)$ and $\beta 1_g(1)$ states. Thus they could unambiguously assign two of the states King reported. Broyer also suggested that very close to the dissociation limit the high density of states would lead to a significant number of $B0_u^+(ab)$ levels being coupled to other weakly bound (ab) states. These quasi-bound $B0_u^+(ab)$ levels had been used by King in his OODR excitation scheme: only through such coupling to the continuum of an (ab) repulsive state could he have achieved sufficient Franck-Condon overlap at the intermediate stage to populate low v levels of an IP destination state. Broyer pointed out that heterogeneous coupling to a $1_u(ab)$ state would give access to the $E0_g^+(1)$,

The work covered in this chapter has been submitted to Chemical Physics.

$\beta 1_g(1)$ and $D'2_g(1)$ states, however to reach the $\delta 2_u(1)$ and $\gamma 1_u(1)$ state he proposed a u/g symmetry-breaking hyperfine mechanism coupling the 0_u^+ (ab) state to a $1_g(ab)$ state. The $1_g(ab)$ and $1_u(ab)$ states involved in King's excitation schemes had not been reported when Broyer proposed his solution though theoretical potential functions had been calculated [117]. These weakly bound states have since been recorded experimentally in this laboratory [93]; the symmetries of King's destination states are now well known, and it appears that Broyer's rationalisation of King's experiment is essentially correct.

King's work suggests a novel way of populating seemingly symmetry forbidden destination states by choosing a coupled intermediate state in the OODR excitation scheme. This technique has been used in this thesis to reach the $\delta 2_u(1)$, $\gamma 1_u(1)$, $D0_u^+(1)$, $F0_u^+(2)$ and $H1_u(2)$ states through a $B0_u^+(ab) \sim 1_g(ab)$ hyperfine coupled intermediate, and the $D'2_g(1)$ state through a $B0_u^+(ab) \sim 1_u(ab)$ heterogeneous coupled intermediate state (see Table 4.6). The hyperfine u/g symmetry-breaking perturbation proposed by Broyer, and required in our excitation of *ungerade* IP states, demands close state resonance to achieve significant coupling of states. For this reason Broyer suggested such coupling would be more likely in areas of high state density, ie near dissociation limits or between quasi-bound states and the continuum of a repulsive state. However hyperfine coupling would also be significant if two bound rovibrational levels came into accidental resonance, with strong Franck-Condon overlap, in some region of the potential energy diagram. Thus rather than choose a quasi-bound intermediate to access the *ungerade* IP states, a perturbed $B0_u^+(ab)$ rovibrational level more than 140cm^{-1} below dissociation has been used in this work. The necessary Franck-Condon scheme to populate any *ungerade* IP state in low v is established through a hyperfine facilitated coupling to a bound $1_g(ab)$ rovibronic level. The $1_g(ab)$ state, which we will call the $c1_g(ab)$ state, has not been reported until now and its analysis is the subject of the next section; the hyperfine coupling mechanism is described in the following section, and the details of the OODR excitation schemes used in this thesis are discussed in the final section.

4.1 The $c1_g(ab)$ intermediate state

The aim of this work is to derive a potential curve for the $1_g(ab)$ state that perturbs a $B0_u^+(ab)$ state intermediate level, so allowing the OODR excitation of *ungerade* IP destination states in low v. This potential function is then used to calculate the Franck-Condon factors and energy separations that govern the strength of hyperfine coupling between the two states: the $B0_u^+(ab)$ state potential is already well known.

Dispersed fluorescence from the $\gamma 1_u(1)$ state reveals the $c1_g(ab)$ vibrational level responsible for this perturbation as the probe laser line, pumping $B0_u^+(ab) \sim c1_g(ab) \rightarrow \gamma 1_u(1)$, will lie over the fluorescence dispersed from the transition, $\gamma 1_u(1) \rightarrow c1_g(ab)$, back to the perturbed intermediate level (see Figure 4.4). Simulation of this dispersed fluorescence will give the valence state potential as the upper state is already well known. If the analysis is extended to include the dispersed fluorescence from the analogous 1_u state in the second ion pair cluster, the $H1_u(2)$ state, and a consistent valence state potential derived, then we can be more confident that a true lower state potential has been arrived at. Unfortunately the $H1_u(2)$ state has not yet been reported and so the first stage in this analysis will be to derive its primary Dunham parameters. This can be achieved from the fluorescence excitation spectrum for the transition $B0_u^+(ab) \sim c1_g(ab) \rightarrow H1_u(2)$, and confirmed by recording and simulating its dispersed fluorescence to a known valence state, the $a1_g(aa)$ state.

The next subsection therefore describes the analysis of the $B0_u^+(ab) \sim c1_g(ab) \rightarrow H1_u(2)$ fluorescence excitation spectrum to give the $H1_u(2)$ state potential. It then confirms this result by simulating the dispersed fluorescence to the $a1_g(aa)$ state. The following subsection then describes the analyses of the $\gamma 1_u(1) \rightarrow c1_g(ab)$ and $H1_u(2) \rightarrow c1_g(ab)$ dispersed fluorescence spectra and derives a consistent lower state potential. The $c1_g(ab)$ state potential is then used in the following section where the u/g symmetry-breaking perturbation is discussed.

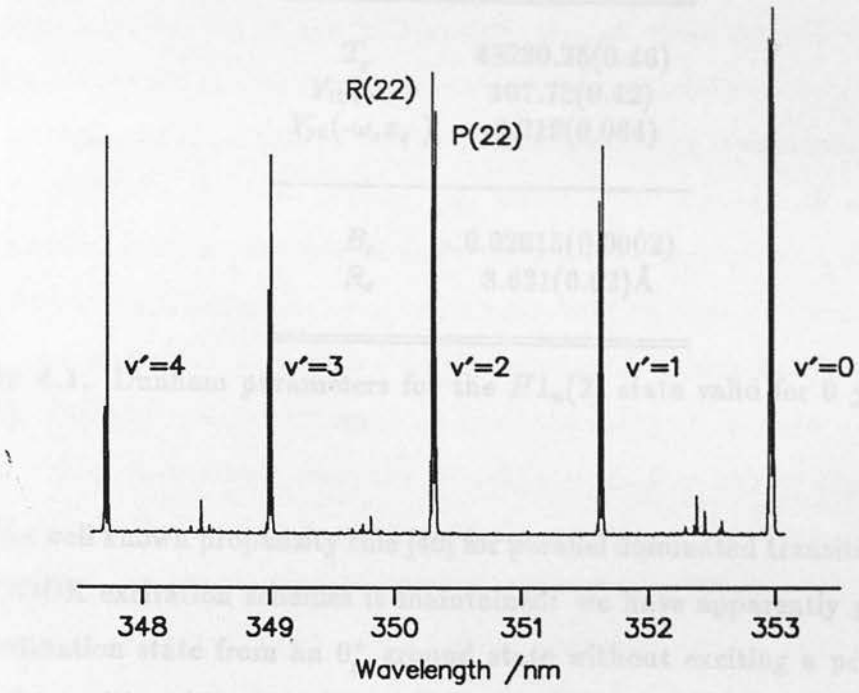

Figure 4.1. OODR $c1_g(ab)(v'' = 14, J'' = 22) \rightarrow H1_u(2)$ fluorescence excitation spectrum (collected at $\lambda = 283$nm).

4.1.1 The $H1_u(2)$ ion pair state

The $H1_u(2)$ ion pair state was populated in a two photon OODR excitation scheme (see Table 4.6):

$$X0_g^+(aa) \overset{(0-59)R(21)}{\longrightarrow} B0_u^+(ab) \overset{(59-v')P,R(22)}{\longrightarrow} H1_u(2) \qquad (4.1)$$

Figure 4.1 shows the fluorescence excitation spectrum for the second OODR step, with $v' = 0 - 4$: the P and R branches are clearly visible, seemingly indicating a parallel transition to an 0_g^+ destination state. The probe laser frequency places the destination state in the second cluster, however it is not one of the *gerade* states all of which are well known (Table 1.4), and thus a u/g symmetry breaking interaction must occur in the intermediate step. Strong fluorescence spectra are recorded from this IP state to the well known $a1_g(aa)$ state, suggesting a parallel transition from an upper state with 1_u symmetry: the second OODR transition must therefore be parallel from an $0_u^+ \sim 1_g$ coupled intermediate.

T_e	48280.25(0.46)
$Y_{10}(\omega_e)$	107.73(0.42)
$Y_{20}(-\omega_e x_e)$	-0.219(0.084)
B_e	0.02015(0.0002)
R_e	3.631(0.02)Å

Table 4.1. Dunham parameters for the $H1_u(2)$ state valid for $0 \leq v \leq 4$ (in cm^{-1}).

The well known propensity rule [40] for parallel dominated transitions in halogen OODR excitation schemes is maintained: we have apparently populated a 1_u destination state from an 0_g^+ ground state without exciting a perpendicular optical transition, hence the high efficiency of the pumping scheme. We find in the next section that the additional quantum of angular momentum comes from a re-alignment of the nuclear spins. We shall assume for the spectral analysis that there is no change of rotational angular momentum due to the hyperfine interaction at the intermediate step, this is confirmed in the following section after an analysis of the coupling mechanism. It should be noted in passing how the OODR technique, once fully understood, makes the symmetry assignment of an unknown destination state relatively straightforward, and how simplified the absorption spectrum becomes when a state specific excitation is achieved.

The term value of the intermediate state is accurately known [119], so the first two vibrational Dunham parameters for the upper state can be derived: these are given in Table 4.1. The confidence range given with these values is twice the standard deviation given by the polynomial fitting algorithm [120]. Since the term values for the first few $H1_u(2)$ levels are all that is required for this study of the $c1_g(ab)$ state, a more detailed vibrational analysis of the $H1_u(2)$ state was not pursued: however it would be possible to extend the vibrational progression using this pumping scheme.

Estimates for the effective rotational parameter, B, can be made from the splittings between the P and R branches, though these are too small to give reliable results for such a heavy molecule. The estimate leads to an R_e^H value that is similar to those known for the other states in the second ion-pair cluster, as expected from the near constant R_e values found amongst IP states in the first cluster. A more accurate value for R_e^H can be derived from the dispersed fluorescence for a transition to a well known valence state as the simulation of this fluorescence will be sensitive to the relative R_e values, so, given the lower state potential the upper state can be fixed absolutely in R-space.

Dispersed fluorescence from the $H1_u(2)(v' = 0, J' = 23) \rightarrow a1_g(aa)$ transition is shown in Figure 4.2, along with the equivalent transition, $\gamma 1_u(1)(v' = 0, J' = 23) \rightarrow a1_g(aa)$, from the first ion pair cluster (Figure 4.4); the $\gamma 1_u(1)$ state was populated using the same OODR excitation scheme. Both the $\gamma 1_u(1)$ and $a1_g(aa)$ potentials have been reported before [16, 18, 34] and the successful simulation confirms those results. The simulation of the fluorescence from the $H1_u(2)$ state gives an R_e^H value of 3.631 ± 0.02Å. Most of the uncertainty in this value reflects the error range of the $a1_g(aa)$ R_e value [16]: the simulation method is very sensitive to changes in ΔR_e as shown by Figure 4.3, where it is systematically altered by ± 0.005Å. The transition dipole function has been assumed constant over the small range in R explored by the upper state vibrational motion: in practice this is found to be a good assumption for all small amplitude *bound* $\rightarrow$ *free* transitions.

The form of these *bound* $\rightarrow$ *free* spectra is determined almost entirely by the upper state function since the lower state continuum wavefunctions tend to have almost constant frequency and amplitude, when well away from their turning points; the gradient of the lower state repulsive wall decides the range in λ that the spectrum occupies (Chapter 2).

Knowing the $H1_u(2)$ and $\gamma 1_u(1)$ state potentials we are now in a position to determine the $c1_g(ab)$ state potential from the dispersed fluorescence spectra of $IP \rightarrow c1_g(ab)$ transitions.

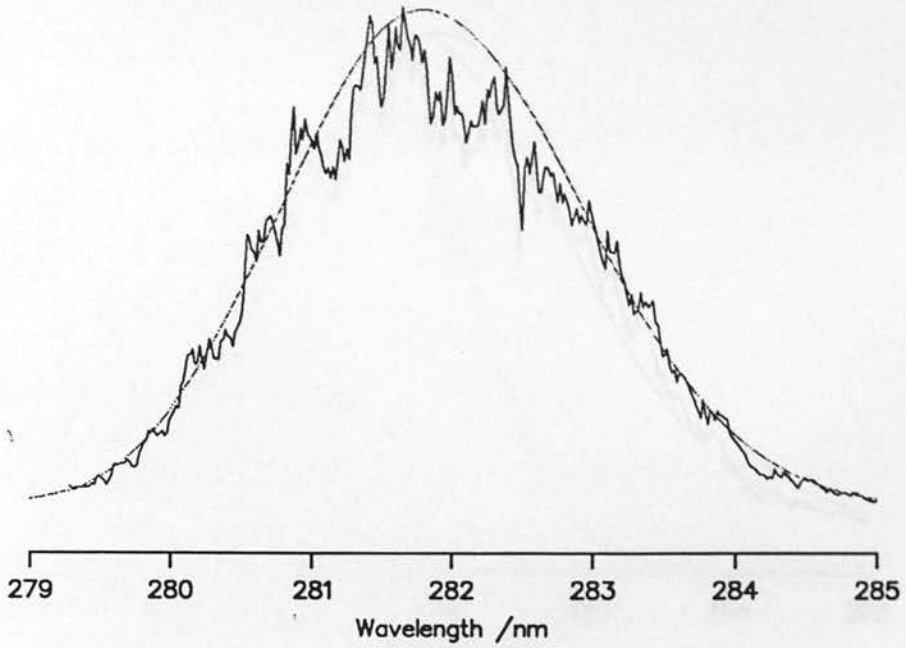

Figure 4.2. $H1_u(2)(v' = 0, J' = 23) \rightarrow a1_g(aa)$ dispersed fluorescence and simulation (broken line).

4.1.2 The $c1_g(ab)$ state potential

Examples of the fluorescence dispersed from $H1_u(2)(v' = 0, J' = 23) \rightarrow c1_g(ab)$ and $\gamma 1_u(1)(v' = 0, J' = 23) \rightarrow c1_g(ab)$ transitions following the OODR excitation of the ion pair state are shown in Figures 4.5 and 4.6. Each spectrum was recorded twice and simulated using a quantum mechanical calculation (Chapter 2) to generate the lower state potential as a function splined between a series of (R, V) knot points: these, and the spectroscopic parameters derived from them, are given in Tables 4.2 and 4.3. A partial RKR analysis was used to derive a first approximation to the potential function and, after refinement, a consistent lower state potential was found. Since the rotational level, and R_e, of the upper state are both well known, the $c1_g(ab)$ state potential can be placed absolutely in R-space.

In both cases the spectrum can be divided into two regions: that of *bound* $\rightarrow$ *bound* fluorescence and that of *bound* $\rightarrow$*free* fluorescence. The point of change

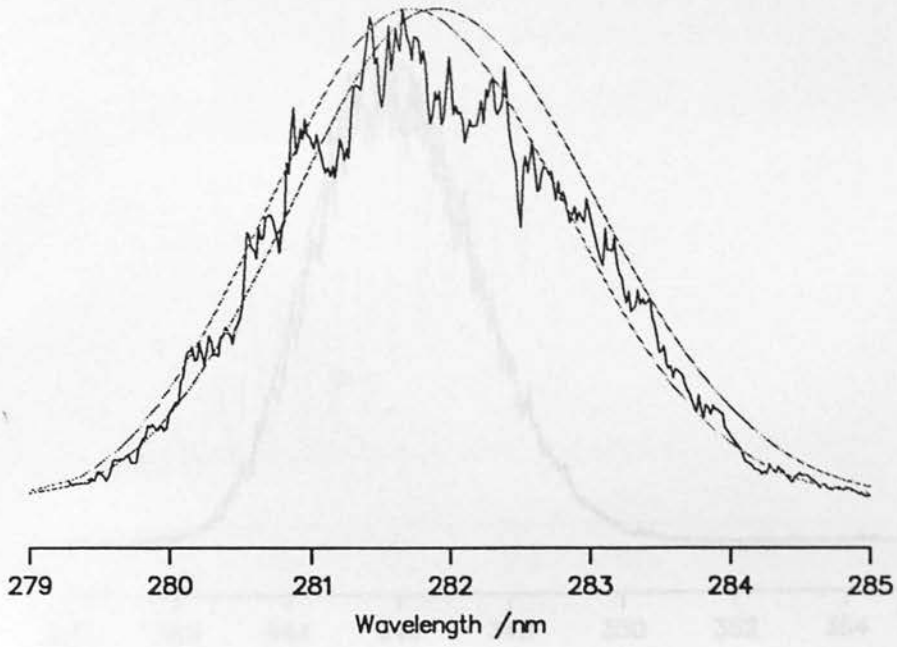

Figure 4.3. $H1_u(2)(v' = 0, J' = 23) \rightarrow a1_g(aa)$ dispersed fluorescence and simulation with ΔR_e altered by ± 0.005Å.

R/Å	V/cm^{-1}	R/Å	V/cm^{-1}
3.531	474	4.198	14.5
3.571	382.5	4.430	69
3.601	325	4.604	126.5
3.641	245.5	4.765	169
3.664	211	5.092	248.5
3.696	169	5.592	337.5
3.738	126.5	6.192	393
3.799	69	7.492	435
3.922	14.5	9.992	459.3
4.047	0.00	10.992	464

Table 4.2. Knot points used for the $c1_g(ab)$ state potential in the simulation of dispersed fluorescence (relative to $c1_g(ab)$ state minimum)

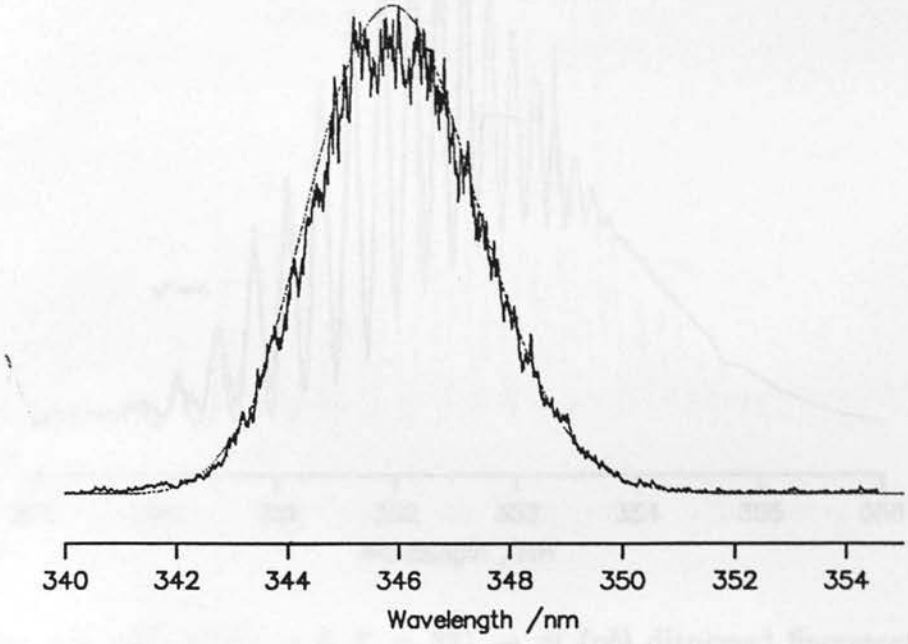

Figure 4.4. $\gamma 1_u(1)(v' = 0, J' = 23) \rightarrow a1_g(aa)$ dispersed fluorescence and simulation (broken line).

T_e	19685(1.5)
D_e	465(1.5)
$Y_{10}(\omega_e)$	29.5(0.4)
$Y_{20}(-\omega_e x_e)$	-0.51(0.04)
B_e	0.01618(0.0016)
R_e	4.052(0.02)Å

Table 4.3. Dunham parameters (in cm^{-1}) for the $c1_g(ab)$ state derived from the cubic splined potential of Table 4.2.

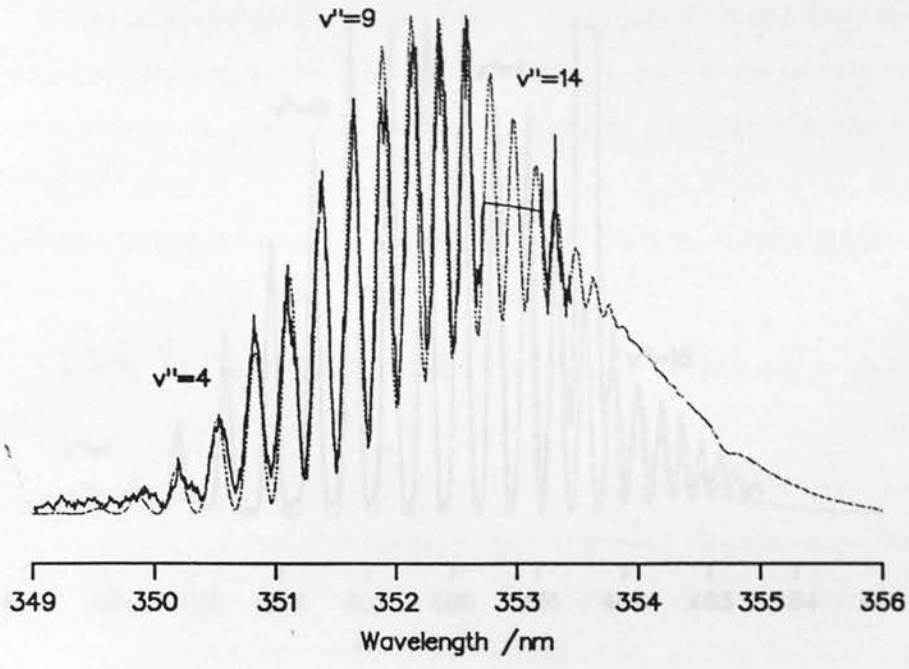

Figure 4.5. $H1_u(2)(v' = 0, J' = 23) \rightarrow c1_g(ab)$ dispersed fluorescence and simulation (broken line).

from one region to the other is not necessarily an abrupt discontinuity in the spectrum since the density of vibrational states increases to infinity as the valence state approaches its dissociation limit, it is well known however: the *bound* $\rightarrow$*free* region must begin at fluorescent wavelengths that sample energies just above the rotational barrier in the lower state's effective potential. Thus for example the *bound* $\rightarrow$*free* region in the $\gamma 1_u(1)(v' = 0, J' = 23) \rightarrow c1_g(ab)$ spectrum begins at $\lambda = 464.5$nm; at shorter wavelengths the fluorescence is to discrete bound $c1_g(ab)$ levels. As discussed in Chapter 2, the form of the spectrum, in the Condon approximation of a constant transition dipole function, depends on the square of the overlap between the upper and lower vibrational states. These low vibrational levels in the IP states typically display a monotonic Mulliken difference potential, unless the lower state potential is almost flat, and the envelope of the spectrum therefore reflects the upper state vibrational function; in the *bound* $\rightarrow$ *bound* region the lower state functions determine the high frequency modulation. The

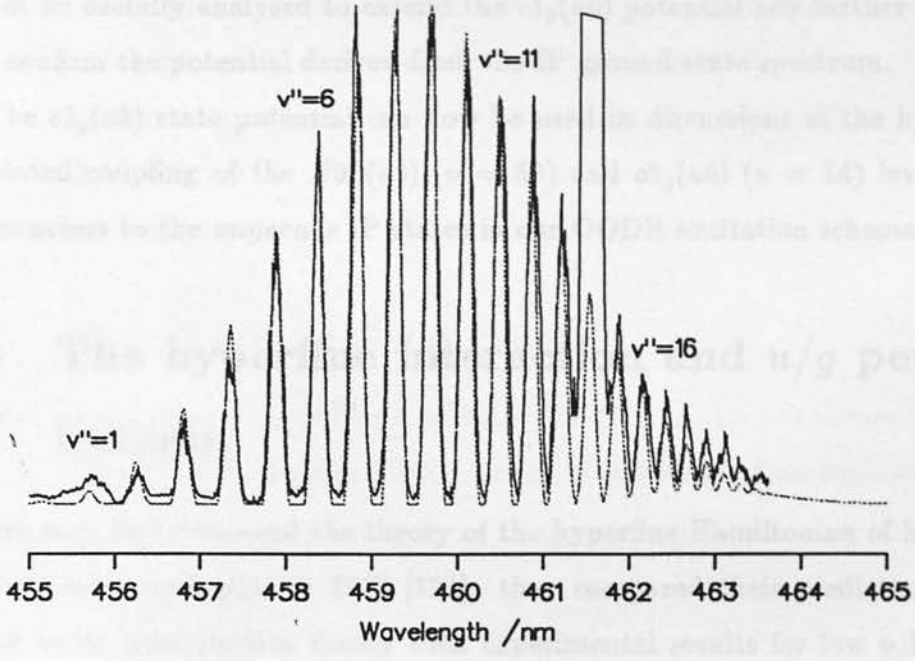

Figure 4.6. $\gamma 1_u(1)(v' = 0, J' = 23) \rightarrow c1_g(ab)$ dispersed fluorescence and simulation (broken line).

energy and amplitude of the lower state vibrational functions depend on the whole of the potential well supporting them, thus a *bound* $\rightarrow$ *bound* transition samples the whole potential surface occupied by the lower state vibrational function. Since all bound levels supported by the $c1_g(ab)$ potential, bar the first, were accessed the experiment effectively probes the complete $c1_g(ab)$ state potential well. Thus, although only strictly valid for the Franck-Condon window of the IP state (3.60 to 3.75Å), the $c1_g(ab)$ state potential has been characterised from $R =$ 3.60 to 6.09Å. Importantly for this particular study this includes the hyperfine $B0_u^+(ab) \sim c1_g(ab)$ coupled level, $v = 14$.

Dispersing fluorescence from higher vibrational levels of the $\gamma 1_u(1)$ state confirms the lower state vibrational numbering given in Figures 4.5 and 4.6: the lowest vibrational level had not been accessed from $IP(v' = 0)$. These spectra, and those for all $\gamma 1_u(1)$ vibrational states except the lowest, show transitions to two overlapping systems: the transition to the $c1_g(ab)$ state continuum overlaps

with transitions to a purely repulsive $1_g(ab)$ state. Consequently their spectra cannot be usefully analysed to extend the $c1_g(ab)$ potential any further but can only confirm the potential derived from the IP ground state spectrum.

The $c1_g(ab)$ state potential can now be used in discussions of the hyperfine facilitated coupling of the $B0_u^+(ab)$ ($v = 59$) and $c1_g(ab)$ ($v = 14$) levels that allows access to the *ungerade* IP states in our OODR excitation schemes.

4.2 The hyperfine interaction and u/g perturbations

Broyer *et al* first discussed the theory of the hyperfine Hamiltonian of homonuclear diatomic molecules in 1978 [121]: they compared their predictions from second order perturbation theory with experimental results for low v levels of iodine's $B0_u^+(ab)$ state, though the scarcity of experimental data prevented a thorough testing of their theory. In 1986 Bacis *et al* performed a similar study this time on B state levels close to dissociation where the weak hyperfine interactions are of similar magnitude to rotational, vibrational, and even electronic energy separations [102]. They undertook a direct diagonalisation of the full hyperfine interaction matrix and were able to show a significant hyperfine coupling, in each case between two rovibronic levels and essentially magnetic dipolar in origin, that mixes the $B0_u^+(ab)$ ($v' = 77, 78$) levels with successive vibrational levels in a $1_g(ab)$ state: the $c1_g(ab)$ state.

This section addresses the theory of the hyperfine interaction then compares its predictions with the u/g coupling recorded experimentally between the $B0_u^+(ab)$ and $c1_g(ab)$ states, though now involving a lower vibrational level in the $B0_u^+(ab)$ state ($v'' = 59$). A complete diagonalisation of the full hyperfine interaction matrix is not attempted since only a magnetic dipolar interaction between the $B0_u^+(ab)$ state and an essentially pure $\psi^{ab}_{3/2}(1_g)$ electronic state is sufficiently strong to reproduce the observed strength of hyperfine coupling. This is consistent with the electronic eigenfunction derived for the $c1_g(ab)$ state by Saute

and Aubert-Frécon [122] who found this configuration dominated (> 70%) the c state electronic wavefunction even at $R = 10$Å, where a stronger mixing with the other 1_g basis function at the (ab) limit, $\psi^{ab}_{1/2}(1_g)$, would have been expected. The perturbation is therefore treated as a two state coupling problem, with the magnetic dipolar interaction mixing two rovibronic levels of 0^+_u and 1_g symmetry, as found by Bacis *et al.*

4.2.1 The hyperfine Hamiltonian

For heavy diatomics, with non-zero nuclear spin, such as I_2, each electronic state Ω, $(= M_{J_A} + M_{J_B})$, can be described in terms of separated atom basis functions (see section 1.1.1):

$$|\, n\beta\Omega v J\tau(I_A I_B) I F M_F\rangle^{(+/-)}_{u,g} = \left(\tfrac{1}{\sqrt{2}}\right)^{|\epsilon|} \{|\, \beta\Omega v J\tau(I_A I_B) I F M_F\rangle_{u,g} + \epsilon\, |\, \beta - \Omega v J\tau(I_A I_B) I F M_F\rangle_{u,g}\}, \tag{4.2}$$

where I is the total nuclear spin, $\mathbf{I} = \mathbf{I_A} + \mathbf{I_B}$; F the total molecular angular momentum, $\mathbf{F} = \mathbf{I} + \mathbf{J}$, with $\mathbf{J} = \mathbf{\Omega} + \mathbf{N}$ and $\mathbf{N}$ the nuclear rotation; v is the vibrational quantum number. β and τ are other quantum numbers pertinent to the electronic and nuclear wavefunction respectively; $\epsilon = 0$ for $\Omega = 0$ states and $\epsilon = \chi_{\sigma v} = \pm 1$ for $\Omega \neq 0$ states, where σ_v is the symmetry operation of reflecting through a molecular plane in the $D_{\infty h}$ group.

The hyperfine Hamiltonian H_{hf} can be written as [121]

$$H_{hf} = H_{hf}(A) + H_{hf}(B) + H_{hf}(A,B), \tag{4.3}$$

where $H_{hf}(A)$ is the hyperfine interaction between the electrons and the nucleus labelled A, and $H_{hf}(A,B)$ the interaction between the two nuclei. This latter term is small and can be omitted in a first approximation, allowing H_{hf} to be expressed as [121]

$$H_{hf} = \sum_{\alpha=A,B} \sum_{k} \sum_{q=-k}^{k} (-1)^q Q^k_q(I_\alpha) V^k_{-q}(e_\alpha), \tag{4.4}$$

where the tensorial operator $\mathbf{Q}^k(I_\alpha)$ acts only on the nuclear spin of atom α and $\mathbf{V}^k(e_\alpha)$ acts on the electrons; $k = 1$ is the magnetic dipolar interaction, $k = 2$ the electric quadrupolar interaction.

The hyperfine matrix element coupling two electronic states, $\mid n\Omega\rangle$ and $\mid n'\Omega'\rangle$, is therefore given by

$$\langle n'\Omega' \mid H_{hf} \mid n\Omega\rangle = \tag{4.5}$$
$$\sum_{\alpha=A,B}\sum_k \langle n'\beta'\Omega'v'J'\tau'(I_AI_B)I'F'M_{F'} \mid \mathbf{Q}^k(I_\alpha).\mathbf{V}^k(e_\alpha) \mid n\beta\Omega vJ\tau(I_AI_B)IFM_F\rangle.$$

With the application of standard methods, the following result is obtained [122]

$$\begin{aligned}
&\langle n'\Omega'J'I'F' \mid H_{hf} \mid n\Omega JIF\rangle = \\
&\qquad \sum_k \delta_{FF'}\delta_{M_FM_{F'}}(-1)^{F+\Delta I+\Delta J+k-\Omega'} \begin{Bmatrix} FI'J' \\ kJI \end{Bmatrix} \\
&\qquad \times[(2I+1)(2I'+1)]^{\frac{1}{2}} \begin{Bmatrix} I_A & I_A & I \\ k & I' & I_A \end{Bmatrix} \\
&\times\langle \tau' I_A M_{I_A} = I_A \mid \mathbf{Q}^{(k)}(I_A) \mid \tau I_A M_{I_A} = I_A\rangle \left[\begin{pmatrix} I_A & k & I_A \\ -I_A & 0 & I_A \end{pmatrix}\right]^{-1} \\
&\qquad \times[(2J+1)(2J'+1)]^{\frac{1}{2}} \begin{pmatrix} J' & k & J \\ -\Omega' & q & \Omega \end{pmatrix} \\
&\qquad \times[\langle n'\beta'\Omega'v' \mid V_q^k(e_A) \mid n\beta\Omega v\rangle + \langle n'\beta'\Omega'v' \mid V_q^k(e_B) \mid n\beta\Omega v\rangle],
\end{aligned} \tag{4.6}$$

where $q = \Delta\Omega = \Omega' - \Omega$, $\Delta I = I - I'$ and $\Delta J = J - J'$. The derivation of this result is given in Appendix B to show the origin of the various terms in the equation. Briefly we are working in a composite coupling regime with two independent subsystems, the nuclear spin and the electronic, each with an irreducible tensor operating acting on the coordinates of one, and not the other, subsystem. The hyperfine matrix element can therefore be separated into three parts: those terms relevant to the coupling of the two subsystems (the first line), those from the nuclear spin subsystem (second and third lines) and those for the electronic subsystem (final two lines). All the Wigner coefficients can be calculated from standard algebraic formulae, and the nuclear matrix element is

known experimentally for $k = 1$ and 2. The electronic matrix element, line 5, is not known but can be estimated for $k = 1$ and 2 from the potential functions for the two states and the known properties of the iodine atom (see Appendix B). The results are given in Table 4.4.[1]

Using this equation we can now calculate the strength of coupling between given $B0_u^+(ab)$ and $c1_g(ab)$ rovibronic states, after first considering how the hyperfine interaction can couple states of opposite parity.

4.2.2 u/g perturbations

For a homonuclear diatomic molecule there exists a symmetry operation in the molecular point group $D_{\infty h}$, i the inversion of electronic coordinates, which determines the u/g parity of the molecular wavefunction. If the two nuclei are not truly identical, then i will no longer be a true symmetry operator of the complete molecular Hamiltonian and u/g levels will mix [123]. This will be the case when the diatomic has nuclei with non-zero nuclear spin: the nuclei may adopt different M_I states and the u/g states of the inversion operator will be coupled through hyperfine interactions involving the nuclear spins.

Consider the 10 states at the (ab) dissociation limit whose electronic wavefunctions can be described in the separated atom coupling scheme as

$$\begin{aligned} |\, n\Omega = 0\rangle_{u/g}^{(+/-)} = \; & \mathcal{A}\; \tfrac{1}{2}\{(|\, \tfrac{3}{2}\tfrac{1}{2}\rangle_A \,|\, \tfrac{1}{2} - \tfrac{1}{2}\rangle_B \pm |\, \tfrac{1}{2} - \tfrac{1}{2}\rangle_A \,|\, \tfrac{3}{2}\tfrac{1}{2}\rangle_B) \\ & \pm(|\, \tfrac{3}{2} - \tfrac{1}{2}\rangle_A \,|\, \tfrac{1}{2}\tfrac{1}{2}\rangle_B \pm |\, \tfrac{1}{2}\tfrac{1}{2}\rangle_A \,|\, \tfrac{3}{2} - \tfrac{1}{2}\rangle_B)\}, \end{aligned} \tag{4.7}$$

[1]The results given for the electronic matrix element in Table 4.4 do not correspond directly with those of Bacis *et al* [122, Table II]. Their matrix elements are defined differently in equation (4.6), with the normalisation integral for the coupling partner of the $B0_u^+(ab)$ state not included if $\Omega \neq 0$. Furthermore their values for the magnetic dipolar interaction do *not* include the spin of the iodine nucleus ($I_A = \frac{5}{2}$); their equations in Section 4.1 should read (see Appendix B)

$$\begin{aligned} \langle \tfrac{3}{2} \| \overline{V}^1 \| \tfrac{3}{2} \rangle &= \sqrt{15} a_{3/2}/\mu_N g_I, \\ \langle \tfrac{1}{2} \| \overline{V}^1 \| \tfrac{1}{2} \rangle &= \sqrt{\tfrac{3}{2}} a_{1/2}/\mu_N g_I, \\ \langle \tfrac{3}{2} \| \overline{V}^2 \| \tfrac{3}{2} \rangle &= \sqrt{5} q_{3/2}. \end{aligned}$$

	$\sum_{A,B}\langle\overline{V_q^1}(e_\alpha)\rangle$ [a]		$\sum_{A,B}\langle\overline{V_q^2}(e_\alpha)\rangle$		$\mu_N g_I I \sum_{A,B}\langle\overline{V_q^1}(e_\alpha)\rangle$	$\frac{1}{2}eQ_I \sum_{A,B}\langle\overline{V_q^2}(e_\alpha)\rangle$
States	ΔI	ΔJ	ΔI	ΔJ	$10^{-3}\mathrm{cm}^{-1}$	$10^{-3}\mathrm{cm}^{-1}$
0_g^+			± 1	$0,\pm 2$	0	-19.1
0_u^-	0	± 1			-240.3	0
0_g^-	± 1	± 1			309.3	0
$B0_u^+$			$0,\pm 2$	$0,\pm 2$	0	-19.1
$c1_g^+$	± 1	0	± 1	$0,\pm 2$	-205.8	0
$c1_g^-$	± 1	± 1	± 1	± 1	-205.8	0
1_g^+	± 1	0	± 1	$0,\pm 2$	59.7	19.1
1_g^-	± 1	± 1	± 1	± 1	59.7	19.1
$1_u'^+$	0	0	$0,\pm 2$	$0,\pm 2$	343.7	0
$1_u'^-$	0	± 1	$0,\pm 2$	± 1	343.7	0
1_u^+	0	0	$0,\pm 2$	$0,\pm 2$	59.7	19.1
1_u^-	0	± 1	$0,\pm 2$	± 1	59.7	19.1
2_g^+			± 1	$0,\pm 2$	0	19.1
2_g^-			± 1	± 1	0	19.1
2_u^+			$0,\pm 2$	$0,\pm 2$	0	19.1
2_u^-			$0,\pm 2$	± 1	0	19.1

[a]

$$\sum_{\alpha=A,B} \langle n'\beta'\Omega'v' \mid V_q^k(e_\alpha) \mid n\beta\Omega v\rangle = \langle v \mid v'\rangle \sum_{\alpha=A,B} \langle n'\beta'\Omega' \mid \overline{V_q^k}(e_\alpha) \mid n\beta\Omega\rangle,$$

and $\langle v \mid v'\rangle$ is known.

Table 4.4. Selection rules and values for the hyperfine magnetic dipolar $\sum_{A,B}\langle\overline{V_q^1}(e_\alpha)\rangle$ and electric quadrupolar $\sum_{A,B}\langle\overline{V_q^2}(e_\alpha)\rangle$ matrix elements between the $B0_u^+(ab)$ and all the states sharing the (ab) dissociation limit (after [122], see Appendix B).

$$| n\Omega \neq 0\rangle_{u/g} = \mathcal{A}\ \tfrac{1}{\sqrt{2}}\{| \tfrac{3}{2}M_1\rangle_A | \tfrac{1}{2}M_2\rangle_B \pm | \tfrac{1}{2}M_2\rangle_A | \tfrac{3}{2}M_1\rangle_B\}, \quad (4.8)$$

with the *ungerade* taking the positive inversion term. The hyperfine matrix element

$$\langle n\Omega \neq 0 \mid H_{hf}(A) \mid n\Omega \neq 0\rangle = \tfrac{1}{2}\{\langle \tfrac{3}{2}M_1 \mid H_{hf}(A) \mid \tfrac{3}{2}M_1\rangle_A \langle \tfrac{1}{2}M_2 \parallel \tfrac{1}{2}M_2\rangle_B \quad (4.9)$$
$$\pm \langle \tfrac{1}{2}M_2 \mid H_{hf}(A) \mid \tfrac{1}{2}M_2\rangle_A \langle \tfrac{3}{2}M_1 \parallel \tfrac{3}{2}M_1\rangle_B\},$$

is in general non-zero. However the functions

$$| 1\rangle = | \frac{3}{2}M_1\rangle_A | \frac{1}{2}M_2\rangle_B, \quad \text{and} \quad | 2\rangle = | \frac{1}{2}M_2\rangle_A | \frac{3}{2}M_1\rangle_B,$$

do diagonalise the hyperfine Hamiltonian since

$$\langle 1 \mid H_{hf}(A) \mid 2\rangle = \langle \tfrac{3}{2}M_1 \mid H_{hf}(A) \mid \tfrac{1}{2}M_2\rangle_A \langle \tfrac{1}{2}M_2 \mid \tfrac{3}{2}M_1\rangle_B = 0, \quad (4.10)$$

but they do not possess inversion symmetry. Thus it follows that the hyperfine interaction can mix the u/g states, breaking the u/g symmetry [122].

For the true homonuclear diatomic only hyperfine interactions can cause this u/g coupling: this is not the case for isotopic molecules such as HD. The centre of mass is no longer the centre of symmetry, and the relevant point group, $C_{\infty v}$, no longer contains the inversion symmetry: all terms involving motion of the nuclei, vibration and rotation for example, are no longer invariant under the inversion operator. The identity of the nuclear charges, however, means that the electronic Hamiltonian will have inversion symmetry and u/g states can be defined for the electronic wavefunctions, though these u/g symmetries can be broken down by rovibronic, or hyperfine, interactions [122].

Returning to our true homonuclear diatomic the hyperfine interactions coupling u/g states are so weak that they will only be observed in favourable circumstances: when two states lie in close energy resonance with significant Franck-Condon overlap. Such situations are likely to arise in areas of the potential energy diagram with a high density of states, near dissociation limits for example. However in our experiments we observe coupling between two levels that are in accidental resonance and find sufficient u/g mixing to access *ungerade* ion pair states from the *ungerade* $B0_u^+(ab)$ state.

4.2.3 Hyperfine $B \sim c$ mixing

In this section we quantify the degree of hyperfine coupling between the $B0_u^+(ab)$ and $c1_g(ab)$ states by recording the fluorescence excitation intensities of a destination state that can only be reached through a hyperfine coupled intermediate. We have chosen the $H1_u(2)$ state (Table 1.4). The coupling in the intermediate step is modelled assuming a two state interaction, and a formula is derived that gives the rate of *ungerade* IP state production from a room temperature ground state population using a hyperfine facilitated OODR excitation scheme. The predictions of this theory are then compared with the observed absorption intensities to derive the electronic matrix element coupling the $B0_u^+(ab)$ and $c1_g(ab)$ states.

The first step in our OODR excitation of IP states is well known: the $X \rightarrow B$ absorption spectrum has been recorded previously [124], thus we can be confident as to which B rovibronic levels we have pumped in the intermediate stage. At the wavelengths we choose for the first OODR step, we excite two transitions to the $B(v'' = 59)$ level within the bandwidth of the pump laser (0.2cm^{-1}),

$$X0_g^+(aa)(0,m) \xrightarrow{P} B0_u^+(ab)(59,m-1), \tag{4.11}$$

and

$$X0_g^+(aa)(0,m+1) \xrightarrow{R} B0_u^+(ab)(59,m+2). \tag{4.12}$$

Each B rovibronic level will be coupled to a c level, though to a differing extent, and thus each can give access to the H state. However each *intermediate* $\rightarrow$ *destination* transition will have a different absorption frequency so their relative absorption intensities, and hence strength of coupling, can be separated. By populating a range of $B0_u^+(ab)(v'' = 59, J'')$ rotational levels and recording their absorption intensity to the $H1_u(2)$ state, we can follow the change in coupling as the $B0_u^+(ab)(v'' = 59)$ and $c1_g(ab)(v'' = 14)$ state rotational manifolds move in and out of resonance.

Rate of *ungerade* IP production

In our excitation experiment we excite the available ground state molecules ($v''' = 0$) of a given rotational level to the intermediate coupled level, then sequentially pump the intermediate population on to the destination state. No rotational relaxation occurs in the intermediate stage (laser pulse length 15ns, collision probability 1:60), thus the strength of absorption to the destination state, after Franck-Condon factors have been taken into account, is determined by the ground state population distribution (a function of I''' and J'''), the strength of coupling in the intermediate stage (a function of the level separation, Δ, and the intermediate state quantum numbers) and the Hönl-London factors for the two parallel OODR transitions. These three factors are therefore inter-related: we will discuss the influence of the interaction strength first, then include the Hönl-London factors and ground state population distribution to give our final expression. The same vibrational levels are excited in each excitation scheme so the Franck-Condon factors can be considered a constant of the analysis and will not be considered further (except where they determine the extent of hyperfine interaction in the intermediate step).

If we consider the intermediate stage as a two state mixing problem, as found for higher vibrational levels by Bacis *et al* [102], then writing the two mixed states, ψ_1 and ψ_2, as

$$\psi_1 = \cos\theta\phi_1 + \sin\theta\phi_2, \tag{4.13}$$

$$\psi_2 = -\sin\theta\phi_1 + \cos\theta\phi_2, \tag{4.14}$$

where ϕ_1 and ϕ_2 are the uncoupled $B0_u^+(ab)$ and $c1_g(ab)$ state rovibronic wavefunctions, we find that solving the secular determinant gives

$$\tan 2\theta = \frac{2H_{12}}{\Delta}. \tag{4.15}$$

Δ is the unperturbed energy separation between the two states, and H_{12} is the hyperfine matrix element coupling the $B0_u^+(ab)$ state level, $|\, I''J''F''\rangle$, with its $c1_g(ab)$ partner. We find later that to achieve significant coupling the two states

ψ_1 and ψ_2 must be close to resonance and their energy separation, Δ, is less than the bandwidth of the pump laser. Consequently both are excited in the OODR excitation scheme, which is more accurately represented as

$$X0_g^+(aa) \longrightarrow \left\{ \begin{array}{c} \psi_1 \\ \psi_2 \end{array} \right\} \longrightarrow IP. \tag{4.16}$$

The intermediate states will be pumped through their ϕ_1 component, and probed through their ϕ_2 component. Assuming the laser signal remains constant during the experiment, the probability of hyperfine facilitated *ungerade* IP production per molecule pumped through a particular $B0_u^+(ab)$ state level, $\mid I''J''F''\rangle$, and its coupling partner will be

$$\begin{aligned} Z_{IP}(I''J''F'') &\propto (\sin\theta \times \cos\theta)^2 + (\cos\theta \times \sin\theta)^2 \\ &= 2\sin^2\theta\cos^2\theta \\ \Longrightarrow Z_{IP}(I''J''F'') &\propto \frac{2H_{12}^2}{4H_{12}^2+\Delta^2}. \end{aligned} \tag{4.17}$$

The hyperfine interaction is so weak that it causes no noticeable energy perturbation of the $B0_u^+(ab)$ and $c1_g(ab)$ state potentials: the experimental $X0_g^+(aa) \rightarrow B0_u^+(ab)$ absorption spectrum reveals a regular progression [124]. If we assume that all F'' states of a given J'' level are degenerate, ie the eigen energy is independent of the nuclear spin, then we can calculate Δ from our knowledge of the $B0_u^+(ab)$ and $c1_g(ab)$ state potentials. Equation (4.6) gives the hyperfine Hamiltonian, H_{12}, provided the potential of the coupling partner is known, and so $Z_{IP}(I''J''F'')$ can be calculated.

The experimental absorption intensity is measured as a function of the $B0_u^+(ab)$ rotational level, J'', ie $J''' + 1$; the nuclear spin state in the B rovibronic level is unchanged from the ground state, $I'' = I'''$ and so $F'' = F''' + 1$. The rate of *ungerade* IP production, using a given $\mid I''J''F'''\rangle$ $B0_u^+(ab)$ state level in the intermediate step, will be a product of the probability of *ungerade* IP production per molecule pumped through the intermediate step, equation (4.17), the parent ground state population for that level (including spin statistics) and the

The polarisation of the pump laser beam will lead to an intermediate state population that is prepared in particular M_J states in the laboratory frame. At low J however the coupling of J with the nuclear spin I will lead to a scrambling of the intermediate M_J states and the probe laser pulse will sample an isotropic population distribution. In such cases the rotational integrals for both steps are the M_J averaged Hönl-London factor and equations (4.18) and (4.19) will apply. At high J the intermediate state population will remain orientated in the laboratory frame and the full rotational integral for the two photon process would need to be solved:

$$S(J';J'';J''') = \sum_{M_J} |\langle J'M_JK=1|\mu_z|J''M_JK=1\rangle|^2 |\langle J''M_JK=0|\mu_z|J'''M_JK=0\rangle|^2.$$

The narrow width of the peaks in figure 4.7 imply that the strength of absorption to the IP state is largely determined by the energy separations of the B and c state rovibronic levels and is independent of the rotational integral. The simpler low J formula, equation (4.19), can therefore be used to derive the hyperfine coupling matrix element, $\sum_{A,B}\langle \overline{V_q^1}(e_\alpha)\rangle$. The rotational integral is important, however, in determining the relative heights of the absorption peaks at $J = 7$ and 22 though this has no bearing on the conclusions drawn from this work.

Note that the polarisation of the laser beams will prepare an M_J specific ion pair population if a high J intermediate state is used in the OODR excitation scheme. Consequently fluorescence from these IP states will be proportional to an M_J specific rotational integral and not the Hönl-London factor, however, as this integral is a constant of all transitions from a given rovibronic level, its influence can be ignored when comparing the relative fluorescence intensities from a particular upper state.

Hönl-London factors for the two parallel OODR transitions. This gives

$$I_{IP}(I''J''F'') \propto (2I''+1)\frac{J''^2(J''+2)}{(J''+1)(2J''+1)}\exp^{-E_{J'''}/kT}\frac{2H_{12}^2}{H_{12}^2+\Delta^2}. \qquad (4.18)$$

The ground state molecule adopts a particular F''' state, and this is one of the quantum numbers determining the strength of coupling experienced in the intermediate step, consequently the probability function Z_{IP} must be averaged over the range of F''' available. Furthermore the Pauli principle restricts the possible combinations of I''' and J''' (and therefore F''') in the ground state distribution, therefore the rate of *ungerade* IP production as a function of the $B0_u^+(ab)$ state rotational level, J'', is

$$I_{IP}(J'') \propto \frac{J''^2(J''+2)}{(J''+1)(2J''+1)}\exp^{-E_{J'''}/kT} \qquad (4.19)$$
$$\times \sum_{I'''\in J'''}\frac{\sum_{F'''}(2I''+1)(2F'''+1)\frac{2H_{12}^2}{4H_{12}^2+\Delta^2}}{\sum_{F'''}(2F'''+1)},$$

where the sum over F''' is from $J'''+I'''$ to $|J'''-I'''|$, and $I'''\in J'''$ gives the restriction on the combination of I and J demanded by the Pauli principle.

Comparison with experiment

A fit between the observed absorption intensities and that calculated from equation (4.19) is shown in figure 4.7, using an electronic matrix element, $\sum_{A,B}\langle\overline{V_q^1}(e_\alpha)\rangle$, of 0.200cm^{-1}. We can therefore identify the $c1_g(ab)$ state's electronic wavefunction at $R\approx 5.5$Å, the region of strong Franck-Condon overlap, as the $\psi_{3/2}^{ab}$ eigenfunction in table 1.3; the accuracy of the fit validates our $c1_g(ab)$ potential derived from the fluorescence spectrum. The absorption intensities were calculated from fluorescence excitation spectra detecting the $H1_u(2)(v'=0,J')\rightarrow a1_g(aa)$ transition around $\lambda = 282$nm with the slitwidths fully opened and monochromator detection centred on the fluorescence maximum; the dispersed fluorescence spectra $H1_u(2)(v'=0,J')\rightarrow a1_g(aa)$ do not change appreciably over the range of J' studied. The same Franck-Condon regime is used for each OODR excitation and the intensities of the P and R transitions are both included: the fluorescence excitation spectrum can therefore be compared directly with equation (4.19).

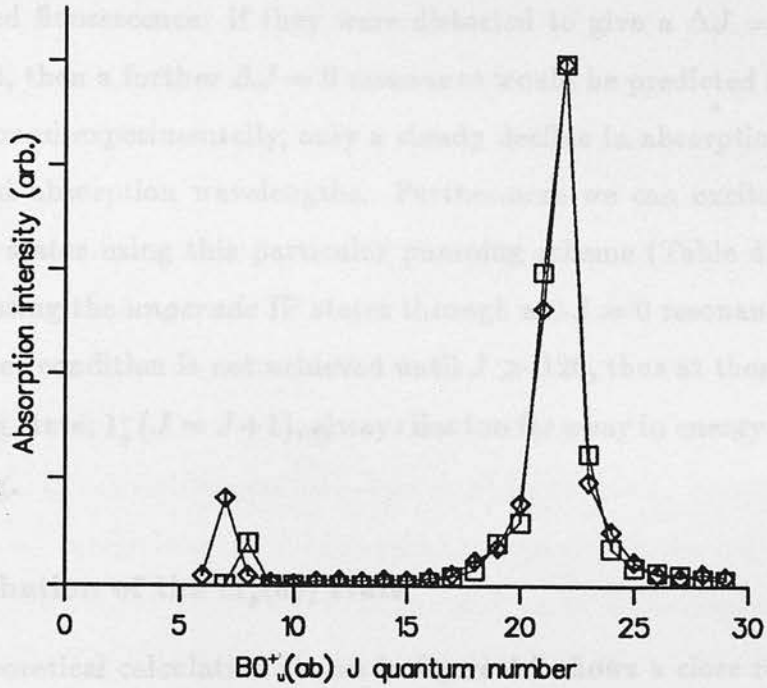

Figure 4.7. Relative intensities of absorption $c1_g(ab)\,(14,J) \rightarrow H1_u(2)\,(0,J\pm1)$: experiment (□) and theory (◇).

Bacis *et al* [102] have shown that the primary hyperfine interaction between the $B0_u^+(ab)$ and $c1_g(ab)$ states is through the magnetic dipole operator, ie with $k = 1$ in equation (4.6). This is consistent with the strength of coupling found in this study: only the magnetic dipolar interaction between the $B0_u^+(ab)$ and $c1_g(ab)$ states is sufficiently strong to reproduce the observed range of excitation intensities. The hyperfine interaction lifts the Ω degeneracy of the $c1_g(ab)$ state and a given $B0_u^+(ab)$ state J level is coupled to three $c1_g(ab)$ state levels: $1_g^-(J-1)$, $1_g^+(J)$, and $1_g^-(J+1)$. Calculations of the strength of the hyperfine matrix element reveal that the coupling is severely limited by the energy separation of the two levels, indeed the $\Delta J = \pm1$ levels move out of significant resonance so quickly, in comparison to the magnitude of the hyperfine Hamiltonian, that only the one level closest to true resonance shows appreciable coupling (see figure 4.7: *unperturbed* resonance at $B(59,7)$ with $c(14,6)$). The strong coupling observed over a few J levels around $B(59,22)$ indicates that the resonance at these levels

must be for $\Delta J = 0$. This is consistent with the potentials derived from the dispersed fluorescence: if they were distorted to give a $\Delta J = -1$ resonance at $J_B = 22$, then a further $\Delta J = 0$ resonance would be predicted for $J_B \approx 35$. This is not found experimentally, only a steady decline in absorption intensity at the expected absorption wavelengths. Furthermore we can excite the $D0_u^+(1)$ and $F0_u^+(2)$ states using this particular pumping scheme (Table 4.6), thus we must be accessing the *ungerade* IP states through a $\Delta J = 0$ resonance. The $\Delta J = +1$ resonance condition is not achieved until $J \gg 120$, thus at these low J, the third coupling state, $1_g^-(J = J+1)$, always lies too far away in energy to give significant coupling.

Perturbation of the $c1_g(ab)$ state

The theoretical calculation shown in figure 4.7 shows a close resemblance to the experimental result in the region of $J = 22$, but wrongly predicts a relatively strong coupling at $B(59,7)$. The predicted interaction is sufficiently strong that we would expect to detect it, yet such an increase in the absorption spectrum was not found.[2] However a strong absorption intensity was found at $B(59,8)$, though this fluorescence excitation frequency was shifted significantly to the blue. The hyperfine interaction is strongly dependent on the state separations so this breakdown of our model is most likely to result from incorrect state potentials. This is not a result of perturbations in the $B0_u^+(ab)$ state as the $X0_g^+(aa) \rightarrow B0_u^+(ab)$ absorption spectrum is well known and reveals no line shifts in this region [124]. The change in hyperfine coupling therefore suggests we should make a closer examination of the $c1_g(ab)$ state potential.

The $c1_g(ab)$ potential was derived from calibrated fluorescence spectra whose upper states were well known, thus the potential could be accurately calculated over the Franck-Condon window of the IP state, which included the vibrational

[2]The hyperfine interactions for J states around 15, although relatively weak, are sufficiently strong to record absorption spectra whose intensities are correctly predicted by our model.

level being considered here. The OODR excitation scheme used in the fluorescence experiments populates the most strongly u/g coupled intermediate level, $B(59,22)$: this intermediate level is known to be unperturbed in energy as the absorption wavelengths to the $H1_u(2)$ state form a regular progression over the range $10 \leq J \leq 30$. The simulation program allows for a centrifugal term to be added to both potentials and so can be used to accurately calculate the $c1_g(ab)$ state potential for the particular J levels involved.[3] Since an R branch tuned probe laser is used the potential given in Table 4.2 will be accurate for J_c levels around 23. Given that we can be confident of the $c1_g(ab)$ state potential for J around 23 (from the fluorescence spectrum) and that the same potential also gives the correct predictions for the hyperfine coupling with the $B0_u^+(ab)$ state for similar J values,[4] then we can be confident that we have the correct $c1_g(ab)$ potential for $J \approx 20$. The shift in the $B0_u^+(ab)(59,8) \sim c1_g(ab)(14,J) \xrightarrow{P,R} H1_u(2)(0,J\pm1)$ absorption wavelength therefore suggests a local perturbation of the lower $c1_g(ab)$ state rotational levels.

Table 4.5 and figure 4.8 give the reconciliation of the fluorescence excitation experiment with our $c1_g(ab)$ state potential. Each absorption spectrum for any given J shows P and R branches, as we would expect: the intermediate state is pumped through its $B0_u^+(ab)$ state character but probed in absorption through the region dominated by the $c1_g(ab)$ wavefunction. We therefore observe a parallel absorption in the second step. The hyperfine coupling does not significantly perturb the interacting states' energies, only coupling their electronic wavefunctions, and to get sufficient hyperfine coupling between the $B0_u^+(ab)$ and $c1_g(ab)$ states the levels must lie close to resonance. Thus whenever we see strong coupling, ie close resonance, we can assume that the $c1_g(ab)$ state level is essentially degenerate with the $B0_u^+(ab)$ state level. Over the range $10 \leq J_B \leq 30$, the dominant hyperfine interaction is between $B(v,J)$ and $c(v',J)$, ie a $\Delta J = 0$ resonance, so

[3]The P and R branches are not resolved in the dispersed fluorescence experiment.

[4]The hyperfine coupling is very sensitive to the separation of the B and c state levels.

Coupling partners		Wavelength[a] /nm			
		R		P	
J_B	J_c	Expt	Model	Expt	Model
16	16	352.977	352.977	352.994	352.994
15	15	352.981	352.981	352.997	352.996
14	14	352.984	352.984	352.999	352.999
13	13	352.988	352.987	353.002	353.001
12	12	352.992	352.991	353.005	353.003
11	11	352.994	352.993	353.007	353.005
10	10	352.998	352.996	353.009	353.006
9	9	352.999	352.998	353.011	353.008
8	9	352.996	352.995	353.007	353.005
7	6	353.006	353.007	353.014	353.013

Table 4.5. Absorption wavelengths for the $c1_g(ab)$ $(14, J_c) \rightarrow H1_u(2)$ $(0, J_c \pm 1)$ spectrum: experiment and model (including homogeneous perturbation at $J_c = 9$).

[a]The experimental spectra were not calibrated for wavelength so have been corrected to give the predicted positions for absorption from $J_B = 16$.

we expect a regular progression of P and R branches to the $H1_u(2)$ state at wavelengths close to those assuming a $c1_g(ab)$ $(14, J) \xrightarrow{P,R} H1_u(2)$ $(0, J \pm 1)$ absorption, with the c state level almost degenerate with its coupling partner $B(59, J)$. This is what is observed (see Table 4.5). Indeed in general when all possible hyperfine couplings are small we expect the $\Delta J = 0$ component to emerge as the major coupling partner: the other levels moving out of resonance more rapidly.

At lower J_B we would expect the resonances with $J_c - 1$ to become the major coupling components between B and c (see figure 4.8: unperturbed $c1_g(ab)$ levels). We would therefore expect a sudden *increase* in the probe *wavelength* in this region when plotted against the B state rotational number since, rather than observing $c1_g(ab)$ $(14, J_B) \xrightarrow{P,R} H1_u(2)$ $(0, J_B \pm 1)$ absorption, we would expect a $c1_g(ab)$ $(14, J_B - 1) \xrightarrow{P,R} H1_u(2)$ $(0, J_B$ and $J_B - 2)$ absorption and $B_c < B_H$.[5] However we observe a *decrease* in the probe wavelength. Therefore the $c1_g(ab)$

[5]ie we expect an absorption out of the intermediate state to an IP rotational level one quantum lower than the B state J quantum number would suggest.

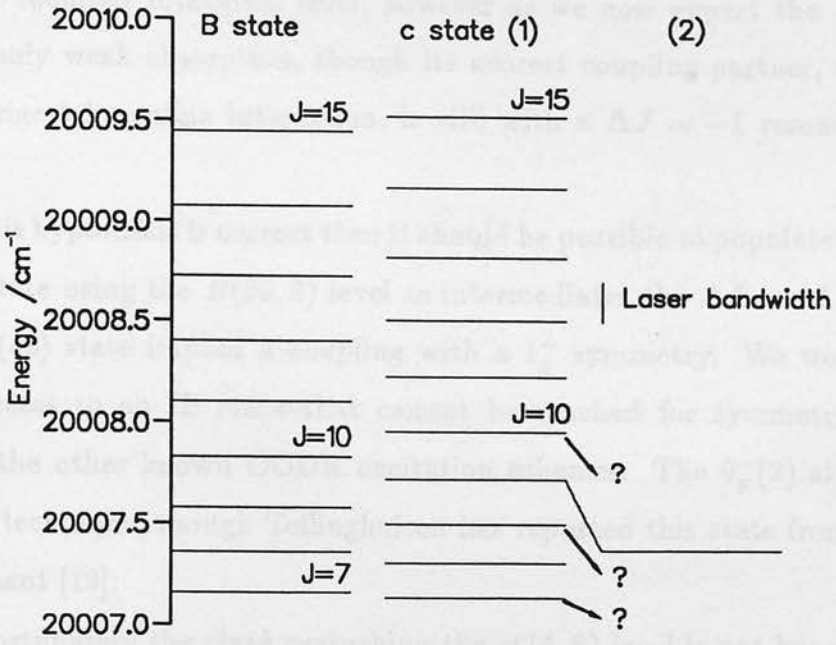

Figure 4.8. Rotational energy levels for $B0_u^+(ab)$ (59,J), and $c1_g(ab)$ (14,J) with (2), and without (1) perturbation.

state must be perturbed at low J such that the rotational level is lowered in energy and the J_B levels are now resonant with the $J_c + 1$. The $B(59,8)$ level becomes closely resonant with the $c(14,9)$ level (a shift of $\approx 0.38\text{cm}^{-1}$) and a strong hyperfine interaction ensues allowing strong absorption to the ion pair state. The $B(59,9)$ level is left with only distant coupling partners and is therefore the weakest absorption system recorded in this J_B range. The hyperfine coupling is very sensitive to the level separation so we should be surprised to see such a strong resonance at $B(59,8)$: it is much more likely that the perturbation would separate hyperfine coupling partners too far to achieve significant interaction. Thus we expect other levels around $B(59,8)$ not to show significant absorption to the ion pair state, even though they may be strongly perturbed.[6] In our absorption experiment we can only record spectra down to $B(59,7)$ as the

[6]It is not possible to determine the energy shift of these other perturbed c state levels from the degree of hyperfine coupling (equation (4.19)) as the coupling is too weak.

$X0_g^+(aa) \rightarrow B0_u^+(ab)$ spectrum becomes too congested at such low J to separate out the required rotational level, however as we now expect the $B(59,7)$ level shows only weak absorption, though its nearest coupling partner, and therefore its strongest hyperfine interaction, is still with a $\Delta J = -1$ resonance to the c state.

If this hypothesis is correct then it should be possible to populate the unknown $0_u^-(2)$ state using the $B(59,8)$ level as intermediate: the $\Delta J = +1$ resonance to the $c1_g(ab)$ state implies a coupling with a 1_g^- symmetry. We would therefore have access to an IP state that cannot be reached for symmetry reasons by any of the other known OODR excitation schemes. The $0_g^-(2)$ still eludes the OODR technique, though Tellinghuisen has reported this state from a discharge experiment [19].

Unfortunately the state perturbing the $c(14,8)$ level is not known, though it must have Ω_g^- symmetry. The most likely interaction is a strong homogeneous coupling to the other 1_g state at the (ab) limit; this state has been represented in spectral simulations by the $a1_g(aa)$ state potential [93] and is bound to $\approx 300\text{cm}^{-1}$.

4.3 The OODR excitation of IP states

This section will describe the OODR excitation schemes used in this thesis to populate IP states in the first and second clusters. One of three excitation schemes is used depending on the symmetry of the destination state: the conventional OODR excitation route through an unperturbed intermediate state reaches the $E0_g^+(1)$, $f0_g^+(2)$ and $\beta 1_g(1)$ states, while schemes with perturbed intermediate states are required to populate the $\delta 2_u(1)$, $\gamma 1_u(1)$, $D0_u^+(1)$, $F0_u^+(2)$, and $D'2_g(1)$ states (see Table 4.6).

Parent state X(v,J)	Transition energy (cm^{-1})	Pumped intermediate level B(v,J)	Intermediate state energy (cm^{-1})	Ion Pair destination
(1,70)	17339.81	(17,69)	17845.00	$E0_g^+(1)$, $f0_g^+(2)$, $\beta 1_g(1)$
(0,7)	20037.77	(78,8)	20146.85	$D'2_g(1)$
(0,21)	19888.41	(59,22)	20012.85	$\delta 2_u(1)$, $\gamma 1_u(1)$, $F0_u^+(2)$ $D0_u^+(1)$, $H1_u(2)$
$c1_g(ab)$ level		(14,22)	20012.85	

Table 4.6. The OODR pumping scheme: the intermediate levels used and their ion pair destinations (see [87]).

OODR excitation through an unperturbed intermediate

$$X0_g^+(aa)(1,70) \xrightarrow{P} B0_u^+(ab)(17,69) \xrightarrow{R} IP(v,70). \qquad (4.20)$$

A conventional OODR excitation scheme is used in this thesis to access the $E0_g^+(1)$, $f0_g^+(2)$ and $\beta 1_g(1)$ ion pair states through a vibrationally excited intermediate state, pumping the inner turning point (Franck-Condon overlap, $\langle v''' \mid v'' \rangle$, of 0.183) and probing low vibrational levels of the destination state from the outer turning point ($B(v''=17)R^{outer} = 3.60$Å, close to R_e^{IP}): see figure 4.9. Parallel transitions in the second step can populate the 0_g^+ ion pair states while the weaker perpendicular Valence→IP transitions access those with 1_g symmetry.

OODR excitation through perturbed intermediates: the $D'2_g(1)$ state

$$X0_g^+(aa)(0,7) \xrightarrow{R} B0_u^+(ab)(78,8) \sim 1_u(ab)(v,J) \xrightarrow{R} IP(n,J+1). \qquad (4.21)$$

The OODR excitation of the $D'2_g(1)$ state using one photon absorption in the second step requires a $B0_u^+(ab) \sim 1_u(ab)$ coupled intermediate to overcome the

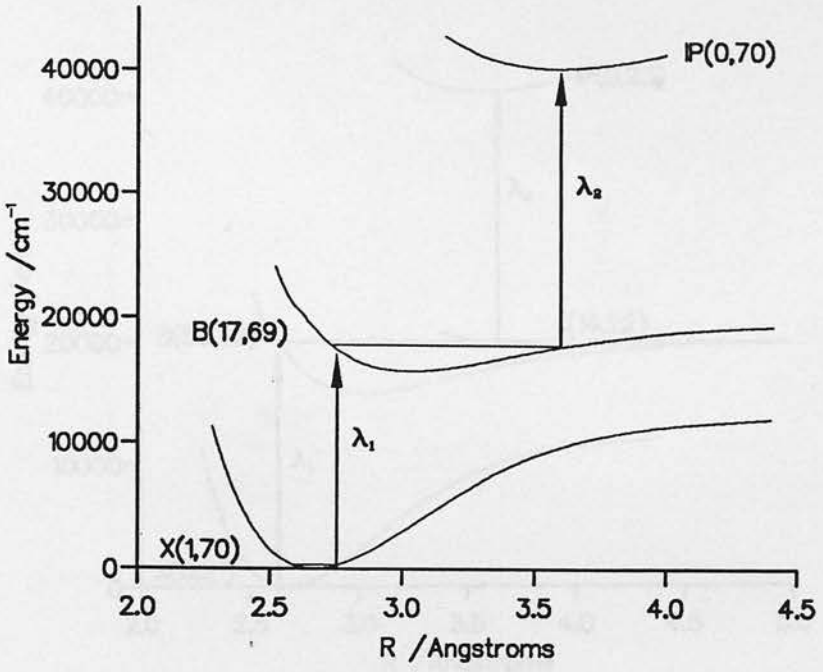

Figure 4.9. OODR excitation scheme for 0_g^+ and 1_g IP states.

$\Delta\Omega = 0, \pm 1$ selection rule. It is thought that a $1_u(ab)$ state performs a similar function in this excitation scheme as the $c1_g(ab)$ state in the excitation of *ungerade* IP states: ie it couples to the $B0_u^+(ab)$ level at large R, and gives strong Franck-Condon overlap to the $D'2_g(1)$ state from close to its inner wall. An accurate potential function for the $1_u(ab)$ state has not been reported, but this is unimportant for our studies as the $D'2_g(1)$ has already been characterised using other excitation techniques notably the discharge experiments performed by Tellinghuisen (see Table 1.4). Therefore the destination state is well known and the OODR scheme is simply used in this thesis to develop a state specific $D'2_g(1)$ population for the lifetime studies (Chapter 5). However this route could also be employed to access the $2_g(3)$ state in the third cluster, and then a more accurate knowledge of the pumping scheme would be required before an unambiguous assignment of the absorption spectrum could be made.

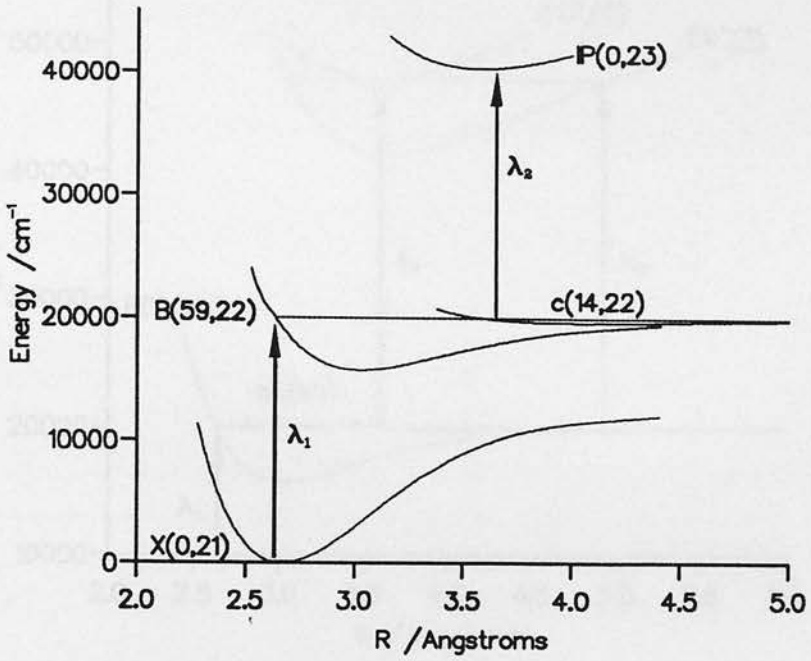

Figure 4.10. OODR excitation scheme for *ungerade* IP states.

OODR excitation of the *ungerade* IP states

$$X0_g^+(aa)(0,21) \xrightarrow{R} B0_u^+(ab)(59,22) \sim c1_g(ab)(14,22) \xrightarrow{R} IP(v,23). \quad (4.22)$$

The two photon OODR excitation of *ungerade* IP states requires a u/g symmetry breaking intermediate to overcome the parity selection rule. Thus we pump the $B0_u^+(ab)$ (59,22) level from the ground state (Franck-Condon overlap 0.065) which we know to be strongly coupled to the $c1_g(ab)$ (14,22) level (Franck-Condon overlap of 0.105 mainly at their outer turning points). Access to the *ungerade* ion pair states is from the inner turning point of the c state vibrational motion, $c(v''=14)R^{inner} = 3.605$Å (see figure 4.10).

One final experiment was performed to confirm the role of this perturbed intermediate state in the OODR absorption to *ungerade* IP states: a fluorescence excitation spectrum was recorded at probe laser wavelengths where excitation to high vibrational levels of a first cluster state, and low vibrational levels of a second cluster state, are possible. The monochromator was set to disperse fluorescence

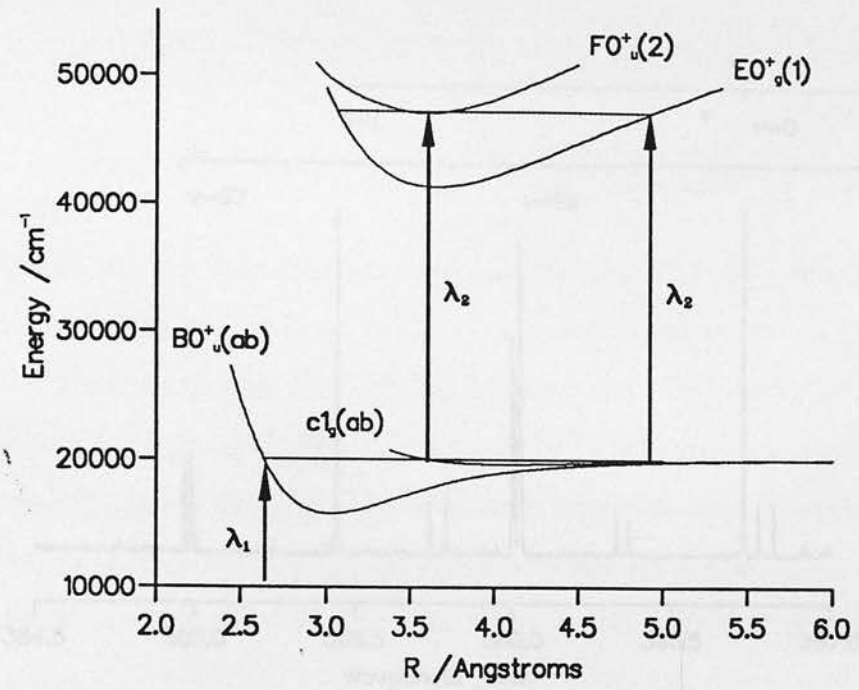

Figure 4.11. OODR excitation scheme for $\lambda = 365$nm through the $B0_u^+(ab)(59,22) \sim c1_g(ab)(14,22)$ intermediate.

around $\lambda = 270$nm, ie for transitions terminating at the ground state, $X0_g^+(aa)$.

Franck-Condon factors dictate that excitation to high v in a first cluster state must be from the outer turning point of the intermediate state vibrational motion (see figure 4.11). We would therefore expect to populate the $E0_g^+(1)$ and $\gamma 1_u(1)$ states through parallel transitions from the $B0_u^+(ab)$ and $c1_g(ab)$ components of the perturbed intermediate, and detect fluorescence if they achieve significant collisional transfer to the $D0_u^+(1)$ state ($p(I_2) = 0.1$Torr); only fluorescence from the $E0_g^+(1)$ state is recorded (see figure 4.12). The Franck-Condon factors for the probe step are very weak, $B0_u^+(ab) \rightarrow E0_g^+(1)$ $\langle v'''|v''\rangle = 0.005$, and perpendicular transitions in the second OODR step will not establish a large enough IP population for significant collisional transfer to the $D0_u^+(1)$ state: no fluorescence excitation of the other first cluster states is detected.

By contrast excitation to a second cluster state in low v must arise through strong Franck-Condon overlap around R_e^{IP}, ie from the inner turning point of

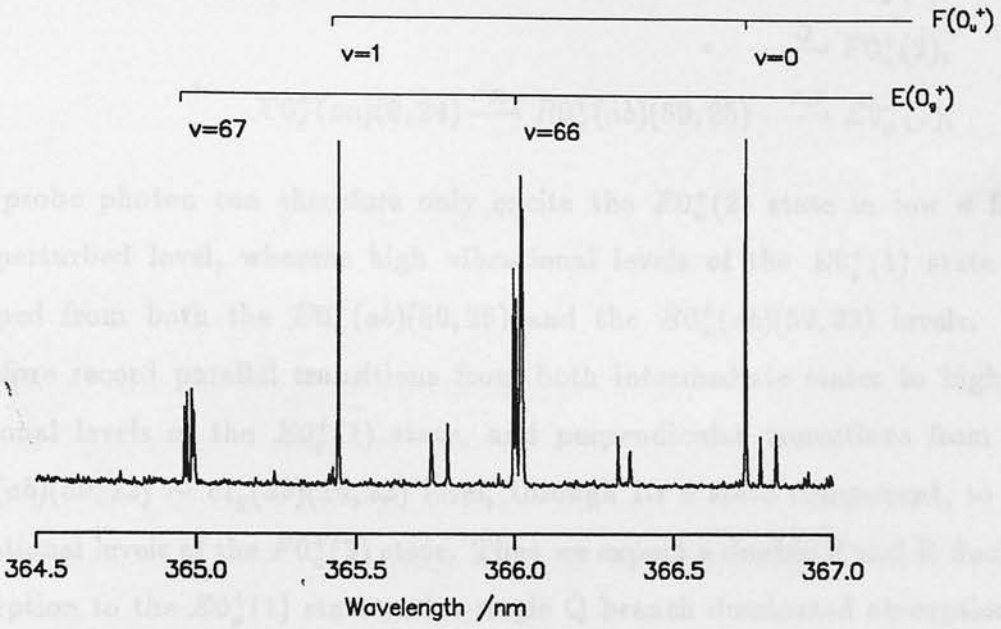

Figure 4.12. Fluorescence excitation spectrum from the perturbed $B0_u^+(ab)$ (59,22) intermediate at $\lambda = 365$nm (collected at 270nm).

the $c1_g(ab)$ state wavefunction (see figure 4.11). The Franck-Condon factors for this probe step are about ten times stronger and both perpendicular and parallel transitions to the second IP cluster may be expected. The monochromator will disperse fluorescence from the $F0_u^+(2) \rightarrow X0_g^+(aa)$ transition, and the vibrational progression of the $F0_u^+(2)$ state is recorded (figure 4.12); the $H1_u(2)$ state lies too high in energy to excite at these wavelengths (see Table 1.4) and is not detected. We can now account for the fluorescence excitation spectrum figure 4.12. Note that the intensities observed in a fluorescence excitation experiment reflect the various Franck-Condon factors in both the excitation and fluorescence of the IP state and the extent that the dispersed fluorescence lies in the wavelength window of the monochromator: a comparison between those observed for different vibronic states is not straightforward.

The pump laser populates two intermediate states, $B0_u^+(ab)$ (59,22) and $B0_u^+(ab)$ (59,25), of which only the first is sufficiently strongly coupled to the $c1_g(ab)$ state

to access *ungerade* IP states (see figure 4.7).

$$X0_g^+(aa)(0,23) \xrightarrow{P} B0_u^+(ab)(59,22) \sim c1_g(ab)(14,22) \xrightarrow{P,R} E0_g^+(1),$$
$$\xrightarrow{Q} F0_u^+(2),$$
$$X0_g^+(aa)(0,24) \xrightarrow{R} B0_u^+(ab)(59,25) \xrightarrow{P,R} E0_g^+(1),$$

The probe photon can therefore only excite the $F0_u^+(2)$ state in low v from the perturbed level, whereas high vibrational levels of the $E0_g^+(1)$ state are pumped from both the $B0_u^+(ab)(59,25)$ and the $B0_u^+(ab)(59,22)$ levels. We therefore record parallel transitions from both intermediate states to high vibrational levels of the $E0_g^+(1)$ state, and perpendicular transitions from the $B0_u^+(ab)(59,22) \sim c1_g(ab)(14,22)$ level, through its c state component, to low vibrational levels of the $F0_u^+(2)$ state. Thus we expect a double P and R doublet absorption to the $E0_g^+(1)$ state and a single Q branch dominated absorption to the $F0_u^+(2)$ state. This is as observed, confirming our picture of the role of the $c1_g(ab)$ state in the perturbation of the $B0_u^+(ab)$ (59,22) level.

Chapter 5 Radiative lifetimes of nine IP states

Halogen and interhalogen excited-state radiative lifetimes have been used to calculate collision cross-sections and elucidate kinetic schemes [4, 8, 94, 125, 126, 127, 128, 129, 130]; they have guided the development of laser systems [4, 8] and been used to locate and quantify couplings between electronic states [131], in particular the $B0_u^+(ab)$ valence state [130, 132, 133, 134, 135]. Lifetime studies of their ion pair states were initially pursued for the development of a laser based on the $D0_u^+(1) \rightarrow X0_g^+(aa)$ transition in I_2 [4, 8]. More recently, Einstein A-coefficients of individual electronic transitions deduced from lifetime measurements have been used to scale transition dipole moment functions obtained from dispersed fluorescence data [15, 91, 136] (see Chapter 7). This last step completes the interpretation of dispersed fluorescence data [36, 40], but is only possible when the lifetime of at least one vibrational level of the upper electronic state has been measured.

Although the lower vibrational levels of the halogen and interhalogen IP states are not predissociated, their lifetimes are expected to be short ($\approx$ 10ns) since they are both highly energetic and all have strong spin-allowed transitions to one or more valence states. This is in contrast with the longer lived valence states whose radiative lifetimes are of the order of 100ns. In low vibrational levels, the detailed difference in lifetimes between IP states reflects subtle changes in their electronic configurations within the broad context of their ion-pair nature, and also in that

The work covered in this chapter has been published in Chemical Physics [92].

of the valence states at large internuclear separations to which they fluoresce. These points are discussed in greater detail in Chapter 6.

In this Chapter the lifetimes in low vibrational levels of nine of the twenty ion-pair states of I_2 are reported: the six states of the first cluster, and three of the six from the second. In the following Chapter the relative fluorescent intensities for the transitions from these states to all the accessible lower states will be analysed. On combining these results with the relative Einstein A-coefficients derived there, the IP to valence transition dipole moment can be deduced for internuclear separations near R_e^{IP}. These are then interpreted in terms of the electronic configuration of the upper IP state. Chapter 7 discusses the $F0_u^+(2) \rightarrow X0_g^+(aa)$ and $f0_g^+(2) \rightarrow B0_u^+(ab)$ transition dipole functions derived from the dispersed fluorescence spectra of high vibrational levels: these functions are calibrated absolutely using the lifetimes analysed here. The measurement of the radiative lifetimes for the IP states is therefore central to the results reported in the following Chapters.

5.1 Results and Analysis

State specific excitation of the ion pair state was achieved using the OODR pumping schemes described in Chapter 4. The experimental configuration and details of data acquisition for these lifetime studies are given in Chapter 2.

Representative examples of the shape of the time-resolved fluorescence, $I_{fl}^{obs}(t)$, for IP→Valence transitions are shown in figures 5.1, 5.2 and 5.3, for short-, intermediate- and longer-lived states respectively, together with their simulation, $I_{fl}^{conv}(t)$, a pulse profile, $P(t)$, and the residual, $I_{fl}^{obs}(t) - I_{fl}^{conv}(t)$. The complete fluorescence decay was simulated by convoluting the pulse profile with a single exponential decay to give a best fit lifetime, τ, and the pre-exponential factor, A:

$$I_{fl}^{conv}(t) = A \int_{t_0}^{t} P(t') \exp^{(t-t')/\tau} dt', \tag{5.1}$$

where t_0 is the pulse arrival time. A first estimate of the lifetime is obtained

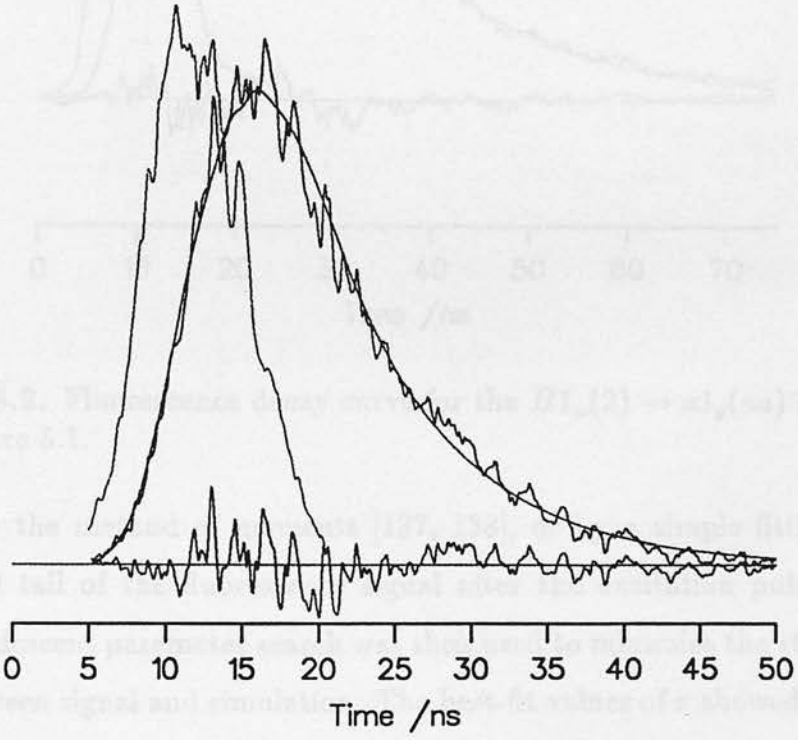

Figure 5.1. Fluorescence decay curve for the $D'2_g(1) \rightarrow A'2_u(aa)$ emission (full line) following excitation by a compressed pulse (...), after the impedance mismatch ripple has been removed. The best fit simulated decay is shown (dashed), together with the residual signal along the base line.

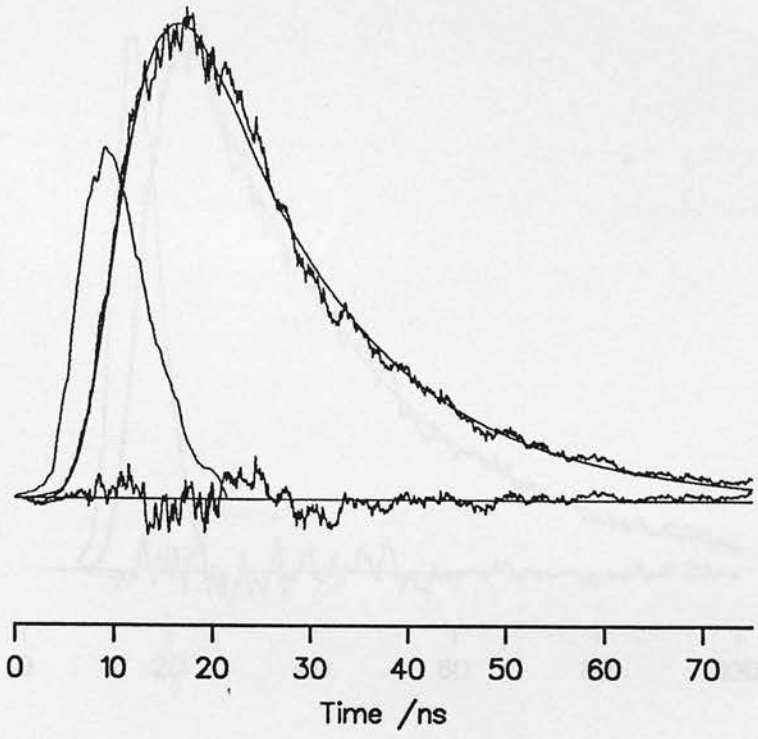

Figure 5.2. Fluorescence decay curve for the $H1_u(2) \rightarrow a1_g(aa)$ emission. Key as in figure 5.1.

either by the method of moments [137, 138], or by a simple fitting of the exponential tail of the fluorescence signal after the excitation pulse is over. A steepest descent parameter search was then used to minimise the standard deviation between signal and simulation. The best-fit values of τ showed no significant dependence on the upper time limit for fitting (generally taken to be 3τ), nor on the choice of initial lifetime, except for the $\gamma 1_u(1)$ state. For this state the long lifetime left a significant cut off error and the method of moments calculation was not used. A slight ringing, possibly resulting from a small impedance mismatch in the collection electronics, was found in all the decay curves and this was filtered out numerically since it did not significantly alter the best estimates of τ, but did reduce the standard deviation of the fit (see figure 5.4). At each pressure for each state at least nine separate fluorescence decays were recorded in three groups of three scans. The uncertainty in a particular fit for τ was ± 0.1ns, as calculated following Bevington [120]. This reflects the low shot to shot variation

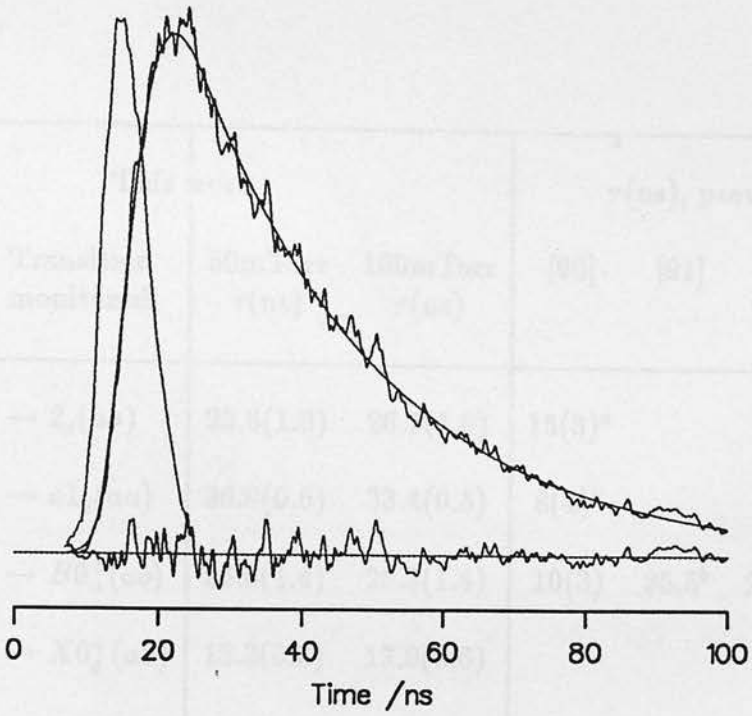

Figure 5.3. Fluorescence decay curve for the $\delta 2_u(1) \rightarrow 2_g(aa)$ emission. Key as in figure 5.1.

in a group of three sequential scans though the levels of uncertainty given with the results suggest a larger overall run to run scatter. The rotational dependence of the lifetimes was not investigated, though Perrot *et al* have shown that the J-dependence is not significant for low v lifetimes of the $E0_g^+(1)$ and $\beta 1_g(1)$ states [91].

Table 5.1 gives the results for the states studied along with a comparison with previously published data where available. Only the long lived $\gamma 1_u(1)$ state showed a significantly pressure dependent lifetime: the values given in table 5.1, assuming a linear extrapolation, suggest a zero-pressure lifetime of 38.6($\pm$0.6)ns. At 100mTorr a γ state molecule has a 5% probability of collision during a single lifetime, assuming a state-changing collision cross-section of 200Å^2 [140]. The F state lifetime is too short for reliable determination by the experimental technique used here as the fluorescence decay has a similar width at half maximum to the pulse profile. Although the impedance mismatch ringing significantly distorts

Ion-pair state	Transition monitored	This work 50mTorr τ(ns)	This work 100mTorr τ(ns)	τ(ns), previous studies [90]	[91]	[89]	
$\delta 2_u(1)$ $v=2$	$\rightarrow 2_g(aa)$	25.8(1.0)	26.7(1.0)	15(3)[a]			
$\gamma 1_u(1)$ $v=0$	$\rightarrow a1_g(aa)$	36.0(0.6)	33.4(0.5)	8(4)[a]			
$E0_g^+(1)$ $v=0$	$\rightarrow B0_u^+(ab)$	26.6(1.4)	25.3(1.4)	10(3)	25.5[b]	28(1)[b]	27(2)[c]
$D0_u^+(1)$ $v=0$	$\rightarrow X0_g^+(aa)$	13.3(0.6)	13.0(0.6)				15.5(0.5)[d]
$\beta 1_g(1)$ $v=2$	$\rightarrow A1_u(aa)$	11.8(0.4)	11.5(0.4)	8(3)[e]	11.4[b]	12(1)[b]	
$D'2_g(1)$ $v=0$	$\rightarrow A'2_u(aa)$	8.5(1.0)[f]	7.7(1.0)	5(3)[g]			6.7(0.5)[d]
$f0_g^+(2)$ $v=0$	$\rightarrow B$	14.0(0.7)	13.4(0.7)				
$F0_u^+(2)$ $v=0$	$\rightarrow X$		4.5(1.0)				
$H1_u(2)$ $v=0$	$\rightarrow a$		15.4(0.2)				

Table 5.1. Radiative lifetimes for nine ion-pair states of I_2 . Experimental uncertainties in brackets ( ).

[a] $v = 1$.
[b] By extrapolation.
[c] $v \approx 46$, [139].
[d] v unknown, [8, 126].
[e] $v = 7$.
[f] Measured at 60mTorr.
[g] $v = 4$.

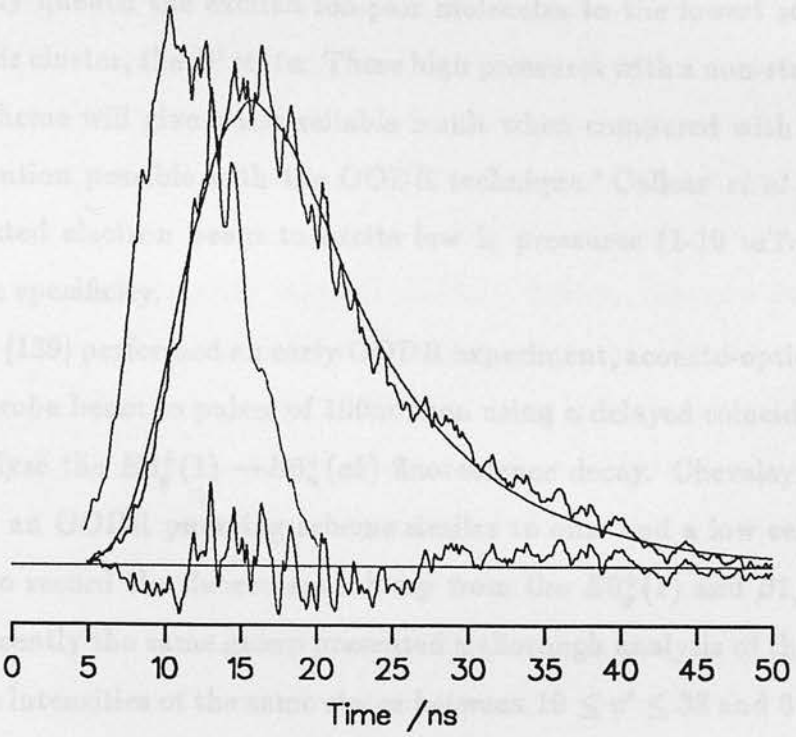

Figure 5.4. Fluorescence decay curve for the $D'2_g(1) \rightarrow A'2_u(aa)$ emission, before impedance mismatch ripple is removed. Key as in figure 5.1.

the decay profile, our experiments suggest the F state lifetime lies in the range 3.5 to 4.5ns. Self-quenching studies after initial pumping of the $f0_g^+(2)$ state ($p(I_2) < 0.3$Torr), have shown that near resonant $f \rightarrow F$ collisional vibronic energy transfer is much more efficient than $F \rightarrow f$ transfer [141]. Such a short F state lifetime suggests that radiative decay is successfully competing with the collisional transfer for the F state population at these low pressures.

5.2 Discussion

5.2.1 Comparison with other measurements

Two of the previous lifetime measurements referred to in Table 5.1 used non-state specific excitation schemes [8, 126]. Sauer and coworkers [126] used an electron beam to excite an Ar/I_2 mixture and then monitored the $D'2_g(1) \rightarrow A'2_u(aa)$ fluorescence at 342nm. They used high buffer gas pressures (344 and 700 Torr)

to collisionally quench the excited ion-pair molecules to the lowest state in the lowest ion-pair cluster, the D' state. These high pressures with a non-state specific excitation scheme will give a less reliable result when compared with the state-specific excitation possible with the OODR technique. Callear *et al* [8] used a 7keV collimated electron beam to excite low I_2 pressures (1-10 mTorr), again with no state specificity.

Rousseau [139] performed an early OODR experiment, acousto-optically modulating the probe beam to pulses of 100ns then using a delayed coincidence technique to analyse the $E0_g^+(1) \rightarrow B0_u^+(ab)$ fluorescence decay. Chevaleyre and coworkers used an OODR pumping scheme similar to ours and a low cell pressure (30 mTorr) to record the fluorescence decay from the $E0_g^+(1)$ and $\beta 1_g(1)$ states [89]. More recently the same group presented a thorough analysis of the lifetimes and radiative intensities of the same states between $10 \leq v' \leq 33$ and $0 \leq v' \leq 28$ respectively [91]: their results are in close agreement with those presents here. They found only a small dependence of τ on v' and for comparison with our results the extrapolation to $v' = 0$ only produces a small correction of less than 1ns.

Early in the application of OODR techniques to these ion pair states, King *et al* [90] also presented a series of lifetime measurements using an excitation scheme and method of analysis closely similar to our own. Although some of their vibronic assignments have since been revised, it is not easy to explain the discrepancy between their results and those presented here and by Broyer's group [91].

5.2.2 Interpretation of results

Radiative lifetimes of states free from predissociation depend on three factors: the Franck-Condon overlap integrals, the radiative frequencies and the transition moments of each of the dipole-allowed transitions of the state

$$1/\tau_{n'v'} = (64\pi^4/3hc^3) \sum_{n''v''} \langle v' \mid \mu_{n'n''}(r) \mid v'' \rangle^2 v^3_{n'v'n''v''}. \qquad (5.2)$$

All the ion pair states have very similar R_e and ω_e values, so we would expect the dominant factor in determining the difference in lifetimes of these electronically similar states to be the v^3 term. This is clearly an important factor and is responsible for the lifetimes of the states in the second cluster, with term values roughly 6000cm^{-1} greater than those in the first cluster, being consistently shorter than the corresponding state in the first cluster. However based solely on this factor, the 0_u^+ state in each cluster, which alone can fluoresce directly to the ground state, should have the shortest lifetime in each group: in the first cluster the $D0_u^+(1)$ state does have one of the shorter lifetimes, but not quite the shortest.[1] Furthermore, if we compare the lifetimes of a u/g pair in a given ion pair cluster we should find them closely similar, after allowing for the v^3 factor, reflecting their identical electronic structure in the $(J_A M_A J_B M_B)$ coupling scheme (except for their different phase under inversion). The 0-0 band of the $E0_g^+(1) \rightarrow B0_u^+(ab)$ fluorescence is at 23412cm^{-1} and that of the $D0_u^+(1) \rightarrow X0_g^+(aa)$ emission is at 32049cm^{-1} so the v^3 factor would predict a lifetime ratio of $\tau_E/\tau_D \approx 2.56$ compared with the observed ratio of 1.98($\pm$0.2) which is not too dissimilar. In contrast, the pair of $\Omega = 2$ states of the first cluster, $\delta 2_u(1)$ and $D'2_g(1)$, have their principal fluorescence originating at 340nm and 342nm, respectively, so the v^3 factor would lead to a lifetime ratio of unity, but $\tau_\delta/\tau_{D'}$ is observed to be 3.2($\pm$0.2).

Considerable differences in the lifetimes of apparently closely related ion-pair states, such as u/g pairs in the same cluster, remain after the v^3 factor has been taken into account, suggesting perhaps that small departures from the simple ion pair model for the excited states (and atom pair model for the lower valence states) produce large changes in the transition dipole functions together with a redistribution of the oscillator strengths among the final valence states. However we find in the next Chapter that on closer analysis, the change in electronic structure of the IP state in a charge transfer process predicts that certain transitions,

[1] Perpendicular transitions from 1_u states can also reach the ground state, but will not significantly alter the upper state lifetime since parallel transitions are approximately 15 times stronger than perpendicular: see Chapter 6

available to an *ungerade* state, are not allowed for their *gerade* partner. Consequently large differences in lifetime can occur between u/g pairs with identical electronic configuration. These points are discussed in greater detail in Chapter 6.

Chapter 6 Einstein A-coefficients and $\mu_{n'}(R_e)$

As has been discussed in Chapter 1, the vibronic spectroscopy of the halogens presents an interesting example of changes in the electronic structure of a state as the bond is stretched over several angstroms. Near dissociation the double set of quantum numbers describing the separated ionic fragments holds good for the molecule and usually several MO configurations are required to obtain a proper description. At small separations, only a single quantum number, Ω, remains and a dominant MO configuration emerges, with possible configuration mixing if there are nearby Rydberg states. The changeover between the two descriptions is noted by increased jj mixing of the various J states of the cation and some mixing of valence and ion pair configurations, however the characteristic clustering of the ion pair term values suggests that around R_e^{IP} the separated-ion, or $(J_A M_A J_B M_B)$, model is good as a first approximation.

The same jj mixing markedly affects the radial dependence of the IP$\rightarrow$Valence transition dipole functions and their variation from one ion pair state to another. Thus the only IP state that can be accessed in a single photon excitation from the ground state (around 2.7Å in I_2) is the lowest 0_u^+ state (the $D0_u^+(1)$ state), but it is known that the second 0_u^+ state (the $F0_u^+(2)$ state) fluoresces strongly back to the ground state from low v' levels (around 3.6Å). The $F0_u^+(2) \rightarrow X0_g^+(aa)$ transition dipole has therefore changed by perhaps an order of magnitude over 1Å (see Chapter 7). Though the ultimate aim may be to derive $\mu_{IP\rightarrow V}$ absolutely as

The work covered in this chapter has been accepted for publication by Molecular Physics [14].

a function of R for all significant IP→Valence transitions, it would be instructive to compare their transition moments at a particular internuclear separation since this gives an insight into the developing electronic configurations of the states involved.

This Chapter reports the relative fluorescent yields of nearly all the strong IP→Valence transitions of the eight lowest IP states of I_2, mostly from $v' = 0$. The detailed Einstein A-coefficients are deduced by combining the dispersed fluorescence data with the lifetime measurements described in the previous Chapter: the detailed transition dipoles, summed over v'', $\sum_{v''} \mu^2_{n'v'n'v''}$, are then deduced. These are used as a probe of the electronic structure of the IP states near R_e. The distribution of fluorescence from a given IP state n' among the various valence states n'' depends on the p_σ versus p_π occupancy in both the upper and lower states. The analysis developed here concentrates on the electronic structure of the IP states and the effect of the composition of the valence states is eliminated by summing $\mu^2_{n'v'n''v''}$ over n''. These partially summed dipoles are then analysed in terms of the $(J_A M_A J_B M_B)$ model to give the relative contributions of the various m_l occupancy patterns available to the I^+ ion for each IP state: this interpretation is possible only if all the strong electronic systems $n' \rightarrow n''$ for a given IP state have been recorded. At the end of the analysis we are able to compare the IP configurations, finding that they differ appreciably from those of the free ions.

In the following Chapter the transition dipole moments are discussed as a function of R for a number of important IP→Valence transitions, demonstrating the changes in electronic structure of these states as the nuclei approach.

6.1 Experimental

State specific excitation of the ion pair states was achieved using the OODR pumping schemes described in Chapter 4; the experimental configuration and data acquisition for these dispersed fluorescence spectra are described in Chapter

2. All data collection conditions (eg. the monochromator slitwidth) were kept constant for all the radiative systems of a given ion pair state and the strongest transition from each ion pair state was recorded before and after each scan of weaker systems to ensure signal stability.

Scattered laser light and strong $B0_u^+(ab) \rightarrow X0_g^+(aa)$ emission at $\lambda > 520$nm limited the spectral range that could be monitored, and transitions from the first cluster to valence states at the third dissociation limit (bb) could not be included. As a consequence the analysis of the radiative systems for the $\beta 1_g(1)$ and $D0_u^+(1)$ states is incomplete though we find later that broad conclusions can be still drawn about their electronic configurations near R_e. Typical dispersed fluorescence spectra consist of a few short vibrational progressions under the envelope of v'. Some of these have been individually reported in the literature, but not their relative intensities, thus the complete fluorescence spectra over $300 \leq \lambda \leq 500$nm are shown in figures 6.1 to 6.6 for the $\delta 2_u(1)$, $\gamma 1_u(1)$, $\beta 1_g(1)$, $D0_u^+(1)$, $E0_g^+(1)$, $H1_u(2)$, $F0_u^+(2)$ and $f0_g^+(2)$ states. These reveal a number of IP$\rightarrow$Valence transitions to previously unknown valence states though only a small Franck-Condon window of the lower state is explored since only the fluorescence intensities from the lowest vibrational level of each IP state is required for this study. Extending the analysis to higher v' would allow a more extensive characterisation of these new states.

6.1.1 Results and analysis

Smoothing each system by computer simulation removes the experimental dependence on laser fluctuations and allows the separation of dispersed fluorescence from that of other systems or scattered laser light. The input to the simulation is the potentials for the two states involved in the form of splined cubic functions $V(R)$ between a small number of (R,V) points, typically experimental RKR pairs (see Chapter 2). The simulated spectrum is very sensitive to the accuracy of these potentials, so the latest available experimental data were used whenever possible, though for a few states approximate functions had to be generated then

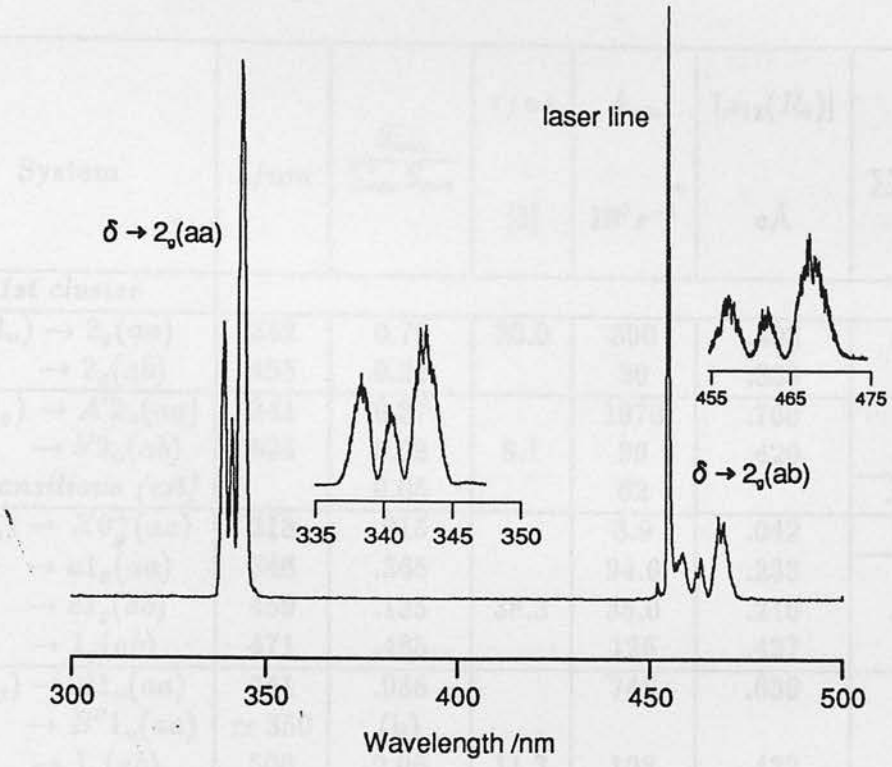

Figure 6.1. Survey spectrum of the dispersed fluorescence from the $\delta 2_u(1)(v' = 2)$ ion pair state.

optimised by fitting to the experimental spectra. References to the data used in the simulation work can be found in Table 6.1.

The only available experimental data for the $\delta 2_u(1)$ state is limited to the early work of King *et al* [34] with theoretical results from Jaffe given by Viswanathan and Tellinghuisen [19]. These suggest that for iodine, as found for bromine [142], the $\delta 2_u(1)$ state is somewhat anomalous amongst the six states of the first ion pair cluster, having a significantly larger R_e value. Our work suggests that King's assignment is incorrect by one quantum: the $v = 0$ level is not seen in absorption from the intermediate state, presumably for Franck-Condon reasons (all transitions to the $\delta 2_u(1)$ state are weak when compared with the other perpendicular transition from this intermediate state, that to the $D0_u^+(1)$ state). King's first assignment should be to $\delta(v' = 1)$ since our δ level is one quantum higher and from the envelope of the dispersed fluorescence is clearly $v' = 2$ (see figure 6.1). Thus, using his figures, the δ state T_e value should be $\approx 41689\text{cm}^{-1}$. Since the $\delta 2_u(1)$

System	λ/nm	$\frac{S_{nm}}{\sum_m S_{nm}}$	τ/ns [5]	A_{nm} $10^5 s^{-1}$	$\lvert\mu_{12}(R_e)\rvert$ eÅ	$\sum \lvert\mu_{\parallel}\rvert^2$	Refs. (d)
1st cluster							
$\delta(2_u) \rightarrow 2_g(aa)$	342	0.79	26.0	300	.408	.277	
$\rightarrow 2_g(ab)$	465	0.21		80	.333		
$D'(2_g) \rightarrow A'2_u(aa)$	341	0.87		1070	.766		(e)
$\rightarrow b'2_u(ab)$	505	0.08	8.1	99	.420	.763	
$\perp$ *transitions (est)*		0.05		62		$\perp$(c)	
$\gamma(1_u) \rightarrow X0_g^+(aa)$	318	.015		3.9	.042	$\perp$	[34, 23]
$\rightarrow a1_g(aa)$	346	.365		94.6	.233		[16, 18]
$\rightarrow c1_g(ab)$	459	.135	38.3	35.0	.216	.283	[12]
$\rightarrow 1_g(ab)$	471	.485		126	.427		
$\beta(1_g) \rightarrow A1_u(aa)$	341	.936		745	.639		
$\rightarrow B''1_u(aa)$	$\simeq$ 350	(b)					
$\rightarrow 1_u(ab)$	500	0.06	11.7	108	.432	.595	
$\rightarrow 1_u(ab)$	$\simeq$ 505	(b)					
$\rightarrow 1_u(bb)$	$\simeq$ 600	(a)					
$\rightarrow 0_u^-(aa)$	351	0.001		0.8	.022	$\perp$	
$D(0_u^+) \rightarrow X0_g^+(aa)$	318	0.89		679	.550		[36, 23]
$\rightarrow a'0_g^+(aa)$	368	0.09	12.5	68.7	.218	.371	[16, 17]
$\rightarrow 0_g^+(ab)$	460	0.02		15.3	.144		
$\rightarrow 0_g^+(bb)$	$\simeq$ 600	(a)					
$E(0_g^+) \rightarrow A1_u(aa)$	335	0.01		3.8	.045		[35, 20]
$\rightarrow B''1_u(ab)$	347	0.015	25.7	5.8	.058	$\perp$	[18]
$\rightarrow B0_u^+(ab)$	423	0.975		376	.627	.394	[15]
2nd cluster							
$H(1_u) \rightarrow a1_g(aa)$	282	.845		549	.413		[12, 16, 18]
$\rightarrow c1_g(ab)$	352	.155	15.4	101	.247	.231	[12]
$\rightarrow 1_g(ab)$	$\simeq$ 399	(b)					
$F(0_u^+) \rightarrow X0_g^+(aa)$	266	.91		2020	.725		[32, 23]
$\rightarrow a'0_g^+(aa)$	300	.09	4.5	200	.273	.600	[16, 17]
$\rightarrow 0_g^+(ab)$	$\simeq$ 355	(b)					
$\rightarrow 0_g^+(bb)$	$\simeq$ 515	(b)					
$f(0_g^+) \rightarrow A1_u(aa)$	282	.0125		9.1	.053		[33, 20]
$\rightarrow B''1_u(aa)$	292	.0125	13.7	9.1	.056	$\perp$	[18]
$\rightarrow B0_u^+(ab)$	341	.975		712	.625	.390	[15]

Table 6.1. Analysis of the integrated fluorescence from ion pair states.
(a) too far red to observe any emission. (b) no fluorescence found in this region.
(c) $\mu_\perp$ calculated from eqn.(6.5) without electronic degeneracy weighting.
(d) references to upper/lower state potentials used in fitting if taken from other work; otherwise parameters given in Section 6.1.1.
(e) Relative intensities for $D'2_g(1) \rightarrow 2_u$ taken from [11].

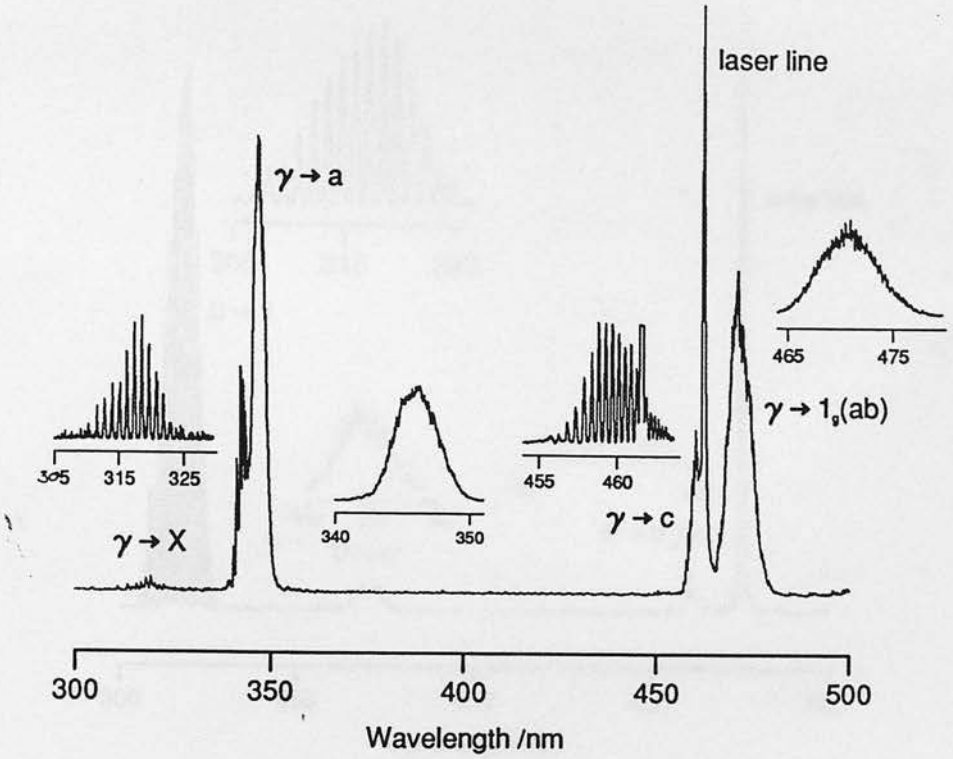

Figure 6.2. Survey spectrum of the dispersed fluorescence from the $\gamma 1_u(1)(v' = 0)$ ion pair state.

state is less well known experimentally, this study only reproduced the shape of the *bound* → *free* spectra observed for $\delta 2_u(1) \rightarrow 2_g(aa)$ and $\delta 2_u(1) \rightarrow 2_g(ab)$ fluorescence, and did not generate accurate valence state potentials.

In analysing fluorescence from the $\gamma 1_u(1)$ state, the valence $1_g(ab)$ potential was approximated by moving the $a1_g(aa)$ potential vertically in energy to the second dissociation limit, and a good match was found with R_e shifted by +0.017Å, to 4.33Å.

The dispersed fluorescence intensities for transitions from the $\beta 1_g(1)$ state are calculated from earlier work [93] and were not accurately calibrated in wavelength, only in intensity. Consequently absolute valence state potentials cannot be generated, only their shape, but this is sufficient for the simulation of the fluorescence and hence the evaluation of the A-coefficients. The fluorescence at 351nm from the $\beta 1_g(1)$ state terminates on the $0_u^-(aa)$ state [19]; fluorescence to the known $B''1_u(aa)$ state would lie approximately 4nm to the red and is not

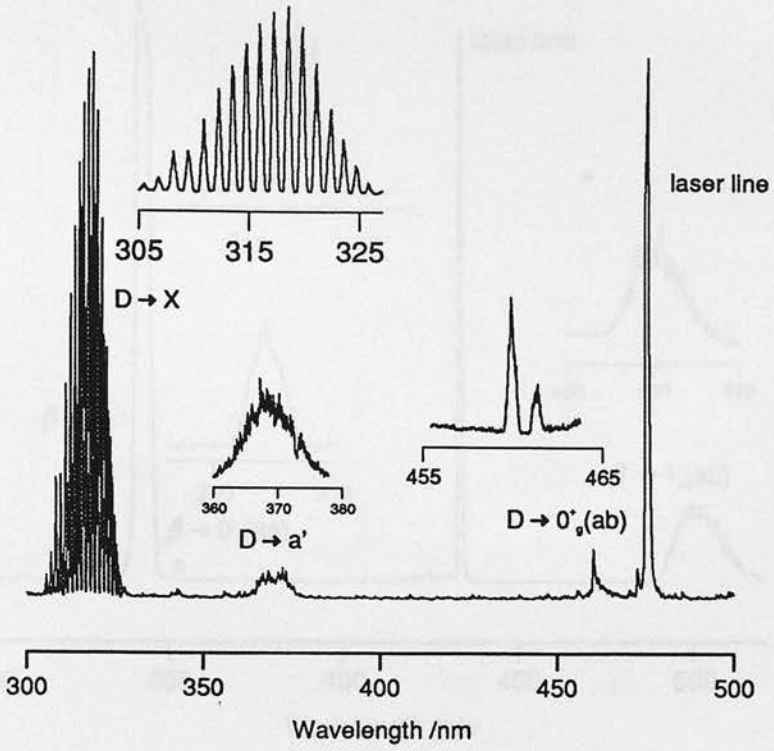

Figure 6.3. Survey spectrum of the dispersed fluorescence from the $D0_u^+(1)(v' = 0)$ ion pair state.

observed.

Simulations of fluorescence terminating on the $0_g^+(ab)$ state were calculated using a Morse function for the valence state, with $D_e = 859\text{cm}^{-1}$, $\omega_e = 68\text{cm}^{-1}$, $\omega_e x_e = 1.23\text{cm}^{-1}$ and $R_e = 3.645\text{Å}$. These parameters should be compared with the results from Ishiwata's group given in Table 1.1, [13]: $D_e = 864\text{cm}^{-1}$, $\omega_e = 64.4\text{cm}^{-1}$, $\omega_e x_e = 1.23\text{cm}^{-1}$ and $R_e = 3.645\text{Å}$.

Although the simulations are indistinguishable from the observed spectra, the purpose of this investigation was only to reproduce the observed spectral shape for subsequent integration so the data given above for valence state potentials should be seen as only approximating to the true potentials. However fitting the dispersed fluorescence is sensitive enough to locate $V''(R)$ to $\pm 2\text{cm}^{-1}$ over the range of R falling within the Franck-Condon window of the upper state (typically $\approx 0.2\text{Å}$). Integrated fluorescent intensities, $S_{n'n''}(v')$, in photons per second, for every recorded electronic transition were then calculated by integrating the

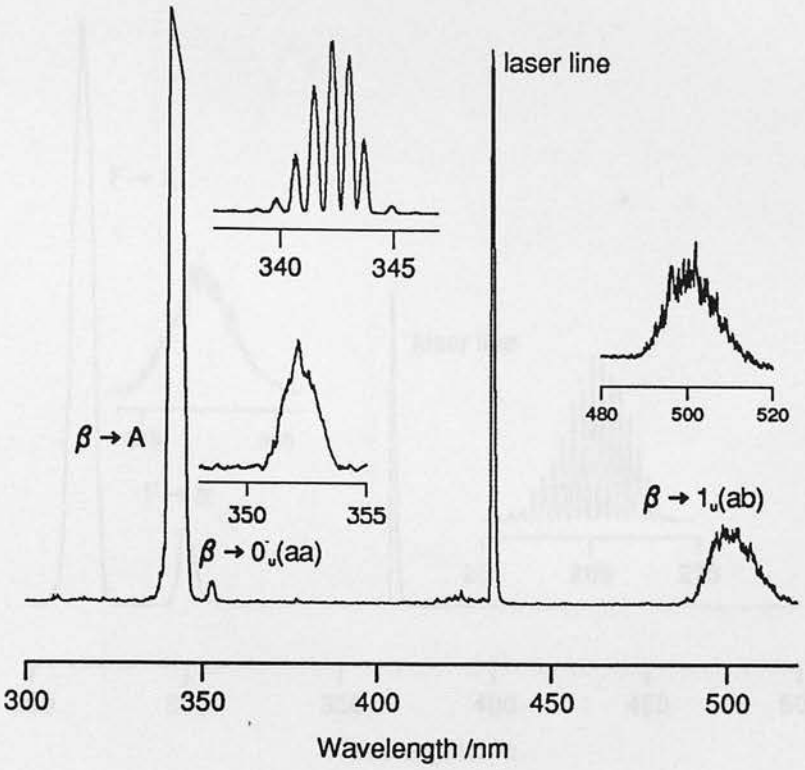

Figure 6.4. Survey spectrum of the dispersed fluorescence from the $\beta 1_g(1)(v' = 0)$ ion pair state.

simulated dispersed fluorescence from each electronic system.

$$S_{n'n''}(v') = \int_{\nu_{min}}^{\nu_{max}} I_{fl}(\nu) d\nu. \tag{6.1}$$

The relative values of $S_{n'n''}(v')$ for a given ion pair state are listed in Table 6.1 and are used in the next section to find the absolute Einstein A-coefficients.

6.2 Broad trends in the A-coefficients

As discussed in the previous Chapter, part of the differences observed in the lifetimes of the various IP states and in the associated A-coefficients arises from the ν_{fl}^3 dependence of the latter:

$$\tau_{n'v'} = 1/\sum_{n''v''} A_{n'v'n''v''}, \tag{6.2}$$

$$A_{n'v'n''v''} = \tilde{\nu}_{fl}^3 \langle v' \mid \tilde{\mu}_{n'n''}(R) \mid v'' \rangle^2 \times 7.2347 \times 10^{-6}, \tag{6.3}$$

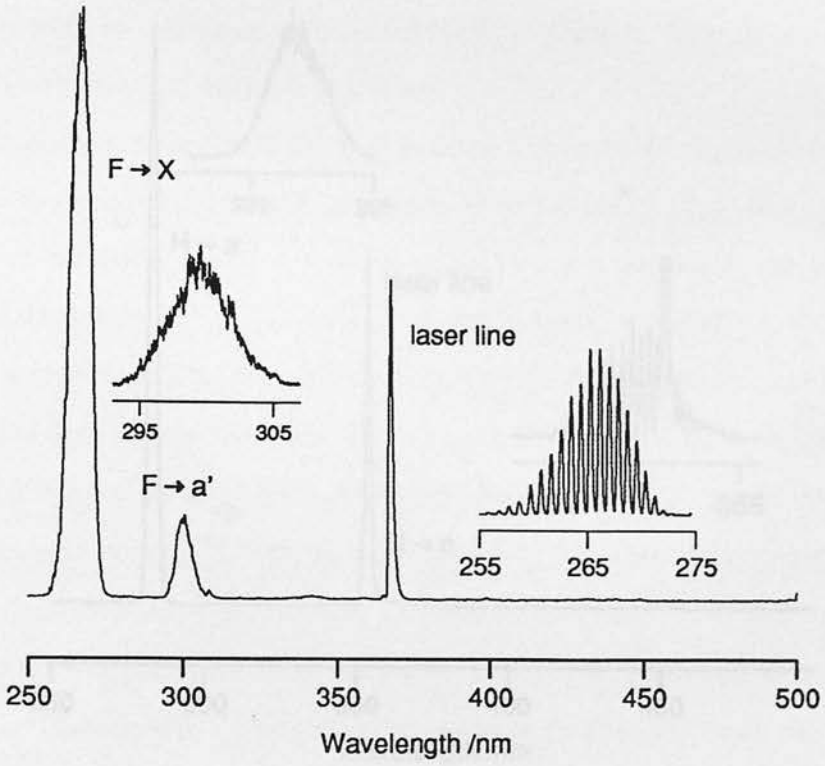

Figure 6.5. Survey spectrum of the dispersed fluorescence from the $F0_u^+(2)(v' = 0)$ ion pair state.

where $\tilde{\nu}$ is in wavenumbers and $\tilde{\mu}_{n'n''}$ is the reduced electronic dipole, $\mu_{n'n''}/\text{eÅ}$. The number of photons per second associated with an electronic transition $n' \rightarrow n''$, relative to that for any other transition from n', is proportional to the sum $S_{n'n''}(v')$ defined in equation (6.1). The vibrationally summed A-coefficients, $\sum_{v''} A_{n'v'n''v''}$, are then calculated by the simple proportion, with $\tau_{n'v'}$ known:

$$\sum_{v''} A_{n'v'n''v''} = \frac{S_{n'n''}(v')}{\sum_{n''} S_{n'n''}(v')} \tau_{n'v'}^{-1}, \tag{6.4}$$

Chapter 5 gives the lifetimes for the low vibrational levels analysed here, in which the amplitude of vibration is sufficiently small that

$$(3h/64\pi^4) \sum_{v''} A_{n'0n''v''} \approx \overline{\nu}^3_{n'n''} \langle 0 \mid \mu^2_{n'n''} \mid 0 \rangle \approx \overline{\nu}^3_{n'n''} \mu^2_{n'n''}(R_e), \tag{6.5}$$

where $\overline{\nu}^3_{n'n''}$ is the median frequency of the transition (typically $\Delta\nu/\nu \simeq 10^{-3}$). Thus we can obtain $|\mu_{n'n''}(R_e)|$ for a given transition $n' \rightarrow n''$ from our measurements of $\tau_{n'v'}$ and the integrated fluorescent intensities for each channel, $S_{n'n''}(v')$.

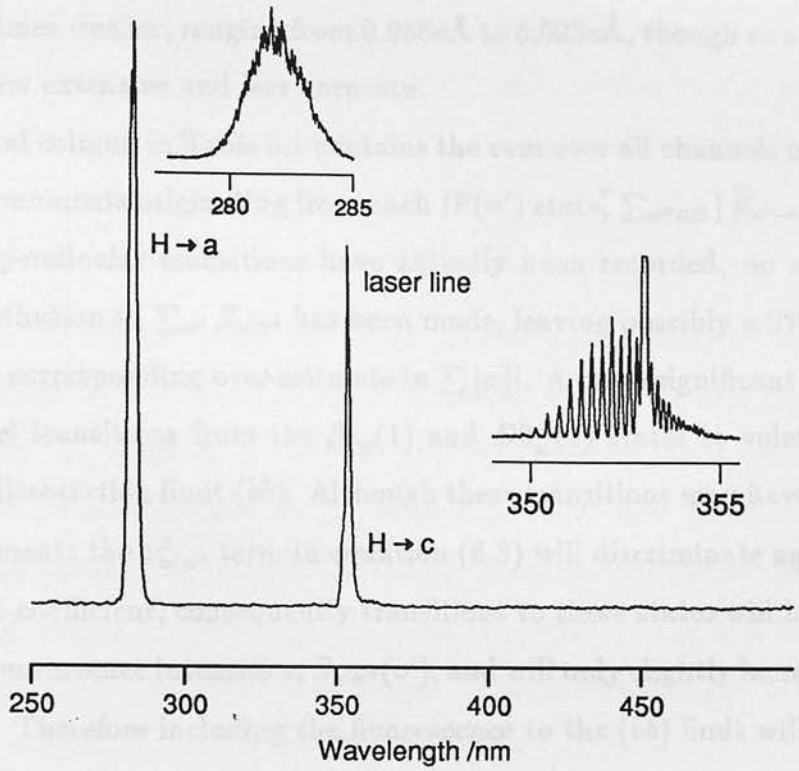

Figure 6.6. Survey spectrum of the dispersed fluorescence from the $H1_u(2)(v' = 0)$ ion pair state.

This approach has been used by Holmes *et al* to calibrate their dipole function for the $f0_g^+(2) \rightarrow B0_u^+(ab)$ transition [15].

The integrated fluorescence intensities are reproducible to within $\pm 5\%$ however this will lead to a correlated error in the Einstein A-coefficients for the transitions from a particular IP state through equation (6.4). The degree of uncertainty in the Einstein A-coefficients is therefore of the order of $\pm 8\%$ if the radiative manifold is dominated by one transition, however a detailed error analysis will not be pursued since we will use the results in column 5 to draw out the broad trends in the IP configurations and will not rely excessively on their quantitative accuracy.

The transition dipoles for all the systems studied in this Chapter are given in the fifth column of Table 6.1. The parallel transition moments show a wide range of values from the largest, the $D'2_g(1) \rightarrow A'2_u(aa)$ at 0.766eÅ, to the $D0_u^+(1) \rightarrow 0_g^+(ab)$ dipole at 0.144eÅ. The perpendicular transition moments are

about 15 times weaker, ranging from 0.058eÅ to 0.022eÅ, though as a consequence they are less extensive and less accurate.

The final column in Table 6.1 contains the sum over all channels of the parallel transition moments originating from each IP(n') state, $\sum_{n''\in\Omega} \mid \widetilde{\mu}_{n'\rightarrow n''} \mid^2$. Except where perpendicular transitions have actually been recorded, no allowance for their contribution to $\sum_{n''} S_{n'n''}$ has been made, leaving possibly a 2% error in the sum and a corresponding over-estimate in $\sum |\mu_{\|}^2|$. A more significant omission are the parallel transitions from the $\beta 1_g(1)$ and $D0_u^+(1)$ states to valence states at the third dissociation limit (bb). Although these transitions may have appreciable dipole moments the $\nu_{n'n''}^3$ term in equation (6.3) will discriminate against a large Einstein A-coefficient, consequently transitions to these states will have small integrated fluorescence intensities, $S_{n'n''}(v')$, and will only slightly increase the sum, $\sum_{n''} S_{n'n''}$. Therefore including the fluorescence to the (bb) limit will correlate to a small reduction in the Einstein A-coefficients for transitions to the lower valence dissociation limits, leading to a small reduction in their transition moments. The sum $\sum_{n''} |\mu_{\|}^2|$ can only increase, however, since the reduced contribution of transitions to the lower dissociation limits will be more than compensated for by the moments of transitions to the (bb) limit. The values given in Table 6.1 for the sum of the squared transition dipoles from these states therefore represent lower limiting values.

Even with this proviso, Table 6.1 suggests an interesting contrast between the sums of the transition dipoles for u/g states of the same cluster: except for their inversion parity, we expect these to have the same electronic structure in the ($J_A M_A J_B M_B$) coupling scheme, yet they have substantially different $\sum_{n''\in\Omega} \mid \widetilde{\mu}_{n'\rightarrow n''} \mid^2$ values. We find later that the differences in these sums reflect the different charge transfer transitions available to *gerade* and *ungerade* states even if they possess the same electronic configuration. Table 6.1 also shows that there can be large differences between the summed dipoles of states of different Ω, or the same Ω and different dissociation products (states from different clusters). While this is expected since the states will necessarily have differing

configurations, the differences are larger than anticipated in the separated atom scheme; we find in Section 6.4 that the field gradient due to the anionic charge drives changes in the cationic configurations as the nuclei approach (Chapter 3).

6.2.1 The transition moment, $M_{\alpha\beta}$

The clue to the relative transition dipole moments from different ion pair states when compared at the same interionic separation lies in the changing occupancy of the p_σ and p_π orbitals in the various JM_J states of the positive ion. Even for I^+, the Russell-Saunders coupling scheme gives the best zeroth order basis to describe the cationic wavefunction, though there is clear evidence of incipient jj coupling mainly through $^3P_2$ -$^1D_2$ and $^3P_0$ -$^1S_0$ mixing and we would also expect electrostatic interactions to couple cationic states in the presence of the anionic field gradient (see Chapter 3), however we shall use the Russell-Saunders configurations as the basis in which to discuss these perturbations. These Russell-Saunders configurations have been listed in Table 3.1 for ease of reference.

In this subsection we will derive formulae for both parallel and perpendicular transition moments from a given IP p^4p^6 microstate to its complementary valence p^5p^5 microstate. These predictions will then be combined with the experimental transition dipole moments to derive, where possible, the upper state electronic structure in terms of the usual superposition of basis configurations.

Parallel transitions

An IP→Valence transition involves the transfer of an electron from the anionic centre to the cationic. There are two electrons available for transfer, those on the anion corresponding to the two vacancies on the cation, and in the parallel case the transfer of both electrons is allowed. Thus the parallel transition moment will be the correctly phased sum of two $\pi \leftrightarrow \pi$ and/or $\sigma \leftrightarrow \sigma$ one electron transition moments. It is simpler to develop the theory using the complementary two electron problem where the anionic centre has two electrons and the cationic centre none, and the one electron spinorbitals in the IP states are denoted by

$|\ a\rangle(\equiv|\ m_l m_s\rangle_a)$, $|\ a'\rangle(\equiv|\ m'_l m'_s\rangle_a)$ on one centre, $|\ b\rangle$, $|\ b'\rangle$ on the other. The corresponding atomic orbitals in the valence states will be denoted by $|\ A\rangle$, etc. The symmetrised IP and valence atom pair microstates having $(m_l m_s)_a(m'_l m'_s)_b$ as good quantum numbers are then

$$\phi^{IP}_{g,u} = \frac{[\|aa'\| \pm \|bb'\|]}{[2(1 \pm S_{ab}S_{a'b'})]^{1/2}}; \qquad \phi^{V}_{g,u} = \frac{[\|AB'\| \mp \|A'B\|]}{[2(1 \pm S_{AB}S_{A'B'})]^{1/2}}, \tag{6.6}$$

where S_{ab} are the overlap integrals $\langle a|b\rangle$ etc, and the upper and lower results refer to g and u functions respectively.[1]

If the IP and valence states are connected by a parallel dipole transition, the orbitals $|\ a\rangle$ and $|\ B\rangle$ are connected by a parallel electron transfer between the two centres that conserves spin, m_s, and orbital angular momentum, m_l, so that Ω has the same value for the two states. The parallel transition dipole between the two states as described in equation (6.6) is therefore, to $\mathcal{O}(S_{ab})$,

$$\begin{aligned}\langle \phi^{IP}_{g,u} \mid \mu_z \mid \phi^{V}_{u,g}\rangle = \quad & \langle a \mid \mu_z \mid A\rangle S_{a'B'} + \langle a' \mid \mu_z \mid B'\rangle S_{aA} \\ & \mp[\langle a' \mid \mu_z \mid A'\rangle S_{aB} + \langle a \mid \mu_z \mid B\rangle S_{a'A'}],\end{aligned} \tag{6.8}$$

where the origin is at the bond centre so that $\langle a \mid \mu_z \mid A\rangle = -\langle b \mid \mu_z \mid B\rangle$ etc. We can now make the following important conclusion and begin to see how the sum of transition dipoles from a u/g pair can differ so markedly: if $|\ a\rangle$ and $|\ a'\rangle$ have the same $|m_l|$ value so that $S_{aB} = S_{a'B'}$ and $\langle a \mid \mu_z \mid B\rangle = \langle a' \mid \mu_z \mid B'\rangle$, then the $g \rightarrow u$ transition dipole is zero, irrespective of the spins.

Rewriting equation (6.8) to introduce the effective transition dipole for one electron transfer, $M_{\alpha\beta}$, we find

$$\langle \phi^{IP}_{g,u} \mid \mu_z \mid \phi^{V}_{u,g}\rangle = M_{a'B'}(R) \mp M_{aB}(R). \tag{6.9}$$

---

[1]The two types of wavefunction described in equation (6.6) are not quite orthogonal and to $\mathcal{O}(S_{ab})$

$$\langle \phi^{IP}_{g,u} | \phi^{V}_{g,u}\rangle = (S_{aB} \pm S_{a'B'})\langle a|A\rangle, \tag{6.7}$$

where the upper and lower results refer to g and u functions respectively and $\langle a|A\rangle$ $(= \langle b|B\rangle$ etc) represents the relaxation (from anionic to neutral) of the orbital as an electron is transferred between centres.

The operational definition for $M_{\alpha\beta}$ is found by including the two IP spinorbitals explicitly

$$\mu_z \|m_l m_s m_l' m_s'\|_a = M_{m_l' m_l'} \|(m_l)_A (m_l')_B\| - M_{m_l m_l} \|(m_l')_A (m_l)_B\|. \qquad (6.10)$$

Hence

$$\|(m_l m_s)_A (m_l' m_s')_B\| \mu_z \|m_l m_s m_l' m_s'\|_a = M_{m_l' m_l'}, \qquad (6.11)$$

which, when all inversion and normalisation terms have been included, is equivalent to equation (6.9). The sign difference in the two terms in equation (6.10) comes from preserving the canonical order in the Slater determinants (see Chapter 3). For parallel transitions electron transfer will either be $\sigma \leftrightarrow \sigma$ or $\pi \leftrightarrow \pi$ and the corresponding one electron dipole moments will be denoted $M_{\sigma\sigma}$ and $M_{\pi\pi}$. $M_{\pi\pi}$ remains positive at all separations, but $M_{\sigma\sigma}$ is negative at large R (adopting a right-handed coordinate system for both ionic centres), passes through zero at some intermediate R, then returns to zero at $R = 0$. In section 6.4 we find that around R_e^{IP}, the two integrals are still of opposite sign.

In the Russell-Saunders coupling scheme the p^4 configuration (Table 3.1) has three basic determinantal structures, each corresponding to different m_l orbital occupancy. Taking these in turn the parallel transition vector $\mu_z \mid JM_J\rangle$ gives

$$\mu_z P_{ab}^{\pm} \|1_a^\alpha \underline{1}_a^\beta\| = \begin{cases} 0 \\ 2M_{\pi\pi}[\|1_A^\alpha \underline{1}_B^\beta\| - \|\underline{1}_A^\beta 1_B^\alpha\|] \end{cases} \qquad (6.12)$$

$$\mu_z P_{ab}^{\pm} \|0_a^\alpha \underline{1}_a^\beta\| = \begin{cases} (M_{\pi\pi} - M_{\sigma\sigma})[\|0_A^\alpha \underline{1}_B^\beta\| + \|\underline{1}_A^\beta 0_B^\alpha\|] \\ (M_{\sigma\sigma} + M_{\pi\pi})[\|0_A^\alpha \underline{1}_B^\beta\| - \|\underline{1}_A^\beta 0_B^\alpha\|] \end{cases} \qquad (6.13)$$

$$\mu_z P_{ab}^{\pm} \|0_a^+ 0_a^-\| = \begin{cases} 0 \\ 2M_{\sigma\sigma}[\|0_A^+ 0_B^-\| - \|0_A^- 0_B^+\|] \end{cases} \qquad (6.14)$$

The permutation operator $P_{ab}^{\pm}$ interchanges the nuclear labels a and b and adds in the permuted structure with the indicated phase to produce the $g(+)$ or $u(-)$ wavefunctions. For the complementary 10 electron case the determinants on the left-hand side describe the two anionic electrons available for transfer, ie those corresponding to the vacancies on the cationic centre. The two alternatives in

equations (6.12)-(6.14) thus refer to IP(g) $\rightarrow$V(u) (upper transition moment) and IP(u) $\rightarrow$V(g) (lower) transitions respectively. The signs of the spins α and β are assigned to give the required M_J value of the cation and may be interchanged if this generates a new determinant; likewise the orbital angular momenta, m_l, may also be changed ($1 \leftrightarrow \underline{1}$). Thus $\mu_z P^{\pm}_{ab}\|0^-_a \underline{1}^-_a\|$ forms a part of the parallel transition moment from an $\Omega = 2$ IP state. It should be remembered when evaluating these relationships that each interchange of columns in the Slater determinant introduces a sign change in the wavefunction: conventionally the determinants are returned to their canonical order, $\|1^+1^-0^+0^-\underline{1}^+\underline{1}^-\|_a\|1^+1^-0^+0^-\underline{1}^+\underline{1}^-\|_b$, and electron transfer $A^- \rightarrow B^+$ has been taken to be positive.

It is clear from equations (6.12)-(6.14) that very large differences between $g \rightarrow u$ and $u \rightarrow g$ charge transfer transition dipoles can arise even if they have the same configuration, especially if the cation has mainly a p_σ^{-2} or p_π^{-2} vacancy configuration, or if $M_{\sigma\sigma} \simeq M_{\pi\pi}$ and the dominant vacancies are $p_\sigma^{-1}p_\pi^{-1}$. The mixing of ion pair and valence state configurations, which depends in part on the overlap described in equation (6.7) and their energy separation, does not affect the above results although the values of the various effective transfer dipoles $M_{\alpha\alpha}$ are modified.

Perpendicular transitions

The consequences of a perpendicular transition for the electronic structure of the IP state are somewhat different from the parallel case since either one, two or no electrons have allowed transitions. Therefore no general rules such as those in equations (6.12)-(6.14) can be generated for the perpendicular case and each configuration must be considered in turn. Thus

$$\mu_{+1} P^{\pm}_{ab}\|1^\alpha_a \underline{1}^\beta_a\| = M_{\sigma\pi}[\|1^\alpha_A 0^\beta_B\| \pm \|0^\beta_A 1^\alpha_B\|], \tag{6.15}$$

in which only one electron transfer is possible with $\Delta m_l = \pm 1$ and the value of m_s has no effect on the result, or

$$\mu_{+1} P^{\pm}_{ab}\|\underline{1}^+_a \underline{1}^-_a\| = M_{\sigma\pi}[(\|\underline{1}^+_A 0^-_B\| \pm \|0^-_A \underline{1}^+_B\|) - (\|\underline{1}^-_A 0^+_B\| \pm \|0^+_A \underline{1}^-_B\|)], \tag{6.16}$$

in which case two electrons can be transferred. In the case

$$\mu_{+1} P^{\pm}_{ab} \| 0^{\alpha}_{a} 1^{\beta}_{a} \| = -M_{\sigma\pi} [\pm \| 1^{\alpha}_{A} 1^{\beta}_{B} \| + \| 1^{\beta}_{A} 1^{\alpha}_{B} \|], \tag{6.17}$$

one electron can be transferred if $\alpha \neq \beta$ (ie for $\Omega = 1$ ion pair states whatever their inversion parity), but for $\alpha = \beta$, giving $\Omega = 0, 2$ ion pair states, one electron is transferable for $g \rightarrow u$ and none for $u \rightarrow g$. Similar conclusions are reached for perpendicular transitions with the polarisation in the opposite sense, ie μ_{-1}, thus the major differences found in the transition dipoles available to parallel transitions out of *ungerade* compared to *gerade* ion pair states are not found for perpendicular transitions. We therefore expect, and find, a much smaller spread in the experimental values for $\mu_{\perp}$.

6.2.2 The ion pair oscillator strength

Chapter 3 showed that any JM_J state of I^+, whatever the coupling scheme, can be written as a linear combination of the three basic determinantal structures $\Delta^{(4)}(ij)$ where i and j label the $|m_l|$ values of the two vacancies at the cationic centre and m_s is chosen to give the appropriate value of Ω:

$$| \Omega_{g,u} \rangle = P^{\pm}_{a,b} [c_{1g,u} \| p^1_{\sigma} p^3_{\pi} \| + c_{2g,u} \| p^2_{\sigma} p^2_{\pi} \| + c_{3g,u} \| p^4_{\pi} \|]_a \times \| p^2_{\sigma} p^4_{\pi} \|_b. \tag{6.18}$$

The dipole operator producing a charge transfer between ionic centres will create a linear combination of the p^{-1} determinantal products on the right-hand side of equations (6.12)-(6.14):

$$\mu_z \sum_{i,j} c_{ij}(n') P^{\pm}_{ab} \Delta^{(4)}_a \Delta^{(6)}_b = \sum_{i,j} c_{ij}(n') (M_{ii} \mp M_{jj}) P^{\pm}_{ab} [\Delta^{(5)}_A(i) \Delta^{(5)}_B(j)], \tag{6.19}$$

where the indices i and j run over all possible combinations of $m_l m_s$ and $m'_l m'_s$ vacancies in $\Delta^{(4)}$ compatible with Ω.

The actual lower states in the transition, the $X0^+_g(aa)$ or $B0^+_u(ab)$ states for example, will also be some linear combination of the 5 electron microstates on the right-hand side of equation (6.19). The detailed transition dipoles for the charge transfer transitions from a given ion pair state to any valence state will then be

given by the projection of the charge transfer part of the state vector $\mu_z \mid JM_J\rangle$ onto these orthogonal valence state eigenfunctions. Saute and Aubert-Frécon [28] have given the $(J_A M_A J_B M_B)$ description of these valence state eigenfunctions at dissociation (see Table 1.3) and discussed their perturbation at large $R(> 7\text{Å})$, but these functions will be unreliable for this work since they will be significantly mixed by $R_e^{IP} = 3.6\text{Å}$. However, if the strength of all charge transfer transitions from a given IP state are known (or at least those of the strongest transitions), then the sum of the squares of their transition dipoles at a given R is

$$\sum_{n'' \in \Omega} \langle IP_{g,u}(n') \mid \mu_z(R) \mid V_{u,g}(n'')\rangle^2 = \sum_{i,j} c_{ij}^2(n')[M_{ii} \mp M_{jj}]^2. \qquad (6.20)$$

Thus the effect of mixing of the valence states is eliminated and the summed transition dipoles from a given IP state, $\sum_{n'' \in \Omega} \mid \tilde{\mu}_{n' \to n''} \mid^2$, depends on the electronic configuration at the cationic centre and on the relevant $M_{\alpha\beta}$ integral. Thus these dipole sums (Table 6.1 column 7) can be interpreted to give the electronic structure at the cationic centre, and by implication the electronic structure of the IP state.

In the next section the experimental results are discussed in the light of this theory to derive the ion pair state electronic configurations around their R_e values. The discussion will mainly be concerned with parallel transitions moments.

6.3 The Ion Pair configurations

To a first approximation the electronic configuration of an IP state can be described by using the Russell-Saunders functions of their diabatic dissociation products in the $(J_A M_A J_B M_B)$ coupling scheme (see Chapter 3), that is neglecting the spin-orbit and intramolecular interactions. In the next section we shall derive the theoretical sum for the squares of the transition dipoles from these simple RS configurations, and find that although these RS functions still dominate the configurations around R_e^{IP}, the small spin-orbit and intramolecular components do significantly alter $\sum_{n'' \in \Omega} \mu_z^2(R)$. We shall discuss the effects of these refinements

to the IP configurations in the sections to follow, after first considering the pure Russell-Saunders functions.

6.3.1 Summed transition dipoles in the RS coupling scheme

In this section we treat the IP state's electronic wavefunction as a symmetrised product of the Russell-Saunders functions for the two separated ions (see Chapter 3): in later sections we will include the effects of spin-orbit coupling and then of the intramolecular interactions.

All the I^+ Russell-Saunders states are described as linear combinations of the $\|\ldots m_l m_s \ldots\|$ microstates as given in Table 3.1, without adjustable parameters. At this level of approximation we would describe the $\Omega = 2(1)$ state as

$$|\, 2_{g,u}(1)\rangle_{RS} = \frac{1}{\sqrt{2}}\{|\, {}^3P_{22}\rangle_a \,|\, {}^1S_{00}\rangle_b \pm |\, {}^1S_{00}\rangle_a \,|\, {}^3P_{22}\rangle_b\}, \tag{6.21}$$

since in the absence of spin-orbit interactions its ionic parents have RS configurations $|\, {}^3P_2\rangle$ and $|\, {}^1S_0\rangle$. Here the cationic configuration is

$$|\, {}^3P_{22}\rangle = \|1^+1^-0^+\underline{1}^+\|, \tag{6.22}$$

and the anionic is

$$|\, {}^1S_{00}\rangle = \|1^+1^-0^+0^-\underline{1}^+\underline{1}^-\|. \tag{6.23}$$

The electronic configurations forming the basis for the valence states (Table 1.3) are described in a similar manner, and so the $\Omega = 2$ state at the (aa) dissociation limit would be

$$|\, 2_{g,u}(aa)\rangle_{RS} = \frac{1}{\sqrt{2}}\{|\, {}^2P_{\frac{3}{2}\frac{3}{2}}\rangle_A \,|\, {}^2P_{\frac{3}{2}\frac{1}{2}}\rangle_B \mp |\, {}^2P_{\frac{3}{2}\frac{1}{2}}\rangle_A \,|\, {}^2P_{\frac{3}{2}\frac{3}{2}}\rangle_B\}, \tag{6.24}$$

with

$$|\, {}^2P_{\frac{3}{2}\frac{3}{2}}\rangle = \|1^+1^-0^+0^-\underline{1}^+\|, \tag{6.25}$$

and

$$|\, {}^2P_{\frac{3}{2}\frac{1}{2}}\rangle = \frac{1}{\sqrt{3}}[\|1^+1^-0^+0^-\underline{1}^-\| - \sqrt{2}\|1^+1^-0^+\underline{1}^+\underline{1}^-\|]. \tag{6.26}$$

It is now relatively straightforward to calculate the transition dipole connecting these two states

$$
\begin{aligned}
&\langle 2_{g,u}(1) \mid \mu_z \mid 2_{u,g}(aa)\rangle \qquad (6.27)\\
&= \tfrac{1}{2\sqrt{3}}[\langle \|1^+1^-0^+\underline{1}^+\|_a \|1^+1^-0^+0^-\underline{1}^+\underline{1}^-\|_b \mid \mu_z \mid \|1^+1^-0^+0^-\underline{1}^+\|_A \|1^+1^-0^+0^-\underline{1}^-\|_B\rangle]\\
&-\tfrac{1}{\sqrt{6}}[\langle \|1^+1^-0^+\underline{1}^+\|_a \|1^+1^-0^+0^-\underline{1}^+\underline{1}^-\|_b \mid \mu_z \mid \|1^+1^-0^+0^-\underline{1}^+\|_A \|1^+1^-0^+\underline{1}^+\underline{1}^-\|_B\rangle]\\
&\qquad\qquad +\ldots\\
&= -\tfrac{1}{\sqrt{6}}[\langle \|1^+1^-0^+\underline{1}^+\|_a \|1^+1^-0^+0^-\underline{1}^+\underline{1}^-\|_b \mid \mu_z \mid \|1^+1^-0^+0^-\underline{1}^+\|_A \|1^+1^-0^+\underline{1}^+\underline{1}^-\|_B\rangle]\\
&\qquad\qquad +\ldots\\
&\qquad \equiv -\tfrac{1}{\sqrt{6}}[\langle \|0^-\underline{1}^-\|_a \mid \mu_z \mid \|\underline{1}^+\|_A \|0^-\|_B\rangle]\\
&\qquad\qquad +\ldots\\
&\qquad\qquad = \mp\sqrt{\tfrac{2}{3}}[M_{\pi\pi} \mp M_{\sigma\sigma}]
\end{aligned}
$$

where the inversion terms have not been written out, and the partial antisymmetriser, $\mathcal{A}$, is assumed. The $\sqrt{\frac{2}{3}}$ coefficient is the projection of the $\mu_z \mid 2_{g,u}(1)\rangle$ charge transfer vector onto the $\mid 2_{u,g}(aa)\rangle$ valence basis function and reflects the extent that the appropriate microstate, in this case $\|0^-\underline{1}^-\|$, is present in the two configurations. Tables 6.2 and 6.3 give these coefficients for the major Russell-Saunders components of the nine IP states considered here.

When we consider the summed transition dipoles, $\sum_{n''\in\Omega} \mu_z^2(R)$, for all parallel transitions from a given ion pair state we remove the dependence on the valence state composition, and the sum depends solely on the upper state configuration. If we describe this configuration as a linear combination of the microstates in equations (6.12)-(6.14)

$$\mid \Omega_{g,u}\rangle = P^{\pm}_{a,b}[c_{1g,u}\|p^1_\sigma p^3_\pi\| + c_{2g,u}\|p^2_\sigma p^2_\pi\| + c_{3g,u}\|p^4_\pi\|]_a \times \|p^2_\sigma p^4_\pi\|_b, \qquad (6.28)$$

then, in the RS scheme, the $2_{g,u}(1)$ states above would have $c_{1g,u} = 1$, and $c_{2g,u} = c_{3g,u} = 0$. Table 6.4 gives these coefficients for the ten possible Russell-Saunders configurations. Since no intramolecular interactions are considered at this level of approximation there is no difference in the orbital occupancy of

Valence	$I^+(^3P_2)I^-(^1S_0)$ RS Ion Pair states						$I^+(^3P_{1,0})I^-(^1S_0)$		
n''	$0_g^+(1)$	$0_u^+(1)$	$1_g(1)$	$1_u(1)$	$2_g(1)$	$2_u(1)$	$0_g^+(2)$	$0_u^+(2)$	$1_u(2)$
0_g^+		$\frac{-2}{3\sqrt{3}}, \frac{-1}{3\sqrt{3}}$		$[\frac{1}{2}]$				$\frac{4}{3\sqrt{6}}, \frac{-1}{3\sqrt{6}}$	$[\frac{1}{6}]$
0_g^+		$0, \frac{-1}{\sqrt{3}}$		$[\frac{1}{2}]$				$0, \frac{-1}{\sqrt{6}}$	$[\frac{-1}{2}]$
0_u^-			$[\frac{1}{2}]$						
0_u^-			$[\frac{-5}{6}]$						
1_g		$[\frac{1}{\sqrt{2}}]$		$\frac{-1}{\sqrt{6}}, \frac{-1}{\sqrt{6}}$		$[\frac{1}{\sqrt{3}}]$		$[0]$	$\frac{1}{\sqrt{6}}, \frac{-1}{\sqrt{6}}$
1_u	$[\frac{1}{3\sqrt{2}}]$		$\frac{1}{\sqrt{6}}$		$[\frac{1}{\sqrt{3}}]$		$[\frac{2}{3}]$		
1_u	$[\frac{-5}{3\sqrt{3}}]$		$\frac{-1}{3}$		$[\frac{4}{3\sqrt{2}}]$		$[\frac{2\sqrt{2}}{3\sqrt{3}}]$		
2_g				$[\frac{-1}{\sqrt{3}}]$		$\sqrt{\frac{2}{3}}, 0$			$[\frac{-1}{\sqrt{3}}]$
2_u			$[\frac{-2}{\sqrt{3}}]$		$-\sqrt{\frac{2}{3}}$				
3_u					$[-\sqrt{2}]$				
0_g^+		$\frac{1}{3\sqrt{3}}, \frac{2}{3\sqrt{3}}$		$[\frac{-1}{2}]$				$\frac{-2}{3\sqrt{6}}, \frac{2}{3\sqrt{6}}$	$[\frac{1}{6}]$
0_g^-				$[\frac{-1}{2}]$					$[\frac{-1}{2}]$
0_u^+	$\frac{1}{\sqrt{3}}$		$[\frac{1}{2}]$				$\sqrt{\frac{-2}{3}}$		
0_u^-			$[\frac{-5}{6}]$						
1_g		$[0]$		$\frac{-1}{\sqrt{12}}, \frac{1}{\sqrt{3}}$		$[-\sqrt{\frac{2}{3}}]$		$[\frac{1}{\sqrt{2}}]$	$\frac{1}{\sqrt{12}}, \frac{1}{\sqrt{6}}$
1_g		$[\frac{1}{\sqrt{3}}]$		$\frac{-1}{2}, 0$		$[0]$		$[\frac{1}{\sqrt{6}}]$	$\frac{1}{2}, 0$
1_u	$[\frac{2}{3}]$		$\frac{1}{\sqrt{12}}$		$[-\sqrt{\frac{2}{3}}]$		$[\frac{-1}{3\sqrt{2}}]$		
1_u	$[\frac{-1}{3\sqrt{3}}]$		$\frac{-1}{6}$		$[\frac{-4}{3\sqrt{2}}]$		$[\frac{-1}{3\sqrt{6}}]$		
2_g				$[\frac{1}{\sqrt{6}}]$		$\frac{-1}{\sqrt{3}}, 0$			$[\frac{1}{\sqrt{6}}]$
2_u			$[\frac{-1}{\sqrt{6}}]$		$\frac{1}{\sqrt{3}}$				
0_g^+		$\frac{-2}{3\sqrt{3}}, \frac{2}{3\sqrt{3}}$		$[0]$				$\frac{4}{3\sqrt{6}}, \frac{2}{3\sqrt{6}}$	$[\frac{2}{3}]$
0_u^-			$[\frac{-1}{3}]$						
1_u	$[\frac{-1}{3\sqrt{3}}]$		$\frac{1}{3}$		$[\frac{4}{3\sqrt{2}}]$		$[\frac{8}{3\sqrt{6}}]$		

Table 6.2. Amplitudes for the transition dipoles from the major spin-orbit components of the lowest nine IP states. The values are the appropriate coefficient for the microstates present in the two configurations involved: where two entries are given the first is for the $\|0_a^\alpha 1_a^\beta\|$ microstate and should be multiplied by $(M_{\pi\pi} + M_{\sigma\sigma})$, the second for the $\|1_a^\alpha 1_a^\beta\|$ microstate and should be multiplied by $2M_{\pi\pi}$. Values in brackets are for perpendicular transitions and should be multiplied by $M_{\sigma\pi}$.The ordering of the valence states is the same as Table 1.3; the Ω degeneracy of electronic states has not been included.

u/g pairs, and we can now demonstrate the inadequacy of the RS scheme for describing the ion pair wavefunction.

Analysing the four *gerade* states $D'2_g(1)$, $\beta 1_g(1)$, $E0_g^+(1)$ and $f0_g^+(2)$, we see from equations (6.12)-(6.14) that their parallel transition moments depend only on the coefficient c_1^2 of the $\|p_\sigma^1 p_\pi^3\|$ microstate since they have the $|M_{\pi\pi} - M_{\sigma\sigma}|$ term in common. The ratio of the c_1^2 coefficients for the four states under Russell-Saunders coupling is 1 : 0.5 : 0.33 : 0.66 while the observed ratios for $\sum_{n'' \in \Omega} \mu_z^2(R)$ are 1 : 0.780 : 0.516 : 0.511. The discrepancy between the $E0_g^+(1)$ and $f0_g^+(2)$ states is particularly significant: these have only the one valence state available for a parallel transition, the $B0_u^+(ab)$ state, so there is no chance that a missing transition could distort the experimental result for $\sum_{n'' \in \Omega} \mu_z^2(R)$. It is clear that the RS coupling scheme does not give a sufficiently subtle description of the ion pair configuration. The breakdown of this scheme for I_2 has been discussed in Chapter 3, and in the remaining sections we shall apply the eigenfunctions derived there to improve the predictions for $\sum_{n'' \in \Omega} \mu_z^2(R)$.

6.3.2 Breakdown of the RS scheme: spin-orbit coupling

The free ion I^+ clearly has a significant degree of jj mixing since it shows an anomalous ordering of the ground ^3P_J multiplet [42, p.108] and we now include this interaction to improve our description of the IP configuration.

If free from perturbations the intervals between the cationic terms can be fitted by two parameters, ζ_{5p}, the spin-orbit interaction for a valence electron in a 5p orbital, and F_2 the Coulomb repulsion between the 5p electrons [41]. It proves impossible to reproduce the 5 I^+ term values in this over-determined case (see Chapter 3), however on leaving the $^1S_0$ term out of the fit, the remaining terms are successfully reproduced and the effects of the spin-orbit coupling on the free ion configurations can be found: the interaction mixes $^3P_2$ with $^1D_2$ and $^3P_0$ and $^1S_0$ configurations, leaving the dominant RS component with a coefficient of approximately 0.9, see Table 3.3.

As the IP states exhibit a strong tendency to cluster with other states of the

Valence	$I^+(^1D_2)I^-(^1S_0)$ RS Ion Pair states						$I^+(^1S_0)I^-(^1S_0)$	
n''	$0_g^+(3)$	$0_u^+(3)$	$1_g(3)$	$1_u(3)$	$2_g(3)$	$2_u(3)$	$0_g^+(4)$	$0_u^+(4)$
0_g^+		$\frac{4}{3\sqrt{6}}, \frac{-1}{3\sqrt{6}}$						$\frac{2}{3\sqrt{3}}, \frac{1}{3\sqrt{3}}$
0_g^+		$0, \frac{1}{\sqrt{6}}$						$0, \frac{-1}{\sqrt{3}}$
1_g				$\frac{1}{\sqrt{3}}$				
1_u			$\frac{-1}{\sqrt{3}}$					
1_u			$\frac{\sqrt{-2}}{3}$					
2_g						$\frac{-1}{\sqrt{3}}$		
2_u					0			
0_g^+		$\frac{4}{3\sqrt{6}}, \frac{2}{3\sqrt{6}}$						$\frac{2}{3\sqrt{2}}, \frac{-2}{3\sqrt{3}}$
0_u^+	0						0	
1_g				$\frac{1}{\sqrt{6}}$				
1_g				$\frac{-1}{\sqrt{2}}$				
1_u			$\frac{-1}{\sqrt{6}}$					
1_u			$\frac{-1}{3\sqrt{2}}$					
2_g						$-\sqrt{\frac{2}{3}}$		
2_u					0			
0_g^+		$\frac{-2}{3\sqrt{6}}, \frac{2}{3\sqrt{6}}$						$\frac{-1}{3\sqrt{3}}, \frac{-2}{3\sqrt{3}}$
1_u			$\frac{\sqrt{2}}{3}$					

Table 6.3. Amplitudes for the parallel transition dipoles from the minor spin-orbit components of the nine lowest IP states. The values are the appropriate coefficient for the microstates present in the two configurations involved: where two entries are given the first is for the $\|0_a^+ 0_a^-\|$ microstate and should be multiplied by $2M_{\sigma\sigma}$, the second for the $\|1_a^\alpha 1_a^\beta\|$ microstate and should be multiplied by $2M_{\pi\pi}$. The ordering of the valence states is the same as Table 1.3; the Ω degeneracy of electronic states has not been included.

RS State $I^-(^1S_0)$ and I^+	c_1^2	c_2^2	c_3^2
$^3P_{22}$	1	0	0
$^3P_{21}$	0.5	0.5	0
$^3P_{20}$	0.33	0.66	0
$^3P_{00}$	0.66	0.33	0
$^3P_{11}$	0.5	0.5	0
$^3P_{10}$	1	0	0
$^1D_{22}$	0	1	0
$^1D_{21}$	1	0	0
$^1D_{20}$	0	0.33	0.66
$^1S_{00}$	0	0.66	0.33

Table 6.4. c_i^2 coefficients for the Russell-Saunders p^4 configurations

same ionic parentage, even down to R_e, and the clusters themselves are separated by a similar energy gap as that between their dissociation products, we might expect the spin-orbit coupling at the cationic centres in the IP wavefunction, in low v, to be close to that of the free ion. We therefore use the cationic configurations of Table 3.3 to form our molecular wavefunction over this range of R, neglecting the effects of intramolecular interactions. The inclusion of the spin-orbit interaction changes the c_i^2 coefficients in the cationic, and therefore molecular, configuration (Table 6.5).

Even with the inclusion of spin-orbit coupling we cannot account for the observed values for the summed transition dipoles, $\sum_{n'' \in \Omega} \mu_z^2(R_e^{IP})$. If we concentrate on the four *gerade* states once more, the $\|p_\sigma^1 p_\pi^3\|$ content is little changed and the predicted ratios turn out to be 1:0.607:0.334:0.619; the discrepancies, particularly between the $E0_g^+(1)$ and $f0_g^+(2)$ states, remain. The reconciliation of the experimental results with the theory must therefore lie in the degree of

JM state[a]	c_1^2	c_2^2	c_3^2
$\|\, 2_{g,u}(1)\rangle$	0.902	0.098	0
$\|\, 1_{g,u}(1)\rangle$	0.548	0.452	0
$\|\, 0^+_{g,u}(1)\rangle$	0.301	0.634	0.065
$\|\, 0^+_{g,u}(2)\rangle$	0.558	0.387	0.055
$\|\, 1_{g,u}(2)\rangle$	0.5	0.5	0
$\|\, 0^-_{g,u}(2)\rangle$	1	0	0
$\|\, 2_{g,u}(3)\rangle$	0.098	0.902	0
$\|\, 1_{g,u}(3)\rangle$	0.935	0.065	0
$\|\, 0^+_{g,u}(3)\rangle$	0.032	0.366	0.602
$\|\, 0^+_{g,u}(4)\rangle$	0.109	0.612	0.278

[a] equation (6.18)

Table 6.5. c_i^2 coefficients after partial jj coupling at I^+.

intramolecular interaction between the two ionic centres, ie on the breakdown of the $(J_A M_A J_B M_B)$ scheme itself.

6.4 Interpreting the IP→Valence transition dipoles

Although quantitative values for the configuration mixing coefficients are subject to assumptions about the composition of the $\Omega = 2(1)$ states, and of the change in the transition moments $M_{\alpha\beta}$ as a function of R, qualitative conclusions can be reached concerning the change in electronic structure of the IP states as they approach R_e. The relative strengths of the $M_{\alpha\beta}$ integrals can also be derived. The reconciliation of these conclusions with the experimental results of other groups studying hyperfine interactions and heterogeneous coupling in the IP states will be discussed in later sections.

6.4.1 The $M_{\alpha\beta}$ integrals

The parallel transition moments: $M_{\sigma\sigma}$ and $M_{\pi\pi}$

The primary intramolecular interaction in the IP states, after the Coulombic attraction between the opposite charges of the two ions, is an r^{-3} charge-quadrupole coupling. This mixes cationic states of the same spin multiplicity and M_J, and so will not couple the $^3P_{22}$ and $^1D_{22}$ RS states. Each has a diagonal matrix element in the charge-quadrupole coupling matrix however, with the $^1D_{22}$ configuration having the larger positive interaction on account of its higher p_σ occupancy (Chapter 3). Since the $^1D_{22}$ RS configuration also has a larger inter-electron repulsion, being a singlet state, the charge-quadrupole coupling will reduce the spin-orbit components of the $\Omega = 2$ IP states and a sufficiently large interaction would completely uncouple the spin-orbit interaction. However at these internuclear separations the strength of intramolecular interaction will be small, and

consequently we can assume that they adopt essentially their spin-orbit configuration at the cationic centre even near R_e.[2] We can therefore use the u/g ratio of the summed dipoles for parallel transitions from the two $\Omega = 2(1)$ states to derive values for the $M_{\sigma\sigma}$ and $M_{\pi\pi}$ integrals.

From equations (6.12)-(6.14) we find

$$\frac{\sum_{n''}\langle \delta 2_u(1) \mid \mu_z \mid V : 2_g(n'')\rangle^2}{\sum_{n''}\langle D'2_g(1) \mid \mu_z \mid V : 2_u(n'')\rangle^2} = \frac{c_1^2[M_{\sigma\sigma}(R_e) + M_{\pi\pi}(R_e)]^2 + c_2^2[2M_{\pi\pi}]^2}{c_1^2[M_{\pi\pi}(R_e) - M_{\sigma\sigma}(R_e)]^2}, \tag{6.29}$$

with $c_1^2 = 0.902$ and $c_2^2 = 0.098$. Since the observed summed dipole for the $D'2_g(1)$ state is greater than that for the $\delta 2_u(1)$ state, it is clear that the two integrals $M_{\sigma\sigma}$ and $M_{\pi\pi}$ must take opposite signs at this R. On substituting the observed values for $\sum_{n''\in\Omega=2} \mid \tilde{\mu} \mid^2$ we find that $M_{\sigma\sigma} = -0.731$eÅ and $M_{\pi\pi} = 0.190$eÅ, where the signs of the integrals have been chosen to agree with the negative $\langle \sigma_a | \sigma_b \rangle$ overlap integral in a right-handed axis set.

The c_1^2 coefficients we have taken for these states are consistent with the *ab initio* calculations published by Li and Balasubramanian who found $c_1^2 = 0.95$ for the $D'2_g(1)$ state at $R = 3.75$Å [118]. The $M_{\alpha\alpha}$ integrals are not particularly sensitive to the choice of c_i coefficients, for example the pure RS configurations with $c_1 = 1$ and $c_2 = c_3 = 0$ give values of -0.700eÅ and 0.173eÅ respectively, and our assumption for the 2(1) electronic configurations is not too critical. However we have assumed that the two sets of transition moments were recorded at the same R, and the $\delta 2_u(1)$ state is the one state in the first IP cluster to have an anomalously large R_e: we should take this into consideration before deriving final values for $M_{\alpha\alpha}$.

King *et al* suggested a value in the region of 4.0Å [34], though the theoretical work of Jaffe gave 3.77Å [19] for R_e^{δ}. This latter figure is consistent with results from this laboratory [143]: the OODR pumping scheme for the $\delta 2_u(1)$ state uses

[2]The charge-quadrupole interaction predicted for these states at R_e leads to only a 3% change from the spin-orbit configuration at the cationic centre, assuming a point charge model at both centres. It would be preferable to use the unique $0^-_{u/g}$ pair in the second cluster since these remain pure RS states even in the presence of spin-orbit coupling and the charge-quadrupole interaction, however only the $g0^-_g(2)$ state has been observed spectroscopically (see Table 1.4).

the $B \sim c$ coupled intermediate state (see Section 4.3) and the Franck-Condon factors for a perpendicular transition from this state are much too weak for the larger R_e. We shall therefore take R_e^δ as having the value 3.77Å, ie about 4% longer than the other states in the first cluster. Ishiwata *et al* have reported the R_e value of the equivalent state in Br_2 excited through its heterogeneous interaction with the $1_u(1)$ state [142] and for this halogen too the $\delta 2_u(1)$ state appears to have an anomalously large R_e value, this time about 5% larger.

Returning to the two electron model we used earlier in discussions of the transition dipole moment, we find from equation (6.8) that the $M_{\alpha\alpha}$ integral comprises of two terms:

$$\begin{aligned}\langle \phi^{IP}_{g,u} \mid \mu_z \mid \phi^{V}_{u,g} \rangle &= \langle a \mid \mu_z \mid A \rangle S_{a'B'} + \langle a' \mid \mu_z \mid B' \rangle S_{aA} \\ &\quad \mp [\langle a' \mid \mu_z \mid A' \rangle S_{aB} + \langle a \mid \mu_z \mid B \rangle S_{a'A'}] \\ &= M_{\alpha\alpha} \mp M_{\beta\beta}, \end{aligned} \tag{6.30}$$

one a one-centre transition dipole multiplied by a two-centre overlap integral and the other a two-centre dipole multiplied by a one-centre overlap integral. It should be remembered that the orbitals in each integral are associated with anionic and neutral centres and so are not translationally equivalent. However if they were $\langle a' \mid \mu_z \mid B' \rangle$ would be identically zero and we see that the strength of the $M_{\alpha\alpha}$ integrals derives from the one-centre dipole; the increased overlap of the p_σ orbitals when compared with the p_π in the two-centre terms gives the $M_{\sigma\sigma}$ integral a larger value than the $M_{\pi\pi}$.

If we neglect the two-centre transition dipole, then the expression for $M_{\alpha\alpha}$ simplifies to

$$M_{\alpha\alpha} = \langle a \mid \mu_z \mid A \rangle S_{a'B'} \sim \frac{1}{2} eRS_{a'B'}. \tag{6.31}$$

Calculating the overlap integrals from Huzinaga's Gaussian basis sets [43], we can estimate how the change in R_e between the two $\Omega = 2(1)$ states affects the transition dipole moments $M_{\sigma\sigma}$ and $M_{\pi\pi}$. Huzinaga's bases may not be reliable at such large R, however the calculations suggest the overlap integral $\langle \sigma_a | \sigma_A \rangle$ is reduced by about 10%, and $\langle \pi_a | \pi_A \rangle$ by as much as 20%, between the two

R_e values. When we include this and the change in R in equation (6.31), then $M_{\sigma\sigma}(\delta) \approx 0.94 M_{\sigma\sigma}(D')$ and $M_{\pi\pi}(\delta) \approx 0.83 M_{\pi\pi}(D')$. Substituting these values in equation (6.29) we find $M_{\sigma\sigma} = -0.739\text{eÅ}$ and $M_{\pi\pi} = 0.181\text{eÅ}$ at $R_e^{D'}$.

The perpendicular transition moment: $M_{\sigma\pi}$

The sum over all final states for the squared dipole moments of perpendicular transitions from $\Omega = 0 \rightarrow 1$ is

$$\sum_{n'' \in \Omega=1} | \tilde{\mu}_{u \rightarrow g} |^2 = [\frac{1}{2} c_{1,u}^2 + c_{2,u}^2 + 4 c_{3,u}^2] M_{\sigma\pi}^2, \tag{6.32}$$

and for $g \rightarrow u$ transitions

$$\sum_{n'' \in \Omega=1} | \tilde{\mu}_{g \rightarrow u} |^2 = [\frac{3}{2} c_{1,u}^2 + c_{2,u}^2 + 4 c_{3,u}^2] M_{\sigma\pi}^2. \tag{6.33}$$

Observing perpendicular transitions from the $E0_g^+(1)$ and $f0_g^+(2)$ states but not from their *ungerade* partners is consistent with these predictions if the $\|p_\sigma^1 p_\pi^3\|$ component dominates the configurations. However only the strongest perpendicular transitions are detectable and only then if they are not swamped by the stronger parallel systems so we may simply have overlooked fluorescence from the $D0_u^+(1)$ and $F0_u^+(2)$ states. The complete manifold of perpendicular transitions has not been observed for any of the IP states, so $\sum_{n'' \in \Omega=1} | \tilde{\mu}_\perp |^2$ is unavailable, however we can set a lower limit for $M_{\sigma\pi}$ using the A-coefficients from the $E0_g^+(1)$ state system: we find $M_{\sigma\pi} > 7 \times 10^{-2}\text{eÅ}$ using the c_1^2 coefficient derived in the next section.

6.4.2 Intramolecular interactions: the IP configurations

The $\gamma 1_u(1)$ and $H1_u(2)$ states

Like the $\delta 2_u(1)$ and $D'2_g(1)$ states, the $\Omega = 1$ states are composed of only two of the three types of $\Delta^{(4)}$ microstate: $\|p_\sigma^1 p_\pi^3\|$ and $\|p_\sigma^2 p_\pi^2\|$, however in this case the charge-quadrupole interaction couples the $^3P_{21}$ and $^3P_{11}$ RS configurations and we must use the values for the $M_{\sigma\sigma}$ and $M_{\pi\pi}$ integrals derived in the previous

section to determine the extent of interaction. The $\gamma 1_u(1)$ and $H1_u(2)$ states have slightly larger R_e values than the $D'2_g(1)$ state and we need to allow for the consequent changes in $M_{\alpha\alpha}$: similar calculations to those above suggest that only the smaller $M_{\pi\pi}$ integral is significantly reduced (to about 0.93 of the value at $R_e^{D'}$) at the larger R_e value of the $\gamma 1_u(1)$ state. We shall use the adjusted values for $M_{\alpha\alpha}$ in the following calculations.

The summed transition dipoles for the $\gamma 1_u(1)$ state give

$$\sum_{n'' \in \Omega=1} | \tilde{\mu}_{u \rightarrow g} |^2 = c_{1,u}^2 [M_{\sigma\sigma}(R_e) + M_{\pi\pi}(R_e)]^2 + c_{2,u}^2 [2M_{\pi\pi}]^2, \qquad (6.34)$$

and the value of the coefficients can be determined completely because of the normalisation condition, $c_{1,u}^2 + c_{2,u}^2 = 1$; we obtain $c_{1,u}^2 = 0.867$ and $c_{2,u}^2 = 0.133$ (if the $M_{\alpha\alpha}$ integrals are not adjusted we find $c_{1,u}^2 = 0.844$ and $c_{2,u}^2 = 0.156$). The same equation holds for the $H1_u(2)$ state and in this case we find $c_{1,u}^2 = 0.555$ and $c_{2,u}^2 = 0.445$.

The $H1_u(2)$ state therefore has c_i coefficients close to those of the free cation, $c_{1,u}^2 = 0.548$ and $c_{2,u}^2 = 0.452$. This disagrees with the *ab initio* results of Li *et al* which gave c_1^2 as high as 0.88 by $R = 4.0$Å, however their $H1_u(2)$ state has a significantly larger R_e than found experimentally and is already close to the MO configuration it adopts at small R, 1342.

The values for the $\gamma 1_u(1)$ state give close to a pure $\|p_\sigma^1 p_\pi^3\| \|p_\sigma^2 p_\pi^4\|$ configuration: the state has adopted some combination of the 1342 and 1432 MO configurations. At smaller R the $\gamma 1_u(1)$ state adopts a 2332 configuration [118] (see Table 1.2), ie $\|p_\sigma^2 p_\pi^2\| \|p_\sigma^2 p_\pi^4\|$ occupancy, which implies a $\frac{1}{\sqrt{2}}\{|\,^3P_{21}\rangle + |\,^3P_{11}\rangle\}$ configuration at the cationic centre: the spin-orbit interaction has been completely uncoupled in the presence of the strong Stark field of the anion.

We are finding that around $R = 3.6$Å, the final MO ordering has yet to be established and the lowest IP states of each symmetry achieve their low energy configurations by minimising the number of p_σ orbitals occupied since these have a larger quadrupole interaction with the anionic charge than the p_π. This stabilisation in the presence of the anionic charge will be balanced against the larger inter-electron repulsion energies and weak spin-orbit interactions in some of the

microstates with low p_σ occupancy. For the $\Omega = 1$ states, both the $\|p_\sigma^1 p_\pi^3\|$ and $\|p_\sigma^2 p_\pi^2\|$ configurations have the same number of electrons occupying the same space orbital, and so are likely to have similar inter-electron repulsion energies, though that of the $\|p_\sigma^2 p_\pi^2\|$ may be slightly higher from interactions with electrons at the anionic centre. Consequently we would expect the intramolecular charge-quadrupole interaction to reduce the c_2^2 component in favour of the c_1^2 in the low energy IP states of a given symmetry, as has been found above.

The $\beta 1_g(1)$ state

We can find the value of the c_1^2 coefficient for the $\beta 1_g(1)$ state since it determines the summed transition dipole uniquely:

$$\sum_{n'' \in \Omega=1} | \tilde{\mu}_{g \to u} |^2 = c_1^2 [M_{\pi\pi}(R_e) - M_{\sigma\sigma}(R_e)]^2. \tag{6.35}$$

However the observed value for $\sum_{n'' \in \Omega=1} | \tilde{\mu}_{g \to u} |^2$ is not sufficiently well known as fluorescence to the $1_u(bb)$ state was not recorded and it is uncertain what contribution this would make to the sum. Using the value of $\sum_{n'' \in \Omega=1} | \tilde{\mu}_{g \to u} |^2$ for the states observed, ie assuming a negligible contribution from the $\beta 1_g(1) \to 1_u(bb)$ transition, we find $c_1^2 = 0.703$ and so $c_2^2 = 0.297$. Li and Balasubramanian were unable to make a convincing assignment for the $\beta 1_g(1)$ configuration from their calculations [118] though a 1_g state at approximately the correct energy is assigned $c_2^2 = 0.89$ for $R = 3.75$Å. This is in complete disagreement with our results and even including an estimate for fluorescence to the $1_u(bb)$ state in our calculation only increases the c_1^2 coefficient. Although no definitive conclusions can be reached about the $\beta 1_g(1)$ state configuration at R_e, it is clear from our results that as with the $\gamma 1_u(1)$ state, the $\|p_\sigma^1 p_\pi^3\|$ component is considerably enhanced over the $\|p_\sigma^2 p_\pi^2\|$ when compared with the free ion configuration, $c_1^2 = 0.548$ and $c_2^2 = 0.452$. Again this reflects the drive to minimise the number of p_σ electrons to achieve a lower energy configuration in the presence of the anionic charge.

The $\Omega = 0$ states

The two $\Omega = 0^+_{u,g}$ pairs in Table 6.1 cannot be analysed quite so completely since all three of the $\Delta^{(4)}$ microstates are present in their molecular configurations after jj mixing.

The sum of the parallel transition dipoles for the $u \rightarrow g$ transitions becomes

$$\sum_{n'' \in \Omega=0} | \tilde{\mu}_{u \rightarrow g} |^2 = c^2_{1,u}[M_{\sigma\sigma}(R_e) + M_{\pi\pi}(R_e)]^2 + c^2_{2,u}[2M_{\pi\pi}]^2 + c^2_{3,u}[2M_{\sigma\sigma}]^2. \quad (6.36)$$

The c_3 coefficient in the final term of equation (6.36) can have a significant effect on the sum since the transition dipole moment, $2M_{\sigma\sigma}$, is the largest of the two electron transition moments, $4M^2_{\sigma\sigma} \approx 2.2e^2\text{Å}^2$ whereas the next largest $[M_{\pi\pi} - M_{\sigma\sigma}]^2$ is approximately $0.85e^2\text{Å}^2$. The lifetimes of the $\Omega = 0^+_u$ states in the first and second cluster will therefore be particularly sensitive to the degree of spin-orbit coupling since the c_3 coefficient is only present in the $|\ ^1D_{20}\rangle$ and $|\ ^1S_{00}\rangle$ RS states. The effect is not so important for the other states in the first two clusters as the $\|p^4_\pi\|$ configuration is not available for their charge transfer transitions.

The sum of the transition dipoles for the *gerade* states is once more equation (6.35), and we can use this to calculate the c^2_1 component for the $E0^+_g(1)$ and $f0^+_g(2)$ states as the $M_{\alpha\alpha}$ integrals do not change significantly over the small variations in R_e: we find $c^2_{1,g} = 0.466$ and 0.461 respectively. If we now assume the $E0^+_g(1)$ and $D0^+_u(1)$ states have the same composition we can determine the complete electronic structure from the observed value of $\sum_{n'' \in \Omega=0} | \tilde{\mu}_{u \rightarrow g} |^2$ for the D state. This gives $c^2_{1,g} = 0.466$, $c^2_{2,g} = 0.444$ and $c^2_{3,g} = 0.090$ (including an estimate for the unknown fluorescence to the $0^+_g(bb)$ state will increase the c^2_3 component at the expense of the c^2_2). There is an appreciable $\|p^4_\pi\|$ component to the configuration, and once again we find a considerable enhancement in the p_π occupancy over the p_σ when compared with the free-ion composition ($c^2_{1,g} = 0.301$, $c^2_{2,g} = 0.634$ and $c^2_{3,g} = 0.065$). However the microstate with lowest p_σ occupancy, $\|p^4_\pi\|$, also has a high degree of inter-electron repulsion and so the extent to which

it is adopted by the lowest $0^+_{u/g}$ state will reflect the balance between the inter-electron repulsion and the charge-quadrupole interaction.

Li and Balasubramanian found a large difference between the $E0^+_g(1)$ and $D0^+_u(1)$ state configurations at $R = 3.75$Å [118]: for the $E0^+_g(1)$ state they found $c_1^2 = 0.95$ and for the $D0^+_u(1)$ $c_2^2 = 0.88$. This is surprising in the light of the close clustering of these states and their common ionic parentage: it is not clear from [118] whether the *ab initio* calculations were able to reproduce this clustering. Although we expect the $D0^+_u(1)$ and $E0^+_g(1)$ states to have similar electronic configurations, until the orbital overlap between centres draws out their differing MO states at small R, they are not expected to show the same transition dipole strengths: the $\|p^4_\pi\|$ component, which is expected to increase in the presence of the anionic field, is only active for charge transfer transitions from *ungerade* IP states (equation (6.12)). Consequently only the fluorescence from the $D0^+_u(1)$ state will gain strength from the large the contribution of the $4M^2_{\sigma\sigma}$, ie c_3^2, component (cf the $F0^+_u(2)$ state below).

A similar proceedure for the $f0^+_g(2)$ and $F0^+_u(2)$ states gives $c^2_{1,g} = 0.461$, $c^2_{2,g} = 0.351$ and $c^2_{3,g} = 0.188$, compared to $c^2_{1,g} = 0.558$, $c^2_{2,g} = 0.387$ and $c^2_{3,g} = 0.055$ in the free ion. Li and Balasubramanian also find considerable enhancement of the $\|p^4_\pi\|$ component though they assign both states to singlet structures around R_e [118]. This must surely be incorrect because the singlet cationic configurations can only arise in the second cluster through the spin-orbit interaction and the $^3P_{00}$ configurations should continue to dominate the $\Omega = 0^+_{u,g}(2)$ configurations at these R; the dominant (triplet) MO configurations will only develop at much smaller separations (see Chapter 7).

One of the most striking features of the ion pair lifetimes reported in Chapter 5 is the short lifetime of the $F0^+_u(2)$ state. This can now be attributed to the enhanced $\|p^4_\pi\|$ component, which contributes almost 70% of the total dipole strength although forming less than 20% of the electronic configuration. The electronic structure of the $F0^+_u(2)$ state around R_e reveals the emergence of a 1441 occupancy (equivalent to $\|p^0_\sigma p^4_\pi\|\|p^2_\sigma p^4_\pi\|$ in the $(J_A M_A J_B M_B)$ scheme), which has

a strong one-electron transition to the ground state configuration, 2440. The 1441 configuration is adopted by the $D0_u^+(1)$ state at smaller separations and we would therefore expect corresponding changes in the $F \rightarrow X$ and $D \rightarrow X$ transition dipole functions as the internuclear separation reached $R \approx R_e^X$ (see Chapter 7). The $F0_u^+(2)$ state appears to adopt more $\|p_\sigma^0 p_\pi^4\|$ component than the $D0_u^+(1)$ state in the presence of the charge-quadrupole interaction, suggesting that the increased inter-electron repulsion of this configuration is not sufficiently compensated for by its negative charge-quadrupole energy at these R to be adopted by the lowest energy state. However a discussion of the u/g splittings between the IP states (Appendix A) suggests that the c_3^2 coefficient is under-estimated here for the $D0_u^+(1)$ state due to the missing fluorescence to the third valence limit.

The intramolecular electronic charge-quadrupole interaction

In Chapter 3 we discussed the interaction between the electronic quadrupole at the cationic centre and the field gradient due to the anionic charge, and were able to predict the degree of mixing of RS states at the cationic centre assuming a point charge model at the two centres. This charge-quadrupole interaction favours p_π over p_σ occupancy in low energy states and we can now compare the percentage of p_σ occupancy revealed by the experimental results in this Chapter with the predictions of the theory (see Table 6.6).

It should be remembered that a number of assumptions have been made in deriving the IP configurations from the experimental results, and given these there is acceptable agreement between the predictions and the results, however the most reliable IP configurations, those of the 1_u states, have a significantly lower p_σ occupancy than that predicted from the charge-quadrupole interaction. This can be seen as a breakdown of the point charge model assumed for the two centres: the anionic valence shell is penetrating the cationic configuration such that the field gradient experienced by a cationic p_σ electron is stronger than predicted and the occupancy of p_π orbitals is even more favoured. The tendency will therefore be for low energy states of a given symmetry to adopt

JM State	Experiment				Charge-Quadrupole, R_e				$R \to \infty$
	c_1^2	c_2^2	c_3^2	p_σ	c_1^2	c_2^2	c_3^2	p_σ	p_σ
$\delta 2_u(1)$	0.902	0.098	0	0.275	0.931	0.070	0	0.268	0.275
$D'2_g(1)$	0.902	0.098	0	0.275	0.931	0.070	0	0.268	0.275
$\gamma 1_u(1)$	0.867	0.133	0	0.283	0.713	0.287	0	0.322	0.363
$\beta 1_g(1)$	0.703	0.297	0	0.324	0.713	0.287	0	0.322	0.363
$D0_u^+(1)$	0.466	0.444	0.090	0.339	0.467	0.472	0.060	0.353	0.392
$E0_g^+(1)$	0.466	?	?	n/a	0.467	0.472	0.060	0.353	0.392
$H1_u(2)$	0.555	0.445	0	0.361	0.382	0.618	0	0.404	0.375
$F0_u^+(2)$	0.461	0.351	0.188	0.291	0.619	0.328	0.053	0.319	0.333
$f0_g^+(2)$	0.461	?	?	n/a	0.619	0.328	0.053	0.319	0.333

Table 6.6. Experimental and theoretical p_σ occupancy in the IP states.

p_π occupancy even more than predicted: consequently the theory underestimates the c_3^2 component in the $D0_u^+(1)$ state and the c_1^2 component in the $\Omega = 1_{u,g}(1)$ states. As expected we find the members of the first cluster are stabilised to a greater extent by the charge-quadrupole interaction than those of the second cluster: the change in p_σ occupancy between $R = R_e$ (column 2) and $R \to \infty$, ie no intramolecular interaction (column 4), is greater than in the equivalent states of the second cluster.[3] The $D0_u^+(1)$ state p_σ occupancy revealed by experiment is probably overestimated: including a significant dipole strength for transitions to the $0_g^+(bb)$ state would increase the c_3^2 component of the configuration at the expense of the c_2^2.

[3]We have assumed in the analysis above that the $\Omega = 2$ configurations are independent of electronic charge-quadrupole interaction.

Comparison with hyperfine experiments

The hyperfine spectroscopy of the ion pair states can be used as a sensitive probe of the state's electronic structure: the theory of the interaction between the nuclear quadrupole moment, Q, and electronic field gradient at the cationic centre, q, is well established and has been used to deduce the major Russell-Saunders components of the cationic configurations in the $E0_g^+(1)$ [48, 50], $f0_g^+(2)$ [49] and $\beta 1_g(1)$ states [50]. Early results in this field were among the first to confirm the dominance of the diabatic dissociation products in the molecular configurations of the ion pair states, though the analyses did not then derive a complete description for the electronic structure [48, 49]. Later studies were to include the spin-orbit coupling at the cationic centre and arrived at improved predictions in some cases, though still some way from the experimental result [50]. A clear problem in the interpretation of results was the large vibrational amplitude of the states studied since the theoretical analyses assumed an electronic configuration unchanged from the separated atom function. Though this may be close to the true configuration at the outer turning point of the vibrational motion, we have found that even by R_e significant mixing of states occurs at the cationic centre driven by the electronic charge-quadrupole interaction which favours p_π occupation over p_σ. The influence of this intramolecular coupling will only increase as the bond shortens and consequently the configuration at the inner turning point is likely to differ significantly from the separated-atom configuration. A more detailed analysis would therefore need to take this into account, perhaps by weighting the contribution of configurations at the turning points of the motion according to the fraction of the vibrational period spent exploring them. This approach has been used for near dissociation levels in the $X0_g^+(aa)$ valence state [26]. Although no experimental data is available for the ground vibrational levels of the IP states these should prove the best test of the theory of hyperfine interactions for these states since the electronic configuration should hardly change over the small vibrational amplitude (0.15Å); consequently it would be instructive to predict the hyperfine interactions for the eigenfunctions derived in the previous

section.

The nuclear quadrupole moment, Q, interacts with the electronic field gradient at the nucleus, q, in an analogous manner to that of the electronic quadrupole at the cationic centre with the field gradient of the anionic charge (see Chapter 3). For the hyperfine interaction the contribution of electrons associated with the anionic centre to the field gradient at the cationic nucleus is neglected, and q depends only on the cationic configuration [26]

$$q = 2\langle {}^{2S+1}\mathrm{L}_{\mathrm{JM}} \mid \sum_e V_{20}(a,e) \mid {}^{2S+1}\mathrm{L}_{\mathrm{JM}} \rangle, \tag{6.37}$$

where a labels one cationic centre and the summation runs over all valence electrons at that centre, and

$$V_{20}(a,e) = -\sqrt{\frac{4\pi}{5}} \frac{e}{4\pi\epsilon_0 r_{ae}^3} P_{20}(\theta_{ae}, \phi_{ae}), \tag{6.38}$$

θ_{ae} and ϕ_{ae} are the angular coordinates of the electronic vector r_{ae}, and P_{20} is the Legendre polynomial. The r_{ae}^{-3} dependence of the interaction gives the justification for ignoring the contribution of the anionic configuration to the field gradient at the cationic centre, $\langle r(5p) \rangle_{\mathrm{I}^-} = 1.42$Å. With this assumption, the molecular coupling constant eQq in the separated atom limit can be equated to the coupling constant of I^+ in its $^3\mathrm{P}_2$ state.

The field gradient operator q is the sum of single electron operators so we can simplify the calculation by considering the contribution of each electron in turn. Knowing the spinorbital occupancy of the ground RS term we can calculate $q_{nlm}(\mathrm{I}^+)$ from

$$\langle Y_{11} \mid P_{20} \mid Y_{11} \rangle = -\frac{1}{5}, \tag{6.39}$$

and

$$\langle Y_{10} \mid P_{20} \mid Y_{10} \rangle = \frac{2}{5}, \tag{6.40}$$

and the eQq constant for the state: thus $eQq(^3\mathrm{P}_{22}) = -\frac{1}{2}\mathrm{eQq}_{510}$. Unfortunately the experimental value of $eQq(^3\mathrm{P}_2)$ has not been reported for I^+ and it must be estimated from the hyperfine structure of the neutral atom. Townes and

State	eQq /MHz
$\delta 2_u(1)$	-466
$D'2_g(1)$	-466
$\gamma 1_u(1)$	-396
$\beta 1_g(1)$	< -384
$D0_u^+(1)$	82
$E0_g^+(1)$	< 400
$H1_u(2)$	221
$F0_u^+(2)$	-382
$f0_g^+(2)$	< 400

Table 6.7. Predicted eQq constants for the some IP states around R_e.

Schwawlow have given $eQq_{510}(\mathrm{I}) = 2293\mathrm{MHz}$ [144, p.243] and suggested a scale factor of 1.15 for the cation [144, p.239]: thus $eQq_{510}(\mathrm{I}^+) = 2637\mathrm{MHz}$.

Since the strength of the hyperfine interaction depends on the orbital angular momenta of the electrons, and not their spins, we can calculate the eQq constants for the three $\Delta^{(4)}$ microstates available to the p^4 configuration

$$\|p_\sigma^1 p_\pi^3\| \ldots eQq = \frac{-1}{2} eQq_{510} \tag{6.41}$$
$$= -1318.5\mathrm{MHz}$$
$$\|p_\sigma^2 p_\pi^2\| \ldots eQq = eQq_{510} \tag{6.42}$$
$$= 2637\mathrm{MHz}$$
$$\|p_\sigma^0 p_\pi^4\| \ldots eQq = -2eQq_{510} \tag{6.43}$$
$$= -5274\mathrm{MHz}.$$

Table 6.7 gives the predicted eQq strengths for the electronic configurations derived in the previous section: only the $\delta 2_u(1)$, $D'2_g(1)$, $\gamma 1_u(1)$, $\beta 1_g(1)$, $D0_u^+(1)$, $F0_u^+(2)$ and $H1_u(2)$ are sufficiently well known (within the assumptions of the analysis); the values for the $E0_g^+(1)$ and $f0_g^+(2)$ states cannot be predicted as only the c_1^2 coefficient has been derived, though upper limits for the interaction

State	eQq /MHz
$E0_g^+(1)$ $v = 8, J = 98$	492
$v = 10, J \approx 14$	484
$v = 11, J = 106$	483
$v = 13, J \approx 14$	481
$v = 16, J \approx 14$	467
$\beta 1_g(1)$ $v = 16, J \approx 14$	136
$f0_g^+(2)$ $v = 44, J = 10$	154
$v = 44, J = 17$	161
$v = 46, J = 17$	161
$v = 46, J = 81$	192

Table 6.8. Experimental eQq constants for the $E0_g^+(1)$, $\beta 1_g(1)$ and $f0_g^+(2)$ states.

can be given. The measurement of hyperfine interactions is very sensitive to the electronic configuration and, given the assumptions required in the analysis above, a close correspondence with experiment is not expected. Rather we have demonstrated a framework in which an eQq experimental result could be interpreted.

Experimental values of eQq have been reported for vibrationally excited levels of the $E0_g^+(1)(v = 8, 10, 11, 13, 16)$ [50, 48], $f0_g^+(2)(v = 44, 46)$ [49] and $\beta 1_g(1)(v = 16)$ [50] states (Table 6.8). The study of the $f0_g^+(2)$ state hyperfine structure showed a significant dependence on rotational excitation, while a strong dependence on vibrational excitation has also been found in the valence states [16, 26]. It is therefore not particularly meaningful to compare the eQq predictions of our eigenfunctions at R_e with these experimental results since their vibrational motion samples regions of the potential where the cationic configuration is likely to have changed significantly from that at the equilibrium separation. However knowing the eQq values for the $E0_g^+(1)$ and $f0_g^+(2)$ states in $v = 0$ would

allow us to complete the description of their electronic configurations

$$\frac{eQq(IP)}{eQq_{510}} = \frac{-c_1^2}{4} + \frac{c_2^2}{2} - c_3^2, \tag{6.44}$$

since in both cases c_1^2 is known and the normalisation condition would make a complete solution possible. Not sufficient data is available at low enough v to make an estimate of eQq for the ground vibrational level of either of these states, however our results give upper limits for the interaction of around 400MHz. If the $f0_g^+(2)$ state has the same configuration as the $F0_u^+(2)$ then its eQq values would be -382MHz: unlike the transition dipole moments the eQq interaction is independent of inversion parity and would make a good test of the similarity between the electronic configurations of a u/g pair around R_e.

Significantly the predicted value for the $\beta 1_g(1)$ state is of the opposite sign to that found experimentally for $v = 16$. Our result arises from the large $\|p_\sigma^1 p_\pi^3\|$ component in the molecular configuration around R_e ($c_1^2 = 0.703$ and $c_2^2 = 0.297$), which has a negative eQq interaction and counters the positive interaction of the $\|p_\sigma^2 p_\pi^2\|$ component. The enhanced c_1^2 component develops since the electronic charge-quadrupole interaction favours p_π occupation increasingly as the bond shortens: at the separated atom limit the cationic configuration has $c_1^2 = 0.548$ and $c_2^2 = 0.452$ which gives an eQq value if 469MHz. Bacis *et al* have suggested [26] that the strength of eQq interaction for vibrationally excited states arises largely from contributions at the two turning points in the vibrational motion, R_1 and R_2, the internuclear separations where the molecule spends a large proportion of its vibrational period. They therefore suggested that

$$eQq(v) \approx P_1 eQq(R_1) + P_2 eQq(R_2), \tag{6.45}$$

where P_i are the weights attributed to each turning point. They took the weighting as proportional to the time spent by the molecule between the turning point and the equilibrium separation for the motion:

$$P_i = \int_{R_i}^{R_e} \psi_v^2 dr. \tag{6.46}$$

The vibrational wavefunction can be calculated from the known potential of the $\beta 1_g(1)$ state and we find that for $v = 16$, $P_1 = 0.463$. Assuming the electronic configuration at the outer turning point is close to the separated atom limit ($eQq = 235$MHz) then we can estimate the eQq at R_1; we find $eQq(R = 3.26) \approx$ 20MHz. This implies an electronic configuration around $R = 3.26$Å of $c_1^2 = 0.66$ and $c_2^2 = 0.34$, close to that found earlier for the equilibrium separation ($R_e =$ 3.61Å).

The strength of eQq interaction in the $f0_g^+(2)$ state at the separated ion limit is zero, and its positive value for $v \approx 45$ therefore reflects the contribution of the electronic configuration at the inner turning point ($R = 3.06$Å). For this vibrational level we find $P_1 = 0.450$ and so $eQq(R = 3.06) \approx 350$MHz. The large positive value for the eQq interaction around $R = 3.05$ suggests that the $\|p_\sigma^2 p_\pi^2\|$ component, the only microstate with positive eQq interaction, is dominating the electronic configuration. This is consistent with our picture of the lowest IP state of a given symmetry adopting lower p_σ occupancy in the presence of the anionic field. The $f0_g^+(2)$ state, being in the second cluster, cannot adopt the $\|p_\sigma^1 p_\pi^3\|$ configuration which is reserved for the lower energy $E0_g^+(1)$ state. The only *gerade* $\|p_\sigma^0 p_\pi^4\|$ configurations at these internuclear separations correlate with the high energy 0442 or the ground state 2440 MO occupancy and we expect this component to disappear from the 0_g^+ states as the bond shortens.

These conclusions can only be tentative since the contribution of the anionic configuration to the field gradient at the cationic centre may no longer be negligible at the inner turning point and the analysis stands on the validity of the approximation in equation (6.45). Furthermore the value of $eQq_{510}(I^+)$ has had to be estimated.

Comparison with estimates for heterogeneous coupling

The pure precession model of van Vleck [145] has been used successfully by Brand and coworkers [40, 146, 147] and by Ishiwata *et al* [142] in estimating the strength of heterogeneous interaction between ion pair states of IBr, ICl and Br_2. Brand

et al have shown that the coupling between states of different Ω is mediated through off diagonal terms in the rotational Hamiltonian

$$\hat{H}_{rot} = \frac{h^2}{8\pi^2\mu r^2}[\hat{J}^2 - \hat{J}_z^2 + \hat{L}^2 - \hat{L}_z^2 + \hat{S}^2 - \hat{S}_z^2 - \hat{J}_+(\hat{L}_- + \hat{S}_-) - \hat{J}_-(\hat{L}_+ + \hat{S}_+) + \hat{L}_+\hat{S}_- + \hat{L}_-\hat{S}_+], \quad (6.47)$$

with the ladder operators taking their usual form. The heterogeneous interaction therefore becomes

$$\langle \Omega \pm 1 v' J | \hat{H}_{rot} | \Omega v J \rangle = \langle \Omega \pm 1 | \hat{L}_\pm + \hat{S}_\pm | \Omega \rangle \langle \Omega \pm 1 v' | \frac{h^2}{8\pi^2\mu r^2} | \Omega v \rangle \times [J(J+1) - \Omega(\Omega+1)]^{\frac{1}{2}}, \quad (6.48)$$

and the strength of interaction reduces to three terms: the third in equation (6.48) is known and the second can be calculated numerically provided the potential functions are known. Brand *et al* then treated the electronic term as a parameter to be found from experimental data and a remarkable similarity with the value predicted by the pure precession hypothesis was found.

In the pure precession model $\mathbf{L} + \mathbf{S}(= \mathbf{J_a})$ is assumed to be a good quantum number, and the electronic term simplifies to

$$\langle \Omega \pm 1 | \hat{L}_\pm + \hat{S}_\pm | \Omega \rangle = [J_a(J_a+1) - \Omega(\Omega+1)]^{\frac{1}{2}}. \quad (6.49)$$

Thus the rotational Hamiltonian can only couple electronic states having common J_a and the strength of interaction is independent of the extent of jj mixing since this conserves J_a (but not L). Consequently the success of the pure precession model is not inconsistent with the significant coupling of J states found above, though we have found that, in contrast with the rotational coupling between IP states, the strength of the IP→Valence transition dipoles can be very sensitive to L state mixing.

Orthogonality of the IP eigenfunctions

Although the true ion pair eigenfunctions will necessarily be orthonormal, it is not possible to test the functions derived above for their orthogonality since the

electronic configurations are not known in sufficient detail; the exact nature of the configuration is ambiguous since two of the three $\Delta^{(4)}$ microstates conceal their Russell-Saunders components. For example:

$$\|p_\sigma^1 p_\pi^3\| = x\|1^+1^-0^+\underline{1}^-\| + \sqrt{1-x^2}\|1^+1^-0^-\underline{1}^+\|, \tag{6.50}$$

for $\Omega = 1$ and for $\Omega = 0^+$

$$\|p_\sigma^2 p_\pi^2\| = y\|1^+0^+0^-\underline{1}^-\| + \sqrt{1-y^2}\|1^-0^+0^-\underline{1}^+\|. \tag{6.51}$$

The mixing coefficients x and y will vary from state to state and so equation (6.18) does not define the electronic wavefunction sufficiently accurately for orthogonality to be established:

$$c_1c_1' + c_2c_2' + c_3c_3' \neq 0, \tag{6.52}$$

even for two orthogonal functions.

Consider the $|\,1(1)\rangle$ and $|\,1(3)\rangle$ configurations after partial jj mixing:

$$|\,1(1)\rangle = 0.950\,|\,{}^3\mathrm{P}_{21}\rangle_{RS} - 0.312\,|\,{}^1\mathrm{D}_{21}\rangle_{RS}, \tag{6.53}$$

and

$$|\,1(3)\rangle = 0.312\,|\,{}^3\mathrm{P}_{21}\rangle_{RS} + 0.950\,|\,{}^1\mathrm{D}_{21}\rangle_{RS}. \tag{6.54}$$

These two configurations are clearly orthonormal however if we expand them to calculate their c_i coefficients we find

$$\begin{aligned}
|\,1(1)\rangle &= 0.950\,|\,{}^3\mathrm{P}_{21}\rangle_{RS} - 0.312\,|\,{}^1\mathrm{D}_{21}\rangle_{RS} \\
&= 0.950[0.707\|1^+0^+0^-\underline{1}^+\| - 0.5\|1^+1^-0^-\underline{1}^+\| - 0.5\|1^+1^-0^+\underline{1}^-\|] \\
&\quad -0.312[0.707\|1^+1^-0^+\underline{1}^-\| - 0.707\|1^+1^-0^-\underline{1}^+\|] \\
&= 0.672\|1^+0^+0^-\underline{1}^+\| - 0.696\|1^+1^-0^-\underline{1}^+\| - 0.254\|1^+1^-0^+\underline{1}^-\|,
\end{aligned}$$

and

$$\begin{aligned}
|\,1(3)\rangle &= 0.312\,|\,{}^3\mathrm{P}_{21}\rangle_{RS} + 0.950\,|\,{}^1\mathrm{D}_{21}\rangle_{RS} \\
&= 0.312[0.707\|1^+0^+0^-\underline{1}^+\| - 0.5\|1^+1^-0^-\underline{1}^+\| - 0.5\|1^+1^-0^+\underline{1}^-\|] \\
&\quad +0.950[0.707\|1^+1^-0^+\underline{1}^-\| - 0.707\|1^+1^-0^-\underline{1}^+\|] \\
&= 0.221\|1^+0^+0^-\underline{1}^+\| + 0.516\|1^+1^-0^-\underline{1}^+\| - 0.828\|1^+1^-0^+\underline{1}^-\|.
\end{aligned}$$

If we were able to perform a similar series of dispersed fluorescence experiments on these hypothetical states as those described above then the analysis would give their c_i^2 coefficients: $c_1^2 = 0.548$ and 0.935, $c_2^2 = 0.452$ and 0.065 respectively, and thus would know that

$$|\, 1(1)\rangle = 0.740\|p_\sigma^1 p_\pi^3\| \pm 0.672\|p_\sigma^2 p_\pi^2\|, \tag{6.55}$$

and

$$|\, 1(3)\rangle = 0.967\|p_\sigma^1 p_\pi^3\| \pm 0.255\|p_\sigma^2 p_\pi^2\|. \tag{6.56}$$

We cannot demonstrate the orthogonality of the two functions (6.55) and (6.56) without knowing the detailed composition of the $\|p_\sigma^1 p_\pi^3\|$ and $\|p_\sigma^2 p_\pi^2\|$ microstates: for the same reasons we cannot test the orthogonality of the configurations derived in the previous section.

6.4.3 Intramolecular interactions: the Valence states

The longest range breakdown of the $(J_A M_A J_B M_B)$ model when applied to the valence states is the r^{-5} interaction between electronic quadrupoles at each atomic centre. This mixes states of the same symmetry in the $(J_A M_A J_B M_B)$ scheme [25, 116]. We shall not derive the strength of interaction and consequent eigenfunctions from first principles but rather use our knowledge of the upper state wavefunction and the transition dipole strength to each lower state in the $(J_A M_A J_B M_B)$ basis to derive the degree of mixing amongst the basis functions.

In general we cannot derive the valence state configurations from the experimental transition dipole strengths again because the ion pair configuration is not sufficiently well known. Without the detailed knowledge of the upper state wavefunction the degree of mixing of lower state basis functions cannot be deduced. However for the $\Omega = 2$ ion pair states we expect the charge-quadrupole interaction to have little effect and the degree of state mixing due to intraionic perturbations should be relatively small on account of the large $^3P_2$ -$^1D_2$ separation. Assuming the $|\, JM\rangle$ states of Table 3.3 are close to the molecular eigenfunctions at R_e, we

can find the lower state eigenfunctions for $\Omega = 2$; this is not possible for any of the other IP states studied here.

The $2_{g,u}$ valence states

Considering parallel transitions from the $D'2_g(1)$ state first, then the spin-orbital occupancy at the cationic centre is given from Table 3.3

$$|\, 2(1)\rangle = 0.950\,|\,{}^3\mathrm{P}_{22}\rangle_{RS} - 0.312\,|\,{}^1\mathrm{D}_{22}\rangle_{RS}. \tag{6.57}$$

We find from equation(6.12) that the ${}^1\mathrm{D}_{22}$ component of the $D'2_g(1)$ state, having $\|p_\sigma^2 p_\pi^2\|$ occupancy at the cationic centre, cannot contribute to the charge transfer transition dipole. Table 6.2 gives the amplitudes for the projection of the $\mu_z\,|\,{}^3P_{22}\rangle$ state vector onto the $(J_A M_A J_B M_B)$ basis set for the valence states and, in the absence of any mixing in the valence state basis, we would expect the transition from the $D'2_g(1)$ to the $2_u(aa)$ state to have twice the dipole of that to the $2_u(ab)$. The experimental results give this ratio as 3.33:1.

If we write the true valence states as a linear combination of the basis functions

$$|\, 2_{u,g}(aa)\rangle = x\,|\,2_{u,g}(1)\rangle + y\,|\,2_{u,g}(2)\rangle, \tag{6.58}$$

and

$$|\, 2_{u,g}(ab)\rangle = y\,|\,2_{u,g}(1)\rangle - x\,|\,2_{u,g}(2)\rangle, \tag{6.59}$$

where $|\,2_{u,g}(1)\rangle$ refers to the basis function at the first valence dissociation limit and $|\,2_{u,g}(1)\rangle$ that at the second dissociation limit, then we find

$$\langle D'2_g(1)\,|\,\mu_z\,|\,2_u(aa)\rangle^2 = 0.902[M_{\pi\pi}(R_e) - M_{\sigma\sigma}(R_e)]^2 \times \{-\sqrt{\frac{2}{3}}x + \frac{1}{\sqrt{3}}y\}^2, \tag{6.60}$$

and

$$\langle D'2_g(1)\,|\,\mu_z\,|\,2_u(ab)\rangle^2 = 0.902[M_{\pi\pi}(R_e) - M_{\sigma\sigma}(R_e)]^2 \times \{-\sqrt{\frac{2}{3}}y - \frac{1}{\sqrt{3}}x\}^2. \tag{6.61}$$

Substituting the observed values for the left-hand side we find $x = 0.993$ and $y = -0.114$, assuming the component at diabatic dissociation still dominates the wavefunction. Thus there is surprisingly little mixing ($< 2\%$) of the two valence

state functions by R_e^{IP}, though this mixing causes a relatively large change (7%) in the observed transition strengths.

Turning to the $\delta 2_u(1)$ state we need to consider the contribution of the spin-orbit component of the IP configuration as this can undergo a charge transfer transition from an *ungerade* upper state (equation (6.12)). Equations (6.60) and (6.61) become

$$\begin{aligned}\langle \delta 2_u(1) \mid \mu_z \mid 2_u(aa)\rangle^2 = \; & 0.902[M_{\pi\pi}(R_e) + M_{\sigma\sigma}(R_e)]^2 \times \{\sqrt{\tfrac{2}{3}}x - \tfrac{1}{\sqrt{3}}y\}^2 \\ & +0.097[2M_{\pi\pi}(R_e)]^2 \times \{-\tfrac{1}{\sqrt{3}}x - \sqrt{\tfrac{2}{3}}y\}^2, \quad (6.62)\end{aligned}$$

and

$$\begin{aligned}\langle \delta 2_u(1) \mid \mu_z \mid 2_u(ab)\rangle^2 = \; & 0.902[M_{\pi\pi}(R_e) + M_{\sigma\sigma}(R_e)]^2 \times \{\sqrt{\tfrac{2}{3}}y + \tfrac{1}{\sqrt{3}}x\}^2 \\ & +0.097[2M_{\pi\pi}(R_e)]^2 \times \{-\tfrac{1}{\sqrt{3}}y + \sqrt{\tfrac{2}{3}}x\}^2. \quad (6.63)\end{aligned}$$

The experimental evidence shows that the ratio of these two transition dipoles is 1.5 : 1, so solving for x and y we find: $x = 0.998$ and $y = 0.062$. Once again a small degree of mixing ($< 1\%$) of the two basis functions has caused a significant change (7%) in the transition dipole.

The large effect of such small coupling on the transition dipole serves as a caveat against interpreting the other IP→Valence dipoles measured at this R in terms of the electronic nature of the lower state: the influence of even a small degree of configuration mixing could effectively disguise the major electronic component. This small degree of mixing between valence state functions is consistent with the large energy splitting between the dissociation limits (both valence states are essentially anti-bonding), $^2P_{3/2} - {}^2P_{1/2} = 7603\text{cm}^{-1}$, however as the nuclei approach each other we would expect the dominant MO configurations to develop: 2341 and 2422 for the $2_g(aa)$ and $2_g(ab)$ states respectively, 2431 and 2332 for the corresponding 2_u states (see figure 1.2). Though the final MO states may not be achieved until internuclear separations of less than 2.75Å [118], these configurations imply that at such R complete mixing of the two basis functions, $\mid 2_{u,g}(1)\rangle$ and $\mid 2_{u,g}(2)\rangle$, has taken place.

Chapter 7 The Transition Dipole as a function of R

In the preceding Chapter we were able to calculate the relative Einstein A-coefficients for the majority of the strong IP(n') $\rightarrow$Valence(n'') charge transfer transitions from their relative fluorescent intensities since

$$\int_{\nu_{min}}^{\nu_{max}} I_{fl}(\nu)d\nu = N_{n'} \sum_{v''} A_{n'v'n''v''}, \tag{7.1}$$

and the ratio of the integrated fluorescence intensities, $S_{n'n''}(v')$, will give the relative Einstein A-coefficients provided the upper state population, $N_{n'}$, is constant. The fluorescence lifetimes, $\tau_{n'v'}$, of these ion pair states are related to the Einstein A-coefficients through

$$\tau_{n'v'} = 1/\sum_{n''v''} A_{n'v'n''v''}, \tag{7.2}$$

and so can be used to calculate the absolute coefficient

$$\sum_{v''} A_{n'v'n''v''} = \frac{S_{n'n''}(v')}{\sum_{n''} S_{n'n''}(v')} \tau^{-1}_{n'v'}. \tag{7.3}$$

The Einstein coefficient itself can be related to the transition dipole moment in the Born-Oppenheimer approximation

$$A_{n'v'n''v''} = \frac{64\pi^4}{3hc^3} \frac{S_{J'}}{2J'+1} \nu^3 \langle v' \mid \mu_{n'n''}(R) \mid v'' \rangle^2, \tag{7.4}$$

where $S_{J'}$ is the rotational Hönl-London factor, and

$$\mu_{n'n''}(R) = \langle n' \mid \mu \mid n'' \rangle, \tag{7.5}$$

The work covered in this chapter has been submitted to Chemical Physics Letters [148].

where $\mu = \sum_i er_i$. With the effect of configuration mixing among the valence states removed by summing the transition dipoles for all possible electronic transitions from a given IP state, we were able to derive the ion pair electronic structure near its equilibrium separation. It was found that although the separated atom configuration proved a fair description, significant mixing of the Russell-Saunders microstates occurs at the cationic centre under the influence of the anionic charge. Thus by R_e^{IP} the electronic configuration has departed from that of the free ions by up to 20% in the first IP cluster. The analysis in the previous Chapter aimed to derive the ion pair configurations at R_e^{IP} and so was concerned with transition moments from low vibrational levels, however we can see from equation (7.5) that any change in the electronic configuration of a state with R will be reflected by suitable changes in the transition dipole function, thus deriving the dependence of $\mu_{n'n''}$ on R can be used as a diagnostic for the changing electronic structure of a state as the bond stretches.

Few transition dipole functions have been reported for the ion pair states of iodine possibly because the first descriptions of new states have tended to come from absorption spectra and those experiments where fluorescence has been dispersed have been analysed for the lower state potential, the influence of the slowly changing dipole function being neglected. Even with this limited information some idea of the change in dipole function with internuclear separation can be inferred: for example it is well known that the $F0_u^+(2)$ state cannot be populated readily through absorption from the ground state, ie at R_e^X (2.66Å), yet fluorescence from this state back to the ground state at R_e^F, (3.60Å), gives one of the most intense transitions of the IP→Valence manifold (see Table 6.1). The $F0_u^+(2) \rightarrow X0_g^+(aa)$ transition dipole must have undergone a large change in strength over the 1Å.

A more quantitative picture for the transition dipole as a function of internuclear separation can be achieved with an ion pair population in a high vibrational level: having a large vibrational amplitude fluorescence from this state will explore a large range of the dipole function and, provided the two state potentials

are sufficiently well known, the R dependence of the transition dipole can be derived. When the fluorescence is to a monotonic Mulliken potential the analysis is relatively straightforward and typically uses the r-centroid approximation [108]; where the difference potential is double valued iterative comparisons of quantum mechanical simulations and the experimental spectrum are required (see Chapter 2). However, as the fluorescence spectrum cannot be corrected for the upper state population, this technique will only give the relative change in the transition dipole with R and as before the fluorescence lifetime, together with the ratio of the fluorescent intensities, is required to achieve an absolute calibration.

The only transition dipole functions for transitions from iodine's ion pair states reported in the literature are from the $E0_g^+(1) \rightarrow B0_u^+(ab)$ transition [88, 91], the $D0_u^+(1) \rightarrow X0_g^+(aa)$ [101], the $\beta 1_g(1) \rightarrow A1_u(aa)$ [91] and the $f0_g^+(2) \rightarrow B0_u^+(ab)$ [15] transitions. Unfortunately for all the functions reported, except that for the $f \rightarrow B$ transition, the wavelength dependence of the detector response, $F(\nu)$, was unknown. This is significant since the square of the dipole function is proportional to the envelope of the spectrum, and hence to $F(\nu)$: the true dipole function will not have been derived without this correction. Since the spectra presented in this thesis have all been corrected for the detector response and the power dependence of the PM tube output, the true transition dipole function can be derived from dispersed fluorescence spectra: we analyse the spectra for the $F0_u^+(2) \rightarrow X0_g^+(aa)$ transition for upper state vibrational levels $v' = 0, 4, 9, 19$ to find the transition dipole function over the range $3.13 \leq R \leq 4.12$Å.

7.1 Results and Analysis

State specific excitation of the $F0_u^+(2)$ state was achieved using the two colour OODR scheme described in Chapter 4:

$$X0_g^+(aa)(0,21) \xrightarrow{R} B0_u^+(ab)(59,22) \sim c1_g(ab)(14,22) \xrightarrow{R} F0_u^+(2)(v',23), \quad (7.6)$$

with $v' = 0, 4, 9$ and 19. The experimental configuration and data acquisition for dispersed fluorescence spectra are described in Chapter 2. It is important

to ensure signal stability for the duration of these slow scans as shot-to-shot fluctuations in the laser signal will lead to changes in the IP population and so to anomalous local spectral intensities. The signal stability was tested by recording the intensity of a strong peak at the red and blue ends of the spectrum before making the scan: if the intensities of these test peaks differed significantly at the end of the scan the spectrum was rejected. Each scan was then repeated until a consistent set of spectra was achieved. While spectra subject to a large signal drift may be rejected in this way, the random shot-to-shot fluctuations cannot be removed completely and this should be borne in mind in the interpretation: after much analysis a dipole function could be derived that exactly reproduced the spectral envelope, however such a dipole function is unlikely to have a physically realistic form and will be convoluted with the random population fluctuations. By ensuring that the dipole function is satisfactory for a range of scans, and for a range of different vibrational levels, this problem of interpretation can to a large extent be avoided.

7.1.1 The $F \rightarrow X$ transition dipole function

Both the $F0_u^+(2)$ [32] and $X0_g^+(aa)$ [23] states are well known and their potentials can be derived from the available RKR data. The functional form of the transition dipole moment can then be deduced by the iterative comparison of experimental spectra with quantum mechanical simulation (see Chapter 2).

The lowest vibrational levels were analysed first ($v' = 0, 4$). Having fluorescence spectra that sample monotonic Mulliken potentials, their intensity envelopes can be analysed in a straightforward manner to give the relative transition dipole moment at the r-centroids, $\langle v' \mid r \mid v'' \rangle$, of each transition $v' \rightarrow v''$ (Chapter 2). In this way the dipole function can be resolved over $3.38 \leq R \leq 3.83$Å, the classical amplitude of the $v' = 4$ level. As higher vibrational levels are excited the transition dipole function can be routinely extended over their greater vibrational amplitudes until the Mulliken difference potential becomes double valued and the spectral intensity over certain wavelengths can no longer be attributed

to one semi-classical transition point. Fluorescence from the $v' = 9$ level samples a difference potential double valued over the range $3.76 \leq R \leq 3.95$Å. The maximum in the Mulliken potential occurs at $R = 3.85$Å so in this case the relative strength of the dipole function is known for one of the semi-classical transition points over the majority of the polytonic region of the difference potential. Therefore the contribution from the second transition point can be inferred: we find that the wavelength region corresponding to the change over from reflection to interference structure is particularly sensitive to the amplitude of $\mu_{n'n''}$ at large R. The monotonic range of the $v' = 9$ difference potential can be analysed routinely as before and extends the dipole function to shorter R, down to 3.28Å.

By $v' = 19$ the vibrational motion samples the transition dipole over $3.13 \leq R \leq 4.12$Å and the difference potential is now double valued over the range $3.64 \leq R \leq 4.12$Å (see Figure 2.7). The maximum in the Mulliken potential will still lie at $R = 3.85$Å since moving to a higher vibrational term merely raises the whole difference potential vertically by the energy $\Delta G_{v'}$: the red extremum remains invariant of v' once a double valued difference potential has been achieved. Analysing the $v' = 19$ fluorescence spectrum in the same manner as that for the $v' = 9$ level we arrive at a first estimate for the $F \rightarrow X$ transition dipole function for $3.13 \leq R \leq 4.12$, however an error in analysing the reflection spectra would be compounded when analysing the interference regions of the more vibrationally excited spectra. In practice such errors are not large and a final round of iterative comparisons of quantum simulation with spectra leaves a smoothly varying, physically plausible dipole function.

The relative fluorescent intensities for all the radiative systems available to the $F0_u^+(2)$ state were recorded in Chapter 6 and combined with the radiative lifetime to give the transition dipole moment at R_e^F, $|\mu_{F\rightarrow X}(R_e)| = 0.725$eÅ. This is used to calibrate the dipole function (see figure 7.1 where the $F0_u^+(2) \rightarrow X0_g^+(aa)$ transition dipole function is compared with the $f0_g^+(2) \rightarrow B0_u^+(ab)$ function); the knot points for the function are given in Table 7.1. Note that although probably exaggerated by the spline fitting, the change in the function's gradient around

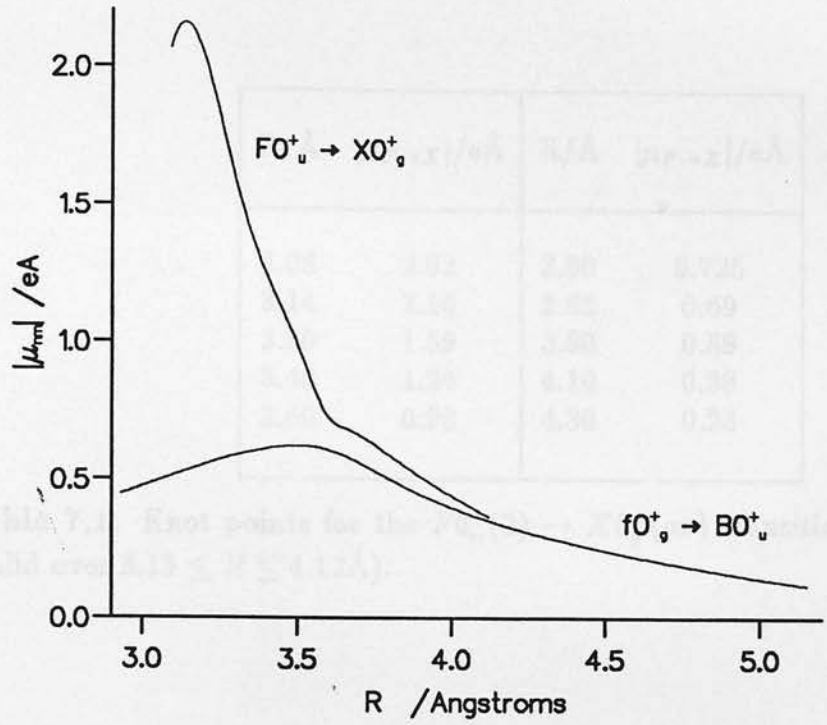

Figure 7.1. $F0_u^+(2) \rightarrow X0_g^+(aa)$ and $f0_g^+(2) \rightarrow B0_u^+(ab)$ transition dipole functions.

R_e^F is required to reproduce the fluorescence envelope of the $v' = 0$ spectrum, probably the most reliable in terms of signal stability on account of its shorter scan time: it appears to presage a significant configuration change in the IP state (see below).

Qualitative Features of the Fluorescence

Figures 7.2 to 7.5 show the dispersed fluorescence spectra for the four vibrational levels along with their quantum mechanical simulations. These spectra are not calibrated for wavelength.

The fluorescence dispersed from the two highest vibrational levels show the expected features of fluorescence to a polytonic Mulliken potential: an invariant red extremum and interference structure at the higher wavelength end of the spectrum. The reflection structure of a monotonic difference potential is clear in

R/Å	$\lvert\mu_{F\to X}\rvert$/eÅ	R/Å	$\lvert\mu_{F\to X}\rvert$/eÅ
3.08	2.02	3.60	0.725
3.14	2.16	3.65	0.69
3.30	1.59	3.80	0.59
3.40	1.24	4.10	0.38
3.50	0.98	4.30	0.28

Table 7.1. Knot points for the $F0_u^+(2) \to X0_g^+(aa)$ transition dipole function (valid over $3.13 \leq R \leq 4.12$Å).

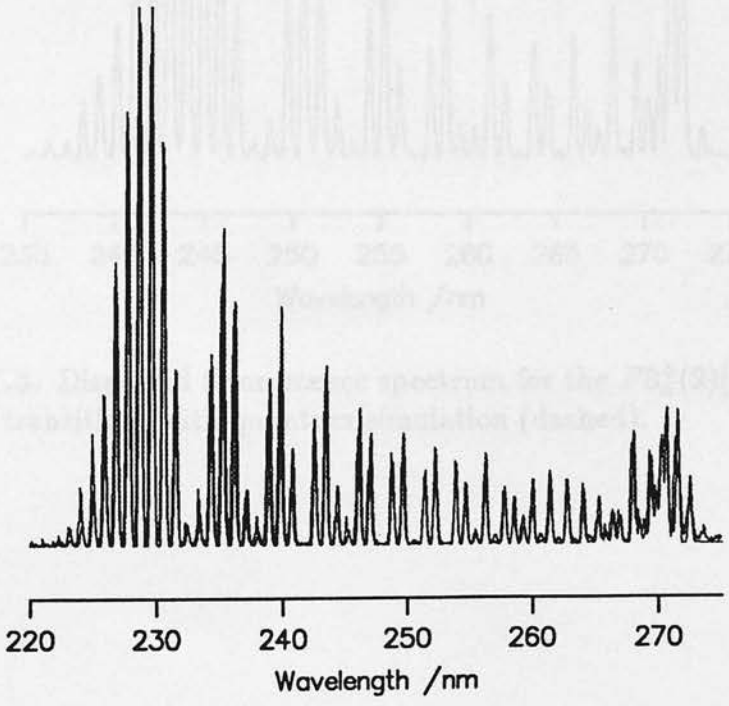

Figure 7.2. Dispersed fluorescence spectrum for the $F0_u^+(2)(v' = 19, J' = 23) \to X0_g^+(aa)$ transition, with quantum simulation (dashed).

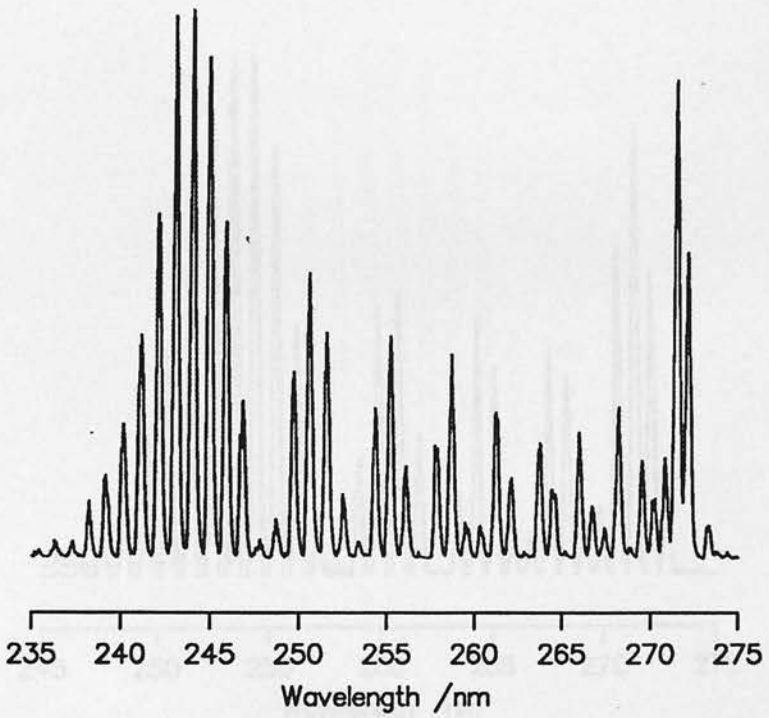

Figure 7.3. Dispersed fluorescence spectrum for the $F0_u^+(2)(v' = 9, J' = 23) \rightarrow X0_g^+(aa)$ transition, with quantum simulation (dashed).

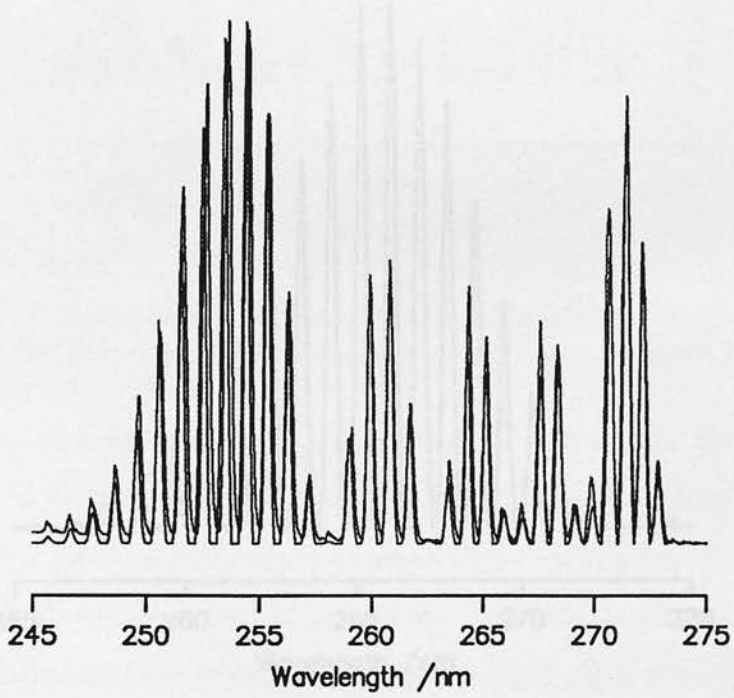

Figure 7.4. Dispersed fluorescence spectrum for the $F0_u^+(2)(v' = 4, J' = 23) \rightarrow X0_g^+(aa)$ transition, with quantum simulation (dashed).

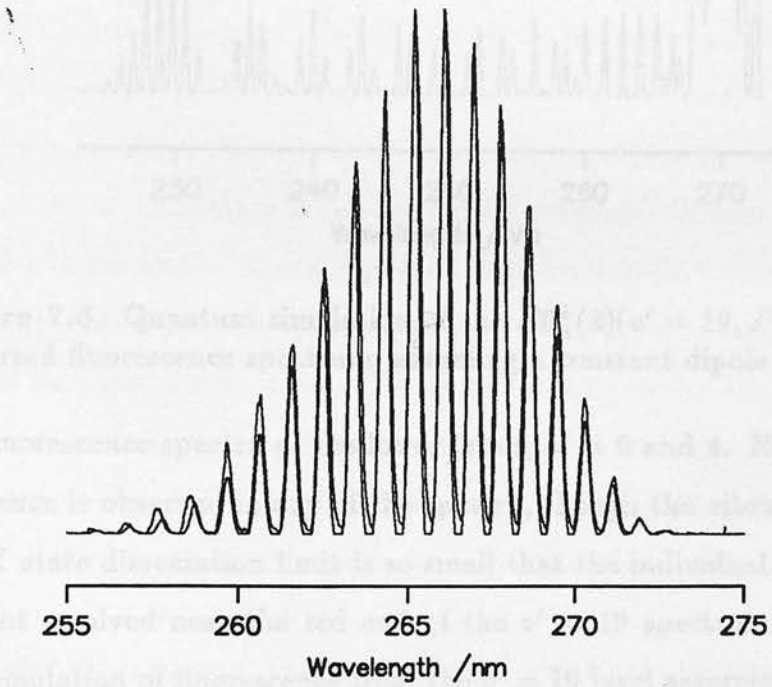

Figure 7.5. Dispersed fluorescence spectrum for the $F0_u^+(2)(v' = 0, J' = 23) \rightarrow X0_g^+(aa)$ transition, with quantum simulation (dashed).

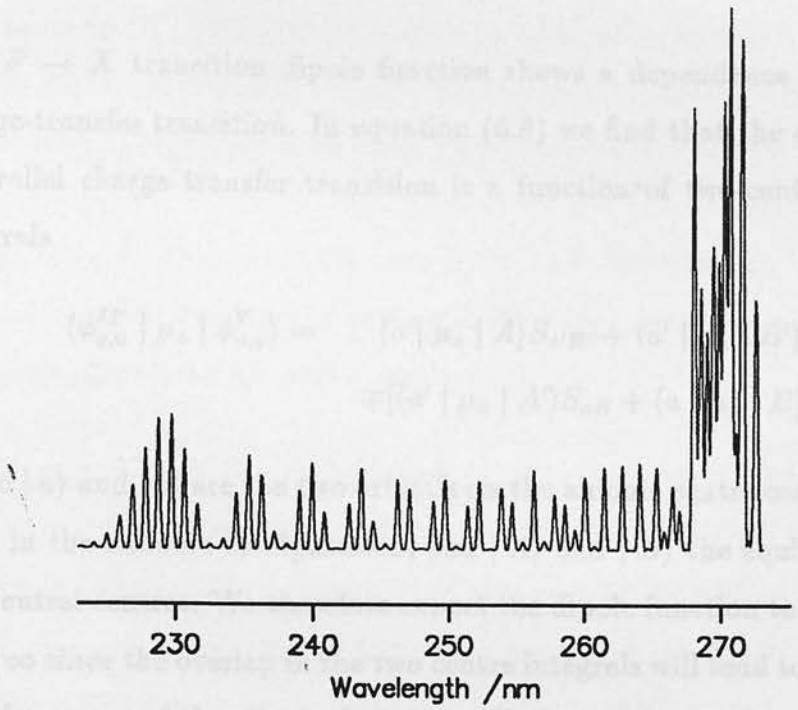

Figure 7.6. Quantum simulation of the $F0_u^+(2)(v' = 19, J' = 23) \rightarrow X0_g^+(aa)$ dispersed fluorescence spectrum, assuming a constant dipole function.

the fluorescence spectra of the lower levels, $v' = 0$ and 4. No *bound* $\rightarrow$ *free* fluorescence is observed in any of the spectra, though the vibrational interval near the X state dissociation limit is so small that the individual transitions $v' \rightarrow v''$ are not resolved near the red end of the $v' = 19$ spectrum. Figure 7.6 shows the simulation of fluorescence from the $v' = 19$ level assuming a constant dipole function and clearly demonstrates the influence of the true transition dipole function. The true function attenuates transitions at longer internuclear separations where the gradient of the difference potential is smallest. Without the effect of the dipole function, transitions in this region would therefore have the strongest fluorescence intensity (equation (2.20)). The influence of the true dipole function is therefore to emphasise the *blue* end of the spectrum.

7.2 Interpretation

The $F \rightarrow X$ transition dipole function shows a dependence on R typical of a charge-transfer transition. In equation (6.8) we find that the dipole moment for a parallel charge transfer transition is a function of two-centre and one-centre integrals

$$\langle \phi^{IP}_{g,u} \mid \mu_z \mid \phi^{V}_{u,g} \rangle = \langle a \mid \mu_z \mid A \rangle S_{a'B'} + \langle a' \mid \mu_z \mid B' \rangle S_{aA} \mp [\langle a' \mid \mu_z \mid A' \rangle S_{aB} + \langle a \mid \mu_z \mid B \rangle S_{a'A'}], \quad (7.7)$$

where $\mid a \rangle$ and $\mid b \rangle$ are the two orbitals on the anionic centre corresponding to the holes in the cationic configuration, and $\mid A \rangle$ and $\mid B \rangle$ the equivalent orbitals for the neutral centres. We therefore expect the dipole function to reduce to zero for $R \rightarrow \infty$ since the overlap in the two centre integrals will tend to zero. The charge transfer terms of the dipole function will also vanish at the united atom limit ($R \rightarrow 0$) though the transition dipole may still have some strength if the valence orbital becomes Rydbergised. Between these two limits the build up of overlap between the two centres will allow the dipole to acquire a significant moment provided the transition involved is dipole allowed. In the following discussion we will describe the changing dipole as the bond shortens from large to small R.

Comparison of the $f \rightarrow B$ and $F \rightarrow X$ dipole functions

The $f \rightarrow B$ transition dipole function (figure 7.1) has been reported in a companion experiment to that described here [15]. This function shows a relatively small rise as the bond length approaches its equilibrium separation and the orbital overlap between the two centres increases; the subsequent decrease in dipole moment beyond the equilibrium separation shadows the emergence of the $f0^+_g(2)$ state's dominant MO configuration at small R, 2242 (see Table 1.2). Transitions from this MO configuration to that adopted by the B state at similar internuclear separations, 2431 [118], is one-electron forbidden thus the dipole function decays as these MO configurations become established.

In comparison we find a dramatic increase occurs in the $F \rightarrow X$ transition dipole around R_e^F, with it rising steeply to a large dipole moment of about 2.16eÅ by $R \approx 3.14$Å. It seems the dipole function peaks at this value since a decrease with shorter R is just accessed from the highest vibrational level studied. As with all charge transfer dipole functions we expect the $F \rightarrow X$ dipole to increase from zero at large R, then return to zero by $R \rightarrow 0$, however the form of the dipole function between these limits can again be interpreted in terms of configuration changes in the electronic states involved.

At large R both the $F0_u^+(2)$ and $f0_g^+(2)$ states should adopt close to their separated atom configurations and we would therefore expect these u/g partners to have the same orbital occupancy. Consequently we might expect the $F \rightarrow X$ dipole moment to be smaller than that for the $f \rightarrow B$ transition since there are other radiative systems competing for the parallel transition dipole from the *ungerade* state. Counteracting this effect will be the strong transition dipole available only to the *ungerade* state through its $\|p_\pi^4\|$ component at the cationic centre (equation (6.14)).

As the internuclear separation decreases from large R to the equilibrium value we find the $F \rightarrow X$ function builds up in a similar manner to the $f \rightarrow B$ function, though the $F \rightarrow X$ dipole is already the stronger suggesting a significant contribution from the $\|p_\pi^4\|\|p_\sigma^2 p_\pi^4\|$ component of the electronic configuration. Around R_e^{IP} this component contributes almost 70% of the $F \rightarrow X$ dipole strength, though forming less than 20% of the electronic configuration (Chapter 6). Although this contribution is not available to the f state the $f \rightarrow B$ dipole maintains its strength since there are no other valence states of 0_u^+ symmetry competing for the oscillator strength. The two dipole functions are therefore of comparable moment until close to R_e^{IP} where they display markedly different character, the $F \rightarrow X$ increasing dramatically and the $f \rightarrow B$ dying away. This must reflect changes in the electronic structure of at least one of the states involved.

We found in Chapter 6 that the $F0_u^+(2)$ state configuration has a significantly larger $\|p_\pi^4\|\|p_\sigma^2 p_\pi^4\|$ component at R_e when compared with the free ion configuration. A $\|p_\pi^4\|\|p_\sigma^2 p_\pi^4\|$ occupancy is equivalent to the 1441 configuration in MO terminology, and will have a dipole allowed charge transfer transition to the ground state configuration 2440. 2440 is presumably the major component of the $X0_g^+(aa)$ state configuration by $R \approx 3$Å: Li and Balasubramanian have suggested it forms 66% of the configuration at $R = 4$Å [118], while Das and Wahl have suggested the $^1\Sigma_g^+$ configurations (2440 and 2422) form the major component from $R \approx 3.7$Å [47]. As the bond shortens we expect the pre-eminence of the 2440 configuration in the $X0_g^+(aa)$ state to increase. The sudden increase in the $F \rightarrow X$ dipole therefore reflects significant changes in the IP configuration: as the $F0_u^+(2)$ state increasingly adopts a $\|p_\pi^4\|$ configuration at the cationic centre it gains oscillator strength for transitions to the 2440 ground state. The charge transfer transition from a $\|p_\pi^4\|\|p_\sigma^2 p_\pi^4\|$ occupancy has the strongest dipole moment available to an IP state (Chapter 6), consequently its contribution dominates the $F \rightarrow X$ transition dipole function. The $\|p_\pi^4\|\|p_\sigma^2 p_\pi^4\|$ occupancy is not active for charge transfer transitions from the $f0_g^+(2)$ state (equation (6.14)) and we therefore see no dramatic change in the $f \rightarrow B$ dipole function: the divergence in the two transition dipole functions does not necessarily mean the two IP states have dramatically different electronic configurations.

As the bond continues to shorten the orbital overlap between the two centres will increase and a dominant MO configuration will emerge for each IP state, 2332 for the $F0_u^+(2)$ state and 2242 for the $f0_g^+(2)$ (see Table 1.2). Both transitions therefore become one electron forbidden and the transition dipole functions decrease as these final MO configurations become established. At these internuclear separations, the $\|p_\pi^4\|\|p_\sigma^2 p_\pi^4\|$ occupancy is the lowest energy configuration available for an *ungerade* IP state and so is taken over by the $D0_u^+(1)$ state: consequently as the $F \rightarrow X$ dipole function decreases we would predict a synchronous increase in the $D \rightarrow X$ dipole function. This is consistent with the *ab initio* studies of Das and Wahl who found a 50% increase in the D state $^1\Sigma_u^+$

component (MO configurations 1441 and 2332) between $R = 3.4$Å and $R = 2.6$Å [47].

The form of the $F \rightarrow X$ dipole function with R therefore reflects the changing contribution of the $\|p_\pi^4\|\|p_\sigma^2 p_\pi^4\|$ component in the IP configuration, in contrast with the $f \rightarrow B$ function which reflects the contribution from the $\|p_\sigma^1 p_\pi^3\|\|p_\sigma^2 p_\pi^4\|$ component.

Part III

Conclusions

Chapter 8 The Ion Pair States of Iodine

This thesis has shown how the *ungerade* ion pair states of I_2 can be populated in low vibrational levels through a two photon Optical-Optical Double Resonance excitation scheme from the *gerade* ground state and employing a u/g coupled intermediate step. The intermediate level pumped in this excitation scheme was first suggested by Danyluk and King in 1977, and the hyperfine Hamiltonian first discussed for the $B0_u^+(ab)$ state of iodine by Broyer *et al* in 1978, however this is the first experimental rationalisation of a hyperfine facilitated pumping scheme. With the symmetry and potential function of the *gerade* coupling partner now established, OODR excitation schemes for any of the *ungerade* IP states can be proposed: a new pumping scheme has been suggested to access the $0_u^-(2)$ state, a state previously unattainable through OODR excitation. The derivation of potential functions for unknown *ungerade* IP states from fluorescence excitation experiments should now be possible. The dominant electronic configuration of the $c1_g(ab)$ state has been deduced to be $\psi_{3/2}^{ab}$ around $R \approx 5.5$Å, and the major Dunham parameters of a new ion pair state, the $H1_u(2)$ state, have been derived for low vibrational levels.

The radiative lifetimes of nine ion pair states have been reported, four for the first time in low v, and these have been combined with the relative fluorescence intensities of the IP→Valence charge transfer transition manifold to derive absolute Einstein A-coefficients for these transitions for the first time. A theoretical model has been developed to describe the charge transfer nature of these transitions, and been used to predict the relative transition dipoles of the various transitions

State	Expt. $\overline{D_e^{u,g}}$	Theory $-\frac{e^2}{R_e} - \frac{1}{2}\Theta_{zz}F'_{zz}$
2(1)	30990	32630
1(1)	30808	31592
$0^+(1)$	30809	31633
$0^+(2)$	31360	31812
1(2)	31208	31488

Table 8.1. Experimental and point charge values for D_e.

available to a particular IP state, assuming a separated atom description applies. The model has been used to deduce the electronic configurations of the IP states around R_e^{IP} and the transition dipole moments for the $p_\sigma \leftrightarrow p_\sigma$ and $p_\pi \leftrightarrow p_\pi$ electron transfer between the two centres. Although subject to various assumptions regarding the electronic configuration of the $\Omega = 2(1)$ states and the R dependence of the dipole functions, the analysis draws out broad trends suggesting the ion pair configurations have departed from the free ion configuration by as much as 20% in the first cluster. This is unexpected given the close clustering of IP states with others of the same diabatic dissociation product, and accounts for the failure of a point charge model in reproducing the splittings between IP states[1] (see Table 8.1) and for the inadequacy of the free ion configurations in the theoretical analysis of hyperfine eQq interactions. The ion pair configurations around R_e^{IP} suggest that the final MO ordering of states has yet to be achieved and the lowest energy states of a given symmetry achieve low energy configurations at the cationic centre by adopting as small a p_σ occupancy in the presence of the anionic field gradient as the inter-electron repulsion and spin-orbit interactions will allow.

[1] though this is subject to the accuracy of the *ab initio* value for $\langle\rho^2\rangle_+$.

It has not been possible to establish whether the two states of a u/g pair have similar electronic configurations at R_e, but the large differences in summed transition dipole moments observed for certain u/g pairs is not inconsistent with them having closely similar configurations: the theoretical model clearly demonstrates that certain, potentially strong, transitions are only allowed for the *ungerade* state. This is seen in the transition dipole functions for the $F0_u^+(2) \rightarrow X0_g^+(aa)$ and $f0_g^+(2) \rightarrow B0_u^+(ab)$ transitions: only the $F \rightarrow X$ dipole grows strongly between $R = 3.6$ and 3.1Å reflecting the increasing contribution of the $\|p_\pi^4\|\|p_\sigma^2 p_\pi^4\|$ component. At R_e^{IP} this is found to contribute 70% of the dipole while making only 20% of the configuration. The $\|p_\pi^4\|\|p_\sigma^2 p_\pi^4\|$ component can make no contribution to charge transfer transitions from a *gerade* IP state and consequently the $f \rightarrow B$ transition moment is weaker by about a factor of 4.

Part IV

Appendices

Appendix A The u/g splitting of Ion Pair states

In Chapter 3 the experimental order of the I^+ atomic states was rationalised in terms of the inter-electron repulsion and spinn-orbit interactions: the larger inter-electron repulsion in the singlet configurations leaves the $^1D_2$ and $^1S_0$ states highest in energy, with the $^1D_2$ term below the $^1S_0$. The ^3P_J states are split by the spin -orbit operator with the $^3P_2$ term lowest of all; the $^3P_0$ state comes next on account of the strong $^3P_0 - {}^1S_0$ spin -orbit interaction, though the $^3P_1$ is not much higher in energy. The energy ordering of the IP clusters at equilibrium is the same in I_2 as found in I^+, with the separation between clusters similar to that between the cationic states on dissociation.[1] Consequently it has been assumed that on forming the molecular electronic wavefunction the IP configuration at the cationic centre around R_e is close to that of the free ion. However we have found in Chapter 6 that there is significant jj mixing at the cationic centre through the intramolecular charge-quadrupole interaction which favours p_π occupation over p_σ. This stabilisation in the presence of the anionic field gradient is offset by the increased inter-electron repulsions and weak spin -orbit interactions associated with some of the p^4 configurations with low p_σ occupancy. Thus, for example, the lowest energy configuration in the charge-quadrupole interaction, $\|p_\sigma^0 p_\pi^4\|$, implies a relatively large inter-electron repulsion at the cationic centre; consequently the final configurations adopted by an IP state at a particular R reflect a play

[1] Although the second IP cluster comprises of the six states dissociating to $^3P_1$ and $^3P_0$ cations, the cationic order is still preserved as the two molecular states dissociating to $^3P_0$ ions, the $f0_g^+(2)$ and $F0_u^+(2)$ states, are the lowest and third lowest members of the cluster.

off between the stabilisation energy in the anionic field and the inter-electron repulsion and spin-orbit energies.

At this stage of our description the IP states are stacked in clusters as u/g pairs at $\Omega(n)$-dependent energies (see Section 3.4), this Appendix discusses the terms that split these u/g pairs to give the final energy ordering observed experimentally.

In the complementary two electron problem in which X^- has two electrons and the cationic centre none, the molecular electronic wavefunction of an IP state is described in the $(J_A M_A J_B M_B)$ coupling scheme as

$$| n\Omega\rangle_{g,u}^{(+/-)} = \sum_i c_i \psi_i, \tag{A.1}$$

where the wavefunction is assumed to be normalised and

$$\psi_i = \frac{1}{\sqrt{2}} \mathcal{A}\{| aa'\rangle \pm | bb'\rangle\}, \tag{A.2}$$

with the positive sign taken by the *gerade* state; the coefficients c_i will depend on R and will vary from state to state. The symmetry labels are defined in equation (1.4) and $| a\rangle (\equiv | m_l m_s\rangle_a)$ denotes the spin orbital occupancy of electron 1 at the anionic centre. The normalisation and anti-symmetriser will be assumed throughout the rest of this section.

The energy of an IP state is given by the Schrödinger equation:

$$\begin{aligned} E &= \langle \Psi \mid H \mid \Psi \rangle \\ &= \sum_{i,j} c_i c_j \langle \psi_i \mid H \mid \psi_j \rangle, \end{aligned} \tag{A.3}$$

with $\hat{H}$ the molecular Hamiltonian for the two electron system. The few off-diagonal terms arise through the inter-electron operator, $\frac{1}{r_{12}}$, and the energy of a particular molecular configuration, Ψ, is essentially determined by the diagonal terms. The energy of the component, ψ_i, is

$$\langle \psi_{u,g} \mid H \mid \psi_{u,g} \rangle = \langle aa' \mid H \mid aa' \rangle \pm \langle aa' \mid H \mid bb' \rangle, \tag{A.4}$$

with a *gerade* state taking the positive sign, and so

$$E \approx \sum_i c_i^2 E_i. \tag{A.5}$$

However we need not make this final approximation and, provided a given u/g pair have the same molecular electronic configuration, the origin of their energy splitting is now clear: the two states will be split, one up and one down, from the $\Omega(n)$-dependent energy, $E_{\Omega(n)}(= \sum_{i,j} c_i c_j \langle \phi_i^a \phi_i^{a'} \mid H \mid \phi_j^a \phi_j^{a'} \rangle)$, by an exchange integral for electron exchange between the two centres, $E_{exc}(= \sum_{i,j} c_i c_j \langle \phi_i^a \phi_i^{a'} \mid H \mid \phi_j^b \phi_j^{b'} \rangle)$. The coefficients c_i give the spin orbital occupancy of the state and therefore the energy $E_{\Omega(n)}$ will include all the spin -orbit, electron repulsion and intramolecular interactions common to the u/g pair and will represent a tier average from which the exchange integral determines the final energies of the two states. The nesting of the IP states in the first cluster suggests that the $E_{\Omega(n)}$ integral is similar for all states in the first cluster and that the exchange integral gets progressively larger with Ω (see Table A.1). It is the sign and strength of the exchange integral that determines the u/g splitting amongst the IP states and will be discussed in more detail in the next Section.

This analysis relies on the u/g pair having the same electronic configuration and we were unable to establish this in Chapter 6 since the complete molecular configuration of no u/g pair could be derived. However we do expect some difference between IP u/g configurations since in most cases they do not have identical R_e values. Any difference must reflect some interaction between the electron clouds of the two centres: as the bond shortens and a single MO configuration is observed the pair will necessarily have different configurations and consequently differing energies. For example the $\|p_\sigma^0 p_\pi^4\| \|p_\sigma^2 p_\pi^4\|$ configuration is a low energy MO occupancy for *ungerade* IP states, but the highest energy MO occupancy for *gerade* IP states, however the close clustering of IP states suggests that even down to R_e the differences in configuration between u/g pairs are small and we shall persist in assuming they are identical when discussing the exchange integral.

State	$T_e(\mathrm{cm}^{-1})$	$\overline{T_e^{u,g}}(\mathrm{cm}^{-1})^a$	$\frac{1}{2}\Delta T_e^{u,g}(\mathrm{cm}^{-1})^b$
first cluster			
$D'2_g(1)$	40388	41039	-650
$\beta 1_g(1)$	40821	41221	-400
$D0_u^+(1)$	41029	41220	-192
$E0_g^+(1)$	41412	41220	192
$\gamma 1_u(1)$	41621	41221	400
$\delta 2_u(1)$	41689	41039	650
second cluster			
$f0_g^+(2)$	47026	47122	-96
$F0_u^+(2)$	47217	47122	96
$G1_g(2)$	47559	47920	361
$H1_u(2)$	48280	47920	-361

[a] $\approx E_{\Omega(n)}$
[b] $\approx E_{exc}$

Table A.1. Exchange integrals and u/g tier averages for the first two IP clusters.

A.1 The Exchange Integral

If the two states in a u/g pair have the same electronic configuration then the energy difference between them is twice the exchange integral, $\sum_{i,j} c_i c_j \langle \phi_i^a \phi_i^{a'} \mid H \mid \phi_j^b \phi_j^{b'} \rangle$). The strength, and sign, of the exchange integral will depend on the IP configuration: the experimental values for T_e give the *gerade* state the lower energy of the pair for every case known bar one, the $0^+_{u,g}$ pair in the first cluster, and the size of u/g splitting seems to increase with Ω (Table A.1). To rationalise the size of the u/g splittings within a cluster we need to consider the exchange integral in more detail; in the following analysis we shall concentrate on the diagonal terms in the energy matrix, however the off-diagonal terms can be readily included and will be discussed later.

In a two electron system the exchange integral gives

$$\langle aa' \mid H \mid bb' \rangle = \langle aa' \mid -\frac{Z_e}{r_{1a}} - \frac{Z_e}{r_{1b}} - \frac{Z_e}{r_{2a}} - \frac{Z_e}{r_{2b}} - \frac{1}{r_{12}} \mid bb' \rangle, \qquad \text{(A.6)}$$

where r_{1a} is the radial coordinate of electron 1 relative to centre a, and r_{12} is the inter-electron separation; Z_e is the effective nuclear charge experienced by the electrons. The exchange integral therefore separates into two familiar terms

$$\begin{aligned} \langle aa' \mid \mathcal{H} \mid bb' \rangle \;=\; & -\langle a \mid \frac{Z_e}{r_{1a}} + \frac{Z_e}{r_{1b}} \mid b \rangle \langle a' \mid b' \rangle - \langle a' \mid \frac{Z_e}{r_{2a}} + \frac{Z_e}{r_{2b}} \mid b' \rangle \langle a \mid b \rangle \\ & + \langle aa' \mid \frac{1}{r_{12}} \mid bb' \rangle. \end{aligned} \qquad \text{(A.7)}$$

We can see that the off-diagonal terms can only arise from the $\frac{1}{r_{12}}$ operator and that the sign of the exchange energy itself will depend on the relative magnitudes and signs of the integrals in equation (A.7) above. In general we expect the integrals to be dominated by the extent of orbital overlap between the two centres in each one electron distribution $\phi^a \phi^b$ (see calculations later) and so exchange terms involving p_σ orbitals should be larger than those involving p_π. Thus we expect the absolute values of

$$\langle \sigma_a \mid \sigma_b \rangle > \langle \pi_a \mid \pi_b \rangle, \qquad \text{(A.8)}$$

and

$$\langle \sigma_a \mid \frac{Z_e}{r_{2a}} + \frac{Z_e}{r_{2b}} \mid \sigma_b \rangle > \langle \pi_a \mid \frac{Z_e}{r_{2a}} + \frac{Z_e}{r_{2b}} \mid \pi_b \rangle. \tag{A.9}$$

Similarly for the inter-electron repulsion integrals we expect

$$\langle \sigma_a\sigma_a \mid \frac{1}{r_{12}} \mid \sigma_b\sigma_b \rangle > \langle \sigma_a\pi_a \mid \frac{1}{r_{12}} \mid \sigma_b\pi_b \rangle > \langle \pi_a\pi_a \mid \frac{1}{r_{12}} \mid \pi_b\pi_b \rangle, \tag{A.10}$$

though the $\langle \pi_a\pi_a \mid \frac{1}{r_{12}} \mid \pi_b\pi_b \rangle$ integral may be large if the $\|1^+1^-\|$ configuration is involved. The signs of these integrals are discussed in the next sections.

The overlap integral

As with their strength, the sign of the overlap integral between the two centres depends on the orbital involved: the overlap between two π orbitals is positive over all space, while that between σ orbitals is negative between the two centres and positive elsewhere if a right-handed axis set is assumed at each centre. Consequently the integral $\langle \pi_a | \pi_b \rangle$ is positive for all internuclear separations, whereas $\langle \sigma_a | \sigma_b \rangle$ is negative at intermediate R and positive at short R: we have found in Chapter 6 that around R_e^{IP} the $\langle \sigma_a | \sigma_b \rangle$ overlap integral is still negative. Both integrals tend to zero as $R \rightarrow \infty$ and to one at the united atom limit where they become the normalisation condition.

The Coulombic attraction integral

This integral will follow the same sign as the overlap integral above and so $\langle \sigma_a \mid \frac{1}{r_{2a}} + \frac{1}{r_{2b}} \mid \sigma_b \rangle$ will be negative and $\langle \pi_a \mid \frac{1}{r_{2a}} + \frac{1}{r_{2b}} \mid \pi_b \rangle$ positive around R_e in the ion pair states.

The inter-electron repulsion integral

This integral calculates the repulsion between the two one-electron distributions $\phi_a\phi_b$ and $\phi'_a\phi'_b$. The strongest repulsion will be expected when both distributions have significant amplitude in the same region of space, ie when both electrons occupy the same space orbital at a centre. Consequently the p_σ^2 and p_π^2 occupancies, when the p_π orbitals both have the same m_l value, will have large repulsive

integrals. For the IP clusters studied the $\|1^+1^-\|$ microstate can only occur in the 2(1) states, and even then only through their spin -orbit components, and the p_π^2 occupancy will more typically have orbitals with differing m_l values giving the weakest of the inter-electron repulsions. The $p_\sigma^1 p_\pi^1$ configuration may be expected to have a repulsion integral whose strength lies somewhere between this and the large p_σ^2 integral. The signs of these integrals will be determined by the relative phases of the two distributions around their maxima provided the r_{12} separation is not too large. Thus we expect the $\langle \sigma_a\sigma_a \mid \frac{1}{r_{12}} \mid \sigma_b\sigma_b\rangle$ and $\langle \pi_a\pi_a \mid \frac{1}{r_{12}} \mid \pi_b\pi_b\rangle$ to be positive and $\langle \sigma_a\pi_a \mid \frac{1}{r_{12}} \mid \sigma_b\pi_b\rangle$ to be negative.

Off-diagonal terms can arise between configurations with related spin orbital occupancy, for example $\|0^+\underline{1}^-\|$ and $\|0^-\underline{1}^+\|$, and the inter-electron repulsion found for $\|1^+\underline{1}^-\|$ will differ from that of $\|1^-\underline{1}^-\|$, however calculations (see later) suggest that these differences are small and the repulsion integrals can be separated into three families in order of increasing strength, depending on whether none, one or both p_σ orbitals are occupied.

The detailed energy ordering of the members of an IP cluster will therefore reflect two factors, the $E_{\Omega(n)}$ and E_{exc} energies. The former will determine the how 'focussed' the cluster is: the first IP cluster in I_2 shows a small spread of T_e values with the $\Omega = 0$ states nested in the $\Omega = 1$, which are in turn nested in the $\Omega = 2$ states. This suggests that the $E_{\Omega(n)}$ energy is similar for all members of the first cluster. The varying size and sign of the exchange energy will depend on the various integrals contributing to it and the reconciliation with experiment is considered in more detail in the next Section. The second IP cluster shows a similar range in T_e values but the cluster is no longer nested: the $E_{\Omega(n)}$ energy varies significantly with Ω in this group of states as would be expected since the lowest u/g pair have different diabatic dissociation products from the others.

A.2 Reconciliation of observed u/g splittings

If we describe the IP state electronic wavefunction according to

$$| \Omega_{g,u} \rangle = P^{\pm}_{a,b}[c_{1g,u}\|p^1_\sigma p^1_\pi\| + c_{2g,u}\|p^0_\sigma p^2_\pi\| + c_{3g,u}\|p^2_\sigma p^0_\pi\|]_a \qquad \text{(A.11)}$$

then we need to discuss the exchange integrals for each of the possible configurations $\|p^m_\sigma p^n_\pi\|$.

We found in Chapter 3 that the $\Omega = 2,1$ states of the first IP cluster cannot adopt the $\|p^2_\sigma p^0_\pi\|$ and around R_e their electronic configurations are dominated by the $\|p^1_\sigma p^1_\pi\|$ component (Chapter 6). Furthermore we find that the *gerade* state of the u/g pair is the lower in energy and consequently the exchange integral must be negative. The integrals $\langle \sigma_a \mid -\frac{1}{r_{1a}} - \frac{1}{r_{1b}} \mid \sigma_b \rangle \langle \pi_a | \pi_b \rangle$ and $\langle \pi_a \mid -\frac{1}{r_{1a}} - \frac{1}{r_{1b}} \mid \pi_b \rangle \langle \sigma_a | \sigma_b \rangle$ are both positive and consequently the negative inter-electron repulsion integrals must be dominating the electron exchange for these states, even though the two electrons occupy different space orbitals at a given centre. If we assume that the repulsion integrals also dominate the exchange interactions of the other two $\|p^m_\sigma p^n_\pi\|$ configurations, where the electrons may occupy the same space orbitals, then their exchange interactions will both be positive. We expect the exchange energy to be largest for the $\|p^2_\sigma p^0_\pi\|$ component since the electrons both occupy the same space orbital, giving large repulsion energies, and there is strong orbital overlap between the centres. We would expect the exchange interaction for the $\|p^1_\sigma p^1_\pi\|$ configuration to be the next strongest, but in this case negative, and that for the $\|p^0_\sigma p^2_\pi\|$ component to be small, positive and negligible when the two p_π orbitals have different m_l. Calculations of the $\|1^+1^-\|$ exchange integral suggest it too is small, presumably on account of the weak p_π overlap between centres, and so the exchange interactions of the $\|p^0_\sigma p^2_\pi\|$ components can be neglected.

Therefore in this model, the exchange energy of the $\Omega = 2(1), 1(1)$ configurations are negative on account of their large $\|p^1_\sigma p^1_\pi\|$ components, with the $\Omega = 2(1)$ states having the larger u/g splitting since they have the larger c^2_1 component (Table A.2). We found in Chapter 6 that the $\Omega = 0^+(1)$ states have a reduced c^2_1 component and a significant c^2_3 coefficient compared with the other members of

$\Omega(n)$	$T_e^g - T_e^u$	c_1^2	c_2^2	c_3^2
2(1)	-1300.7	0.902	0.098	0
1(1)	-800.3	0.867	0.133	0
$0^+(1)$	383.2	0.466	0.444	0.090
1(2)	-721.2	0.555	0.445	0
$0^+(2)$	-191.5	0.461	0.351	0.188

Table A.2. u/g splittings and electronic configurations for some IP states of iodine.

their cluster. The c_3^2 configuration, $\|p_\sigma^2 p_\pi^0\|$, has the largest inter-electron repulsion energy which will therefore make a significant positive contribution to the $\Omega = 0^+(1)$ exchange energy. From Table A.2 we find that the exchange integral for this pair has changed sign: the c_3^2 component must make the dominant contribution overriding the negative contribution from the $\|p_\sigma^1 p_\pi^1\|$ component. It is not surprising in the light of this that the $0^+(1)$ states have the smallest u/g splitting, ie the smallest E_{exc} energy.

Outside the first cluster, the only other u/g pairs known experimentally are the $\Omega = 1$ and $\Omega = 0^+$ states in the second cluster. Once more the $\Omega = 1$ states can only adopt $\|p_\sigma^1 p_\pi^1\|$ and $\|p_\sigma^0 p_\pi^2\|$ components: that the *gerade* states still lies below the *ungerade* suggests that even a reduced c_1^2 coefficient determines the sign of the exchange energy; the contribution from the $\|p_\sigma^0 p_\pi^2\|$ component is small. The separation between the $\Omega = 1$ states in the second cluster is smaller than that of the first cluster as expected given their reduced c_1^2 coefficient, however it is not as small as might have been anticipated. This may reflect the various off-diagonal terms that have been neglected along with the small dependence of the exchange integral on the detailed spinnorbital occupancy within a $\|p_\sigma^m p_\pi^n\|$ family. The $\Omega = 0^+(2)$ states do not show the anomalous u/g ordering displayed by the $0^+(1)$ states, in spinte of their similar electronic configuration: if anything the

analysis of Chapter 6 suggested that the c_3^2 coefficient was even larger in the $0^+(2)$ states than the $0^+(1)$ and we would therefore expect a similar reversed ordering with an even greater u/g splitting in the second cluster. This is not observed and the most likely explanation is the missing contribution of fluorescence to the (bb) dissociation limit in the analysis for the $D0_u^+(1)$ state configuration. Including this contribution would enhance the c_3^2 component of the $D0_u^+(1)$ state at the expense of the c_2^2 component giving a larger positive contribution to the exchange integral of the $\Omega = 0^+(1)$ state.

It should be remembered that this description assumes the two states of a u/g pair have the same electronic configuration: although the configurations are similar (Chapter 6), this is clearly not exactly true as the IP states do not have identical R_e values. Consequently their exchange integrals will be slightly different, and the model of an equal and opposite energy shift from some $\Omega(n)$ dependent average will not hold. A complete account of the IP energy ordering awaits an accurate *ab initio* treatment to derive the exchange integrals and the extent of intramolecular interaction between the electron distributions at each centre, however this qualitative picture should point to the important terms determining the experimentally observed IP order.

Numerical Integrations

The various terms contributing to the exchange integrals of the various configurations can be calculated numerically using a Gaussian basis set, however the basis sets available may not be reliable at such large R since they are optimised for ground state energies and will be most accurate at short radii from the nucleus. Calculations using the basis sets of Huzinaga [43] for the I^- ion give the exchange energies shown in Table A.3. The large range in each value demonstrates the unreliability of the Gaussian function for a valence orbital at such large R: the range arises from the differing results using each of Huzinaga's three basis sets, all of which give similar total energies for the I^- ground state. Note that in these integrations the electrons are each in a molecular distribution $\phi_a\phi_b$

ϕ	ϕ'	$\langle\phi_a\phi'_a \mid \frac{1}{r_{12}} \mid \phi_b\phi'_b\rangle$ (cm^{-1})	$\sum\langle\phi_a \mid \frac{1}{r_{a,b}} \mid \phi_b\rangle\langle\phi'_a\mid\phi'_b\rangle$ (cm^{-1})	E_{exc} (cm^{-1})
σ^α	σ^β	11900 ± 615	9500 ± 1275	$4290 \rightarrow 510$
σ^α	π^β	-2850 ± 330	-2545 ± 615	$-1250 \rightarrow 640$
σ^α	π^α	-1470 ± 330	-2545 ± 615	$130 \rightarrow 2020$
π^α	π^β	790 ± 130	660 ± 110	$370 \rightarrow -110$
π^α	π^α	330 ± 110	660 ± 110	$-110 \rightarrow -550$

Table A.3. The exchange integrals for the p^2 configuration at R_e^{IP}; confidence ranges reflect the results using each of the different basis sets given by Huzinaga.

about two cationic centres; ϕ_i are anionic orbitals. The estimation of the screening constants for such a distribution is not straightforward and the calculations assume both electrons are completely screened from the nuclei, ie $Z_e = 1$. The integrals have been calculated numerically in a stepwise fashion over a segment of R-space, using the cylindrical symmetry, and the final result estimated by extrapolating the step size to zero. Unfortunately the results of the integration are inconclusive though they do reveal the strong $\|p_\sigma^2 p_\pi^0\|$ exchange energy, and the sign change for the $\|p_\sigma^1 p_\pi^1\|$ integral lies within the range of values calculated for this energy. Except for the $\|p_\sigma^2 p_\pi^0\|$ configuration the repulsion energy is of the same order as the Coulombic attraction integrals suggesting that the long range behaviour of the orbital is not correctly reproduced in Huzinaga's basis functions.

Appendix B Hyperfine Hamiltonian for a heavy molecule

We aim to derive an expression for the general matrix element of the hyperfine Hamiltonian for a heavy diatomic molecule. The result (equation (B.11)) has been given by Bacis *et al* [122, equation (6)] in a comprehensive paper discussing the theory of the hyperfine interactions and u/g perturbations of a heavy diatomic. In a companion paper [102] this theory was applied to near dissociation vibrational levels of the $B0_u^+(ab)$ state of I_2, where a u/g symmetry breaking perturbation was proposed coupling the B with a $1_g(ab)$ state. In a recent paper studying the hyperfine structure of the $E0_g^+(1)$ and $\beta 1_g(1)$ states Tiemann *et al* re-wrote Bacis' result to simplify the appearance of the reduced matrix elements [50]: their result is similar to that derived here.

A detailed derivation is written out to gain an understanding of the origin of the terms in the final equation: it can then be used to calculate the strength of the $B \sim c$ coupling interaction for comparison with experimental results (see section 4.2). Throughout this derivation reference will be made to some general theorems on the matrix elements of irreducible tensor operators; these can be found in standard texts [114, 149, 150, 151], but are repeated in Appendix C for ease of reference.

B.1 The hyperfine matrix elements

For heavy diatomics such as I_2 each electronic state Ω, $(= M_{J_A} + M_{J_B})$, can be described in terms of separated atom basis functions (see section 1.1.1):

$$|\, n\beta\Omega v J\tau(I_A I_B) I F M_F\rangle^{(+/-)}_{u,g} = \left(\tfrac{1}{\sqrt{2}}\right)^{|\epsilon|} \{|\, \beta\Omega v J\tau(I_A I_B) I F M_F\rangle_{u,g} + \epsilon\,|\, \beta - \Omega v J\tau(I_A I_B) I F M_F\rangle_{u,g}\}, \quad \text{(B.1)}$$

where I is the total nuclear spin, $\mathbf{I} = \mathbf{I_A} + \mathbf{I_B}$; F the total molecular angular momentum, $\mathbf{F} = \mathbf{I} + \mathbf{J}$, with $\mathbf{J} = \mathbf{\Omega} + \mathbf{N}$ and $\mathbf{N}$ the nuclear rotation; v is the vibrational quantum number. β and τ are other quantum numbers pertinent to the electronic and nuclear wavefunction respectively; $\epsilon = 0$ for $\Omega = 0$ states and $\epsilon = \chi_{\sigma v} = \pm 1$ for $\Omega \neq 0$ states, where σ_v is the symmetry operation of reflecting through a molecular plane in the $D_{\infty h}$ group.

The hyperfine Hamiltonian H_{hf} can be written as [121]

$$H_{hf} = H_{hf}(A) + H_{hf}(B) + H_{hf}(A,B), \quad \text{(B.2)}$$

where $H_{hf}(A)$ is the hyperfine interaction between the electrons and the nucleus labelled A, and $H_{hf}(A,B)$ the interaction between the two nuclei. This latter term is small and can be omitted in a first approximation, allowing H_{hf} to be expressed as [121]

$$H_{hf} = \sum_{\alpha=A,B} \sum_{k} \sum_{q=-k}^{k} (-1)^q Q^k_q(I_\alpha) V^k_{-q}(e_\alpha), \quad \text{(B.3)}$$

where the tensorial operator $\mathbf{Q}^k(I_\alpha)$ acts only on the nuclear spin of atom α and $\mathbf{V}^k(e_\alpha)$ acts on the electrons.

The hyperfine matrix element coupling two electronic states, $|\, n\Omega\rangle$ and $|\, n'\Omega'\rangle$, is therefore given by

$$\langle n'\Omega' \mid H_{hf} \mid n\Omega\rangle = \quad \text{(B.4)}$$
$$\textstyle\sum_{\alpha=A,B} \sum_k \langle n'\beta'\Omega' v' J'\tau'(I_A I_B) I' F' M_{F'} \mid \mathbf{Q}^k(I_\alpha).\mathbf{V}^k(e_\alpha) \mid n\beta\Omega v J\tau(I_A I_B) I F M_F\rangle.$$

We have a composite coupling system with two subsystems, the nuclear and the electronic, each with an irreducible tensor operator acting on the one, and

not the other, subsystem's space so we can separate the two subsystems using equation (C.2) from Appendix C. The subsystems are characterised by I and J respectively, which couple to give F, so

$$\langle n'\Omega' \mid H_{hf} \mid n\Omega\rangle = \sum_{\alpha=A,B}\sum_{k}\delta_{FF'}\delta_{M_F M_{F'}}(-1)^{I+J'+F}\left\{\begin{array}{ccc} F & J' & I' \\ k & I & J \end{array}\right\}$$
$$\times\langle\tau'(I_AI_B)I' \mid \mathbf{Q}^{(k)}(I_\alpha) \mid \tau(I_AI_B)I\rangle\langle n'\beta'\Omega'v'J' \mid \mathbf{V}^{(k)}(e_\alpha) \mid n\beta\Omega vJ\rangle. \quad \text{(B.5)}$$

We can now treat each coupling subsystem separately to derive the matrix elements on the right-hand side of the equation. The tensor operator $\mathbf{Q}^{(k)}(I_\alpha)$ acts on the nuclear spin of the molecule, I, which is the vector addition of the nuclear spins of the individual nuclei, thus we need to apply equation (C.3) from Appendix C to reduce the problem to the reduced matrix elements of operators acting at each nuclei:

$$\langle\tau'(I_AI_B)I' \mid \mathbf{Q}^{(k)}(I_A) \mid \tau(I_AI_B)I\rangle = \quad \text{(B.6)}$$
$$(-1)^{I_A+I_B+I+k}[(2I+1)(2I'+1)]^{\frac{1}{2}}\left\{\begin{array}{ccc} I_A & I' & I_B \\ I & I_A & k \end{array}\right\}\langle\tau' I_A\|\mathbf{Q}^{(k)}(I_A)\|\tau I_A\rangle,$$

and similarly when $\mathbf{Q}^{(k)}(I_B)$ acts on nucleus B. The reduced matrix elements on the right-hand side can be related to experimental data for the iodine atom by using the Wigner-Eckart Theorem (Appendix C equation (C.1)) which gives:

$$\langle\tau' I_A M_{I_A} = I_A \mid \mathbf{Q}^{(k)}(I_A) \mid \tau I_A M_{I_A} = I_A\rangle = \quad \text{(B.7)}$$
$$(-1)^{I_A-I_B}\left(\begin{array}{ccc} I_A & k & I_A \\ -I_A & 0 & I_A \end{array}\right)\langle\tau' I_A\|\mathbf{Q}^{(k)}(I_A)\|\tau I_A\rangle.$$

The matrix element on the left-hand side is the nuclear dipole magnetic moment, $\mu_N g_{I_A} I_A$, for $k = 1$, the nuclear electric quadrupole moment, $\frac{1}{2}eQ_{I_A}$, for $k = 2$, etc, all of which are known experimentally for the iodine atom. Thus,

$$\langle\tau' I_A\|\mathbf{Q}^{(k)}(I_A)\|\tau I_A\rangle = \langle\tau' I_A M_{I_A} = I_A \mid \mathbf{Q}^{(k)}(I_A) \mid \tau I_A M_{I_A} = I_A\rangle$$
$$\times\left[\left(\begin{array}{ccc} I_A & k & I_A \\ -I_A & 0 & I_A \end{array}\right)\right]^{-1}. \quad \text{(B.8)}$$

Next we return to equation (B.5) to consider the matrix element for the electronic subsystem. In Hund's case (c) Ω is the z-component of the total molecular angular momentum without nuclear spin, **J**, so we can apply equation (C.4) from Appendix C to give:

$$\langle n'\beta'\Omega'v'J' \mid \mathbf{V}^{(k)}(e_A) \mid n\beta\Omega vJ\rangle = [(2J+1)(2J'+1)]^{\frac{1}{2}} \begin{pmatrix} J' & k & J \\ -\Omega' & q & \Omega \end{pmatrix} \times \langle n'\beta'\Omega'v' \mid \mathbf{V}^{(k)}(e_A) \mid n\beta\Omega v\rangle, \quad \text{(B.9)}$$

where the matrix element on the right-hand side contains the M_J dependent $3-j$ coefficient and can be related to experimental data for the iodine atom: this will be developed in the next section. We can now combine equations (B.5), (B.6), (B.8) and (B.9) to get the final result:

$$\begin{aligned} \langle n'\Omega' \mid H_{hf} \mid n\Omega\rangle = & \\ & \sum_k \delta_{FF'}\delta_{M_F M_{F'}}(-1)^{I+J'+F+I+k} \begin{Bmatrix} F & J' & I' \\ k & I & J \end{Bmatrix} \\ & \times[(2I+1)(2I'+1)]^{\frac{1}{2}} \begin{Bmatrix} I_A & I' & I_A \\ I & I_A & k \end{Bmatrix} \\ & \times\langle \tau' I_A M_{I_A} = I_A \mid \mathbf{Q}^{(k)}(I_A) \mid \tau I_A M_{I_A} = I_A\rangle \left[\begin{pmatrix} I_A & k & I_A \\ -I_A & 0 & I_A \end{pmatrix} \right]^{-1} \\ & \times[(2J+1)(2J'+1)]^{\frac{1}{2}} \begin{pmatrix} J' & k & J \\ -\Omega' & q & \Omega \end{pmatrix} \\ & \times[\langle n'\beta'\Omega'v' \mid V_q^k(e_A) \mid n\beta\Omega v\rangle + \langle n'\beta'\Omega'v' \mid V_q^k(e_B) \mid n\beta\Omega v\rangle], \end{aligned} \quad \text{(B.10)}$$

since I_2 is homonuclear.

On rearranging we get

$$\begin{aligned}\langle n'\Omega' \mid H_{hf} \mid n\Omega\rangle = & \\ & \sum_k \delta_{FF'}\delta_{M_F M_{F'}}(-1)^{F+\Delta I+\Delta J+k-\Omega'} \begin{Bmatrix} FI'J' \\ kJI \end{Bmatrix} \\ & \times[(2I+1)(2I'+1)]^{\frac{1}{2}} \begin{Bmatrix} I_A & I_A & I \\ k & I' & I_A \end{Bmatrix} \\ & \times\langle \tau' I_A M_{I_A} = I_A \mid \mathbf{Q}^{(k)}(I_A) \mid \tau I_A M_{I_A} = I_A\rangle \left[\begin{pmatrix} I_A & k & I_A \\ -I_A & 0 & I_A \end{pmatrix}\right]^{-1} \\ & \times[(2J+1)(2J'+1)]^{\frac{1}{2}} \begin{pmatrix} J' & k & J \\ -\Omega' & q & \Omega \end{pmatrix} \\ & \times[\langle n'\beta'\Omega'v' \mid V_q^k(e_A) \mid n\beta\Omega v\rangle + \langle n'\beta'\Omega'v' \mid V_q^k(e_B) \mid n\beta\Omega v\rangle],\end{aligned} \tag{B.11}$$

where $q = \Delta\Omega = \Omega' - \Omega$, $\Delta I = I - I'$ and $\Delta J = J - J'$. In equation (B.11) the first line includes terms relating to the coupling of the two subsystems in the composite coupling scheme, $\mathbf{F} = \mathbf{I} + \mathbf{J}$; the second and third lines contain the terms relating to the nuclear spin subsystem, the fourth and fifth lines those terms relating to the electronic coordinates. All the Wigner coefficients in equation (B.11) can be calculated from standard formulae and the matrix element for the nuclear subsystem has a known value from experiment: the evaluation of the electronic matrix element is considered in the next section.

B.2 The electronic reduced matrix element

The general expression (B.11) line 5 involves a $\langle V_q^k(e_\alpha)\rangle$ term that needs to be evaluated before fits with experimental data can be made. Vigué *et al* [152] have shown that to a good approximation

$$\sum_{\alpha=A,B} \langle n'\beta'\Omega'v' \mid V_q^k(e_\alpha) \mid n\beta\Omega v\rangle = \langle v \mid v'\rangle \sum_{\alpha=A,B} \langle n'\beta'\Omega' \mid \overline{V_q^k}(e_\alpha) \mid n\beta\Omega\rangle, \tag{B.12}$$

for $k = 1$ or 2. $\langle v \mid v'\rangle$ is the Franck-Condon overlap between the interacting states and the matrix element on the right-hand side, $\langle \overline{V_q^k}(e_\alpha)\rangle$, involves only

the electronic wavefunctions and a M_J dependent $3-j$ coefficient. The Franck-Condon overlap between the two states can be calculated numerically from the potential functions for the two states: the $\langle\overline{V_q^k}(e_\alpha)\rangle$ term can be related to known experimental data.

Since we are concerned with highly excited vibrational states, the molecule will spend a large amount of its vibrational period near the outer turning point of its motion. Furthermore the significant Franck-Condon overlap between the interacting states also lies at the outer turning point of their vibrational motions, so, to calculate the $\langle\overline{V_q^k}(e_\alpha)\rangle$ term, we should best describe the electronic wavefunctions using the separated atom basis set outlined in section 1.1.1. In this basis the 10 states at the (ab) dissociation limit have normalised electronic wavefunctions of the form (see Table 1.3)

$$|\, n\Omega=0\rangle_{u/g}^{(+/-)} = \mathcal{A}\ \tfrac{1}{2}\{(|\,\tfrac{3}{2}\tfrac{1}{2}\rangle_A\,|\,\tfrac{1}{2}-\tfrac{1}{2}\rangle_B \pm |\,\tfrac{1}{2}-\tfrac{1}{2}\rangle_A\,|\,\tfrac{3}{2}\tfrac{1}{2}\rangle_B) \pm(|\,\tfrac{3}{2}-\tfrac{1}{2}\rangle_A\,|\,\tfrac{1}{2}\tfrac{1}{2}\rangle_B \pm |\,\tfrac{1}{2}\tfrac{1}{2}\rangle_A\,|\,\tfrac{3}{2}-\tfrac{1}{2}\rangle_B)\}, \tag{B.13}$$

$$|\, n\Omega\neq 0\rangle_{u/g} = \mathcal{A}\ \tfrac{1}{\sqrt{2}}\{|\,\tfrac{3}{2}M_1\rangle_A\,|\,\tfrac{1}{2}M_2\rangle_B \pm |\,\tfrac{1}{2}M_2\rangle_A\,|\,\tfrac{3}{2}M_1\rangle_B\}, \tag{B.14}$$

with the *ungerade* taking the positive inversion term. All 10 states can therefore be written

$$|\, n\Omega\rangle = \sum_m C_m\,|\,J_mM_m\rangle_A\,|\,J'_mM'_m\rangle_B, \tag{B.15}$$

and we need to calculate matrix elements of the form

$$\begin{aligned}&\sum_{\alpha=A,B}\langle n'\beta'\Omega'\,|\,\overline{V_q^k}(e_\alpha)\,|\,n\beta\Omega\rangle \\ &=\textstyle\sum_{l,m}\sum_{\alpha=A,B} C_lC_m\langle J_lM_l\,|\,\overline{V_q^k}(e_\alpha)\,|\,J_mM_m\rangle_\alpha\langle J'_lM'_l\,|\,J'_mM'_m\rangle_\beta \\ &=\textstyle\sum_{l,m}\sum_{\alpha=A,B}\delta_{J_mJ_l}\delta_{M'_mM'_l}C_lC_m\langle J_lM_l\,|\,\overline{V_q^k}(e_\alpha)\,|\,J_mM_m\rangle_\alpha.\end{aligned} \tag{B.16}$$

The matrix elements on the right-hand side contain the M_J dependent $3-j$ coefficient from equation (B.9)

$$\langle JM'\,|\,\overline{V_q^{(k)}}\,|\,JM\rangle = \begin{pmatrix} J & k & J \\ -M' & 0 & M\end{pmatrix}\langle J\|\overline{V^k}\|J\rangle. \tag{B.17}$$

The reduced matrix element can be calculated from the experimental magnetic dipolar and electric quadrupolar hyperfine parameters, a_J and q_J,

$$\langle JM = J \mid \overline{V_q^{(k)}} \mid JM = J \rangle = \begin{pmatrix} J & k & J \\ -J & 0 & J \end{pmatrix} \langle J \| \overline{V^k} \| J \rangle$$

$$\Rightarrow \langle \frac{3}{2} \| \overline{V^1} \| \frac{3}{2} \rangle = \sqrt{15} a_{\frac{3}{2}} / \mu_N g_I, \tag{B.18}$$

$$\langle \frac{1}{2} \| \overline{V^1} \| \frac{1}{2} \rangle = \sqrt{\tfrac{3}{2}} a_{\frac{1}{2}} / \mu_N g_I, \tag{B.19}$$

$$\langle \frac{3}{2} \| \overline{V^2} \| \frac{3}{2} \rangle = \sqrt{5} q_{\frac{3}{2}}, \tag{B.20}$$

where μ_N is the nuclear magneton and g_I the appropriate nuclear g-factor. For I_2 $a_{\frac{3}{2}} = 827$MHz, $a_{\frac{1}{2}} = 6591$MHz [153] and $eq_{\frac{3}{2}}Q_I = 2292.8$MHz [144, p.243], so a complete calculation of the matrix elements on the left-hand side of equation (B.16) can be made for all 10 (ab) states that couple with the $B0_u^+(ab)$ state, with $k = 1$ and 2. The results are given in Table 4.4.

Appendix C Some Theorems on the Matrix Elements of Irreducible Tensor Operators

The results given below are quoted from standard texts [114, 149, 150, 151].

The Wigner-Eckart Theorem

For the basis functions $|\,\tau jm\rangle$, with jm as angular momentum quantum numbers and τ the additional quantum numbers needed to completely specify the state, the Wigner-Eckart theorem states

$$\langle \tau' j' m' \mid \mathbf{T}^{(k)}_q \mid \tau j m \rangle = (-1)^{j'-m'} \begin{pmatrix} j' & k & j \\ -m' & q & m \end{pmatrix} \langle \tau' j' \| \mathbf{T}^{(k)} \| \tau j \rangle \qquad \text{(C.1)}$$

where the symbol in brackets is a Wigner *3-j* coefficient and $\langle \tau' j' \| \mathbf{T}^{(k)} \| \tau j \rangle$ the reduced matrix element of the irreducible tensor operator, $\mathbf{T}^{(k)}$. Numerical values for the Wigner *3-j* coefficient can be calculated from the algebraic formulae for the related Clebsch-Gordan coefficients given in Brink and Satchler [114, p.36], and are non-zero only if the elements in the second row sum to zero; the term on the left-hand side is usually known from experimental data for $\tau' = \tau$ and $j' = j = m' = m$, so the reduced matrix element can be evaluated. The matrix elements of the tensorial operator therefore factorise into two parts: the projection (geometry) dependent terms are contained in the Wigner *3-j* coefficient while the reduced matrix element depends on the detailed physical interactions themselves.

Reduction of matrices for composite systems

If the tensor operators $\mathbf{T}^{(k)}$ and $\mathbf{U}^{(k)}$ act on subsystems 1 and 2 respectively of a system, with subsystem 1 characterised by the angular momentum $\mathbf{j_1}$ and subsystem 2 by angular momentum $\mathbf{j_2}$, then the matrix elements of the scalar product of these two tensor operators in the coupled basis $\mathbf{J} = \mathbf{j_1} + \mathbf{j_2}$ are given by

$$\langle \tau_1' j_1' \tau_2' j_2' J' M' \mid \mathbf{T}^{(k)}.\mathbf{U}^{(k)} \mid \tau_1 j_1 \tau_2 j_2 J M \rangle = \tag{C.2}$$
$$\delta_{JJ'}\delta_{MM'}(-1)^{j_1+j_2'+J} \begin{Bmatrix} J & j_2' & j_1' \\ k & j_1 & j_2 \end{Bmatrix} \langle \tau_1' j_1' \| \mathbf{T}^{(k)} \| \tau_1 j_1 \rangle \langle \tau_2' j_2' \| \mathbf{U}^{(k)} \| \tau_2 j_2 \rangle,$$

where the symbol in braces is a Wigner *6-j* coefficient and τ_i represents additional quantum numbers characterising subsystem i. Numerical values for the Wigner *6-j* coefficients can be calculated from the algebraic formulae for the related Racah coefficients also given in Brink and Satchler [114, p.43]. Note that the two tensor operators must commute.

For a tensor operator $\mathbf{T}^{(k)}$ acting only on the space of subsystem 1, the relationship between its matrix element in the coupled and uncoupled representation is

$$\langle \tau_1' j_1' \tau_2 j_2 J' \mid \mathbf{T}^{(k)} \mid \tau_1 j_1 \tau_2 j_2 J \rangle = (-1)^{j_1'+j_2+J+k}[(2J+1)(2J'+1)]^{\frac{1}{2}} \times \begin{Bmatrix} j_1' & J' & j_2 \\ J & j_1 & k \end{Bmatrix} \langle \tau_1' j_1' \| \mathbf{T}^{(k)} \| \tau_1 j_1 \rangle. \tag{C.3}$$

Note that the states have common quantum numbers in the subsystem not acted upon by the tensor operator, all other terms are zero.

Rotation Matrix Elements

From Brink and Satchler [114, Appendix 5]

$$\int \mathcal{D}^C_{cc'}(\alpha\beta\gamma)\mathcal{D}^A_{aa'}(\alpha\beta\gamma)\mathcal{D}^B_{bb'}(\alpha\beta\gamma)\sin\beta d\beta d\alpha d\gamma = [(2C+1)(2B+1)]^{\frac{1}{2}} \begin{pmatrix} A & B & C \\ a & b & c \end{pmatrix} \begin{pmatrix} A & B & C \\ a' & b' & c' \end{pmatrix}. \tag{C.4}$$

Bibliography

[1] S.R.Langhoff, C.W.Bauschlicher, and H.Partridge. *Comparison of ab initio Quantum Chemistry with Experiment for Small Molecules.* Reidel, Dordrecht, 1985. ed. R.J.Bartlett.

[2] U.Wolf and E.Tiemann. *Chem. Phys.*, 119:407–418, 1988.

[3] C.A.Brau. *Excimer Lasers.* Springer, Berlin, 1984.

[4] A.B.Callear and M.P.Metcalfe. *Chem. Phys. Lett.*, 43:197–200, 1976.

[5] L.D.Mikheev, A.R.Shirokikh, A.V.Startsev, and V.S.Zuev. *Optics Comm.*, 26:237–239, 1978.

[6] K.P.Killeen and J.G.Eden. *J. Opt. Soc. Am. B*, 2:430–432, 1985.

[7] K.P.Killeen and J.G.Eden. *Appl. Phys. Lett.*, 43:539–541, 1983.

[8] A.B.Callear, P.Erman, and J.Kurepa. *Chem. Phys. Lett.*, 44:599–601, 1976.

[9] M.Diegelmann, K.Hohla, F.Rebentrost, and K.L.Kompa. *J. Chem. Phys.*, 76:1233–1246, 1982.

[10] M.J.Shaw, C.B.Edwards, F.O'Niell, C.Fotakis, and R.J.Donovan. *Appl. Phys. Lett.*, 37:346–348, 1980.

[11] J.Tellinghuisen. *J. Phys. Chem.*, 87:5136–5140, 1983.

[12] P.J.Jewsbury, K.P.Lawley, T.Ridley, and R.J.Donovan. Submitted to *Chemical Physics.*

[13] T.Ishiwata, H.Othoshi, M.Sakaki, and I.Tanaka. *J. Chem. Phys.*, 80:1411–1416, 1984.

[14] K.P.Lawley, P.J.Jewsbury, T.Ridley, P.R.R.Langridge-Smith, and R.J.Donovan. Accepted by *Molecular Physics.*

[15] A.J.Holmes, K.P.Lawley, T.Ridley, R.J.Donovan, and P.R.R.Langridge-Smith. *J. Chem. Soc. Faraday Trans.*, 87:15–18, 1991.

[16] S.Churassy, F.Martin, R.Bacis, J.Vergès, and R.W.Field. *J. Chem. Phys.*, 75:4863–4868, 1981.

[17] F.Martin, S.Churassy, R.Bacis, R.W.Field, and J.Vergès. *J. Chem. Phys.*, 79:3725–3737, 1983.

[18] J.Tellinghuisen. *J. Chem. Phys.*, 82:4012–4016, 1985.

[19] V.S.Viswanathan and J.Tellinghuisen. *J. Mol. Spec.*, 101:285–299, 1983.

[20] K.S.Viswanathan, A.Sur, and J.Tellinghuisen. *J. Mol. Spec.*, 86:393–405, 1981.

[21] J.Tellinghuisen. *J. Mol. Spec.*, 94:231–252, 1982.

[22] J.B.Koffend, A.M.Sibai, and R.Bacis. *J. Phys.*, 43:1639–1651, 1982.

[23] R.J.Leroy. *J. Chem. Phys.*, 52:2683–2689, 1970.

[24] G.Herzberg. *Spectra of Diatomic Molecules*, volume 1 of *Molecular Spectra and Molecular Structure.* Van Nostrand, Princeton, 1950.

[25] R.S.Mulliken. *J. Chem. Phys.*, 55:288–308, 1971.

[26] R.Bacis, M.Broyer, S.Churassy, J.Vergès, and J.Vigué. *J. Chem. Phys.*, 73:2641–2650, 1980.

[27] J.P.Pique, R.Bacis, M.Broyer, S.Churassy, and J.B.Koffend. *J. Chem. Phys.*, 80:1390–1393, 1984.

[28] M.Saute and M.Aubert-Frécon. *J. Chem. Phys.*, 77:5639–5646, 1982.

[29] G.W.King and T.D.McLean. *J. Mol. Spec.*, 135:207–222, 1989.

[30] T.Ishiwata, A.Tokunaga, T.Shinzawa, and I.Tanaka. *J. Mol. Spec.*, 117:89–101, 1986.

[31] A.R.Hoy and A.W.Taylor. *J. Mol. Spec.*, 126:484–485, 1987.

[32] T.Ishiwata, T.Kusayanagi, T.Hara, and I.Tanaka. *J. Mol. Spec.*, 119:337–351, 1986.

[33] J.S.Hickmann, C.R.M.de Oliveira, and R.E.Francke. *J. Mol. Spec.*, 127:556–558, 1988.

[34] G.W.King, I.M.Littlewood, and J.R.Robins. *Chem. Phys.*, 56:145–156, 1981.

[35] J.C.D.Brand, A.R.Hoy, A.K.Kalkar, and A.B.Yamashita. *J. Mol. Spec.*, 95:350–358, 1982.

[36] T.Ishiwata and I.Tanaka. *Laser Chem.*, 7:79–93, 1987.

[37] A.R.Hoy and R.H.Lipson. *Chem. Phys.*, 140:187–193, 1990.

[38] J.P.Perrot, B.Femelat, M.Broyer, and J.Chevaleyre. *Mol. Phys.*, 61:97–108, 1987.

[39] J.Tellinghuisen, S.Fei, X.Zheng, and M.C.Heaven. *Chem. Phys. Lett.*, 176:373–378, 1991.

[40] J.C.D.Brand and A.R.Hoy. *Appl. Spec. Rev.*, 23:285–328, 1987.

[41] E.U.Condon and G.H.Shortley. *The Atomic Theory of Atomic Spectra.* Cambridge University Press, Cambridge, 1963.

[42] C.E.Moore. *Atomic Energy Levels*, volume 3. National Bureau of Standards, Washington, 1971.

[43] S.Huzinaga(ed.), J.Andzelm, M.Kłobukowski, E.Radzio-Andzelm, Y.Sakai, and H.Tatewaki. *Gaussian Basis Sets for Molecular Calculations*, volume 16 of *Physical Sciences Data*. Elsevier, New York, 1984.

[44] J.C.D.Brand and A.R.Hoy. *J. Mol. Spec.*, 97:379–386, 1983.

[45] J.Tellinghuisen. *Can. J. Phys.*, 62:1933–1940, 1984.

[46] R.J.Donovan, M.A.MacDonald, K.P.Lawley, A.J.Yencha, and A.Hopkirk. *Chem. Phys. Lett.*, 138:571–574, 1987.

[47] G.Das and A.C.Wahl. *J. Chem. Phys.*, 69:53–62, 1978.

[48] J.B.Koffend, R.Bacis, M.Broyer, J.P.Pique, and S.Churassy. *Laser Chem.*, 1:343–355, 1983.

[49] A.J.Bouvier, R.Bacis, A.Bouvier, M.Broyer, S.Churassy, and J.P.Perrot. *Optics Comm.*, 51:403–408, 1984.

[50] H.Knöckel, H.Richter, M.Siese, and E.Tiemann. *Mol. Phys.*, 68:917–930, 1989.

[51] M.Wu and P.M.Johnson. *J. Chem. Phys.*, 90:74–80, 1989.

[52] A.Hiraya, K.Shobotake, R.J.Donovan, and A.Hopkirk. *J. Chem. Phys.*, 88:52–57, 1988.

[53] A.R.Hoy, S.M.Jaywant, and J.C.D.Brand. *Mol. Phys.*, 60:749–759, 1987.

[54] A.Kvaran, A.Yencha, R.J.Donovan, and A.Hopkirk. Accepted by *Chemical Physics Letters.*

[55] R.W.Wood. *Philos. Mag.*, 24:673, 1912.

[56] J.C.McLennan. *Proc. Roy. Soc. (London) A*, 88:289, 1914.

[57] R.S.Mulliken. *Phys. Rev.*, 36:1440–1450, 1930.

[58] R.S.Mulliken. *Rev. Mod. Phys.*, 4:1–86, 1932.

[59] R.S.Mulliken. *J. Chem. Phys.*, 8:234–243, 1940.

[60] R.S.Mulliken. *J. Chem. Phys.*, 7:14–34, 1939.

[61] R.S.Mullliken. *Phys. Rev.*, 50:1017–1027, 1936.

[62] J.I.Steinfeld, R.N.Zare, L.Jones, M.Lesk, and W.Klemperer. *J. Chem. Phys.*, 42:25–33, 1965.

[63] H.Cordes. *Z. Physik*, 97:603–624, 1935.

[64] J.A.Myer and J.A.R.Samson. *J. Chem. Phys.*, 52:716–718, 1970.

[65] P.Venkateswarlu. *Can. J. Phys.*, 48:1055–1080, 1970.

[66] J.Tellinghuisen, M.R.McKeever, and A.Sur. *J. Mol. Spec.*, 82:225–245, 1980.

[67] A.G.Briggs and R.G.W.Norrish. *Proc. Roy. Soc.*, A276:51–68, 1963.

[68] A.Sur and J.Tellinghuisen. *J. Mol. Spec.*, 88:323–346, 1981.

[69] J.Tellinghuisen and D.K.Chakraborty. *Chem. Phys. Lett.*, 134:565–569, 1987.

[70] H.Hemmati and G.J.Collins. *Chem. Phys. Lett.*, 75:488–493, 1980.

[71] J.Tellinghuisen. *Chem. Phys. Lett.*, 49:485–490, 1977.

[72] A.L.Guy, K.S.Viswanathan, A.Sur, and J.Tellinghuisen. *Chem. Phys. Lett.*, 73:582–588, 1980.

[73] S.H.Lin, Y.Fujimura, H.J.Neusser, and E.W.Schlag. *Multiphoton Spectroscopy of Molecules.* Quantum Electronics- Principles and Applications. Academic Press, Orlando, 1984.

[74] M.N.R.Ashfold. *Mol. Phys.*, 58:1–20, 1986.

[75] F.W.Dalby, G.Petty-Sil, M.H.L.Pryce, and C.Tai. *Can. J. Phys.*, 55:1033–1046, 1977.

[76] K.K.Lehmann, J.Smolarek, and L.Goodman. *J. Chem. Phys.*, 69:1569–1573, 1978.

[77] A.D.Williamson and R.N.Compton. *Chem. Phys. Lett.*, 62:295–299, 1979.

[78] T.Ridley, K.P.Lawley, R.J.Donovan, and A.Yencha. *Chem. Phys.*, 148:315–323, 1990.

[79] J.C.Miller. *J. Phys. Chem.*, 91:2589–2592, 1987.

[80] D.L.Rousseau and P.F.Williams. *Phys. Rev. Lett.*, 33:1368–1372, 1974.

[81] A.R.Hoy and J.C.D.Brand. *Chem. Phys.*, 109:109–115, 1986.

[82] K.Chen, L.E.Steenhoek, and E.S.Yeung. *Chem. Phys. Lett.*, 59:222–225, 1978.

[83] T.Ishiwata, A.Ishiguro, and K.Obi. *J. Mol. Spec.*, 147:321–333, 1991.

[84] J.Si, T.Ishiwata, and K.Obi. *J. Mol. Spec.*, 147:334–345, 1991.

[85] T.Ishiwata, A.Ishiguro, and K.Obi. *J. Mol. Spec.*, 147:300–320, 1991.

[86] K.Kasatani, Y.Tanaka, K.Shibuya, M.Kawasaki, K.Obi, H.Sato, and I.Tanaka. *J. Chem. Phys.*, 74:895–899, 1981.

[87] M.D.Danyluk and G.W.King. *Chem. Phys.*, 22:59–70, 1977.

[88] J.Tellinghuisen. *Phys. Rev. Lett.*, 34:1137–1140, 1975.

[89] J.Chevaleyre, J.P.Perrot, J.M.Chastan, S.Valignat, and M.Broyer. *Chem. Phys.*, 67:59–64, 1982.

[90] G.W.King, I.M.Littlewood, and J.R.Robins. *Chem. Phys.*, 68:129–136, 1982.

[91] J.P.Perrot, B.Femelat, J.L.Subtil, M.Broyer, and J.Chevaleyre. *Mol. Phys.*, 61:85–95, 1987.

[92] P.J.Jewsbury, K.P.Lawley, T.Ridley, F.F.Al-Adel, P.R.R.Langridge-Smith, and R.J.Donovan. *Chem. Phys.*, 151:103–109, 1991.

[93] A.J.Holmes. PhD thesis, Edinburgh University, 1989.

[94] R.J.Donovan, A.J.Holmes, P.R.R.Langridge-Smith, and T.Ridley. *J. Chem. Soc. Faraday Trans.*, 84:541–548, 1988.

[95] G.R.Harrison. *Wavelength Tables.* John Wiley and Sons, New York, 1939.

[96] M.Born and J.R.Oppenheimer. *Ann. Phys.*, 84:457, 1927.

[97] K.P.Lawley and R.Wheeler. *J. Chem. Soc. Faraday Trans.*, 77:1133–1141, 1981.

[98] D.I.Austin. PhD thesis, Edinburgh University, 1987.

[99] V.V.Eryomin and N.E.Kuz'menko. *Chem. Phys.*, 136:127–139, 1989.

[100] J.Tellinghuisen. *Photodissociation and Photoionisation*, volume 60 of *Advances in Chemical Physics.* John Wiley and Sons, Chichester, 1985. ed. K.P.Lawley.

[101] J.Telinghuisen. *Chem. Phys. Lett.*, 29:359–363, 1974.

[102] J.P.Pique, F.Hartmann, S.Churassy, and R.Bacis. *J. Phys.*, 47:1917–1929, 1986.

[103] A.Dalgarno, G.Herzberg, and T.L.Stephens. *Astrophys. J.*, 162:L49–L53, 1970.

[104] R.S.Mulliken. *J. Chem. Phys.*, 55:309–314, 1971.

[105] J.Tellinghuisen. *J. Mol. Spec.*, 103:455–465, 1984.

[106] L.D.Landau and E.M.Lifshitz. *Quantum Mechanics-Nonrelativistic Theory.* Pergamon, London, 1958.

[107] J.Tellinghuisen, G.Pichler, W.L.Snow, M.E.Hillard, and R.J.Exton. *Chem. Phys.*, 50:313, 1980.

[108] C.Noda and R.N.Zare. *J. Mol. Spec.*, 95:254–270, 1982.

[109] P.Jewsbury and K.Lawley. *Chem. Phys.*, 141:225–239, 1990.

[110] Russell and Saunders. *Astrophys. J.*, 61:38, 1925.

[111] J.C.Slater. *Phys. Rev.*, 38:1109–1144, 1931.

[112] J.C.Slater. *Phys. Rev.*, 34:1293–1322, 1929.

[113] A.D.Buckingham. *Quarterly Reviews*, 13:183–214, 1959.

[114] D.M.Brink and G.R.Satchler. *Angular Momentum.* Oxford Library of the Physical Sciences. Oxford University Press, Oxford, 1962.

[115] J.P.Desclaux. *At. Data Nucl. Data Tables*, 12:311–406, 1973.

[116] T.Y.Chang. *Reviews of Modern Physics*, 39:911–942, 1967.

[117] E.P.Gordeev, S.Ya.Umansky, and A.I.Voronin. *Chem. Phys. Lett.*, 23:524–528, 1973.

[118] J.Li and K.Balasubramanian. *J. Mol. Spec.*, 138:162–180, 1989.

[119] J.Hutson, S.Gerstenkorn, P.Luc, and J.Sinzelle. *J. Mol. Spec.*, 96:266–278, 1982. see erratum in JMS 97:224, 1983.

[120] ed. P.R.Bevington. *Data Reduction and Error Analysis for the Physical Sciences.* MacGraw-Hill, New York, 1969.

[121] M.Broyer, J.Vigué, and J.C.Lehmann. *J. Phys.*, 39:591–609, 1978.

[122] J.P.Pique, F.Hartmann, S.Churassy, and R.Bacis. *J. Phys.*, 47:1909–1916, 1986.

[123] P.R.Bunker. *Molecular Symmetry and Spectroscopy.* Academic Press, New York, 1979.

[124] S.Gerstenkorn and P.Luc. *Atlas du Spectre d'Absorption de la Molecule d'Iode.* Centre National de la Recherche Scientifique, Paris, 1978.

[125] M.A.A.Clyne and I.S.McDermid. *Electronically excited states of small molecules.* Dynamics of the Excited State. John Wiley and Sons, New York, 1982. (ed. K.P.Lawley).

[126] M.C.Sauer, W.A.Mulac, R.Cooper, and F.Grieser. *J. Chem. Phys.*, 64:4587–4591, 1976.

[127] J.Tellinghuisen and L.F.Phillips. *J. Phys. Chem.*, 90:5108–5120, 1986.

[128] S.J.Harris, W.C.Natzle, and C.B.Moore. *J. Chem. Phys.*, 70:4215–4219, 1979.

[129] M.Kitamura, T.Kondow, K.Kuchitsu, T.Munakata, and T.Kasuya. *Chem. Phys. Lett.*, 118:130–133, 1985.

[130] G.A.Capelle and H.P.Broida. *J. Chem. Phys.*, 58:4212–4222, 1973.

[131] G.W.Holleman and J.I.Steinfeld. *Chem. Phys. Lett.*, 12:431–433, 1971.

[132] T.Suzuki and T.Kasuya. *J. Chem. Phys.*, 81:4818–4825, 1984.

[133] J.Tellinghuisen. *J. Chem. Phys.*, 57:2397–2402, 1972.

[134] C.D.Olson and K.K.Innes. *J. Chem. Phys.*, 64:2405–2411, 1976.

[135] M.A.A.Clyne and M.C.Heaven. *J. Chem. Soc. Faraday Trans.*, 76:49–66, 1980.

[136] A.V.Stolyarov, N.E.Kuz'menko, Ya.A.Harya, and R.S.Ferber. *J. Mol. Spec.*, 137:251–267, 1989.

[137] J.N.Demas. *Excited State Lifetime Measurements.* Academic Press, New York, 1983. Chapter 8.

[138] D.V.O'Connor and D.Phillips. *Time-correlated Single Photon Counting.* Academic Press, New York, 1984. Chapter 6.

[139] D.L.Rousseau. *J. Mol. Spec.*, 58:481–483, 1975.

[140] K.P.Lawley. *Chem. Phys.*, 127:363–371, 1988.

[141] T.Ridley. Private communication.

[142] T.Ishiwata, T.Hara, K.Obi, and I.Tanaka. *J. Phys. Chem.*, 95:2763–2769, 1991.

[143] T.Ridley, K.P.Lawley, and R.J.Donovan. Unpublished results.

[144] C.H.Townes and A.L.Schawlow. *Microwave Spectroscopy.* New York Dover, London, 1975.

[145] J.H.van Vleck. *Phys. Rev.*, 33:467–506, 1929.

[146] J.C.D.Brand, A.R.Hoy, and A.C.Risbud. *J. Mol. Spec.*, 113:47–53, 1985.

[147] D.Bussieres and A.R.Hoy. *Can. J. Phys.*, 62:1941–1946, 1984.

[148] P.J.Jewsbury, K.P.Lawley, T.Ridley, and R.J.Donovan. Submitted to *Chemical Physics Letters.*

[149] R.L.Cook and F.C.de Lucia. *Am. J. Phys.*, 39:1433–1454, 1971.

[150] M.Weissbluth. *Atoms and Molecules.* Academic Press, New York, 1978.

[151] A.R.Edmonds. *Angular Momentum in Quantum Mechanics.* Investigations in Physics. Princeton University Press, Princeton, 1957.

[152] J.Vigué, M.Broyer, and J.C.Lehmann. *Phys. Rev. Lett.*, 42:883–887, 1979.

[153] E.Luc-Koenig, C.Morillon, and J.Vergès. *Physica*, 70:175–189, 1973.

University Regulations

Whilst pursuing postgraduate research at the Department of Chemistry I have attended the following conferences in fulfilling University regulations

- High Resolution Spectroscopy Group (Royal Society of Chemistry), Nottingham University, December 1989.
- Joint Heriot-Watt/Edinburgh Laser Spectroscopy Colloquium, Heriot-Watt University, March 1990.
- High Resolution Spectroscopy Group (Royal Society of Chemistry), University College London, December 1990.
- SRS users, Daresbury Laboratory, March 1991.

I delivered papers from my work at the Heriot-Watt and UCL meetings. I have also attended various University courses as required by my work

- Fortran programming (EUCS)
- Emas-to-Unix transition (EUCS)
- Uniras guide (EUCS)
- Lasers (Physics)
- Theoretical Chemistry (Chemistry)

I have regularly attended the Departmental and Laser Group research seminars, presenting my work to both groups.

Publications

Chemical Physics 141 (1990) 225–239
North-Holland

A MODEL FOR THE RELATIVE INTENSITIES AMONG ION PAIR→VALENCE TRANSITIONS IN THE HEAVIER HALOGENS AND RARE GAS HALIDES

Philip JEWSBURY and Kenneth LAWLEY
University of Edinburgh, Department of Chemistry, West Mains Road, Edinburgh EH9 3JJ, UK

Received 17 July 1989

The separated atom or $(J_A M_A J_B M_B)$ coupling scheme is applied to the electronic structure of both ion pair and valence states of the heavier halogens and rare gas halides. Relative transition moments from low vibrational levels of selected ion pair states to all the valence states and the resulting radiative lifetimes are derived. $\sigma \leftrightarrow \sigma$ electron transfer between atomic orbitals is assumed for parallel transitions. Russell–Saunders coupling is used for the atomic or ionic basis functions in the reference model. Departures from the model arising from partial *jj* coupling in the halogen positive ions and from intramolecular electrostatic effects each produce characteristic changes in the relative intensities of the various fluorescent systems from a given ion pair state. The effect of J and M_J state mixing between asymptotically degenerate valence states is discussed and ion pair→valence transition intensities are shown to be a sensitive function of this mixing.

1. Introduction

The spectroscopy of the ion pair (IP) states of diatomic molecules is unusual in that, depending on the amplitude of the vibrational motion, two quite different descriptions of the electronic configurations are explored. At small separations, typically vertically above the equilibrium separation of the ground state, $r_e(X)$, a description in terms of single molecular orbital configurations is appropriate with some mixing due to spin–orbit coupling and electron correlation. At larger separations the most compact description of an IP state is the product of atomic ion states, $A^+(J_A M_A)B^-(J_B M_B)$, which implies separate spin–orbit coupling on each ion as required in the dissociation limit. In the case of valence and Rydberg states such an asymptotic configuration, then the product of neutral atom states is only reached well beyond the equilibrium separations and is difficult to access experimentally. The evidence for an essentially unperturbed product ion description of IP states around their equilibrium separation, $r_e(IP)$, is slightly indirect, being mainly drawn from the perturbations observed in vibrational term values due to Coriolis coupling [1], from the hyperfine splitting [2] and, more directly, from the general arrangement of molecular electronic term values which closely follows that of the separated ions. The principal application of the model has been to the I^+ ion in I_2 and ICl, though J_A still seems to remain a good quantum number for Br^+ in Br_2 [3,4]. In section 3 we apply the $(J_A J_B)$ coupling scheme as a limiting model to both IP and valence states of the halogens and rare gas excimers and derive some lifetimes and integrated intensity ratios for the fluorescence that is such a striking feature of the spectroscopy of these states.

The treatment of Coriolis coupling in the low vibrational levels of ion pair states has invoked the pure precession model of Van Vleck [5]. For our purposes, in which rotational coupling of the electronic motion to the overall molecular rotation can be neglected, the relevant part of this model amounts to treating J and M of the two ions separately as good quantum numbers and if the negative ion is a halide ion ($J_B = M_B = 0$) the ion pair state is classified by $(J_A M_A)$ alone. Furthermore, in calculating transition matrix elements we will apply the same model to the lower valence states, which will thus be specified by $(J''_A M''_A J''_B M''_B)$ and are, in effect, atom-pair (AP) states with symmetry imposed interchange of the labels A and B in the homonuclear case. This has been called simply the $(J_A J_B)$ model by Herzberg [6] who introduced it as a hypothetical case and by Saute and

0301-0104/90/$ 03.50

Aubert-Frecon [7] in discussing the asymptotic behaviour of the valence states of iodine. Gordeev et al. [8] earlier used this model for the valence states of chlorine and bromine and its principal application has been to the asymptotic energy splitting of these states, though the $J_A J_B$ coupling scheme has also been applied to the magnetic predissociation of the B state of iodine [9]. The longest range breakdown of the $J_A J_B$ model arises from the r^{-3} quadrupole–charge interaction in IP states and the r^{-5} quadrupole–quadrupole interaction in AP states. These are discussed briefly in section 3.3 and in appendix C. Overall, the smaller the spin–orbit coupling the larger the separation at which the model breaks down. Among the halogens the model will thus hold better for compounds of Br and I; in Cl_2 the model, if applicable to any useful extent, could only be used beyond the outer minimum of IP states and not at the inner rydbergised minimum [10,11].

The $(J_A J_B)$ coupling scheme has not been applied to the IP↔valence transitions of the halogens apparently because Mulliken's influential paper "Iodine Revisited" [12] was couched entirely in MO terminology and addressed mainly IP←X absorption. However, fluorescence from low vibrational levels v' of IP states and even some regions of dispersed fluorescence (e.g. the red extremum) from very high v' levels is dominated by transitions around $r_e(\mathrm{IP})$. We suggest that the $(J_A J_B)$ coupling scheme is appropriate in these cases rather than Hund's case (a) or case (c) (in which the atomic states are not specified). In contrast, Dunning and Hay [13] use an MO basis with configuration interaction in their discussion of the spectroscopy of the rare gas halides.

2. Transition dipole moments in the $J_A J_B$ coupling scheme

Ion pair state wavefunctions for the homonuclear halogens in the $(J_A J_B)$ model are of the form

$$|n\Omega\rangle_{g,u} = \mathscr{A}\{|JM\rangle_A|00\rangle_B \pm |00\rangle_A|JM\rangle_B\}/\sqrt{2} \tag{1}$$

and for the interhalogens or rare gas halides, A^+B^-,

$$|n\Omega\rangle = \mathscr{A}\{|JM\rangle_A|00\rangle_B\}, \tag{2}$$

where $\mathscr{A}$ is the partial antisymmetriser for electron permutation between the two ions and $\Omega = |M|$. n sequentially numbers states that have the same Ω value in ascending order of energy. Thus in the halogen IP$(0^+_{g,u})$ states, $0^+_{g,u}(1)$ correlate with $A^+(^3P_{20})$, $0^+_{g,u}(2)$ with $A^+(^3P_{00})$, $0^+_{g,u}(3)$ with $A^+(^1D_{20})$, $0^+_{g,u}(4)$ with $A^+(^1S_0)$, the unique pair $0^-_{g,u}$ with $A^+(^3P_{10})$ and so forth. The index n thus also numbers the cluster to which the state belongs, a cluster referring to a group of different Ω states correlating with the same J state of the positive ion. An essential ingredient of the $(J_A J_B)$ coupling scheme for IP states is that there is no mixing of different J states of A^+ under the strong Stark field of the neighbouring anion.

The valence state wavefunctions in the homonuclear case are similarly approximated by

$$|n\Omega\rangle_{g,u} = \mathscr{A}\{|J_1M_1\rangle_A|J_2M_2\rangle_B \pm |J_2M_2\rangle_A|J_1M_1\rangle_B \pm |J_1M_2\rangle_A|J_2M_1\rangle_B \pm |J_2M_1\rangle_A|J_1M_2\rangle_B\}/2, \tag{3}$$

where $\Omega = |M_1 + M_2|$ and the last pair of terms will only be present for $\Omega = 0$ states and then only if new configurations are thereby generated. In (3) n numbers states of a given Ω value in the order, with one exception, given in table 1 of ref. [7] in which the energy ordering at very long range ($R > 6$ Å) in I_2 is discussed. Our aim here is simply to establish a numbering scheme based as closely as possible on the energies of states at long range so we have reversed the order in ref. [7] of the first two configurations, $X(0^+_g(1))$ and $a'(0^+_g(2))$

$$X(0^+_g(1)) = (1/\sqrt{2})[|3/2, 1/2\rangle_A|3/2, -1/2\rangle_B - |3/2, -1/2\rangle_A|3/2, 1/2\rangle_B], \tag{4}$$

$$a'(0^+_g(2)) = (1/\sqrt{2})[|3/2, 3/2\rangle_A|3/2, -3/2\rangle_B - |3/2, -3/2\rangle_A|3/2, 3/2\rangle_B]. \tag{5}$$

The former now has what is almost certainly the dominant configuration of the ground state at intermediate and large separations – both for the reasons discussed by Saute and Aubert-Frecon [7] and from spectroscopic evidence to be presented in section 3. Once again it is assumed that there is no mixing of $J = 3/2$ and $J = 1/2$

atomic states which at long range could be induced by multipole fields or dispersion forces. In these AP states, unlike the IP states, there will be long range mixing between asymptotically degenerate states of the same Ω value that correspond to different combinations of M''_A and M''_B, e.g. $0^+(1)$ and $0^+(2)$ in the first cluster of table 1 below, and we return to this point in section 3.2. The numbering of the AP states in the $(J_A M_A J_B M_B)$ approximation for heteronuclear diatomics is given in table 1. The orthogonality of IP and AP states, together with the related question of IP–valence configuration interaction is discussed in appendix B.

The atomic and ionic wavefunctions are now used explicitly in the Russell–Saunders (RS) coupling scheme, as was done in the applications [1–4] of the pure precession model to IP states. Although there is clear evidence in I^+ and to a lesser extent in Br^+ of incipient *jj* coupling mainly through $^3P_2$–$^1D_2$ and $^3P_0$–$^1S_0$ mixing (responsible for the anomalous order of J levels in the ground state multiplet of I^+, see ref. [14, p. 301], we will use the Russell–Saunders description in terms of $(LSJM_J)$ as the basis in which these perturbations can be discussed. The general form of a p^n configuration valence atomic wavefunction, the filled core levels omitted, is then

$$|^{2S+1}L_{JM}\rangle = \sum_{k,M_L,M_S} \langle kM_L M_S | LSJM_J \rangle \Delta^{(n)}(kM_L M_S)\,, \tag{6}$$

where $\Delta^{(n)}(kM_L M_S)$ is a single Slater determinant of n p-type spin-orbitals with resultant components M_l and M_s. The overall sign of any $\Delta^{(n)}$ is based on the canonical order

$$\Delta^{(6)} = \|1^+1^-0^+0^-1^+1^-\|\,. \tag{7}$$

Table 1
Diatomic valence (AP) wavefunctions in the $(J_A M_A J_B M_B)$ coupling scheme for the heteronuclear case illustrated by ICl

Electronic state of separated atoms	Case (c) $\Omega(n)$	Molecular wavefunction
$I(^2P_{3/2})+Cl(^2P_{3/2})$	$0^+(1)$	$(1/\sqrt{2})[\|3/2, 1/2\rangle_1\|3/2, -1/2\rangle_a - \|3/2, -1/2\rangle_1\|3/2, 1/2\rangle_a]$
	$0^+(2)$	$(1/\sqrt{2})[\|3/2, 3/2\rangle_1\|3/2, -3/2\rangle_a - \|3/2, -3/2\rangle_1\|3/2, 3/2\rangle_a]$
	$0^-(1)$	$(1/\sqrt{2})[\|3/2, 1/2\rangle_1\|3/2, -1/2\rangle_a + \|3/2, -1/2\rangle_1\|3/2, 1/2\rangle_a]$
	$0^-(2)$	$(1/\sqrt{2})[\|3/2, 3/2\rangle_1\|3/2, -3/2\rangle_a + \|3/2, -3/2\rangle_1\|3/2, 3/2\rangle_a]$
	1(1)	$\|3/2, 3/2\rangle_1\|3/2, -1/2\rangle_a$
	1(2)	$\|3/2, -1/2\rangle_1\|3/2, 3/2\rangle_a$
	1(3)	$\|3/2, 1/2\rangle_1\|3/2, 1/2\rangle_a$
	2(1)	$\|3/2, 3/2\rangle_1\|3/2, 1/2\rangle_a$
	2(2)	$\|3/2, 1/2\rangle_1\|3/2, 3/2\rangle_a$
	3(1)	$\|3/2, 3/2\rangle_1\|3/2, 3/2\rangle_a$
$I(^2P_{3/2})+Cl(^2P_{1/2})$	$0^+(3)$	$(1/\sqrt{2})[\|3/2, 1/2\rangle_1\|1/2, -1/2\rangle_a + \|3/2, -1/2\rangle_1\|1/2, 1/2\rangle_a]$
	$0^-(3)$	$(1/\sqrt{2})[\|3/2, 1/2\rangle_1\|1/2, -1/2\rangle_a - \|3/2, -1/2\rangle_1\|1/2, 1/2\rangle_a]$
	1(4)	$\|3/2, 3/2\rangle_1\|3/2, -1/2\rangle_a$
	1(5)	$\|3/2, 1/2\rangle_1\|1/2, 1/2\rangle_a$
	2(3)	$\|3/2, 3/2\rangle_1\|1/2, 1/2\rangle_a$
$I(^2P_{1/2})+Cl(^2P_{3/2})$	$0^+(4)$	$(1/\sqrt{2})[\|1/2, -1/2\rangle_1\|3/2, 1/2\rangle_a + \|1/2, 1/2\rangle_1\|3/2, -1/2\rangle_a]$
	$0^-(4)$	$(1/\sqrt{2})[\|1/2, -1/2\rangle_1\|3/2, 1/2\rangle_a - \|1/2, 1/2\rangle_1\|3/2, -1/2\rangle_a$
	1(6)	$\|1/2, -1/2\rangle_1\|3/2, 3/2\rangle_a$
	1(7)	$\|1/2, 1/2\rangle_1\|3/2, 1/2\rangle_a$
	2(4)	$\|1/2, 1/2\rangle_1\|3/2, 3/2\rangle_a$
$I(^2P_{1/2})+Cl(^2P_{1/2})$	$0^+(5)$	$(1/\sqrt{2})[\|1/2, 1/2\rangle_1\|1/2, -1/2\rangle_a - \|1/2, -1/2\rangle_1\|1/2, 1/2\rangle_a]$
	$0^-(5)$	$(1/\sqrt{2})[\|1/2, 1/2\rangle_1\|1/2, -1/2\rangle_a + \|1/2, -1/2\rangle_1\|1/2, 1/2\rangle_a]$
	1(8)	$\|1/2, 1/2\rangle_1\|1/2, 1/2\rangle_a$

If more than one combination of the spins and spatial orbitals is possible for a given value of M_L and M_S, the index k numbers these sequentially, e.g. for $M_L=M_S=0$

$$\Delta^{(4)}(100)=\|1^+1^-1^+1^-\|\,,\quad \Delta^{(4)}(200)=\|1^+0^+0^-1^-\|\,,\quad \Delta^{(4)}(300)=\|1^-0^+0^-1^+\|\,. \tag{8}$$

The rules for generating the coefficients $\langle kM_LM_S|LSJM_J\rangle$ are quite standard (see e.g. Condon and Shortley [14]) but specific values for the p^4 and p^5 configurations used here do not seem to be readily accessible. They will be frequently referred to and so are enumerated in appendix A. A complete transition dipole matrix element in, for instance, the heteronuclear halogen case

$$\mu_{12}=\langle A^+(J_1'M_1')B^-|\mu_z|A(J_1''M_1'')B(J_2''M_2'')\rangle \tag{9}$$

is thus composed of a sum of transition moments between primitive determinants,

$$\mu_{12}=\sum\langle k_1'M_{L1}'M_{S1}'|L_1'J_1'M_1'\rangle_A\langle k_1''M_{L1}''M_{S1}''|L_1''J_1''M_1''\rangle_A\langle k_2''M_{L2}''M_{S2}''|L_2''J_2''M_2''\rangle_B$$
$$\times\langle\Delta_A^{(5)}(k_1''M_{L1}''M_{S1}'')\Delta_B^{(5)}(k_2''M_{L2}''M_{S2}'')|\sum_i\mu_{zi}|\Delta_B^{(6)}\Delta_A^{(4)}(k_1'M_{L1}'M_{S1}')\rangle\,, \tag{10}$$

where the first sum is over all k, M_L and M_S compatible with Ω and the second over all p electrons. In the homonuclear case when $J_1=J_2$ or $M_1=M_2$ the interchange of Js or Ms between A and B, as in eqs. (1) and (3), must be included with the appropriate overall normalization. In an IP→AP dipole allowed parallel transition an electron is transferred either between two p_σ atomic orbitals, one on each centre, or between two p_π AOs. For a perpendicular transition the transfer in the (J_AJ_B) model must be $p_\sigma^{(A)}\leftrightarrow p_\pi^{(B)}$. The evaluation of (10) is much simplified by the following approximation. Since we are concerned with transitions occurring at separations around r_e of the IP state (typically $\approx$3–3.5 Å) where the overlap of atomic orbitals on the two centres is already quite small (otherwise the J_AJ_B model would not hold for the IP states) we assume that $p_\sigma\leftrightarrow p_\sigma$ transfer is dominant. Theoretical plausibility can be given to this assumption by considering the one electron integrals involving the overlap of Slater orbitals $(x, y, z)\exp(-\alpha R)$ with exponents empirically adjusted to give the known radii of the atoms or ions involved. $\langle p_\pi|\mu_z|p_\pi\rangle^2$ is then found to be between 1% and 5% of $\langle p_\sigma|\mu_z|p_\sigma\rangle^2$ at $\alpha R_e\approx 4$. Dunning and Hay [15] find that σ–σ charge transfer transition moments in the Xe halides are about 10 times larger than π–π moments, with σ–π transition moments only a few percent of σ–σ values. With this assumption the one electron operator in eq. (9) or (10) can only connect IP and AP configurations that differ by the transfer of one electron from one atom to the other with spin unchanged and which have an unchanged p_σ occupancy. A typical non-vanishing contribution to the dipole matrix element in (10) for $AB(\Omega=0)\rightarrow A^+B^-(\Omega=0)$ would be

$$\langle\|1^+1^-0^-1^-\|_A\|1^+1^-0^+0^-1^+1^-\|_B\mu_z\|1^+1^-0^+0^-1^-\|_A\|1^+1^-0^-1^+1^-\|_B\rangle \tag{11}$$

(but no A^-B^+ configuration is accessible by σ-electron transfer from this AP configuration). A perpendicular transition e.g. $IP(\Omega=1)\rightarrow AP(\Omega=0)$ would typically involve the electron transfer

$$\langle\|1^-0^+0^-1^-\|_A\|1^+1^-0^+0^-1^+1^-\|_B\mu_{-1}\|1^+1^-0^+0^-1^-\|_A\|1^+1^-0^-1^+1^-\|_B\rangle\,. \tag{12}$$

In evaluating (11) we can write the operation of μ_z on an atomic p orbital as

$$\mu_z|p_\sigma\rangle_{A,B}=\pm|p_\sigma\rangle_{B,A}M_{\sigma\sigma}(r)\,, \tag{13}$$

where

$$M_{\sigma\sigma}(r)=\langle p_\sigma(A)|\mu_z|p_\sigma(B^-)\rangle \tag{14}$$

and the p_σ orbital on A is that of the neutral atom but $p_\sigma(B^-)$ has the more diffuse character of the negative ion.

In the operation on the product of Slater determinants the number of column interchanges N_p as the electron is moved to the canonical form of the final state must be counted and the antisymmetrisation factor $(-1)^{N_p}$ included. Thus, the only σ–σ transfer possible from the AP ($J_A = J_B = 3/2$, $|M_A| = |M_B| = 1/2$; $\Omega = 0$) configuration to A^-B^+ would involve

$$\mu_{z_1}\mathcal{A}\|1^+1^-0^+-1^+-1^-\|_A\|1^+1^-0^--1^+-1^-\|_B$$

$$= (-1)^4\mathcal{A}\|1^+1^-0^+0^--1^+-1^-\|_A\|1^+1^--1^+-1^-\|_B M_{\sigma\sigma}(r)\langle B^+|B\rangle^4\langle A^-|A\rangle^5, \quad (15)$$

where the overlap integrals $\langle A^+|A\rangle = \langle p(A^+)|p(A)\rangle$ etc., represent the relaxation of the remaining p electrons when one is transferred. If the electron is transferred from A to B, an extra sign change is introduced

$$= -(-1)^4\mathcal{A}\|1^+1^--1^+-1^-\|_A\|1^+1^-0^+0^--1^+-1^-\|_B M_{\sigma\sigma}(r)\langle A^+|A\rangle^4\langle B^-|B\rangle^5. \quad (16)$$

The operation of μ_{-1} on the ket in (12) for a perpendicular transfer A→B would similarly result only in the IP configuration

$$-(-1)^6\mathcal{A}\|1^-0^+0^--1^-\|_A\|1^+1^-0^+0^--1^+-1^-\|_B M_{\sigma\pi}\langle B^-|B\rangle^5\langle A^+|A\rangle^4 \quad (17)$$

but the operation of μ_{+1} would nullify the ket. The resultant combination of products of determinants on the two centres is then resolved with the help of the inverse of eq. (6) into $(SLJM_J)$ states to identify the contribution of each molecular state in the (J_AJ_B) coupling scheme. It is slightly easier to do this if the dipole operation is carried out on the AP state since in the resulting combination of IP structures $\Delta^{(4)}(kM_LM_S)\Delta^{(6)}$, only the $\Delta^{(4)}$ configurations have to be resolved into the spectroscopic states $(SLJM_J)$ of the positive ion. The transition moments to the various states represented are then proportional to the overall coefficient $\zeta_{n'n''\Omega}$ of each IP$(n'\Omega)$ state in the expansion,

$$\langle \mathrm{IP}(n'\Omega)|\mu_z|\mathrm{AP}(n''\Omega)\rangle = \zeta_{n'n''\Omega}M_{\sigma\sigma}(r)\langle A^+|A\rangle^4\langle B^-|B\rangle^5, \quad (18)$$

with the positive ion relaxation term replaced by $\langle A^+|A\rangle^5$ in the rare gas (Rg) halides. A corresponding set of coefficients $\xi_{n'n''\Omega}$ can be defined for $\pi\leftrightarrow\pi$ electron transfer and would be associated with $M_{\pi\pi}$.

As a simple application of the model, we first calculate the relative transition amplitudes of the nine possible IP↔valence transitions in the rare gas halide excimers. The numbering of the states and their wavefunctions in the $(J_AM_AJ_BM_B)$ coupling scheme are given in table 2, together with Hay and Dunning's notation [13,15] and the coefficients $\zeta_{n'n''\Omega}$ are listed in table 3. $\Delta\Omega = 1$ transition dipoles are to be multiplied by the two centre integral $M_{\sigma\pi}$ as introduced in eq. (17). The corresponding results for the first cluster of IP states of the homonuclear halogens are given in table 4. Table 5 contains the relative amplitudes of all the $0_u^+ \rightarrow 0_g^+$ transitions from all the homonuclear halogen IP states. Table 6 covers some of the same transitions as table 3 but for the heteronuclear

Table 2
Wavefunctions for the rare gas halide valence and excimer (IP) states in the J_AJ_B coupling scheme. The energy ordered sequential numbering of states, used in table 3, is given on the left and the corresponding spectroscopic notation on the right

$\Omega(n)$	Valence state wavefunctions	
$\frac{1}{2}(1)$	$\|0,0\rangle_{Rg}\|3/2, 1/2\rangle_X$	X(1/2)
$\frac{3}{2}(1)$	$\|0,0\rangle_{Rg}\|3/2, 3/2\rangle_X$	A(3/2)
$\frac{1}{2}(2)$	$\|0,0\rangle_{Rg}\|1/2, 1/2\rangle_X$	A(1/2)
$\Omega(n)$	Ion pair state wavefunctions	
$\frac{1}{2}(3)$	$\|3/2, 1/2\rangle_{Rg^+}\|0,0\rangle_{X^-}$	B(1/2)
$\frac{3}{2}(2)$	$\|3/2, 3/2\rangle_{Rg^+}\|0,0\rangle_{X^-}$	C(3/2)
$\frac{1}{2}(4)$	$\|1/2, 1/2\rangle_{Rg^+}\|0,0\rangle_{X^-}$	D(1/2)

Table 3
ζ coefficients (eq. (18)) for parallel and perpendicular transitions in the rare gas halides. The type of electron transfer is indicated as a suffix. Although the $\frac{3}{2}(1)\leftrightarrow\frac{3}{2}(2)$ transition is a parallel one, it requires $\pi\leftrightarrow\pi$ transfer and the electronic matrix element is $M_{\pi\pi}(r)$

	IP	Valence		
		$\frac{1}{2}(1)$	$\frac{3}{2}(1)$	$\frac{1}{2}(2)$
	$\frac{1}{2}(3)$	$-[2/3]_{\sigma\sigma}$	$[\sqrt{2/3}]_{\sigma\pi}$	$[\sqrt{2}/3]_{\sigma\sigma}$
	$\frac{3}{2}(2)$	$[\sqrt{2/3}]_{\sigma\pi}$	$[1]_{\pi\pi}$	$-[\sqrt{1/3}]_{\sigma\pi}$
	$\frac{1}{2}(4)$	$[\sqrt{2}/3]_{\sigma\sigma}$	$-[\sqrt{1/3}]_{\sigma\pi}$	$-[1/3]_{\sigma\sigma}$

Table 4
The amplitudes $\zeta_{n'n''\Omega}$ (eq. (18)) of the transition dipoles connecting the lowest cluster of IP states (correlating with $A^+(^3P_2)$) and all the accessible valence states in the homonuclear case. Values in brackets are for perpendicular transitions and must be multiplied by $M_{\sigma\pi}(r)$. Valence states in the first block correlated with $J_A=3/2$, $J_B=3/2$ atomic states, those in the second block with $J_A=3/2$, $J_B=1/2$ and the final pair of states with $J_A=1/2$, $J_B=1/2$

Valence	IP						
	$0_g^+(1)$	$0_u^+(1)$	$1_g(1)$	$1_u(1)$	$2_g(1)$	$2_u(1)$	Valence
$0_g^+(1)$		$-2/3\sqrt{3}$		$[1/2]$			X
$0_g^+(2)$		0		$[1/2]$			a'
$1_g(1)$		$[1/\sqrt{2}]$		$-1/\sqrt{6}$		$[1/\sqrt{3}]$	a
$1_u(1)$	$[1/3\sqrt{2}]$		$-1/\sqrt{6}$		$[1/\sqrt{3}]$		A
$1_u(2)$	$[-5/3\sqrt{3}]$		1/3		$[4/3\sqrt{2}]$		
$2_g(1)$				$[-1/\sqrt{3}]$		$\sqrt{2/3}$	
$2_u(1)$			$[-2/\sqrt{3}]$		$\sqrt{2/3}$		A'
$3_u(1)$					$[-\sqrt{2}]$		
$0_g^+(3)$		$1/3\sqrt{3}$		$[-1/2]$			
$0_u^+(1)$	$-1/\sqrt{3}$		$[1/2]$				B
$1_g(2)$		[0]		$-1/\sqrt{12}$		$[-\sqrt{2/3}]$	
$1_g(3)$		$[1/\sqrt{3}]$		$-1/2$		[0]	
$1_u(3)$	[2/3]		$-1/\sqrt{12}$		$[-\sqrt{2/3}]$		
$1_u(4)$	$[-1/3\sqrt{3}]$		1/6		$[-4/3\sqrt{2}]$		
$2_g(2)$				$[1/\sqrt{6}]$		$-1/\sqrt{3}$	
$2_u(2)$			$[-1/\sqrt{6}]$		$-1/\sqrt{3}$		
$0_g^+(4)$		$-2/3\sqrt{3}$		[0]			
$1_u(5)$	$[-1/3\sqrt{3}]$		$-1/3$		$[4/3\sqrt{2}]$		
IP	E	D	β	γ	D'	δ	

case $A^+(J_A)B^-$. The J_AJ_B model predicts exactly the same coefficients ζ for the corresponding states correlating with $A^-B^+(J_B)$ when $J_A=J_B$.

3. Discussion

3.1. Radiative lifetimes

Transitions will either be bound→bound or bound→free. For the former we can write for the total fluorescent intensity associated with a given electronic transition $n'\rightarrow n''$ and summed over all lower vibrational states v''

Table 5
All the (IP) $0_u^+ \rightarrow$ valence 0_g^+ transitions in the homonuclear halogens. The coefficients for $\sigma \rightarrow \sigma$ electron transfer are given. Zeros indicate that the necessary e-transfer is $\pi \rightarrow \pi$. The spectroscopic state of X^+ in each IP state is given at the foot of each column

Valence	IP			
	$0_u^+(1)$	$0_u^+(2)$	$0_u^+(3)$	$0_u^+(4)$
X: $0_g^+(1)$	$-2/3\sqrt{3}$	$\frac{1}{3}\sqrt{2/3}$	$-\frac{4}{3}\sqrt{2/3}$	$4/3\sqrt{3}$
a': $0_g^+(2)$	0	0	0	0
$0_g^+(3)$	$1/3\sqrt{3}$	$-\frac{1}{3}\sqrt{2/3}$	$-\frac{4}{3}\sqrt{2/3}$	$4/3\sqrt{3}$
$0_g^+(4)$	$-2/3\sqrt{3}$	$\frac{1}{3}\sqrt{2/3}$	$\frac{1}{3}\sqrt{2/3}$	$-2/3\sqrt{3}$
$IP(X^+)$	$D(^3P_2)$	$F(^3P_0)$	$F'(^1D_2)$	$?(^1S_0)$

Table 6
The transition amplitude $\zeta_{n'n''\Omega}$ for the lowest cluster of heteronuclear halogen IP states A^+B^- correlating with $A^+(^3P_2)$. The zeros indicate that the transition is forbidden to $\sigma \leftrightarrow \sigma$ electron transfer because the p-orbital vacancy on the B atom in the AP state is in a p_π orbital and only becomes allowed by $\pi \rightarrow \pi$ transfer

Valence	IP			Valence	IP		
	$0^+(1)$	$1(1)$	$2(1)$		$0^+(1)$	$1(1)$	$2(1)$
$0^+(1)$	$2/3\sqrt{6}$			1(4)		$1/2\sqrt{3}$	
$0^+(2)$	0			1(5)		1/6	
1(1)		$1/\sqrt{6}$		2(3)			$1/\sqrt{3}$
1(2)		0		$0^+(4)$	$2/3\sqrt{3}$		
1(3)		$-1/3\sqrt{2}$		1(6)		0	
2(1)			$-\sqrt{2/3}$	1(7)		$-1/3$	
2(2)			0	2(4)			0
$0^+(3)$	$1/3\sqrt{3}$			$0^+(5)$	$2/3\sqrt{6}$		
				1(8)		$1/3\sqrt{2}$	

$$\sum_{v''} I_{n'v'n''v''} = (64\pi^4/3hc^3) \sum_{v''} \langle v' | \mu_{n'n''}(r) | v'' \rangle^2 \nu^3_{n'v'n''v''} \approx \nu^3_{n'n''} \langle v' | \mu^2_{n'n''}(r) | v' \rangle \approx \nu^3_{n'n''} \mu^2_{n'n''}(r_e^{(n')}) , \qquad (19)$$

where the last two approximations (see ref. [16] for the more general expressions) only hold for the lowest IP vibrational states and $\nu_{n'n''}$ is the ν-centroid of the fluorescence (which will have a width $\Delta\nu$ much less than $\nu_{n'n''}$ itself). The same approximate relationship will hold for the integrated area under the continuum envelope of fluorescence from a bound→free transition, measured with the same monochromator slitwidth. The radiative lifetime of an IP ($v' \approx 0$) state is then, neglecting the contribution of perpendicular transitions, given by

$$1/\tau_{n'} = \sum_{n''} A_{n'n''} = \sum_{n''} (\zeta_{n'n''\Omega} M_{\sigma\sigma} + \xi_{n'n''\Omega} M_{\pi\pi})^2 \nu^3_{n'n''} [\langle A^+ | A \rangle^4 \langle B^- | B \rangle^5]^2 \qquad (20)$$

and in the following discussion we will drop the term in $M_{\pi\pi}$.

Lifetimes of the halogen IP states. The $E(0_g^+) \rightarrow B(0_u^+)$ transition (IP $0_g^+(1) \rightarrow$ AP $0_u^+(1)$ of table 4) is unique in that the B state is the only one of its symmetry among the valence states. There is thus no long range atomic J-state mixing due to the quadrupole–quadrupole interaction and the only departure from the $(J_A J_B)$ model in the B state comes at short range from rydbergisation or from configuration mixing with the various IP 0_u^+ states. These perturbing states are about 40000 cm^{-1} away and such mixing is small [17]. The calculated lifetime of the E state of I_2, using the appropriate ζ coefficient from table 4, is

$$1/\tau(E) = \tfrac{1}{3}(64\pi^4/3hc^3)\,\nu_{EB}^3 M_{\sigma\sigma}^2(r_e(E))[\langle I^+|I\rangle^4\langle I^-|I\rangle^5]^2 . \quad (21)$$

The product of the three factors $M_{\sigma\sigma}(r)$, $\langle I^+|I\rangle^4$ and $\langle I^-|I\rangle^5$ involving details of the atomic orbitals can then be deduced from the observed lifetime of 26 ns for the E state [18]. Provided that $r_e(IP)$ does not change appreciably from one IP state to another so that the $M_{\sigma\sigma}(R)$ terms in eq. (20) remain constant, the lifetimes of all the other IP($v''=0$) states can be deduced within the framework of the ($J_A J_B$) model. Broadly speaking, the two IP($\Omega=2$) states have the shortest lifetimes because they have the maximum fractional vacancy in the p_σ orbital of the positive ion, followed by the $\Omega=1$ states and then the $\Omega=0$ pair. These results are modified to some extent by the ν^3 factor which favours these IP states that can fluoresce to the more deeply bound valence states, but the effect of small changes ≈ 500 cm^{-1} in the estimates of $\nu_{n'n''}$ on τ is only $\approx \pm 1$ ns.

Similarly, mixing of valence states of the same Ω value that are asymptotically degenerate may redistribute some of the fluorescence, but lifetimes are only affected at the 10% level unless transition to the ground state is strongly involved. At this level of approximation, the only source of a difference in lifetime between pairs of g and u homonuclear IP states that have the same positive ion quantum numbers lies in the ν^3 factor and the slight difference in r_e of the two states (itself a result of the exchange interaction).

Taking the example of the relative fluorescence lifetimes of the β and E states of I_2, applying eq. (20) to the β state requires a knowledge of $\nu_{n'n''}$ for all five parallel transitions from this state. The red extremum λ_M of the $\beta(v'=16)\rightarrow$A fluorescence has been observed at 3432 Å [18], where transitions occur around r_e of the IP state. This corresponds to the A state potential having dropped 850 cm^{-1} below its asymptote. Assuming the other four transitions to end in valence states that are bound by ≈ 200 cm^{-1} at the point of transition relative to the appropriate atomic asymptote, we estimate $\nu(\beta\rightarrow 1_u(3)) = \nu(\beta\rightarrow 1_u(4)) = 21000$ cm^{-1}, $\nu(\beta\rightarrow 1_u(5)) = 13400$ cm^{-1} and obtain for the lifetime of the β state $\tau_\beta = 12$ ns. Perrot et al. [18] give $\tau_\beta = 11$ ns, extrapolated to $v'=0$. Perpendicular transitions not included here can only shorten the calculated lifetime. Other observed lifetimes are very sparse in the literature. $\tau = 6$–7 ns has been recorded for the vibrationally quenched D′(2_g) state of I_2 [19]; with the principal fluorescence from this state, D′$\rightarrow$A′($2_u(1)$), peaking at 29300 cm^{-1}, and the second fluorescence system D′(2_g)$\rightarrow 2_u(2)$ observed to occur at 19600 cm^{-1} [20], we calculate $\tau_{D'} = 5$ ns. Spin–orbit mixing of the $^3P_{22}$ and $^1D_{22}$ states of I^+ will somewhat lengthen the lifetime of the lower 2_g and 2_u states and shorten that of the upper $2_{g,u}(2)$ pair because (see appendix A) the electronic configuration of the $^1D_{22}$ state is the single configuration $\|1^+1^-0^+0^-\|$ which has no σ-orbital vacancy.

3.2. Relative fluorescence intensities

Making the same approximations as for the radiative lifetime, eq. (19), the ratio of the integrated intensity of two emission systems from transitions originating in the same low vibrational level of an IP state n' to two different valence states $n''=1$ and 2 is

$$I_{n'1}/I_{n'2} \approx (\nu_{n'1}/\nu_{n'2})^3[\mu_{n'1}(r_e^{(n')})/\mu_{n'2}(r_e^{(n')})]^2 \approx (\nu_{n'1}/\nu_{n'2})^3[\zeta_{n'1\Omega}/\zeta_{n'2\Omega}]^2 , \quad (22)$$

where the restriction to σ↔σ transfer has been made.

3.2.1. Fluorescence from the rare gas halide excimer states

We will not analyse the spectra of the rare gas halides in detail, but only indicate the way in which the ζ elements of the transition dipole matrix in table 3 can be used. In the reference model the relative intensities of the B[1/2]$\rightarrow$A[1/2] and B[1/2]$\rightarrow$X[1/2] transitions are

$$I_{B\rightarrow A}/I_{B\rightarrow X} \approx (\zeta_{B\rightarrow A}/\zeta_{B\rightarrow X})^2(\nu_{B\rightarrow A}/\nu_{B\rightarrow X})^3 = \tfrac{1}{2}(\nu_{B\rightarrow A}/\nu_{B\rightarrow X})^3 ,$$

and exactly the same coefficient of one half half applies to the ratio of D$\rightarrow$A to D$\rightarrow$X fluorescence. The ratio of transition moments $\mu_{D\rightarrow X}:\mu_{B\rightarrow X}$ is seen to be $1/\sqrt{2}$ assuming R_e unchanged. In the xenon halides all four transitions are recorded as being strong, with the B$\rightarrow$X fluorescence being the strongest. A quite different pattern of

intensities in fluorescence is predicted from the fully spin–orbit decoupled Hund's case (a) type description of the two valence $\Omega = 1/2$ states. With S, L, M_L of the halogen atom as good quantum numbers we have

$$X[1/2](^2\Sigma_{1/2}) = \|1^+1^-0^+ - 1^+ - 1^-\|_{\mathrm{Hal}}\|p^6\|_{\mathrm{Rg}} = (1/\sqrt{3})[|^2P_{1/21/2}\rangle - \sqrt{2}|^2P_{3/21/2}\rangle]|^1S_0\rangle ,$$

$$A[1/2](^2\Pi_{1/2}) = \|1^+1^-0^+0^- - 1^-\|_{\mathrm{Hal}}\|p^6\|_{\mathrm{Rg}} = (1/\sqrt{3})[\sqrt{2}|^2P_{1/21/2}\rangle + |^2P_{3/21/2}\rangle]|^1S_0\rangle . \quad (23)$$

It is clear that both the D→A and B→A transitions must now involve π↔π electron transfer. Indeed it can be seen at once from the σ↔σ ζ coefficients in table 3 that these same transitions both vanish for the linear combinations of basis states taken in eq. (23). Thus, irrespective of the coupling scheme adopted for the ion pair states, two of the four IP[1/2]→AP[1/2] transitions will be very weak in the (SLM_L) coupling scheme, contrary to observation. When detailed comparison with experiment is made, departures from the ratios predicted in the $(J_A M_A J_B M_B)$ basis will undoubtedly be observed which can be quantitatively interpreted in terms of J state mixing as outlined in section 3.3.

3.2.2. Fluorescence from the halogen IP states

We now apply (22) to the dispersed fluorescence from D′ (2_g) state (i.e. the $2_g(1)$ state of table 4). Tellinghuisen [20] has observed fluorescence from the transition D′ → $^3\Delta_u(2_u(2))$ in I_2 to be centered at 5100 Å and the well known D′ → A′ (IP $2_g(2)$ → AP $2_u(1)$) fluorescence has its red extremum at 3400 Å. So, from table 4 we predict the intensity ratio $I(D' \to A')/I(D' \to {}^3\Delta_u) = 6.75$. Tellinghuisen reports that the former transition accounts for 87% of the total emission and the D′ → $^3\Delta_u$ for 8%, implying a ratio of 11:1 in integrated intensity. Spin–orbit mixing of the $^3P_{22}$ and $^1D_{22}$ states of I^+ will not alter this branching ratio. Mixing of the $J = 3/2$ and $J = 1/2$ atomic states will decrease the p_σ occupancy from that in the asymptotic description of the A′ state and increase it in the orthogonal $2_u(2)$ state. The effect would be further to favour the D′ → A′ emission.

Ishiwata et al. [21] have detected two emission systems in the dispersed fluorescence from the F′ state of I_2 (the $0_u^+(3)$ state of table 5), to X($0_g^+(1)$) and to the $0_g^+(2)$ state with red extrema at 236 and 310 nm respectively. Using the coefficients of table 5, we predict the relative intensities of these systems to be 2.27:1, and there should be a third, much weaker system at around 420 nm with an intensity of 0.1 relative to the 236 nm system. Unfortunately, the authors do not record the relative intensities of the observed transitions.

Several authors [22,23] have pointed out the apparent anomaly that, while the Cordes bands (D←X) in I_2 are seen strongly in absorption and the F←X transition is never seen, both systems are seen strongly in fluorescence near their red extrema. Fluorescence from the F(0_u^+) state of I_2 is observed to have a red extremum at 270 nm [24]. From table 5, the relative intensity is

$$I_{F\to X} : I_{D\to X} \approx \tfrac{8}{27}(37310)^3 : \tfrac{4}{27}(31000)^3 = 3.49:1$$

(neglecting the small difference in r_e of the two states), assuming equal populations of the two emitting states. In the particular spectrum of iodine reported in ref. [24], the relative values of I_{fl} at the two red extrema were roughly equal indicating a population ratio [D]:[F] ≈ 3.5. The intensity of fluorescence at λ_M contains the semiclassical factor $v(r_m)^{-1}\kappa^{-2/3}$ where $v(r_m)$ is the relative velocity of the two atoms at the classical point of transition r_m, so a simple comparison of I_{fl} (λ_M) in two systems assumes that the curvatures of the Mulliken difference potentials $\kappa_{FX} = V''_F(r) - V''_X(r)$ and $\kappa_{DX} = V''_D(r) - V''_X(r)$ at $r = r_e$ are identical at their maxima and that the velocities $v(r_m)$ are equal in the two states. The F′ ($0_u^+(3)$) → X fluorescence at its red extremum should be even stronger. Estimating $\lambda_M \approx 44700\ \mathrm{cm}^{-1}$, we find $I_{F'X} : I_{DX} = 24:1$. This enhanced intensity, apart from the more favourable ν^3 factor, comes from the increased p_σ vacancy in the $I^+(^1D_{2M})$ state compared with the $^3P_{2M}$ states.

Fluorescence from the D(0_u^+) state of I_2 has been much studied and in principle should exhibit four emission systems arising from parallel transitions to the four 0_g^+ valence states. However, although the D→X emission is strong ($\lambda_M \approx 31000\ \mathrm{cm}^{-1}$), the transition to the weakly bound a′ ($0_g^+(2)$) state, which should lie roughly 4000

cm^{-1} to the red of the D→X red extremum is only weakly seen. This implies that there is very little mixing at separations ≈3.6 Å between the AP configurations $0_g^+(1)$ and $0_g^+(2)$, eqs. (4) and (5). In the $0_g^+(2)$ state (see appendix A) the p_σ orbitals on both atoms are full and so there is no possibility of σ→σ electron transfer (all $\zeta_{n'20}=0$) and any intensity in a charge transfer band must come either from π→π transfer or from atomic M_J state mixing between the first two 0_g^+ reference states. The relative intensities of the three remaining transitions are predicted to be in the ratios

$$I_{D\to 0_g(3)} : I_{D\to X} \approx \tfrac{1}{27}(21900)^3 : \tfrac{4}{27}(31000)^3 = 8.81\times 10^{-2},$$

$$I_{D\to 0_g(4)} : I_{D\to X} \approx \tfrac{4}{27}(14300)^3 : \tfrac{4}{27}(31000)^3 = 9.81\times 10^{-2},$$

with the wavelength of the hitherto unobserved $D\to 0_g^+(4)$ emission being displaced by the atomic multiplet separation $I(^2P_{1/2})-I(^2P_{3/2})$ to the red of the centroid of the $D\to 0_g^+(3)$ fluorescence. Among the perpendicular transitions, D→a($1_g(1)$) is predicted to be unusually strong,

$$I_{D\to 1_g(1)} : I_{D\to X} \approx \tfrac{1}{2}(30000)^3 : \tfrac{4}{27}(31000)^3 = 3.06(M_{\sigma\pi}/M_{\sigma\sigma})^2,$$

and will presumably lie about 1000 cm^{-1} to the red of λ_M D→X fluorescence. But the most intense fluorescence of all from the lowest cluster of IP states should come from the D′→A′ transition (λ_M observed at 3400 Å):

$$I_{D'\to A'} : I_{D\to X} \approx \tfrac{2}{3}(29400)^3 : \tfrac{4}{27}(31000)^3 = 3.84$$

and indeed this system is very prominent in fluorescence from high pressure discharges in I_2.

3.3. Departures from the RS $J_AM_AJ_BM_B$ coupling scheme

Configuration mixing in the RS $J_AM_AJ_BM_B$ basis arises from two causes. Firstly, spin–orbit coupling in the free atoms leads to a partial breakdown of the Russell–Saunders description. Secondly, electrostatic effects (including electron exchange) lead to a mixing of atomic or ionic J states in the molecular valence or IP states. After an analysis of the atomic term values, spin–orbit coupling can be allowed for almost completely and should properly be included in the basic model which will still retain $J_AM_AJ_BM_B$ as good quantum numbers. We will return to this point in a subsequent paper in which new experimental data on the lifetimes of the first cluster of ion pair states in I_2 will be presented. The longest range source of interionic (JM) state mixing is the r^{-3} quadrupole (Θ)–charge (q) interaction. In the axially symmetric field gradient of a spherical cation, M_J is conserved and mixing occurs only between states of the same total spin S. In the p^4 configuration of A^+ the $M_J=0$ components of the $J=2$ and $J=0$ states are mixed, as are the $M_J=1$ components of $J=2$ and $J=1$. Only the $^3P_{10}$, $^3P_{22}$ and $^1D_{22}$ and $^1D_{21}$ states remain unperturbed by these electrostatic effects. In the p^5 configuration of Rg^+ ions or the halogen atoms the $^2P_{3/2,1/2}$ and $^2P_{1/2,1/2}$ states are similarly mixed. The extent of mixing in first order is discussed in appendix C. The coefficient of mixing of the minor component in an ion pair wavefunction involving any of the above A^+ states will range from about 0.5 to 0.2 in the sequence Cl^+Cl^- to I^+I^-. The model has essentially broken down for the IP states of Cl_2 and partially for BrCl near their equilibrium separation and these are better described in terms of Hund's case (a) configurations, though still with ($S_AL_AS_BL_B$) as good quantum numbers. Departures from the J_AJ_B coupling scheme are handled in the usual superposition of states fashion, and we now illustrate the effect of configuration mixing in this basis.

3.3.1. Configuration mixing in the rare gas halides

In the Rg halide IP states, the effect of the interionic field gradient is to mix the B[1/2] and D[1/2] states. In terms of products of single centre determinantal configurations having M_L and M_S as good quantum numbers (i.e. $^2\Sigma_{1/2}$ and $^2\Pi_{1/2}$ basis) we can write for an $\Omega=1/2$ state

$$|[1/2](n)\rangle = |[c_{n1}\|1^+1^-0^+ - 1^+ - 1^-\| + c_{n2}\|1^+1^-0^+0^- - 1^-\|]\rangle |X^-\rangle . \qquad (24)$$

Hay and Dunning [15] in an ab initio MO treatment of the Xe halides find $c_1 \approx 0.84$, $c_2 \approx 0.54$ for the B state with rather little change between fluoride and iodide. These values are close to those of the free ion $Xe^+(^2P_{3/2})$; $c_1 = 0.816$, $c_2 = 0.577$. In terms of our $(J_A M_A J_B M_B)$ free atom basis (numbered as in table 2),

$$|B[1/2]\rangle = \cos\theta_{BD}|[1/2](3)\rangle + \sin\theta_{BD}|[1/2](4)\rangle ,$$

$$|D1/2]\rangle = -\sin\theta_{BD}|[1/2](3)\rangle + \cos\theta_{BD}|[1/2](4)\rangle . \tag{25}$$

The passage towards the pure Σ and Π configurations in the valence states will produce another rotation $\mathbf{R}_{AP}$ in the [1/2](1), [1/2] AP basis of table 2. The transformed transition dipole matrix is, as usual, $\mathbf{R}_{IP}\mu\mathbf{R}_{AP}$. In the case of the rare gas halides, we see from table 3 that in the 2×2 matrix of μ in the $\Omega = 1/2$ basis, one row is a multiple $(\sqrt{2})$ of the second, i.e. in the $(J_A M_A J_B M_B)$ basis $\mu_{B\to A}/\mu_{B\to X} = \mu_{D\to A}/\mu_{D\to X}$. Thus, a rotation of the IP basis (mixing the B and D states) cannot affect the $\mu_{B\to A}/\mu_{B\to X}$ ratio. A little algebra shows that in that case only we can write

$$\frac{I_{B\to X}}{I_{B\to A}} = \left(\frac{\zeta_{31} + \tan\theta_{XA}\zeta_{32}}{-\tan\theta_{XA}\zeta_{31} + \zeta_{32}}\right)^2 \left(\frac{\nu_{B\to X}}{\nu_{B\to A}}\right)^3 , \tag{26}$$

where $\tan\theta_{XA}$ refers to the mixing between the valence X[1/2] and A[1/2] states. In XeBr, Setser and Ku [25] found the branching ratio for the B→X and B→A[1/2] fluorescence to be 1:0.24. The two emission spectra peak at 282 and 324 nm respectively. Assuming the upper states to be fully vibrationally quenched so that we can interpret the results in terms of state coupling at R_e of the B state, we use the ζ coefficients from table 3 in (26) to find $\tan\theta_2 = 0.161$, implying a roughly 16% mixture of the $^2P_{1/2}$ Br atomic state with the $^2P_{3/2}$ state in XeBr(X) at a separation of about 3.38 Å.

3.3.2. Configuration mixing in the halogen IP states

In contrast to the Rg^+ ions, spin–orbit coupling in the halogen positive ions produces some S state mixing as described in section 3.3, though the quantum numbers $J_A M_A J_B M_B$ remain good. We can illustrate the effect of this passage towards *jj*-coupling by the simple two state problem presented by the mixing in the free ion of the $^3P_{2M}$ and $^1D_{2M}$ RS states of I^+

$$|^3P_{2M}\rangle = c_1|^3P_{2M}\rangle^{(RS)} + c_2|^1D_{2M}\rangle^{(RS)} . \tag{27}$$

For I^+, using the following values for the spin–orbit coupling parameter ζ_{5p} and the electrostatic interaction F_2 (as defined by Condon and Shortley), $\zeta_{5p} = 5774\ cm^{-1}$, $F_2 = 1411\ cm^{-1}$, which reproduce the observed $^3P_2$ and $^1D_2$ term values in I^+, we find $c_1 = 0.952$, $c_2 = -0.307$ in eq. (27). The transition-dipole ζ coefficients tabulated in the Russell–Saunders basis must be appropriately transformed. From tables 4 and 5, the corresponding ζ coefficients for the first two non-zero transitions from the D state in the homonuclear halogens would be:

$$D(0_u^+) \to 0_g^+(1) ; \quad \zeta_{110} = -(2/3\sqrt{3})c_1 + (4\sqrt{2}/3\sqrt{3})c_2 ,$$

$$D(0_u^+) \to 0_g^+(3) ; \quad \zeta_{130} = (1/3\sqrt{3})c_1 + (4\sqrt{2}/3\sqrt{3})c_2$$

(the transition to the second valence state $0_g^+(2)$ remains very weak until mixing of the atomic M_J states is introduced). For I^+ the effect on fluorescent intensities will be significant if the minor spin–orbit component happens to have a particularly large transition dipole moment to the lower state under discussion as in the case illustrated here, where the D→X transition dipole is almost doubled. In practice, the matrix of the combined spin–orbit and electrostatic perturbations in the IP states must be diagonalised before observed fluorescent intensity ratios can be interpreted in terms of *J* and *M* state mixing in the valence states of the halogens. We reserve a discussion of specific cases until new experimental data on relative intensities in fluorescence are presented in a later paper.

Qualitatively, it is worth noting that the effect of *J* state mixing in the positive halogen ion under the influence

of the field gradient of B^- is to cause the lowest IP 0^+ state (or the lowest g/u pair in the homonuclear case) to have an enhanced contribution from the configuration (see eqs. (C.8) and (C.9))

$$|0^+(1)\rangle = [\|1^+1^-0^- - 1^-\| + \|1^+0^+ - 1^+ - 1^-\|]_A[\|1^+1^-0^+0^- - 1^+ - 1^-\|]_B \quad (28)$$

(i.e. (1342) occupancy in MO terms for the u state or (1432) for the g state) through mixing of the $^3P_{20}$ and $^3P_{00}$ atomic states while its partner state, $0^+(2)$ is forced to adopt more of the configuration

$$|0^+(2)\rangle = [\|1^+0^+0^- - 1^-\| + \|1^-0^+0^- - 1^+\|]_A[\|1^+1^-0^+0^- - 1^+ - 1^-\|]_B \quad (29)$$

(i.e. (2332) $^3\Sigma_u^-$ or $[(2242)+2422)]$ $^3\Sigma_g^-$) than is predicted by the (J_AJ_B) model. This will tend to shorten the lifetime of the IP $0^+(1)$ state and lengthen that of $0^+(2)$, because the configuration in eq. (29) cannot be converted to an AP configuration by $\sigma\leftrightarrow\sigma$ electron transfer. However, if the valence states are assumed to retain their unperturbed configurations given by the J_AJ_B coupling scheme (see table 1), the relative intensities of the four IP$(0^+)\rightarrow$valence(0^+) transitions from each ion pair state are unchanged by this perturbation of the upper state.

4. Conclusions

The consistent application to both valence and ion pair (IP) states of the separated atom coupling scheme, in which $(J_AM_AJ_BM_B)$ are good quantum numbers, provides a framework in which the lifetimes of low vibrational levels of ion pair states and the relative intensities of major portions of IP→valence fluorescence can be discussed. The model is a limiting one, strictly only applicable as $r\rightarrow\infty$ and, if Russell–Saunders coupling is used for the atomic JM states, only for cases of weak spin–orbit interaction. In spite of these approximations, departures from the model may not be serious around r_e of the IP states of the heavier halogens and rare gas halides, and they will be systematically dependent on the strength of spin–orbit coupling and interionic or interatomic electrostatic effects, both of which can be quantitatively allowed for at long range. Breakdown of the model in the valence states will probably be more serious even before some IP–valence configuration interaction ensues at smaller r. Nevertheless, we suggest that the $J_AM_AJ_BM_B$ coupling scheme provides the best basis for discussing IP→valence transitions around r_e of IP states of the heavier halogens and rare gas halides.

In charge transfer transitions at long range, overlap between p_σ orbitals is much better than between p_π orbitals on different centres and these overlap integrals remain a parameter after the consequences of the angular momentum coupling have been dealt with. The crudest form of the model applied to parallel transition consists in neglecting $\pi\leftrightarrow\pi$ electron transfer in comparison with $\sigma\leftrightarrow\sigma$. To complete the model, the Russell–Saunders coupling scheme is used to describe the atomic JM states. The relative intensities of all the parallel transitions from low vibrational levels of any IP state then depend upon a one electron transfer integral $M_{\sigma\sigma}(r)$ (or $M_{\sigma\pi}(r)$ for perpendicular transitions) and the ζ coefficients giving the projection of the state resulting from this electron transfer onto the AP final state in the $J_AM_AJ_BM_B$ basis. Representative tables of $\zeta_{n'n\text{-}\Omega}$ are given from which the relative strengths of selected molecular IP↔AP transitions can be reduced to ratios of the appropriate electron transfer integrals and the characteristic ν^3 factors. Since all the ion pair states of a given compound have very similar r_e values, the relative fluorescent intensities of the various electronic systems are essentially completely determined by algebraic factors.

The model is intended as a framework in which the extent of the breakdown of atomic spin–orbit coupling under incipient bond formation can be quantitatively discussed, although the limited body of experimental evidence on lifetimes and relative fluorescent intensities from low vibrational levels if I_2 and ICl is not inconsistent with the model in even its crudest form.

Acknowledgement

The stimulus for this work came from the experimental program of the Laser Spectroscopy Group at Edinburgh, and the authors have benefitted from many discussions with all the members of that group, especially R.J. Donovan, P.R.R. Langridge-Smith and T. Ridley.

Appendix A

The details of the atomic configurations in the Russell–Saunders coupling scheme which form the basis of the discussion of the diatomic halogens at long range are as follows, where the numerical coefficients are the $\langle kM_LM_S|LSJM_J\rangle$ of eq. (4).

p^5 configuration:

$$^2P_{3/2,3/2} = \|1^+1^-0^+0^-1^+\|,$$

$$^2P_{3/2,1/2} = (1/\sqrt{3})[\|1^+1^-0^+0^-1^-\| - \sqrt{2}\|1^+1^-0^+1^+1^-\|],$$

$$^2P_{1/2,1/2} = (1/\sqrt{3})[\|\sqrt{2}\|1^+1^-0^+0^-1^-\| + \|1^+1^-0^+1^+1^-\|].$$

p^4 configuration:

$$^1S_0 = (1/\sqrt{3})[\|1^+0^+0^-1^-\| - \|1^-0^+0^-1^+\| + \|1^+1^-1^+1^-\|],$$

$$^1D_{2,2} = \|1^+1^-0^+0^-\|,$$

$$^1D_{2,1} = (1/\sqrt{2})[\|1^+1^-0^+1^-\| - \|1^+1^-0^-1^+\|],$$

$$^1D_{2,0} = (1/\sqrt{6})[-\|1^+0^+0^-1^-\| + \|1^-0^+0^-1^+\| + 2\|1^+1^-1^+1^-\|],$$

$$^3P_{0,0} = -(1/\sqrt{6})[\|1^+0^+0^-1^-\| + \|1^-0^+0^-1^+\| + \sqrt{2}\|1^+0^+1^+1^-\| + \sqrt{2}\|1^+1^-0^-1^-\|],$$

$$^3P_{1,1} = -\tfrac{1}{2}[\sqrt{2}\|1^+0^+0^-1^+\| + \|1^+1^-0^-1^+\| + \|1^+1^-0^+1^-\|],$$

$$^3P_{1,0} = (1/\sqrt{2})[-\|1^+1^-0^-1^-\| + \|1^+0^+1^+1^-\|],$$

$$^3P_{2,2} = \|1^+1^-0^+1^+\|,$$

$$^3P_{2,1} = \tfrac{1}{2}[\|1^+1^-0^-1^+\| + \|1^+1^-0^+1^-\| - \sqrt{2}\|1^+0^+0^-1^+\|],$$

$$^3P_{2,0} = (1/\sqrt{6})[\|1^+1^-0^-1^-\| + \|1^+0^+1^+1^-\| - \sqrt{2}\|1^+0^+0^-1^-\| - \sqrt{2}\|1^-0^+0^-1^+\|].$$

Appendix B

The simple product IP and AP wavefunctions used above are not orthogonal:

$$\langle \mathrm{IP}(n'\Omega)|\mathrm{AP}(n''\Omega)\rangle = \sum \langle k'M'_LM'_S|L'J'M'\rangle_A \langle k''M''_LM''_S|L''J''M''\rangle_A \langle k''M''_LM''_S|L''J''M''\rangle_B \times \langle \Delta_A^{(5)}(k''M''_lM''_s)\Delta_B^{(5)}(k''M''_LM''_S)|\Delta_B^{(6)}\Delta_A^{(4)}(k'M'_lM'_s)\rangle . \quad (B.1)$$

Making the same restriction to $p_\sigma \leftrightarrow p_\sigma$ electron transfer that led to eqs. (13) and (14), we can formally project a p_σ orbital for the purposes of evaluating the overlap integral as follows

$$|p_\sigma\rangle_{A,B} = |p_\sigma\rangle_{B,A} S_{\sigma\sigma}(r), \quad (B.2)$$

where $S_{\sigma\sigma}(r)$ is the two centre overlap integral between p_σ orbitals analogous to $M_{\sigma\sigma}(r)$ in (18). The overlap

between AP($n''\Omega$) and IP($n'\Omega$) will thus be proportional to exactly the same $\zeta_{n'n''\Omega}$ coefficients that govern the transition dipole. Furthermore, from standard first-order perturbation theory in a non-orthogonal basis, the extent of mixing of a given pair of AP and IP states is also proportional to $\zeta_{n'n''\Omega}$ and so the relative transition moments between various upper and lower states are unchanged.

Appendix C

In the p^n atomic positive ion configuration, with mean square electron radius $\langle p|\rho^2|p\rangle_+$, the matrix elements of the charge–quadrupole interaction under Russell–Saunders coupling are (see e.g. ref. [26] for the diagonal terms in the $J=3/2$ case)

$$\langle J_1|\tfrac{1}{2}\Theta_{zz}F'_{zz}|J_2\rangle = e^2\langle {}^{2S+1}L_{J1M}|\sum_{i=1,n} Y_{20}(\theta_i)|{}^{2S+1}L_{J2M}\rangle\langle\rho^2\rangle_+/r_{AB}^3, \tag{C.1}$$

where r_{AB} is the ionic separation, F'_{zz} the field gradient and it is assumed in the off-diagonal elements that the radial p-wavefunctions are identical in the two J states of the positive ion. Using the expansion for the atomic ion states in terms of Slater determinants given in appendix A we have explicitly for the angular integrals in eq. (C.1) for the triplet states of $A^+(p^4)$ ions

$$\langle {}^3P_{20}|\sum Y_{20}(\theta_i)|{}^3P_{20}\rangle = 1/5, \quad \langle {}^3P_{20}|\sum Y_{20}(\theta_i)|{}^3P_{00}\rangle = \sqrt{2}/5,$$
$$\langle {}^3P_{21}|\sum Y_{20}(\theta_i)|{}^3P_{21}\rangle = 1/10, \quad \langle {}^3P_{21}|\sum Y_{20}(\theta_i)|{}^3P_{11}\rangle = 3/10,$$
$$\langle {}^3P_{22}|\sum Y_{20}(\theta_i)|{}^3P_{22}\rangle = -1/5, \quad \langle {}^3P_{10}|\sum Y_{20}(\theta_i)|{}^3P_{10}\rangle = -1/5,$$
$$\langle {}^3P_{11}|\sum Y_{20}(\theta_i)|{}^3P_{11}\rangle = 1/10, \tag{C.2}$$

and for the $Rg^+(p^5)$ ions

$$\langle {}^2P_{3/2,3/2}|\sum Y_{20}(\theta_i)|{}^2P_{3/2,3/2}\rangle = -1/5, \quad \langle {}^2P_{3/2,1/2}|\sum Y_{20}(\theta_i)|{}^2P_{3/2,1/2}\rangle = 1/5,$$
$$\langle {}^2P_{3/2,1/2}|\sum Y_{20}(\theta_i)|{}^2P_{1/2,1/2}\rangle = \sqrt{2}/5 \tag{C.3}$$

(zero elements omitted). In all cases only mixing between two J states having the same spin multiplicity is induced if spin–orbit coupling is neglected. The first-order expression for the coefficient c of J state mixing,

$$|LSJ_1M\rangle^{(1)} = |LSJ_1M\rangle^{(0)} + c^{(1)}|LSJ_2M\rangle^{(0)} \tag{C.4}$$

is then

$$c^{(1)} = (e^2\langle LSJ_1M|\sum Y_{20}(\theta_i)|LSJ_2M\rangle\langle\rho^2\rangle_+/r_{AB}^3)[E_X^{(0)}(LSJ_1M) - E_X^{(0)}(LSJ_2M)], \tag{C.5}$$

where we have assumed that the zeroth-order splitting between the two states at a finite r (i.e. with the Coulomb interaction included) remains that of the ionic electronic term values. Then, in the following cases we find for the extent of electrostatically induced mixing in the $(J_AM_AJ_BM_B)$ basis used in this paper

$I_2(D)$; $[I^+({}^3P_{20})\rangle + c|I^+({}^3P_{00}\rangle]$, $c=0.21$ $(\langle\rho^2\rangle_+ = 1.87\,\text{Å}^2)$,

ICl(E); $[I^+({}^3P_{20})\rangle + c|I^+({}^3P_{00}\rangle]$, $c=0.28$ $(\langle\rho^2\rangle_+ = 1.87\,\text{Å}^2)$,

$Br_2(D)$; $[|Br^+({}^3P_{20})\rangle + c|Br^+({}^3P_{00})\rangle]$, $c=0.39$ $(\langle\rho^2\rangle_+ = 1.34\,\text{Å}^2)$,

XeI(B(1/2)); $[|Xe^+({}^2P_{3/21/2})\rangle + c|Xe^+({}^2P_{1/21/2})\rangle]$, $c=0.11$ $(\langle\rho^+\rangle_+ = 1.66\,\text{Å}^2)$, (C.6)

where the atomic radii are taken from ref. [27]. For Cl_2 the first-order treatment will break down near r_e.

Diagonalizing the 2×2 matrix of the charge–quadrupole interaction among triplet positive ion RS states $^3P_{20}$ and $^3P_{00}$ at an estimated $r_e = 2.9$ Å [10] gives

$$Cl_2(0_u^+(1)); \quad [c_1|Cl^+(^3P_{20})\rangle + c_2|Cl^+(^3P_{00})\rangle], \quad c_1 = 0.70 \quad (\langle\rho^2\rangle_+ = 1.05\ \text{Å}^2). \tag{C.7}$$

Although the full four state coupling problem with the spin–orbit operator explicitly included, should be solved (see Chang [28] for the corresponding treatment of valence states at long range), there is no doubt that a better description of Cl^+ in the lowest IP ($\Omega = 0$) state near the outer minimum is the fully L–S decoupled Hund's case (a) one.

$$|Cl^+\rangle = (1/\sqrt{2})[\|1^+1^-0^- - 1^-\| + \|1^+0^+ - 1^+ - 1^-\|] = (1/\sqrt{3})[|^3P_{20}\rangle - \sqrt{2}|^3P_{00}\rangle], \tag{C.8}$$

and the overall state classified as $^3\Pi_0^+$. The wavefunction of the second root would be

$$|Cl^+(0^+(2))\rangle = (1/\sqrt{2})[\|1^+0^+0^- - 1^-\| + \|1^-0^+0^- - 1^+\|] = (1/\sqrt{3})[\sqrt{2}|^3P_{20}\rangle + |^3P_{00}\rangle], \tag{C.9}$$

making the complete state $^3\Sigma_0^-$. Combined with the Cl^- p^6 wavefunction, the overall configuration of Cl_2 in its lowest $0_{g,u}^+$ pair of IP states becomes the simple molecular orbital one $\sigma_g\pi_u^4\pi_g^3\sigma_u^2$ and $\sigma_g\pi_u^3\pi_g^4\sigma_u^2$. These triplet structures are reached in the heavier halogen IP $0_g^+(1)$ and $0_u^+(1)$ states only on the repulsive wall of the potential. From the result of an ab initio calculation, Balasubramanian [29] attributes the configuration $^3\Sigma_0^-$ (2332) to the lowest IP 0_u^+ state if Br_2 at its calculated r_e of 3.14 Å, whereas the above diagonalisation of the quadrupole–charge interaction predicts the $^3\Pi_{0+}$ state to lie lower. It is not clear what effect the full inclusion of spin–orbit coupling would have on the ab initio result.

References

[1] J.C.D. Brand, U.D. Deshpande, A.R. Hoy and S.M. Jaywant, J. Mol. Spectry. 100 (1983) 416; D. Bussieres and A.R. Hoy, Can. J. Phys. 62 (1984) 1941.
[2] R. Bacis, M. Broyer, S. Churassy, J. Verges and J. Vigue, J. Chem. Phys. 73 (1980) 2641.
[3] T. Ishiwata, T. Hara, K. Obi and I. Tanaka, J. Chem. Phys. 87 (1987) 2513.
[4] T. Ishiwata, K. Obi and I. Tanaka, J. Mol. Spectry. 127 (1988) 353.
[5] J.H. Van Vleck, Phys. Rev. 33 (1929) 467.
[6] G. Herzberg, Molecular Spectra and Molecular Structure, Vol. 1. Spectra of Diatomic Molecules (Van Nostrand, Princeton, 1950) p. 319.
[7] M. Saute and M. Aubert-Frecon, J. Chem. Phys. 77 (1982) 5639.
[8] E.P. Gordeev, S.Ya. Umansky and A.I. Voronin, Chem. Phys. Letters 44 (1976) 36.
[9] S.D. Peyerimhoff and R.J. Buenker, Chem. Phys. 57 (1981) 279.
[10] T. Shinzawa, A. Tokunaga, T. Ishiwata and I. Tanaka, J. Chem. Phys. 83 (1985) 5407.
[11] E.P. Gordeev, S.Ya. Umansky and A.I. Voronin, Chem. Phys. Letters 23 (1973) 524.
[12] R.S. Mulliken, J. Chem. Phys. 55 (1971) 288.
[13] T.H. Dunning and P.J. Hay, J. Chem. Phys. 69 (1978) 134.
[14] E.U. Condon and G.H. Shortley, The Theory of Atomic Spectra (Cambridge Univ. Press, Cambridge, 1963).
[15] P.J. Hay and T.H. Dunning, J. Chem. Phys. 69 (1978) 2209.
[16] J. Tellinghuisen, Chem. Phys. Letters 105 (1984) 241.
[17] K. Balasubramanian, Chem. Phys. 95 (1985) 225.
[18] J.P. Berrot, B. Flemelat, J.L. Subtil, M. Broyer and J. Chevalyre, Mol. Phys. 61 (1987) 85.
[19] M.C. Sauer, W.A. Mulac, R. Cooper and F. Grieser, J. Chem. Phys. 64 (1976) 4587.
[20] J. Tellinghuisen, J. Phys. Chem. 87 (1983) 5136.
[21] T. Ishiwata, H. Ohtoshi, M. Sakaki and I. Tanaka, J. Chem. Phys. 80 (1984) 1411.
[22] A.R. Hoy and J.C.D. Brand, Chem. Phys. 109 (1986) 109.
[23] R.J. Donovan, B.V. O'Grady, K. Shobotake and A. Hiraya, Chem. Phys. Letters 122 (1985) 612.
[24] R.J. Donovan, M.A. McDonald, K.P. Lawley, A.J. Yencha and A. Hopkirk, Chem. Phys. Letters 138 (1987) 571.
[25] D.W. Setser and J. Ku, in: Photodissociation and Photochemistry Above 6 eV (Elsevier, Amsterdam, 1985).
[26] J. Tellinghuisen, A.K. Hays, J.M. Hoffmann and G.S. Tisone, J. Chem. Phys. 65 (1976) 4473.
[27] J.P. Desclaux, At. Data Nucl. Data Tables 12 (1973) 312.
[28] T.Y. Chang, Revs. Mod. Phys. 39 (1967) 911.
[29] K. Balasubramanian, Chem. Phys. 119 (1988) 41.

Chemical Physics 151 (1991) 103–109
North-Holland

Determination of the radiative lifetimes of nine ion-pair states of I_2

P.J. Jewsbury, K.P. Lawley [1], T. Ridley, F.F. Al-Adel [2], P.R.R. Langridge-Smith and R.J. Donovan

Department of Chemistry, University of Edinburgh, West Mains Road, Edinburgh, EH9 3JJ, UK

Received 20 August 1990

The radiative lifetimes of 9 out of the 20 possible ion-pair states of I_2 have been measured using two-colour optical–optical double-resonance excitation. A pulse-shortened dye laser was used to populate the final state. Lifetimes for all six states in the first cluster – $\delta(2_u)$, $\gamma(1_u)$, $D(0_u^+)$, $D'(2_g)$, $\beta(1_g)$ and $E(0_g^+)$ – have been measured again in view of the often discordant literature values. The lifetimes of three states in the second ion-pair cluster ($H(1_u)$, $F(0_u^+)$ and $f(0_g^+)$) are reported for the first time. No significant pressure dependence was found up to 100 m Torr, with the exception of the longest lived γ state.

1. Introduction

Halogen and interhalogen excited-state radiative lifetimes have been used to calculate collision cross sections and to elucidate kinetic schemes [1–10]; they have guided the development of laser systems [9–10] and have been used by early workers to locate and quantify couplings between electronic states [11], in particular the $B(0_u^+)$ valence state [8,12–15] where lifetimes are shortened by predissociation. These couplings are important in the application of the optical–optical double-resonance (OODR) technique since they allow a large range of further excited states to be reached in the second resonant step. This is particularly pertinent for I_2 whose complete first ion-pair cluster, comprising the six states dissociating to $I^+(^3P_2)$ and $I^-(^1S_0)$ ions, can be populated from the $B(0_u^+)$ intermediate state, in some cases indirectly using states accidentally coupled to the B state. Lifetime studies of these ion-pair (IP) states were initially pursued for the development of a laser based on the D→X transition in I_2 [9–10]. More recently, Einstein *A*-coefficients of individual electronic transitions deduced from lifetime measurements have been used to put transition dipole moment functions obtained from dispersed fluorescence data on an absolute basis [16–18]. This last step completes the interpretation of dispersed fluorescence data [19,20], but is only possible when the lifetime of at least one vibrational level of the upper electronic state has been measured. Although the lower vibrational levels of the halogen and interhalogen IP states are not predissociated, their lifetimes are expected to be short (≈ 10 ns) since they are both highly energetic and all have strong spin-allowed charge transfer transitions to one or more valence states. This may be contrasted with the longer lived valence excited states with radiative lifetimes of about 100 ns. In low vibrational levels, the detailed difference in lifetimes between IP states reflects subtle changes in their electronic configuration within the broad context of their ion-pair nature and also in that of the valence states at large interatomic separations to which they fluoresce.

As part of a continuing study we report the lifetimes in low vibrational levels of nine out of the twenty ion-pair states of I_2. We include the six states of the first ion-pair cluster [$D'2_g$, $v=2$), $\beta(1_g, v=2)$, $D(0_u^+, v=0)$, $E(0_g^+, v=0)$, $\gamma(1_u, v=0)$ and $\delta(2_u, v=2)$] correlating with $I^+(^3P_2)+I^-(^1S_0)$, and three of the six states in the second cluster [$f(0_g^+, v=0)$, $F(0_u^+, v=0)$ and $H(1_u, v=0)$ correlating with $I^+(^3P_{1,0})+I^-(^1S_0)$]. In a second paper in prepara-

[1] Author for correspondence.

[2] Permanent address: Laser Research Laboratory, KFUPM/RI, Box 732, 31261 Dhahran, Saudi Arabia.

0301-0104/91/$ 03.50

tion [21] we shall present the relative fluorescent intensities and detailed Einstein A-coefficients for transitions from these states to all the accessible lower valence states. Relative IP to valence transition dipole moments will then be analysed in terms of the mixing of pure Russell–Saunders ionic or atomic states under the influence of interatomic and spin–orbit forces [22].

2. Experimental

2.1. The pump and probe lasers

Two-colour optical–optical double resonance was used to excite the ion-pair states of I_2, employing the $B(0_u^+)$ state as the resonant intermediate level. The experimental configuration is shown in fig. 1. The pulsed output from a high-power excimer laser (Lambda Physik EMG 201 MSC), operating on the 308 nm XeCl (B→X) transition, was used to pump two dye lasers simultaneously. The first dye laser (Lambda Physik FL2002) selectively excited single rovibronic levels of the $B(0_u^+)$ state; the second dye laser (Lambda Physik FL3002E) with pulses shortened to 4 ns half width (measured on a Tetronix 2445 oscilloscope) by a pulse compressor (Lambda Physik FL90), pumped molecules from the B state to the various ion-pair states. Coumarin 307 and Coumarin 102 were used as the pump and probe dyes to access the D′ and D states, Coumarin 307 and Coumarin 47 for the γ and δ states, Rhodamine 6G and Bis MSB (stilbene) for the E(β) states, Rhodamine 6G and PTP for the f state and Coumarin 307 with DMQ for the F and H states. The I_2 samples (0.05 and 0.1 Torr) were held in cylindrical glass cells with spectrosil quartz windows and the path lengths so arranged that the collinear, counterpropagating pulsed outputs from the two dye lasers arrived together. Fluorescence was collected at right angles to the laser paths and imaged on to the entrance slit of a monochromator (Jobin-Yvon HRS2; $f/7$, 0.6 m); dispersed fluorescence at the exit slit was monitored by a photomultiplier (Hamamatsu R928: rise time 2.2 ns, whose transient output was fed into a Stanford Research Systems SR250 gated integrator (gate width less than 2 ns), interfaced to an IBM PC microcomputer. The gate scanning and data collection were controlled by a Stanford Research Systems SR265 software package; after down loading to the local mainframe, data were manipulated as described below. The boxcar gate was scanned across the fluorescence decay profile collected at the wavelength of the strongest transition in each ion-pair system over 50, 75 or 100 ns, depending on the lifetime of the state. The transitions monitored are given in table 1.

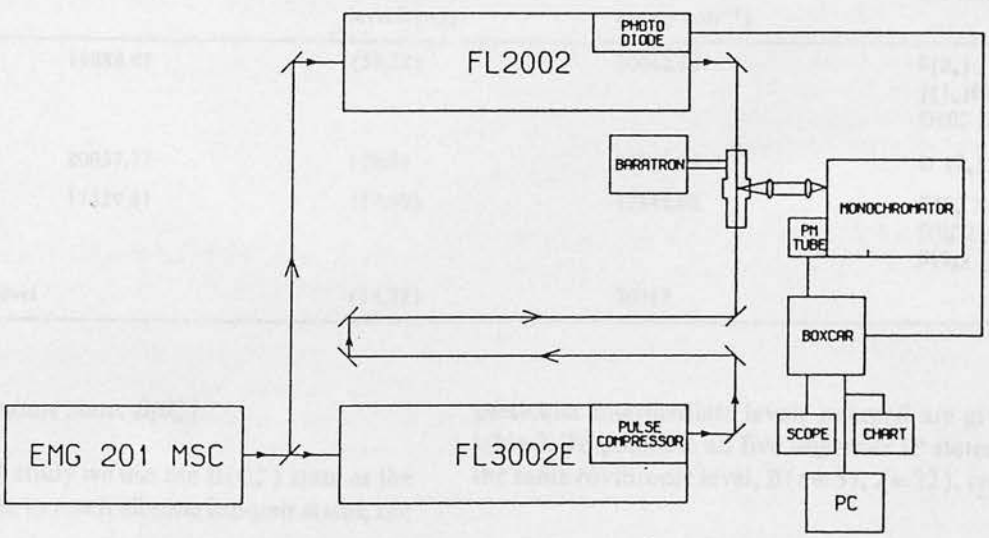

Fig. 1. Schematic diagram of the experimental apparatus.

Table 1
Radiative lifetimes for nine ion-pair states of I_2. Experimental uncertainties are given in brackets ( )

This work				τ(ns), previous studies			
Ion-pair state	Transition monitored	50 mTorr τ(ns)	100 mTorr τ(ns)	ref. [24]	ref. [16]	ref. [25]	
$\delta(2_u)$ $v=2$	$\rightarrow 2_g$ (aa)	25.8 (1.0)	26.7 (1.0)	15 (3)[a]			
$\gamma(1_u)$ $v=0$	$\rightarrow$a: 1_g (aa)	36.0 (0.6)	33.4 (0.5)	8 (4)[a]			
$E(0_g^+)$ $v=0$	$\rightarrow$B: 0_u^+ (ab)	26.6 (1.4)	25.3 (1.4)	10 (3)	25.5[d]	28 (1)[d]	27 (2)[f]
$D(0_u^+)$ $v=0$	$\rightarrow$X: 0_g^+ (aa)	13.3 (0.6)	13.0 (0.6)				15.5 (0.5)[e]
$\beta(1_g)$ $v=2$	$\rightarrow$A: 1_u (aa)	11.8 (0.4)	11.5 (0.4)	8 (3)[b]	11.4[d]	12 (1)[d]	
$D'(2_g)$ $v=0$	$\rightarrow$A′: 2_u (aa)	8.5 (1.0)[g]	7.7 (1.0)	5 (3)[c]			6.7 (0.5)[e]
$f(0_g^+)$ $v=0$	$\rightarrow$B	14.0 (0.7)	13.4 (0.7)				
$F(0_u^+)$ $v=0$	$\rightarrow$X		4.5 (1.0)				
$H(1_u)$ $v=0$	$\rightarrow$a		15.4 (0.2)				

[a] $v=1$. [b] $v=7$. [c] $v=4$. [d] By extrapolation. [e] v unknown [2,9]. [f] $v\approx 46$, [26]. [g] Measured at 60 mTorr.

Table 2
The OODR pumping scheme; the B($v'J'$) levels used and their perturbations (see ref. [23])

Parent state X(v, J)	Transition energy (cm^{-1})	Pumped intermediate level B(v, j)	Intermediate state energy (cm^{-1})	Ion pair destination
(0,21)	19888.41	(59,22)	20012.85	$\delta(2_u)$ $\gamma(1_u)F(0_u^+)$ $D(0_u^+)H(1_u)$
(0,7)	20037.77	(78,8)	20146.85	$D'(2_g)$
(1,70)	17339.81	(17,69)	17845.00	$E(0_g^+)$ $f(0_g^+)$ $\beta(1_g)$
perturbing 1_g(ab) level		(14,22)	20013	

2.2. The intermediate state, $B(0_u^+)$

In this OODR study we use the $B(0_u^+)$ state as the intermediate state to reach all nine ion-pair states; the particular intermediate levels pumped are given in table 2. To populate all five *ungerade* IP states from the same rovibronic level, B($v=59, J=22$), requires

coupling between the B state and a 1_g(ab) state [#1]. There are two such states, the lower is shallowly bound and the other purely repulsive. The perturbation comes from the bound state because we have observed that in the 460 nm region the transition $\gamma(v'=0, J'\approx 23) \rightarrow 1_g(v''=14, J''\approx 22)$ lies under the probe pulse (the 1_g vibrational assignment comes from vibrational term values derived from dispersed fluorescence data to be presented [21]). The B and 1_g(ab) rovibronic levels in question are nearly resonant, have strong Franck–Condon overlap near their outer classical turning points and can couple through the hyperfine nuclear magnetic dipole [27]. This coupling is clearly efficient enough for collisional transfer out of the resonant B rovibronic level, which competes with the probe stage, not to be significant at our sample pressures; at 100 m Torr a B state molecule has about a 1 in 60 chance of collision in the duration of the probe pulse, assuming a generous collisional cross section of 75 Å^2 [8]. An ion-pair state of *ungerade* symmetry is then accessed near its potential minimum ($\approx$3.6 Å) by a vertical transition in the final excitation stage from the very shallow bound 1_g(ab) state.

The OODR scheme to populate the D′ ion-pair state uses a rovibronic level, B(v=78, J=8), close to the B state dissociation limit as the intermediate. Rotational coupling to a 1_u(ab) state at large R gives access to the D′(2_g) ion-pair state near its potential minimum [25] by excitation at the inner turning point of the 1_u state. The E and f states are readily accessed with two parallel transitions using the B(v=17, J=69) level as the intermediate.

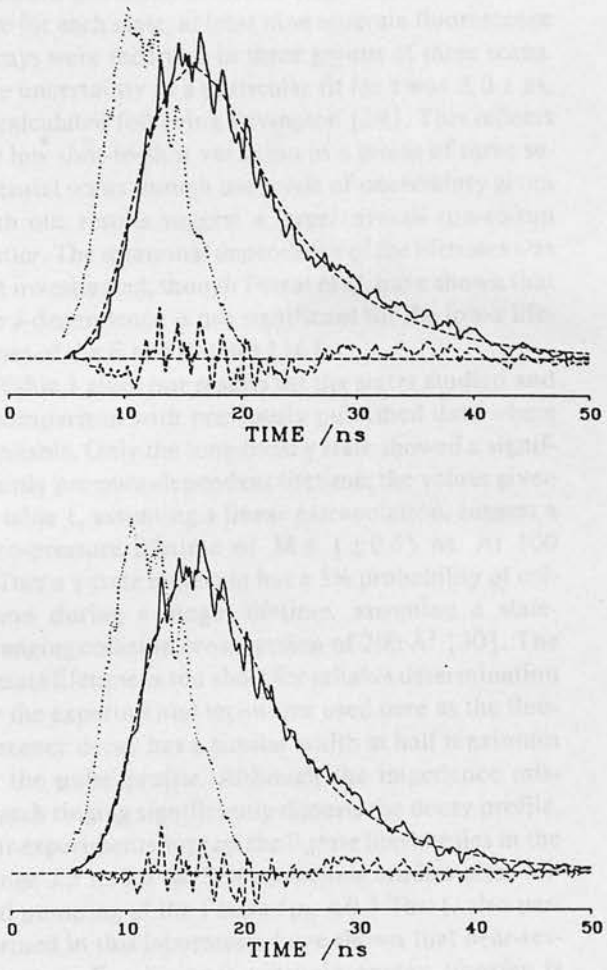

Fig. 2(a). Fluorescence decay curve for the D′→A′ emission (full line) following excitation by a compressed pulse (....), before impedance-mismatch ripple removed. The best-fit simulated decay is also shown (—), together with the residual signal along the base line. (b) Fluorescence decay curve for the D′→A′ emission after the impedance mismatch ringing has been removed (full line).

3. Results and analysis

Representative examples of the shape of the time-resolved fluorescence, $I_n^{obs}(t)$, are shown in figs. 2–4, for short-, intermediate- and longer-lived states, respectively, together with their simulation, $I_n^{conv}(t)$, a pulse profile $P(t)$ and the residual, $I_n^{obs}(t) - I_n^{conv}(t)$. The complete fluorescence decay was simulated by convoluting the pulse profile with a single exponential decay to give a best-fit lifetime, τ, and the pre-exponential factor, A:

$$I_n^{conv}(t) = A\int_{t_0}^{t} P(t')\exp(t'-t)/\tau\,dt' ,$$

where t_0 is the pulse arrival time. A first estimate of the lifetime was obtained either by the method of moments [28], or by a simple fitting of the exponential tail of the fluorescence signal after the excitation pulse is over. A steepest-descent parameter search was

[#1] Here a refers to a ground and b to a spin–orbit excited-state atom as the adiabatic dissociation products of the molecular state.

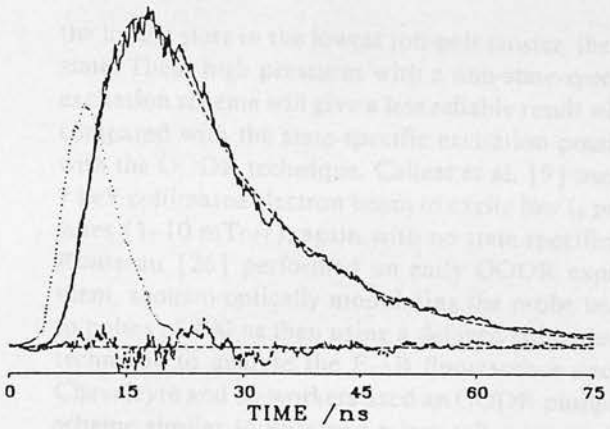

Fig. 3. The fluorescence decay curve for the H→a emission after the impedance mismatch ringing has been removed. Key as in fig. 2(a).

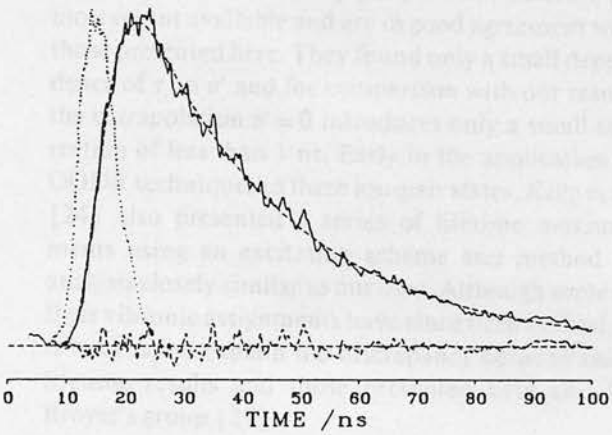

Fig. 4. The fluorescence decay curve for the $\delta \rightarrow 2_g(aa)$ emission after the impedance mismatch ringing has been removed. Key as in fig. 2.

then used to minimise the standard deviation between signal and simulation. The best-fit values of τ showed no significant dependence on the upper time limit for fitting (generally taken to be 3τ), nor on the choice of initial lifetime, except for the γ state. For this state the long lifetime left a significant cut-off error and the method of moments calculation was not used. A slight ringing, possibly resulting from a small impedance mismatch in the collection electronics, was found in all the decay curves recorded and this was filtered out numerically since this did not significantly alter the best estimates of τ, but did reduce the standard deviation of the fit (fig. 2b). At each pressure for each state, at least nine separate fluorescence decays were recorded in three groups of three scans. The uncertainty in a particular fit for τ was ± 0.1 ns, as calculated following Bevington [29]. This reflects the low shot-to-shot variation in a group of three sequential scans though the levels of uncertainty given with our results suggest a larger overall run-to-run scatter. The rotational dependence of the lifetimes was not investigated, though Perrot et al. have shown that the J-dependence is not significant for the low-v lifetimes of the E and β states [16].

Table 1 gives our results for the states studied and a comparison with previously published data where available. Only the long-lived γ state showed a significantly pressure-dependent lifetime: the values given in table 1, assuming a linear extrapolation, suggest a zero-pressure lifetime of 38.6 (± 0.6) ns. At 100 mTorr a γ state molecule has a 5% probability of collision during a single lifetime, assuming a state-changing collision cross section of 200 Å^2 [30]. The F state lifetime is too short for reliable determination by the experimental technique used here as the fluorescence decay has a similar width at half maximum to the pulse profile. Although the impedance mismatch ringing significantly distorts the decay profile, our experiments suggest the F state lifetime lies in the range 3.5 to 5.5 ns. Self-quenching studies after initial pumping of the f state ($p_{I_2} < 0.3$ Torr), also performed in this laboratory, have shown that near-resonant f→F collisional vibronic energy transfer is much more efficient than F→f transfer. Such a short F state lifetime suggests that radiative decay is successfully competing with collisional transfer for the F state population at these low I_2 pressures.

4. Discussion

4.1. Comparison with other measurements

Two of the previous lifetime measurements referred to in table 1 used non-state-specific excitation schemes [2,9]. Sauer and co-workers [2] used an electron beam to excite an Ar/I_2 mixture and then monitored the $D' \rightarrow A'$ fluorescence at 342 nm. They used high buffer gas pressures (344 and 700 Torr) to quench the excited ion-pair molecules collisionally to

the lowest state in the lowest ion-pair cluster, the D' state. These high pressures with a non-state-specific excitation scheme will give a less reliable result when compared with the state-specific excitation possible with the OODR technique. Callear et al. [9] used a 7 keV collimated electron beam to excite low I_2 pressures (1–10 mTorr), again with no state specificity. Rousseau [26] performed an early OODR experiment, acousto-optically modulating the probe beam to pulses of 100 ns then using a delayed coincidence technique to analyse the E→B fluorescence decay. Chevaleyre and co-workers used an OODR pumping scheme similar to ours and a low cell pressure (30 mTorr) to record the fluorescence decay from the E and β states [25]. More recently the same group presented a thorough analysis of the lifetimes and radiative intensities of the same states between $10 \leqslant v' \leqslant 33$ and $0 \leqslant v' \leqslant 28$ respectively [16]. Their results are the most recent available and are in good agreement with those presented here. They found only a small dependence of τ on v' and for comparison with our results the extrapolation $v' = 0$ introduces only a small correction of less than 1 ns. Early in the application of OODR techniques to these ion-pair states, King et al. [24] also presented a series of lifetime measurements using an excitation scheme and method of analysis closely similar to our own. Although some of their vibronic assignments have since been revised, it is not easy to explain the discrepancy between their lifetime results and those presented here and by Broyer's group [27].

4.2. Interpretation of results

Radiative lifetimes of states free from predissociation depend on three factors: the Franck–Condon overlap integrals, the radiative frequencies and the transition moments of each of the dipole-allowed transitions of the state

$$1/\tau_{n'v'} = (64\pi^4/3hc^3) \sum_{n''v''} \langle v' | \mu_{n'n''}(r) | v'' \rangle^2 \nu^3_{n'v'n''v''} .$$

All the ion-pair states have very similar R_e and ω_e values and so the dominant factor in determining the differences in lifetimes of electronically similar states is the ν^3 factor. This is clearly an important factor and is responsible for the lifetimes of the states in the second cluster, with term values roughly 6000 cm^{-1} greater than those in the first cluster, being consistently shorter than the corresponding state in the first cluster. Based solely on this factor, the 0_u^+ state in each cluster, which alone can fluoresce directly to the ground state, should have the shortest lifetime in its group. In the first cluster the D state does have one of the shorter lifetimes, but not quite the shortest. Furthermore, if we compare the $E(0_g^+)$ and $D(0_u^+)$ states, in which the I^+ ion is in the same JM_J state, the lifetimes should be very similar after allowing for the ν^3 factor. The 0–0 band of the E→B fluorescence is at 23 412 cm^{-1} and that of the D→X emission is at 32 049 cm^{-1} so the ν^3 factor would predict a lifetime ratio $\tau_E/\tau_D \approx 2.56$ compared with the observed ratio of 1.98 (±0.2), which is not too dissimilar. In contrast, the pair of $\Omega = 2$ states of the first cluster, δ and D', have their principal fluorescence originating at 340 nm and 342 nm, respectively, so the ν^3 factor would lead to a lifetime ratio of unity, but $\tau_\delta/\tau_{D'}$ is observed to be 3.2 (±0.2). Relatively small departures from the simple ion-pair model for the excited states (and the atom-pair model for the lower valence state) have clearly produced large changes in the transition dipole together with some redistribution of the oscillator strength among the final valence states. A fuller discussion of these points will be made in a paper reporting the relative fluorescent intensities of transitions from the ion-pair states to their respective valence states [21].

5. Conclusions

Radiative lifetimes with a precision of at least ±1.5 ns for nine out of the twenty ion-pair states of I_2 have been determined, (table 1). In every case the decay data could be adequately fitted by the convolution of the excitation pulse with a single exponential decay function. No significant pressure dependence of the lifetimes was found up to 100 mTorr, except for the longest lived state, the $\gamma(1_u)$ state. There is almost an order of magnitude range in the lifetimes, from the shortest lived F state (≈4.5 ns) to the $\gamma(1_u)$ state (38 ns). Considerable differences in lifetime of apparently closely related ion-pair states (e.g., g/u pairs

in the same cluster) remain after allowing for the ν^3 factor in the Einstein A-coefficients.

Acknowledgements

PJJ would like to thank ICI plc for the award of a Scientific Scholarship. PRRL-S would like to thank Rainer Patzel (Lambda Physik) for the original loan of an FL90 pulse compression unit. FFAl-A gratefully acknowledges the support of the British Council and KFUPM.

References

[1] M.A.A. Clyne and I.S. McDermid, Electronically excited states of small molecules, in: Dynamics of the Excited State, ed. K.P. Lawley (Wiley, New York, 1982).

[2] M.C. Sauer Jr., W.A. Mulac, R. Cooper and F. Grieser, J. Chem. Phys. 64 (1976) 4587.

[3] J. Tellinghuisen and L.F. Phillips, J. Chem. Phys. 90 (1986) 5108.

[4] R.J. Donovan, A.J. Holmes, P.R.R. Langridge-Smith and T. Ridley, J. Chem. Soc. Faraday Trans. II 84 (1988) 541.

[5] M.C. Heaven and L.J. van de Burgt, American Institute of Physics Conference Proceedings 146 (1986) 555.

[6] S.J. Harris, W.C. Natzle and C.B. Moore, J. Chem. Phys. 70 (1979) 4215.

[7] M. Kitamura, T. Kondow, K. Kuchitsu, T. Munakata and T. Kasuya, Chem. Phys. Letters 118 (1985) 130.

[8] G.A. Capelle and H.P. Broida, J. Chem. Phys. 58 (1973) 4212.

[9] A.B. Callear, P. Erman and J. Kurepa, Chem. Phys. Letters 44 (1976) 599.

[10] A.B. Callear and M.P. Metcalfe, Chem. Phys. Letters 43 (1976) 197.

[11] G.W. Holleman and J.I. Steinfeld, Chem. Phys. Letters 12 (1971) 431.

[12] T. Suzuki and T. Kasuya, J. Chem. Phys. 81 (1984) 4818.

[13] J. Tellinghuisen, J. Chem. Phys. 57 (1972) 2397.

[14] C.D. Olsen and K.K. Innes, J. Chem. Phys. 64 (1976) 2405.

[15] M.A.A. Clyne and M.C. Heaven, J. Chem. Soc. Faraday Trans. II 76 (1970) 49.

[16] J.P. Perrot, B. Femelat, J.L. Subtil, M. Broyer and J. Chevaleyre, Mol. Phys. 61 (1987) 85.

[17] A.V. Stolyarov, N.E. Kuz'menko, Ya.A. Harya and R.S. Ferber, J. Mol. Spectry. 137 (1989) 251.

[18] A.J. Holmes, K.P. Lawley, T. Ridley, R.J. Donovan and P.R.R. Langridge-Smith, J. Chem. Soc., Faraday Trans. II, to appear.

[19] J.C.D. Brand and H.R. Hoy, Appl. Spectry. Rev. 23 (1987) 285.

[20] T. Ishiwata and I. Tanaka, Laser Chem. 7 (1987) 79.

[21] R.J. Donovan, P.J. Jewsbury, P.R.R. Langridge-Smith, K.P. Lawley and T. Ridley, to be published.

[22] P.J. Jewsbury and K.P. Lawley, Chem. Phys. 141 (1990) 225.

[23] M.D. Danyluk and G.W. King, Chem. Phys. 22 (1977) 59.

[24] G.W. King, I.M. Littlewood and J.R. Robins, Chem. Phys. 68 (1982) 129.

[25] J. Chevaleyre, J.P. Perrot, J.M. Chastan, S. Valignat and M. Broyer, Chem. Phys. 67 (1982) 59.

[26] D.L. Rousseau, J. Mol. Spectry. 58 (1975) 481.

[27] M. Broyer, J. Vigue and J.C. Lehmann, J. Phys. (Paris) 39 (1978) 591.

[28] J.N. Demas, Excited State Lifetime Measurements, (Academic, New York, 1983) ch. 8;
D.V. O'Connor and D. Phillips, Time-correlated Single Photon Counting, (Academic, New York, 1984) ch. 6.

[29] Data Reduction and Error Analysis for the Physical Sciences, ed. P.R. Bevington (McGraw-Hill, New York, 1969) p. 245.

[30] K.P. Lawley, Chem. Phys. 127 (1988) 363.